

The University of Sheffield



**Control of Current Harmonics in
Dual Three-phase Permanent Magnet
Synchronous Machine Systems**

Luocheng Yan

A thesis submitted for the degree of Doctor of Philosophy

Department of Electronic and Electrical Engineering

The University of Sheffield

Mappin Street, Sheffield, S1 3JD, UK

August 2022

ABSTRACT

Compared to conventional three-phase permanent magnet synchronous machines (PMSMs), dual three-phase (DTP) PMSMs exhibit higher power rating, power/torque sharing capability, and fault-tolerant capability, as well as lower torque ripples. They also maintain the merits of PMSMs, i.e. high power density, high torque density, and high efficiency. However, the major current harmonics are only limited by low impedance composed of resistance and leakage inductance, which makes DTP PMSMs suffer more from current harmonics. This thesis investigates the new and novel control techniques of DTP PMSMs, with particular reference to the control of current harmonics.

A novel virtual impedance technique is proposed to increase the machine equivalent impedance of the DTP PMSM system. It enhances the voltage harmonic disturbance rejection capability and contributes to current harmonic suppression in a wide range of frequencies. In addition, the virtual impedance can also reduce the system sensitivity to parameter variation, which helps to enhance the dynamic performance.

By using the proposed virtual impedance technique, the current harmonics can be reduced but cannot be completely eliminated or cannot track the required current harmonic references. To solve this problem, a new concept of virtual multi three-phase systems is proposed to enhance the current harmonic control in DTP PMSMs. The multiple synchronous reference frames are combined with the virtual multi three-phase systems for establishing current harmonic regulators. Compared to the existing control methods, the proposed method has higher dynamic current harmonic control capability and stability. The proposed concept is further extended to the current harmonic control of the conventional three-phase PMSMs, and also shows improved dynamic performance and stability.

The scaling errors in current measurement will generate non-general current harmonics, which cannot be controlled by current harmonic regulators. An online scaling error correction method is proposed to suppress the current harmonics and torque ripples. The method is based on the injection of a high-frequency carrier voltage, and the control of corresponding high-frequency current harmonics is independent from the torque and speed regulation. The proposed method will not produce any high-frequency torque ripples since it only requires high-frequency injection in the harmonic subspace of DTP PMSMs. In contrast, three-phase PMSMs with high-frequency signal injection usually suffer from significant high-frequency torque ripples.

All the investigations have been carried out by theoretical analyses, simulations, and experimental verification.

ACKNOWLEDGMENT

Words cannot express my gratitude to my supervisor, Professor Zi-Qiang Zhu, for his invaluable guidance and constructive comments throughout this PhD project. Prof. Zhu provided me such a chance to work with one of the top electrical machine and drive research groups in the world. Every meeting and conversation with Prof. Zhu were vital in inspiring me to think outside the box, from multiple perspectives to form a comprehensive and objective critique. Prof. Zhu's guidance is preciously important in my PhD research and will continuously affect my life in the future.

I would like to appreciate Protean Electric for the sponsorship and technical support, leading to such an invaluable experience collaborating with industry. In particular, I would like to thank Dr. Yuan Ren, Dr. Chengwei Gan, Mr. Simon Brockway, and Dr. Chris Hilton in Protean Electric for their help and care during the three years' PhD life.

I would also like to extend my sincere thanks to my brothers and friends around the world. The time we share back in China and here in the United Kingdom is my most precious memory of the past three years. Life without you guys is less colourful just like a TV in black and white.

Special thanks to my families, for their endless love and unconditional support before and during my PhD study. LaoTou and LaoMa, I missed you every single day for the last three years, and I hope you happy and healthy forever.

Finally, to my old friend Miss Jingyi Chen, thank you for your encourage, accompany, and love over the past years. I hope you could find your pastures new and be always like a child girl, always simple, always innocent, and always happy.

CONTENT

ABSTRACT	I
ACKNOWLEDGMENT	II
LIST OF ABBREVIATIONS	VI
LIST OF SYMBOLS	VIII
CHAPTER 1 GENERAL INTRODUCTION	1
1.1 Introduction of DTP PM Machines	5
1.2 Modelling of DTP PM Machines	7
1.2.1 Modelling of Single Three-Phase PM Machines.....	7
1.2.2 Double Three-phase dq Model	8
1.2.3 Vector Space Decomposition Model.....	10
1.3 Field Oriented Control of DTP PM Machines	14
1.3.1 Field Oriented Control of Single Three-phase PM Machines	14
1.3.2 Double Synchronous Reference dq Frame Control of DTP PM Machines.....	16
1.3.3 VSD Control of DTP PM Machines.....	18
1.4 Direct Torque Control of DTP PM Machines.....	25
1.5 Model Predictive Control of DTP PM Machines	28
1.6 Scope of Research and Contributions	30
1.6.1 Scope of Research	30
1.6.2 Contributions	34
CHAPTER 2 ENHANCEMENT OF VOLTAGE HARMONIC DISTURBANCE REJECTION CAPABILITY IN DUAL THREE-PHASE PMSM SYSTEM BY USING VIRTUAL IMPEDANCE	36
2.1 Introduction.....	37
2.2 Control System of DTP PMSM	39
2.2.1 Electrical Machine Model	40
2.2.2 Inverter Model	42
2.2.3 Basic Current Control Loops in Two Subspaces.....	43
2.3 Proposed Control Strategy.....	45
2.3.1 Current Regulator with Virtual Impedance	45
2.3.2 Determination of Virtual Impedance Values.....	47
2.3.3 Parametric Uncertainty	50
2.4 Comparison with Existing Methods.....	51

2.4.1 PIR Regulator	51
2.4.2 Active Damping.....	53
2.4.3 Compensation of Inverter Nonlinearity and Back EMF Harmonics	54
2.4.4 Additional PI Gains	55
2.5 Experimental Verification	55
2.6 Conclusion	62
CHAPTER 3 MULTIPLE SYNCHRONOUS REFERENCE FRAME CURRENT HARMONIC REGULATION OF DUAL THREE-PHASE PMSM WITH ENHANCED DYNAMIC PERFORMANCE AND SYSTEM STABILITY	63
3.1 Introduction	64
3.2 MSRF-based Current Harmonic Control in DTP PMSM System	66
3.2.1 Electrical Machine Model in MSRF.....	66
3.2.2 Basic MSRF Current Regulation.....	69
3.3 Proposed Control Strategy.....	71
3.3.1 Phase Shifting and Current Decomposition.....	71
3.3.2 Current Regulator Design.....	77
3.3.3 Stability Analysis and Phase Compensation	79
3.3.4 Implementation.....	82
3.4 Experimental Verification	85
3.4.1 Current Harmonic Detection and Regulation	85
3.4.2 Comparison with Other MSRF-based Methods	89
3.5 Conclusion	94
CHAPTER 4 CONTROL OF CURRENT HARMONICS FOR DUAL THREE-PHASE PMSMS BY VIRTUAL MULTI THREE-PHASE SYSTEMS	95
4.1 Introduction	96
4.2 Analysis of Decomposition Capability of VSD Techniques in Multi Three-phase Systems.....	97
4.3 Virtual Multi Three-phase System	100
4.4 Simulation Results.....	106
4.5 Experimental Verification	110
4.6 Discussion.....	115
4.6.1 Torque Performance Improvement.....	115
4.6.2 Flux Weakening Operation.....	115
4.6.3 Unbalance Issue.....	116
4.6.4 Extension to Other Multi Three-phase Machine	116
4.7 Conclusion	117

CHAPTER 5 CURRENT MEASUREMENT GAIN COMPENSATION USING HIGH-FREQUENCY SIGNAL INJECTION IN DUAL THREE-PHASE PMSM SYSTEMS	119
5.1 Introduction	120
5.2 Effect of Scaling Error	122
5.3 Scaling Error Correction Using High-Frequency Signal Injection	128
5.4 Simulation Verification	134
5.5 Conclusion	138
CHAPTER 6 ARBITRARY CURRENT HARMONIC DECOMPOSITION AND REGULATION FOR PERMANENT MAGNET SYNCHRONOUS MACHINES	139
6.1 Introduction	140
6.2 Harmonic Analysis of PMSM System	140
6.2.1 General Harmonics with Odd Orders	141
6.2.2 Harmonics with Even Orders	142
6.2.3 Asymmetry among Phases	143
6.2.4 Arbitrary Harmonic Electrical Model	144
6.3 Proposed Control Strategy	148
6.3.1 Arbitrary Current Harmonic Decomposition	148
6.3.2 Current Harmonic Regulation	152
6.4 Experimental Verification	156
6.5 Conclusion	163
CHAPTER 7 GENERAL CONCLUSION	164
7.1 Virtual Impedance Technique	165
7.2 Virtual Multi Three-phase Systems	166
7.3 Improved MSRF Current Regulators	169
7.4 Scaling Error Correction in Current Measurement	170
7.5 Future Work	170
REFERENCES	172
APPENDIX A EXPERIMENTAL SYSTEM SETUP	186
APPENDIX B PUBLICATIONS	188

LIST OF ABBREVIATIONS

A/D	Analog/digital
AC	Alternating current
CPU	Central processing unit
EV	Electric vehicle
DC	Direct current
DOB	Disturbance observer
DSP	Digital signal processor
DTC	Direct torque control
DTP	Dual three-phase
DTP PMSM	Dual three-phase permanent magnet synchronous machine
EMF	Electromotive force
ESO	Extended state observer
FFT	Fast Fourier transformation
FOC	Field oriented control
I/O	Input/output
IGBT	Insulated-gate bipolar transistor
IPM	Interior permanent magnet
LPF	Low pass filter
LUT	Look-up table
MDO	Measurement-disturbance-observer
MMF	Magnetomotive force
MPC	Model-based predictive control
MSRF	Multiple synchronous reference frame
MTP	Multi three-phase

MTPA	Maximum torque per ampere
PC	Personal computer
PTP	Pentuple three-phase
PI	Proportional integral
PIR	Proportional integral resonant
PM	Permanent magnet
PMSM	Permanent magnet synchronous machine
PR	Proportional resonant
PWM	Pulse width modulation
QTP	Quadruple three-phase
SPM	Surface-mounted permanent magnet
SRF	Synchronous reference frame
SVPWM	Space vector pulse width modulation
THD	Total harmonic distortion
TTP	Triple three-phase
VSD	Vector space decomposition
VSI	Voltage source inverter
VV	Voltage vector

LIST OF SYMBOLS

Symbol	Explanation of symbol	Unit
*	Reference value	
$e_\alpha, e_\beta, e_{z1}, e_{z2}$	Back EMF in $\alpha\beta$ and z_1z_2 subspaces	V
e_d, e_q, e_{zd}, e_{zq}	Back EMF in SRF of $\alpha\beta$ and z_1z_2 subspaces	V
$L_{ab}, L_{bc}, L_{ca},$ $L_{ax}, L_{yb}, L_{zc}, \text{ etc.}$	Mutual-inductances between two phases	mH
L_d, L_q	dq -axis self-inductances in SRF	mH
L_D, L_Q	dq -axis self-inductances in SRF of $\alpha\beta$ subspace	mH
L_σ	Leakage inductance	mH
L_s	Synchronous inductance	mH
L_v	Virtual inductance	mH
L_1, L_2	Asymmetric self-inductances	mH
M_1, M_2	Asymmetric mutual-inductances	mH
M_d, M_q	dq -axis mutual-inductances in SRF	mH
R_s	Stator phase resistance	Ω
R_v	Virtual resistance	Ω
R_1, R_2	Asymmetric resistances	Ω
i_a, i_b, i_c	Phase A, B, C currents	A
i_{am}, i_{bm}, i_{cm}	Measured phase A, B, C currents	A
$i_\alpha^{k+1}, i_\beta^{k+1},$ $i_{z1}^{k+1}, i_{z2}^{k+1}$	Predicted currents in $\alpha\beta$ and z_1z_2 subspaces at instant $k+1$	A
i_d, i_q	dq -axis currents in SRF	A
i_{d1}, i_{q1}	dq -axis currents of first three-phase set in SRF	A

i_{d2}, i_{q2}	dq -axis currents of second three-phase set in SRF	A
$i_{dq1}, i_{dq5}, i_{dq7},$ i_{dq11}, i_{dq13}	Complex vectors of 1st, 5th, 7th, 11th, and 13th current components in MSRF	A
i_x, i_y, i_z	Phase X, Y, Z currents	A
i_{xm}, i_{ym}, i_{zm}	Measured phase X, Y, Z currents	A
$i_\alpha, i_\beta, i_{z1}, i_{z2}$	Currents in $\alpha\beta$ and z_1z_2 subspaces	A
$i_{\alpha m}, i_{\beta m}, i_{z1m},$ i_{z2m}	Measured currents in $\alpha\beta$ and z_1z_2 subspaces	A
$i_{c_am}, i_{c_\beta m},$ i_{c_z1m}, i_{c_z2m}	Measured high-frequency currents in $\alpha\beta$ and z_1z_2 subspaces	A
i_{dq}^h	h^{th} current harmonic in h^{th} SRF	A
$\Delta i_\alpha, \Delta i_\beta, \Delta i_{z1},$ Δi_{z2}	Current measurement errors in $\alpha\beta$ and z_1z_2 subspaces	A
$i_{\alpha\beta}, i_{z_1z_2}$	Complex vector of currents in $\alpha\beta$ and z_1z_2 subspaces	A
$i_{\alpha\beta 1}, i_{\alpha\beta 5}, i_{\alpha\beta 7},$ $i_{\alpha\beta 11}, i_{\alpha\beta 13}$	Complex vectors of 1st, 5th, 7th, 11th, and 13th current components in stationary two-phase frame	A
I_m^h	Amplitude of the h^{th} current harmonic	A
u_a, u_b, u_c	Phase A, B, C voltages	V
u_d, u_q	dq -axis voltages in SRF	V
u_{d1}, u_{q1}	dq -axis voltages of first three-phase set in SRF	V
u_{d2}, u_{q2}	dq -axis voltages of second three-phase set in SRF	V
u_x, u_y, u_z	Phase X, Y, Z voltages	V
$u_\alpha, u_\beta, u_{z1}, u_{z2}$	Voltages in $\alpha\beta$ and z_1z_2 subspaces	V
u_d, u_q, u_{zd}, u_{zq}	Voltage in SRF of $\alpha\beta$ and z_1z_2 subspaces	V
u_{dq}^h	h^{th} voltage harmonic in h^{th} SRF	V

K_c, K_{zc}, k_c, k_n	Gain coefficients of PI regulators	rad/s
k_c^h	Gain coefficient of h^{th} current harmonic PI regulator	—
K_a, K_b, K_x, K_y	Gain coefficient errors in current measurement	—
K_{D1}, K_{D2}, K_{D3}	Gain tuning coefficients	—
k_R	Resonant coefficient	—
γ_s	Phase angle of stator flux linkage	Degree
θ_e	Rotor position electrical angle	Degree
θ_0^h	Initial phase angle of the h^{th} current harmonic	Degree
θ^h	Phase angle of the h^{th} current harmonic	Degree
ϕ^h	Delay compensation angle	Degree
$\psi_{fa}, \psi_{fb}, \psi_{fc}$	Phase A, B, C PM flux linkages	Wb
$\psi_{fa}^e, \psi_{fb}^e, \psi_{fc}^e$	Even-order harmonic PM flux linkages	Wb
ψ_{fd}	d -axis PM flux linkage in SRF	Wb
$\psi_{fx}, \psi_{fy}, \psi_{fz}$	Phase X, Y, C PM flux linkages	Wb
ψ_{mag}	Magnitude of stator flux linkage	Wb
$\psi_\alpha, \psi_\beta, \psi_{z1}, \psi_{z2}$	Stator flux linkages in $\alpha\beta$ and z_1z_2 subspaces	Wb
$\psi_{f1}, \psi_{f5}, \psi_{f7},$ ψ_{f11}, ψ_{f13}	Amplitudes of 1st, 5th, 7th, 11th, and 13th PM flux linkages	Wb
$\psi_{fdq1}, \psi_{fdq5},$ $\psi_{fdq7}, \psi_{fdq11},$ ψ_{fdq13}	Complex vectors of 1st, 5th, 7th, 11th, and 13th PM flux linkage components	Wb
ψ_{dq}^h	h^{th} PM flux linkage harmonic in h^{th} SRF	Wb
ω_m	Mechanical angular speed of rotor	rad/s
ω_e	Electrical angular speed of rotor	rad/s
ω_n	Natural frequency	rad/s

ω_{cn}	Cut-off angular frequency of LPF	rad/s
s	Complex variable for Laplace transform	—
V_{dc}	DC link voltage	V
B	Friction coefficient	Nms/rad
J	Inertia of rotor	kgm ²
j	$\sqrt{-1}$	—
p	Number of pole pairs	—
h	Order of harmonic	—
ξ	Damp ratio	—
$\Delta v(t)$	Instantaneous error voltage due to dead-time voltage	V
V_{dead}	Amplitude of dead-time voltage	V
V_{sat}	Saturation voltage drop of the switching device	V
V_d	Forward voltage drop of the freewheeling diode	V
T_L	Load torque	Nm
t_c	Convergence time	s
T_{dead}	Dead time	μ s
T_e	Electromagnetic torque	Nm
T_s	Switching period	μ s
T_{on}	Turn-on time	μ s
T_{off}	Turn-off time	μ s
T_d	Delay time	μ s
ΔT_{e_peak}	Peak-to-peak value of torque ripples	Nm
ΔI	Current overshoot	A
Δe	Steady-state error	A
U_c, I_c, f_c	High-frequency carrier voltage, current, frequency	V,A,Hz

ΔU	Dead time voltage matrix	—
U_{abc}	Phase voltage matrix	—
U_{dq}^h	h^{th} voltage harmonic matrix in h^{th} SRF	—
I_{abc}	Phase current matrix	—
$I_{\alpha\beta}$	Current matrix in two stationary frame	—
$I_{\alpha\beta v}$	Virtual current matrix in two stationary frame	—
I_{dq}^h	h^{th} current harmonic matrix in h^{th} SRF	—
R	Resistance matrix	—
L_{abc}	Inductance matrix	—
L_{dq}^h	h^{th} inductance matrix in h^{th} SRF	—
Ψ_{fabc}	PM flux linkage matrix	—
Ψ_{fabc}^e	Even harmonic PM flux linkage matrix	—
Ψ_{dq}^h	h^{th} PM flux linkage harmonic matrix in h^{th} SRF	—

CHAPTER 1

GENERAL INTRODUCTION

In the last decades, the fields of new materials, novel electrical machine topologies, power electronics, microprocessors, control strategies, and bearing technologies develop rapidly. Under such a background, permanent magnet (PM) machines have been gaining popularity in both academia and industry, due to the advantages of high torque density, high power density, and high efficiency [ZHU07][NAK05]. Compared to the three-phase PM machines which are generally employed in industrial applications, the multiphase machines (more than three-phases) are advantageous for many industrial applications that require high power rating, smooth torque, power/torque sharing capability, and fault-tolerant capability. In recent decades, there has been a significant and increasing number of published technical and review papers that discuss the topologies, modeling methods, control strategies, pulse-width-modulation (PWM) techniques, and applications of multiphase electrical machines [LEV07][LEV08][LEV16][BOJ06].

The early application of multiphase machines was in the field of ship propulsion, which is still its main application area: five-phase PM machines [PAR05][ZAH16], six-phase PM machines [QIA16], and fifteen-phase machines [TER04] are successfully applied in ship propulsion. The increased emphasis on environmental protection has accelerated the development of greener modes of electrified transportation and has led to the rise of renewable energy industries. The advantages of multiphase machines attract researchers to utilize them in electric and hybrid electric vehicles (EVs), e.g., on-board battery chargers for EVs with three-phase machines [PIR19], five-phase machines [SUB16], six-phase machines [SOU10][SUB16], and nine-phase machines [BOD17]. Besides, they are also considered preferable solutions for wind power generation systems due to the power sharing capability [CHE14], modularity [GJE14], additional degrees of freedom [GON14], and fault-tolerant capability [GON16] provided by their multiphase topologies. Furthermore, electric aircrafts have received much attention in the modern commercial and military aerospace industries [DE10][BOJ16][THO09], where multiphase machines have exhibited irreplaceable fault tolerance capability compared with conventional three-phase machines in recent years. The multiphase machines mentioned above can be classified into two kinds, according to the number of phases: multi-three-phase (MTP)

(6-, 9-, 12-, and 15-... phases) machines as shown in Fig. 1.1(a), and other multiphase (4- [MEC04], 5- [DOR13], 7- [SCU20], and 11- [ABD10]... phases) machines, as shown in Fig. 1.1(b).

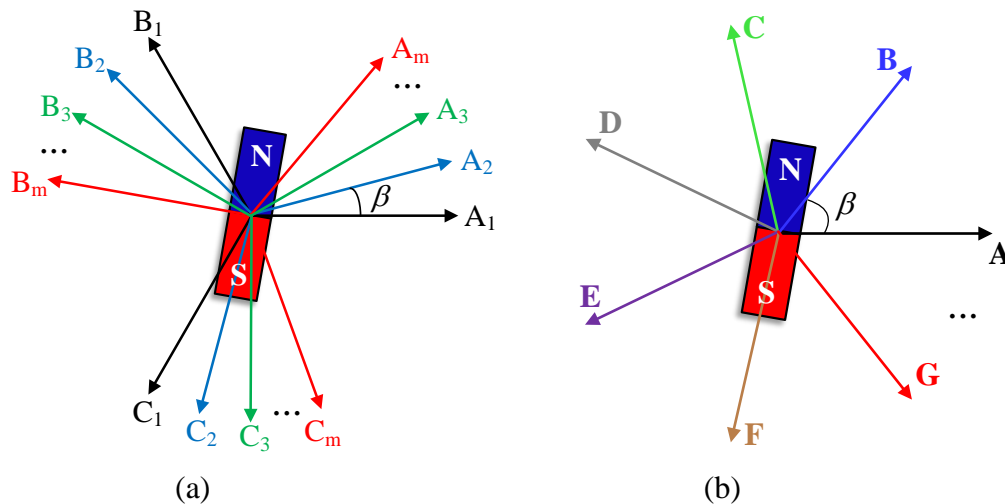


Fig. 1.1. Winding axes of multiphase machines. (a) Multi-three-phase machines. (b) Other multiphase machines.

Since commercial three-phase inverters and many advanced control techniques can be utilized for the drive of each three-phase set of MTP machines, MTP machines have become more popular in recent years. Considering the recent developments in PM materials, MTP PM machines are currently especially attractive. The MTP PM machines not only exhibit the merits of multiphase machines but also retain the advantages of PM machines, such as high torque density, high power density, and high efficiency. In terms of the machine drives, the winding sets can be fed by multiple generic and modular three-phase inverters as presented in Fig. 1.2. The DC links of these inverters can be connected to the same power source, Fig. 1.2(a), or isolated power sources, Fig. 1.2(b). This means that the drive topologies do not need to be redesigned and can be flexibly connected to fit different applications. For the common power source, it is usually employed in the applications that only have a single power supply, such as electric vehicles. This drive topology makes it possible to achieve interleave techniques for the purpose of reducing the DC link ripples and minimizing the DC link capacitor. For the isolated power source, it is feasible to applications with multiple power supplies/consumptions, such as the ship propulsion system and winding power generation, and the power can be freely exchanged among several isolated systems through multiphase windings.

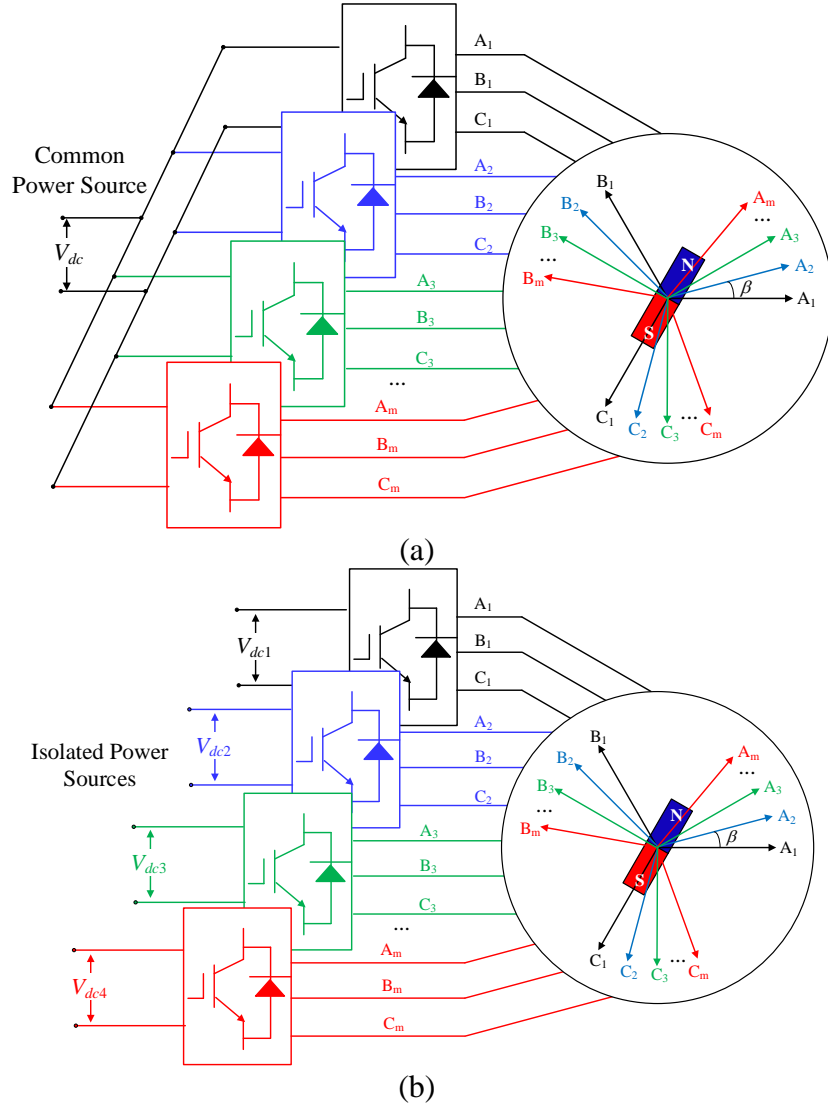


Fig. 1.2. Drive topologies of multi-three-phase machines. (a) Common power source. (b) Isolated power sources.

The advantages mentioned above motivate the development of multi-three-phase PM machines, and the existing design and control technologies of multi-three-phase PM machines are summarized in Fig. 1.3 based on current research and relevant papers. The control part of multi-three-phase PM machines can be divided into modeling methods, control strategies, pulse width modulation (PWM), and other technologies. To be more precise, the modeling methods can be divided into multi individual three-phase dq model and vector space decomposition (VSD) model. The control strategies include field oriented control (FOC), direct torque control (DTC), and model predictive control (MPC). The PWM technologies include the overmodulation, voltage vector selection, and carrier phase shifting. There are also other control technologies such as fault tolerant control and sensorless control. The relevant papers are also listed accordingly in Fig. 1.3, and the key papers are marked in red.

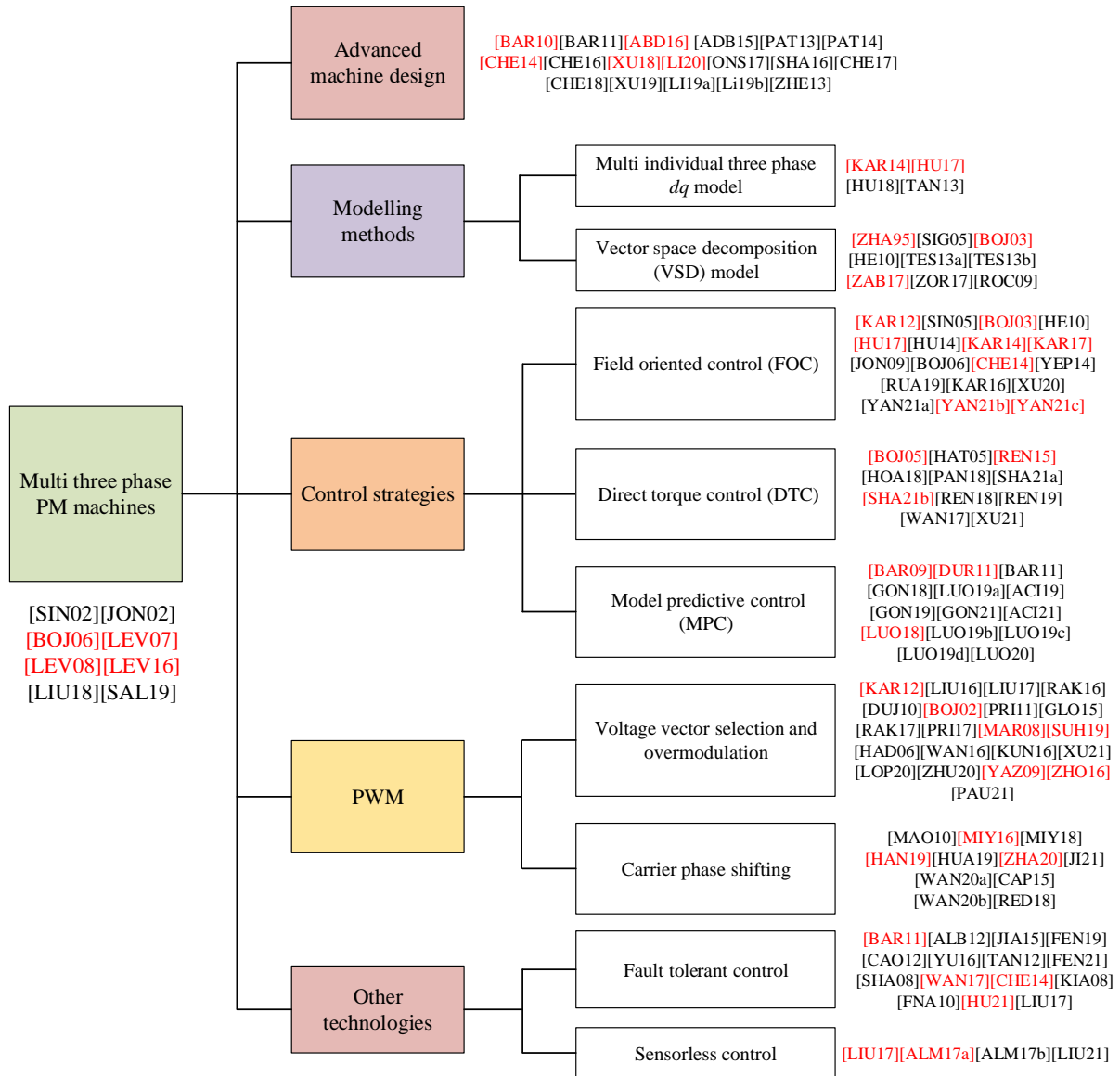


Fig. 1.3. Development of existing design and control technologies of multi-three-phase PM machines.

Among the multi-three-phase PM machines, dual-three-phase (DTP) PM machines are one of the most popular because the main advantages of multi-three-phase PM machines are maintained and the phase number is not increased too much compared to conventional three-phase machines. More importantly, most technologies of the DTP PM machines are generic and also applicable for other multi-three-phase PM machines. Therefore, this thesis will focus on the control of DTP PM machine systems. This chapter will review the main modeling methods and control strategies of DTP PM machines.

This chapter is partially published in *Energies* [ZHU21]

[ZHU21] Z. Q. hu, S. Wang, B. Shao, L. Yan, P. Xu, and Y. Ren, “Advances in dual-three-phase permanent magnet synchronous machines and control techniques,” *Energies.*, vol. 14, no. 22, Aug. 2021.

1.1 Introduction of DTP PM Machines

The conventional three-phase PM machines have one set of three-phase windings, and the spatial phase shifting angle between two adjacent phases is 120 electrical degrees, as shown in Fig. 1.4(a). As described in the name, the DTP PM machines have two sets of three-phase winding with isolated neutral points, and the spatial phase shifting angle between the two sets can be 0 electrical degree in Fig. 1.4(b), 60 electrical degrees in Fig. 1.4(c), and 30 electrical degrees in Fig. 1.4(d). Compared to other kinds of DTP PM machines, the machine with 30 electrical degrees phase shifting shows advantageous performance, such as greatly reduced spatial harmonics and elimination of the 6th harmonic in the torque ripple. Thus, it is more attractive to the industry and academia. It should be noted that all the DTP PM machines mentioned and investigated in this thesis are this kind of machines, i.e. the DTP PM machines with 30 electrical degrees phase shifting between two three-phase sets.

The drive topologies are shown in Fig. 1.5. The single three-phase PM machine is driven by the conventional three-phase inverter, and each phase of the machine is connected to the common point between two switches in each bridge of the inverter. The drive of the DTP machine can be simply derived from the drive of single three-phase machines, as shown in Fig. 1.5(b). Two three-phase inverters are used to drive the two winding sets of the machine, respectively, and the DC links of the two inverters can be connected to the same or different DC power supplies.

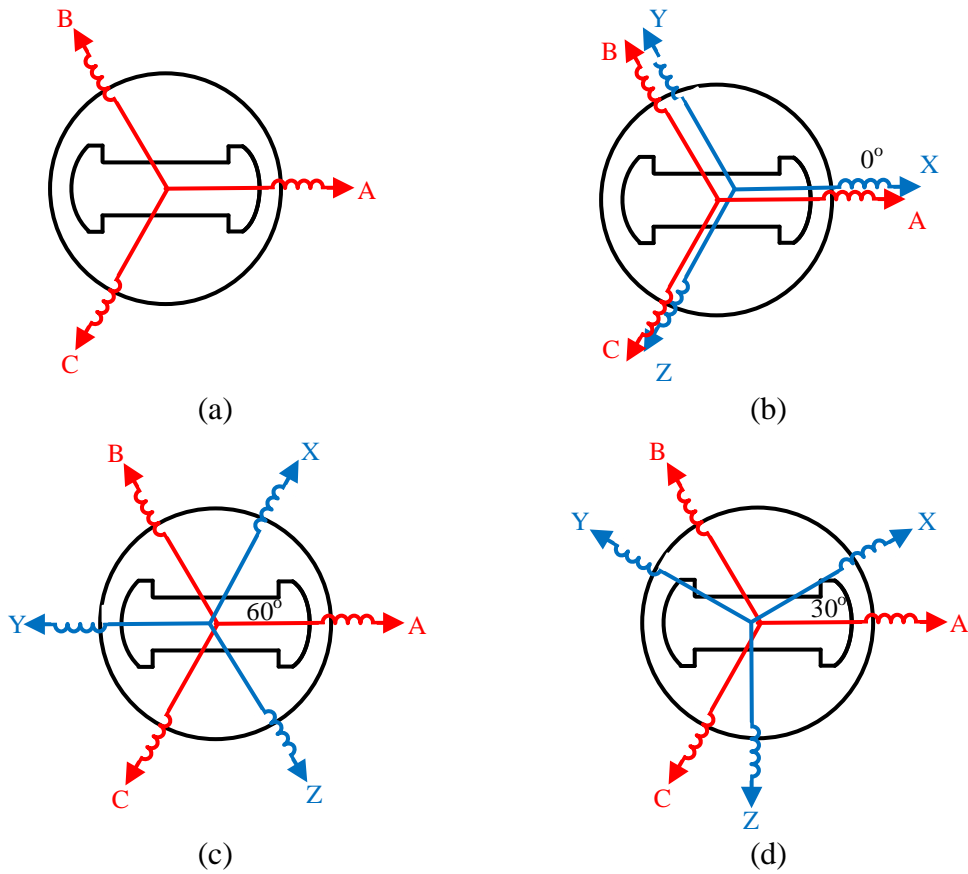


Fig. 1.4. Winding axes of three-phase and DTP PM machines. (a) Single three-phase PM machine. (b) DTP PM machine with 0 degree phase shifting. (c) DTP PM machine with 60 degree phase shifting. (d) DTP PM machine with 30 degree phase shifting.

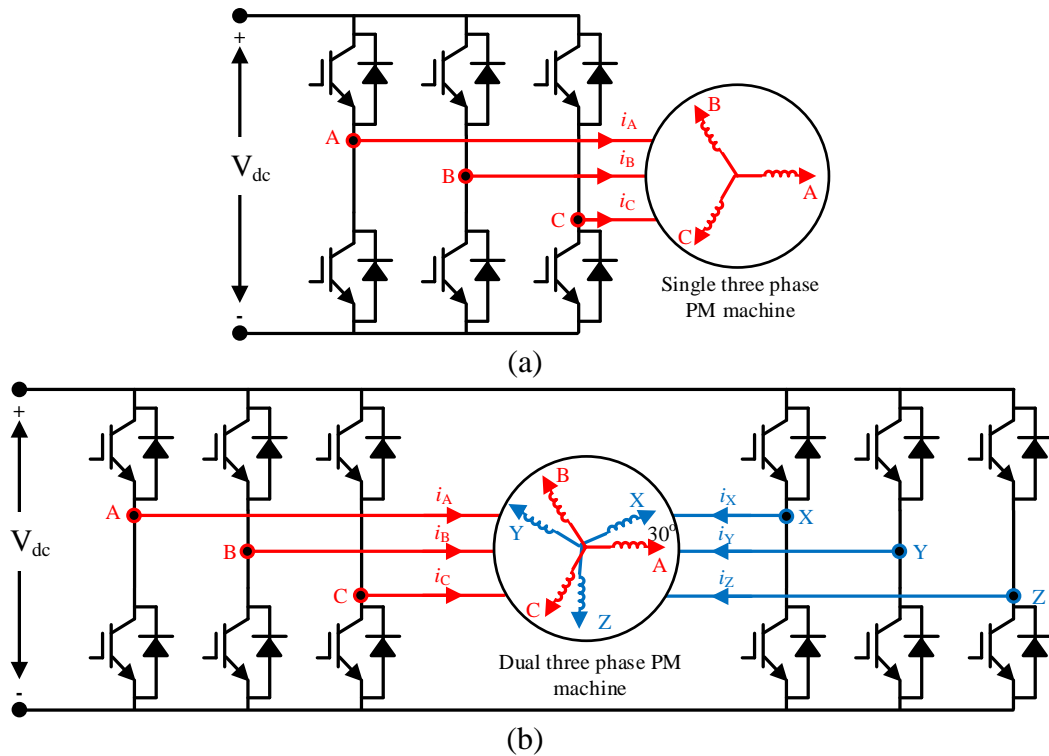


Fig. 1.5. Drive topologies. (a) Single three-phase PM machine. (b) DTP PM machine.

1.2 Modelling of DTP PM Machines

1.2.1 Modelling of Single Three-Phase PM Machines

Ignoring hysteresis and eddy current losses, the voltage equation of the conventional three-phase PM machines in the stationary ABC frame can be written as

$$\begin{bmatrix} u_a \\ u_b \\ u_c \end{bmatrix} = \begin{bmatrix} R_s & 0 & 0 \\ 0 & R_s & 0 \\ 0 & 0 & R_s \end{bmatrix} \begin{bmatrix} i_a \\ i_b \\ i_c \end{bmatrix} + \frac{d}{dt} \begin{bmatrix} L_{aa} & L_{ba} & L_{ca} \\ L_{ab} & L_{bb} & L_{cb} \\ L_{ac} & L_{bc} & L_{cc} \end{bmatrix} \begin{bmatrix} i_a \\ i_b \\ i_c \end{bmatrix} + \frac{d}{dt} \begin{bmatrix} \psi_{fa} \\ \psi_{fb} \\ \psi_{fc} \end{bmatrix} \quad (1-1)$$

where $[u_a \ u_b \ u_c]^T$, $[i_a \ i_b \ i_c]^T$, and $[\psi_{fa} \ \psi_{fb} \ \psi_{fc}]^T$ are the three-phase voltage, current, and PM flux linkage, respectively. R_s is the stator phase resistance. L represents the phase self-inductance or mutual-inductance between two phases. Using ABC- dq transformation (1-2), the voltage equation above can be transformed into the synchronous reference dq frame.

$$\mathbf{C}(\theta_e) = \frac{2}{3} \begin{bmatrix} \cos \theta_e & \cos \left(\theta_e - \frac{2}{3} \pi \right) & \cos \left(\theta_e + \frac{2}{3} \pi \right) \\ -\sin \theta_e & -\sin \left(\theta_e - \frac{2}{3} \pi \right) & -\sin \left(\theta_e + \frac{2}{3} \pi \right) \end{bmatrix} \quad (1-2)$$

where θ_e is the electrical angle of rotor position. Neglecting zero sequence components, left multiply both sides of the equation (1-1) by the transformation matrix (1-2) yields the voltage equation in synchronous reference dq frame as

$$\begin{bmatrix} u_d \\ u_q \end{bmatrix} = \begin{bmatrix} R_s & 0 \\ 0 & R_s \end{bmatrix} \begin{bmatrix} i_d \\ i_q \end{bmatrix} + \frac{d}{dt} \begin{bmatrix} L_d i_d \\ L_q i_q \end{bmatrix} + \omega_e \begin{bmatrix} 0 & -1 \\ 1 & 0 \end{bmatrix} \begin{bmatrix} L_d i_d + \psi_{fd} \\ L_q i_q \end{bmatrix} \quad (1-3)$$

where $[u_d \ u_q]^T$ and $[i_d \ i_q]^T$ are the voltage and current in dq -axes. ω_e is the electrical angular speed of rotor. L_d and L_q are the dq -axis inductances. ψ_{fd} is the d -axis PM flux linkage, and theoretically there is no q -axis PM flux linkage due to the field oriented frame transformation. The torque equation and mechanical equation are as follows [YAN19]

$$T_e = \frac{3}{2} p \psi_{fd} i_q + \frac{3}{2} p (L_d - L_q) i_d i_q \quad (1-4a)$$

$$J \frac{d\omega_m}{dt} = T_e - t_L - B \omega_m \quad (1-4b)$$

where p is the pole pair number. t_L is the load torque. ω_m is the mechanical angular speed of

rotor. B is the friction coefficient and J is the inertia of rotor.

1.2.2 Double Three-phase dq Model

The three-phase PM machine model in synchronous reference dq frame described in Section 1.2.1 can be extended to each three-phase set of the DTP PM machines, and thus, the double three-phase dq model is derived. The machine voltage equation and flux linkage equation in stationary frame can be expressed as

$$\begin{bmatrix} u_a \\ u_b \\ u_c \\ u_x \\ u_y \\ u_z \end{bmatrix} = \begin{bmatrix} R_s & 0 & 0 & 0 & 0 & 0 \\ 0 & R_s & 0 & 0 & 0 & 0 \\ 0 & 0 & R_s & 0 & 0 & 0 \\ 0 & 0 & 0 & R_s & 0 & 0 \\ 0 & 0 & 0 & 0 & R_s & 0 \\ 0 & 0 & 0 & 0 & 0 & R_s \end{bmatrix} \begin{bmatrix} i_a \\ i_b \\ i_c \\ i_x \\ i_y \\ i_z \end{bmatrix} + \frac{d}{dt} \begin{bmatrix} \psi_a \\ \psi_b \\ \psi_c \\ \psi_x \\ \psi_y \\ \psi_z \end{bmatrix} \quad (1-5)$$

$$\begin{bmatrix} \psi_a \\ \psi_b \\ \psi_c \\ \psi_x \\ \psi_y \\ \psi_z \end{bmatrix} = \begin{bmatrix} L_{aa} & L_{ba} & L_{ca} & L_{xa} & L_{ya} & L_{za} \\ L_{ab} & L_{bb} & L_{cb} & L_{xb} & L_{yb} & L_{zb} \\ L_{ac} & L_{bc} & L_{cc} & L_{xc} & L_{yc} & L_{zc} \\ L_{ax} & L_{bx} & L_{cx} & L_{xx} & L_{yx} & L_{zx} \\ L_{ay} & L_{by} & L_{cy} & L_{xy} & L_{yy} & L_{zy} \\ L_{az} & L_{bz} & L_{cz} & L_{xz} & L_{yz} & L_{zz} \end{bmatrix} \begin{bmatrix} i_a \\ i_b \\ i_c \\ i_x \\ i_y \\ i_z \end{bmatrix} + \begin{bmatrix} \psi_{fa} \\ \psi_{fb} \\ \psi_{fc} \\ \psi_{fx} \\ \psi_{fy} \\ \psi_{fz} \end{bmatrix} \quad (1-6)$$

where ψ represents the stator flux linkage variable and ψ_f represents the PM flux linkage variable.

Based on the study in [KAR14][HU17], the ABC- dq transformation (1-2) can be extended as

$$\mathbf{C}_{DTP}(\theta_e) = \frac{2}{3} \begin{bmatrix} \mathbf{C}(\theta_e) & 0 \\ 0 & \mathbf{C}\left(\theta_e - \frac{\pi}{6}\right) \end{bmatrix} \quad (1-7)$$

Left multiply both sides of equations (1-5) and (1-6) by the transformation matrix (1-7) yields the voltage equations of each three-phase set as

$$\begin{aligned} \begin{bmatrix} u_{d1} \\ u_{q1} \end{bmatrix} &= \begin{bmatrix} R_s & 0 \\ 0 & R_s \end{bmatrix} \begin{bmatrix} i_{d1} \\ i_{q1} \end{bmatrix} + \frac{d}{dt} \begin{bmatrix} L_d i_{d1} \\ L_q i_{q1} \end{bmatrix} + \omega_e \begin{bmatrix} 0 & -1 \\ 1 & 0 \end{bmatrix} \begin{bmatrix} L_d i_{d1} + \psi_{fd} \\ L_q i_{q1} \end{bmatrix} \\ &+ \frac{d}{dt} \begin{bmatrix} M_d i_{d2} \\ M_q i_{q2} \end{bmatrix} + \omega_e \begin{bmatrix} 0 & -1 \\ 1 & 0 \end{bmatrix} \begin{bmatrix} M_d i_{d2} \\ M_q i_{q2} \end{bmatrix} \end{aligned} \quad (1-8)$$

$$\begin{aligned} \begin{bmatrix} u_{d2} \\ u_{q2} \end{bmatrix} &= \begin{bmatrix} R_s & 0 \\ 0 & R_s \end{bmatrix} \begin{bmatrix} i_{d2} \\ i_{q2} \end{bmatrix} + \frac{d}{dt} \begin{bmatrix} L_d i_{d2} \\ L_q i_{q2} \end{bmatrix} + \omega_e \begin{bmatrix} 0 & -1 \\ 1 & 0 \end{bmatrix} \begin{bmatrix} L_d i_{d2} + \psi_{fd} \\ L_q i_{q2} \end{bmatrix} \\ &+ \frac{d}{dt} \begin{bmatrix} M_d i_{d1} \\ M_q i_{q1} \end{bmatrix} + \omega_e \begin{bmatrix} 0 & -1 \\ 1 & 0 \end{bmatrix} \begin{bmatrix} M_d i_{d1} \\ M_q i_{q1} \end{bmatrix} \end{aligned}$$

where “1” and “2” in the subscript represent the variables of the first and second sets, respectively. Since the two neutral points are isolated, the zero-sequence components of two sets are also neglected. M_d and M_q are the mutual inductance between the two three-phase winding sets in dq -axes, and they satisfy

$$\begin{aligned} L_d &= M_d + L_\sigma \\ L_q &= M_q + L_\sigma \end{aligned} \quad (1-9)$$

Equations in (1-8) represent the double three-phase machine model in dq -axes and can be depicted in Fig. 1.6. Compared to the model of single three-phase machines, the double three-phase dq model of the DTP machines includes more terms with M_d and M_q in the voltage equations. These terms are introduced by the magnetic coupling between the two sets of three-phase windings, which means the currents in one set will generate flux linkage in the other set, leading to the induced electromotive force and motion electromotive force in the voltage equations.

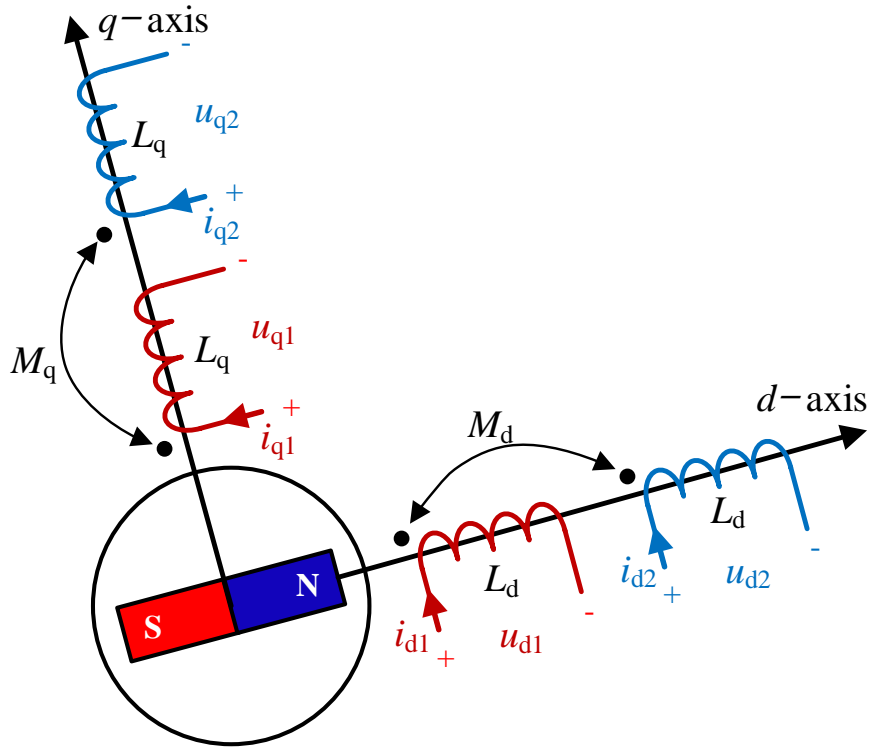


Fig. 1.6. Double three-phase machine model in dq -axes.

The electromagnetic torque in the double three-phase dq model can be expressed as

$$T_e = \frac{3}{2}p \left(\psi_{fd}(i_{q1} + i_{q2}) + (L_d - L_q)(i_{d1}i_{q1} + i_{d2}i_{q2}) \right. \\ \left. + (M_d - M_q)(i_{d1}i_{q2} + i_{d2}i_{q1}) \right) \quad (1-10)$$

According to (1-10), for the surface mounted type DTP PM machines, the d - and q - axis inductances as well as the mutual inductances are equal, and the torque can be regarded as the sum of two parts which are individually provided by the two three-phase sets. However, for the interior type DTP PM machines, due to the salient effect of the machine, there are additional reluctance torque which is co-produced by the currents from two sets. The DTP and single three-phase PM machines have the same mechanical equation, i.e. equation (1-4b), and thus the mechanical equation of DTP PM machines is not repetitively written in this section.

1.2.3 Vector Space Decomposition Model

Vector space decomposition (VSD) is a group of mathematical transformations to separate the components with different phase angle relationship. Since the phase angle relationship of the harmonics is different from the fundamental, it is applicable to use VSD to separate the harmonic components of voltage, current, and flux linkage in the DTP PM machines. Actually, the ABC- $\alpha\beta z$ transformation in general three-phase systems shown below can also be understood as one of the VSD transformations.

$$\begin{bmatrix} v_\alpha \\ v_\beta \\ v_z \end{bmatrix} = \frac{2}{3} \begin{bmatrix} 1 & -\frac{1}{2} & -\frac{1}{2} \\ 0 & \frac{\sqrt{3}}{2} & -\frac{\sqrt{3}}{2} \\ \frac{1}{2} & \frac{1}{2} & \frac{1}{2} \end{bmatrix} \begin{bmatrix} v_a \\ v_b \\ v_c \end{bmatrix} \quad (1-11)$$

where “ v ” represents the variables in the corresponding axis.

The axis definition of the ABC- $\alpha\beta z$ transformation is shown in Fig. 1.7. The α - and z -axes are aligned to the axis of phase A, and β -axis is delayed by 90 degrees with respect to α axis. It is known that the zero-sequence components, e.g., the 3rd and the 9th, can be decomposed from the phase variables into z -axis using the ABC- $\alpha\beta z$ transformation (1-11), while the other components, e.g., the fundamental, 5th, and 7th harmonics, are decomposed in α - and β -axes.

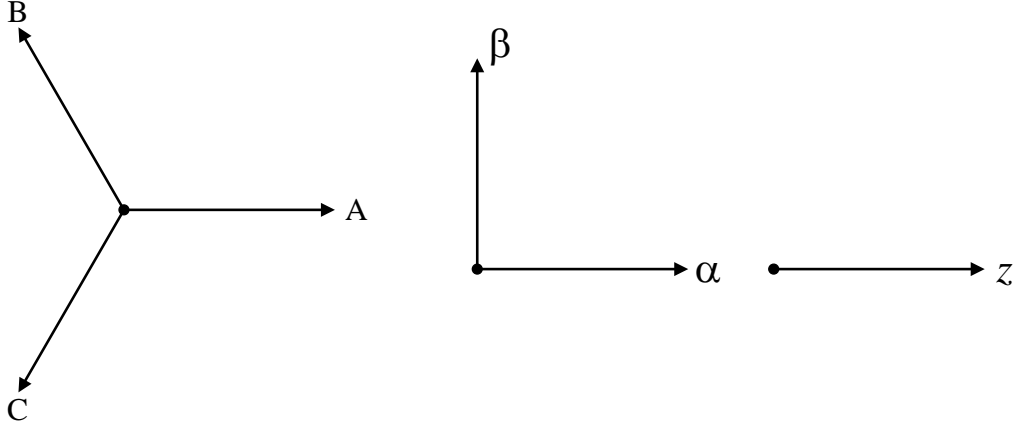


Fig. 1.7. Definition of axes in ABC- $\alpha\beta z$ transformation.

In terms of the DTP PM machines, based on the study in [ZHA95], the VSD transformation can be expressed as follows

$$\begin{bmatrix} v_\alpha \\ v_\beta \\ v_{z1} \\ v_{z2} \\ v_{o1} \\ v_{o2} \end{bmatrix} = \frac{1}{3} \begin{bmatrix} 1 & -\frac{1}{2} & -\frac{1}{2} & \frac{\sqrt{3}}{2} & -\frac{\sqrt{3}}{2} & 0 \\ 0 & \frac{\sqrt{3}}{2} & -\frac{\sqrt{3}}{2} & \frac{1}{2} & \frac{1}{2} & -1 \\ 1 & -\frac{1}{2} & -\frac{1}{2} & -\frac{\sqrt{3}}{2} & \frac{\sqrt{3}}{2} & 0 \\ 0 & \frac{\sqrt{3}}{2} & -\frac{\sqrt{3}}{2} & -\frac{1}{2} & -\frac{1}{2} & 1 \\ 1 & 1 & 1 & 0 & 0 & 0 \\ 0 & 0 & 0 & 1 & 1 & 1 \end{bmatrix} \begin{bmatrix} v_a \\ v_b \\ v_c \\ v_x \\ v_y \\ v_z \end{bmatrix} \quad (1-12)$$

The definition of the axes in the VSD transformation is shown in Fig. 1.8. Similar to the ABC- $\alpha\beta z$ transformation (1-11), the phase variables, i.e., the current, voltage, and flux linkage, can be decomposed into three orthogonal axis frames, which are also known as three subspaces or subplanes in many studies. To avoid confusion, this thesis employs the “subspace” to describe them. The three subspaces are the $\alpha\beta$ subspace (fundamental-related), the z_1z_2 subspace (main-harmonic-related), and the o_1o_2 subspace (zero-sequence related). These subspaces possess the following properties:

- The fundamental component of the machine variables and the k th order harmonics ($k=12m\pm 1$, $m=1,2,3,\dots$) are transformed into the $\alpha\beta$ subspace. It should be pointed out that the $\alpha\beta$ subspace have been chosen in way of that they are related to the air gap flux. Hence, the variables in the $\alpha\beta$ subspace will produce a substantial MMF in the machine airgap and thus will be torque production, and electromechanical energy conversion

related.

- Harmonics with $h=6n\pm 1$ ($n = 1, 3, 5, \dots$), i.e., the 5th, 7th, 17th, 19th, ... harmonics, are mapped into the z_1z_2 subspace. As the z_1z_2 subspace is orthogonal to the $\alpha\beta$ subspace, the variables in this subspace will not be related to the generation of any MMF in the air gap, and thus will not contribute to any torque or torque ripples.
- Zero-sequence $l=3m$ ($m = 1, 2, 3, \dots$) harmonics, which are also non-electromechanical energy conversion related, are mapped into the o_1o_2 subspace to form the conventional zero sequence components. When two sets of three-phase windings have two isolated neutral points, no zero-sequence current path will exist in the o_1o_2 subspace. Hence, the machine model can be simplified from a six-dimensional system to a four-dimensional system for isolated neutral point topology.

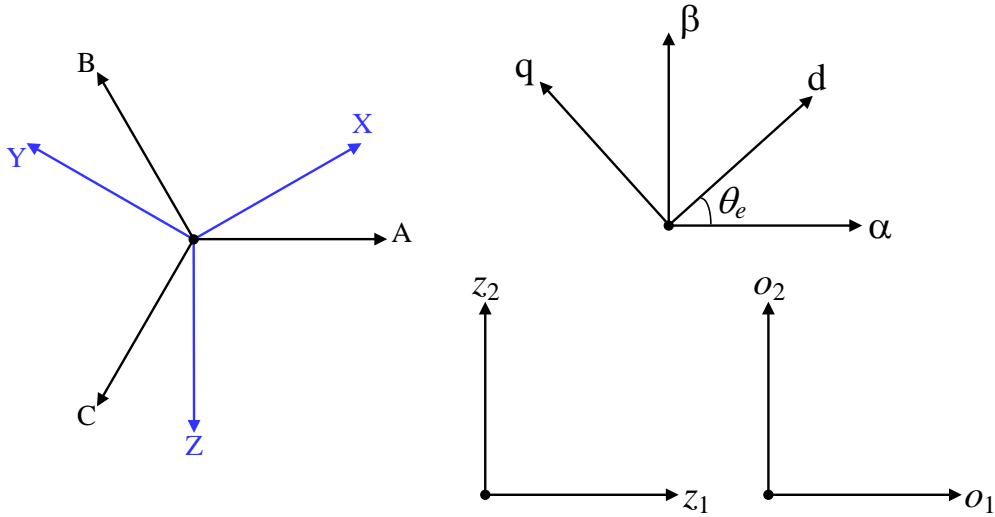


Fig. 1.8. Definition of axes in VSD transformation of DTP PM machines.

Neglecting the zero-sequence subspace, the VSD model of the DTP PM machine can be established as below through left multiplying both sides of the equations (1-5) and (1-6) by the transformation matrix of (1-12).

$$\begin{bmatrix} u_\alpha \\ u_\beta \\ u_{z1} \\ u_{z2} \end{bmatrix} = \begin{bmatrix} R_s & 0 & 0 & 0 \\ 0 & R_s & 0 & 0 \\ 0 & 0 & R_s & 0 \\ 0 & 0 & 0 & R_s \end{bmatrix} \begin{bmatrix} i_\alpha \\ i_\beta \\ i_{z1} \\ i_{z2} \end{bmatrix} + \frac{d}{dt} \begin{bmatrix} \psi_\alpha \\ \psi_\beta \\ \psi_{z1} \\ \psi_{z2} \end{bmatrix} \quad (1-13)$$

$$\begin{bmatrix} \psi_\alpha \\ \psi_\beta \\ \psi_{z1} \\ \psi_{z2} \end{bmatrix} = \begin{bmatrix} L_\alpha & 0 & 0 & 0 \\ 0 & L_\beta & 0 & 0 \\ 0 & 0 & L_\sigma & 0 \\ 0 & 0 & 0 & L_\sigma \end{bmatrix} \begin{bmatrix} i_\alpha \\ i_\beta \\ i_{z1} \\ i_{z2} \end{bmatrix} + \begin{bmatrix} \psi_{f\alpha} \\ \psi_{f\beta} \\ 0 \\ 0 \end{bmatrix} \quad (1-14)$$

where L_α and L_β are the α - and β -axis inductances, respectively. L_σ is the leakage inductance. Since the $\alpha\beta$ and z_1z_2 subspaces are orthogonal, the machine variables in the one subspace are decoupled and isolated to them in the other subspace, which results in the diagonal resistance and inductance matrices. As studied in [ZHA95], the fundamental components of machine variables are mapped in $\alpha\beta$ subspace, and the torque and energy conversion only happen in the $\alpha\beta$ subspace. To simplify the machine model and further provide the guideline for the design of the current/torque regulator, the machine model in $\alpha\beta$ subspace is further transformed to synchronous reference dq frame as

$$\begin{bmatrix} u_d \\ u_q \end{bmatrix} = \begin{bmatrix} R_s & 0 \\ 0 & R_s \end{bmatrix} \begin{bmatrix} i_d \\ i_q \end{bmatrix} + \frac{d}{dt} \begin{bmatrix} L_D i_d \\ L_Q i_q \end{bmatrix} + \omega_e \begin{bmatrix} 0 & -1 \\ 1 & 0 \end{bmatrix} \begin{bmatrix} L_D i_d + \psi_{fd} \\ L_Q i_q \end{bmatrix} \quad (1-15)$$

where

$$\begin{bmatrix} u_d \\ u_q \end{bmatrix} = \begin{bmatrix} \cos(\theta_e) & \sin(\theta_e) \\ -\sin(\theta_e) & \cos(\theta_e) \end{bmatrix} \begin{bmatrix} u_\alpha \\ u_\beta \end{bmatrix} \quad (1-16)$$

$$\begin{bmatrix} i_d \\ i_q \end{bmatrix} = \begin{bmatrix} \cos(\theta_e) & \sin(\theta_e) \\ -\sin(\theta_e) & \cos(\theta_e) \end{bmatrix} \begin{bmatrix} i_\alpha \\ i_\beta \end{bmatrix}$$

$$\begin{bmatrix} L_D & 0 \\ 0 & L_Q \end{bmatrix} = \begin{bmatrix} \cos(\theta_e) & \sin(\theta_e) \\ -\sin(\theta_e) & \cos(\theta_e) \end{bmatrix} \begin{bmatrix} L_\alpha & 0 \\ 0 & L_\beta \end{bmatrix} \begin{bmatrix} \cos(\theta_e) & \sin(\theta_e) \\ -\sin(\theta_e) & \cos(\theta_e) \end{bmatrix}^T$$

The phase angle relationship between the dq -axes and the $\alpha\beta$ -axes is shown in Fig. 1.8. Comparing equation (1-15) with the single three-phase PM machine model (1-3), it is easy to find that the DTP PM machine model in $\alpha\beta$ subspace has the same format with the single three-phase PM machine model, which implies that the current/torque regulator in this subspace can be designed in the same ways as they are in single three-phase PM machine systems. The machine model in z_1z_2 subspace remains as

$$\begin{bmatrix} u_{z1} \\ u_{z2} \end{bmatrix} = \begin{bmatrix} R_s & 0 \\ 0 & R_s \end{bmatrix} \begin{bmatrix} i_{z1} \\ i_{z2} \end{bmatrix} + \frac{d}{dt} \begin{bmatrix} L_\sigma i_{z1} \\ L_\sigma i_{z2} \end{bmatrix} \quad (1-17)$$

The main harmonics, e.g. the 5th and 7th, are mapped in z_1z_2 subspace, and it is clearly seen from (1-17) that the current in this subspace is only restricted by the resistance and the leakage inductance, which are usually very small. This determines the DTP PM machines will suffer

more from the current harmonics compared to single three-phase PM machines if without effective suppression of these current harmonics. Both equations (1-15) and (1-17) build up the VSD electrical model of DTP PM machines. In terms of the torque model, due to the fact that the average torque and torque ripples are only relevant to variables in $\alpha\beta$ subspace, the electromagnetic torque can be expressed by the cross-product of the flux linkage and current in the stationary $\alpha\beta$ frame of $\alpha\beta$ subspace as

$$T_e = 3p(\psi_\alpha i_\beta - \psi_\beta i_\alpha) \quad (1-18)$$

or by the cross-product of the flux linkage and current in the synchronous reference dq frame of $\alpha\beta$ subspace as

$$T_e = 3p[(L_d - L_q)i_d i_q + \psi_{fd} i_q] \quad (1-19)$$

The main current harmonics are not mapped in $\alpha\beta$ subspace, which means there is no 6th harmonics in i_d , i_q , and ψ_{fd} . Therefore, even if there are significant 5th and 7th current harmonics existing in phase current, the 6th torque ripple does not exist in DTP PM machines as it does in single three-phase machines. The elimination of the 6th torque ripple is one of the key superiorities of DTP PM machines. Compared with the torque equation (1-10) in double three-phase dq model, the torque equation (1-19) in VSD model is greatly simplified and is more practical in the torque estimation of DTP PM machines.

1.3 Field Oriented Control of DTP PM Machines

1.3.1 Field Oriented Control of Single Three-phase PM Machines

To understand the FOC of DTP PM machines, it is necessary to introduce the FOC of the conventional three-phase PM machines first. The block diagram of FOC is shown in Fig. 1.9. The single three-phase PM machine is connected to the general three-phase inverter and the three-phase currents i_a , i_b , and i_c are measured and transformed to the synchronous reference dq frame as i_d and i_q which are further used as the current feedback of two proportional integral (PI) current regulators. The current references i_d^* and i_q^* are usually determined by the torque reference based on the torque equation (1-4a), while for a speed closed-loop regulation system, i_d^* and i_q^* are determined by the speed regulator. It is worth noting that the interior PM (IPM) machines have unequal d - and q -axis inductances, which means there are many combinations of i_d^* and i_q^* to achieve the same torque reference according to (1-4a). In this

regard, the maximum torque per ampere (MTPA) strategy is usually applied to optimize i_d^* and i_q^* , and hence maximize the torque with a constant current amplitude or minimize the current amplitude with a constant torque. However, the surface-mounted PM (SPM) machines have equal d - and q -axis inductances, the torque is only proportional to i_q according to (1-4a). This makes $i_d^* = 0$ generally employed in the control of SPM machines.

The outputs of the PI current regulators are regarded as the voltage reference in synchronous reference dq frame, and they will be inversely transformed to the stationary $\alpha\beta$ frame. Space vector pulse width modulation (SVPWM) technique is employed to convert the voltage reference in the stationary $\alpha\beta$ frame to the drive signals of the three-phase inverter. It should be mentioned that Fig. 1.9 merely shows the basic framework of FOC, and it can be improved by modifying the components in the block diagram, for example, replacing the PI regulator with PI-resonant (PIR) regulator to suppress current harmonics [YEP15], improve the speed regulator to reduce speed/torque ripples [XIA15], and so on. This thesis focuses on the control of DTP PM machines, and hence will not discuss more details about the FOC in conventional three-phase PM machines.

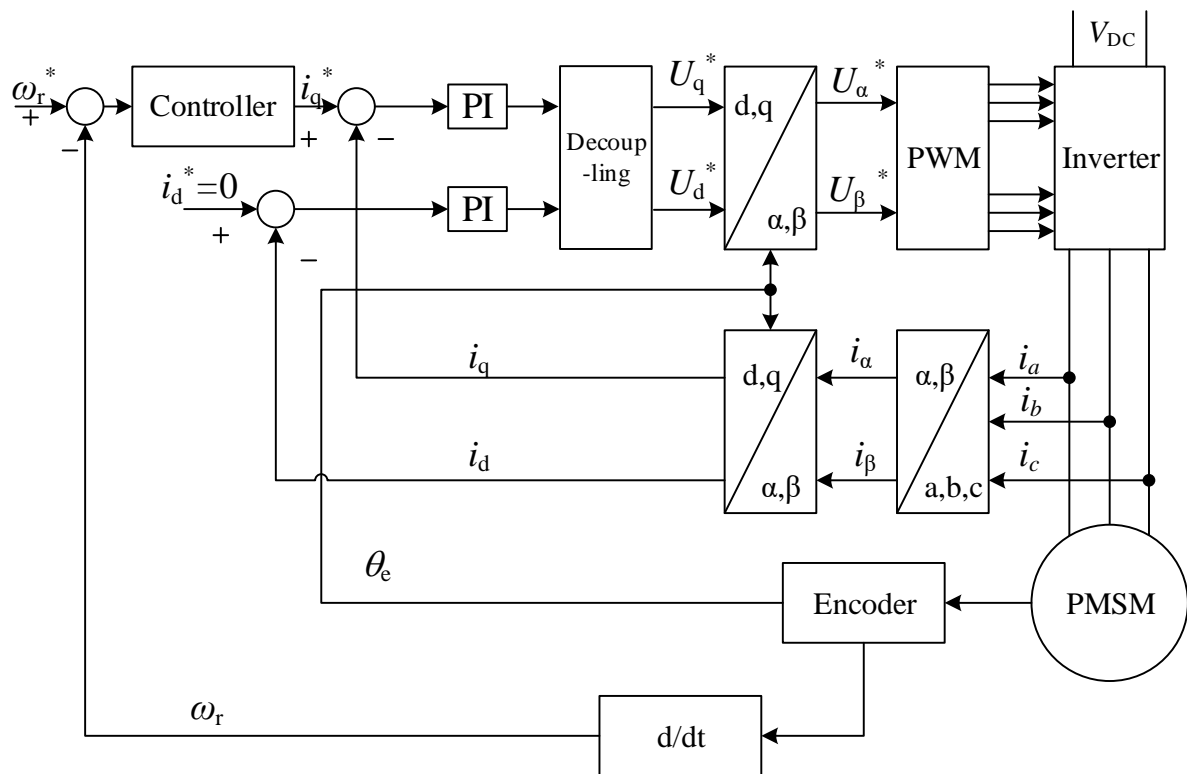


Fig. 1.9. Block diagram of field oriented control of conventional three-phase PM machines.

1.3.2 Double Synchronous Reference dq Frame Control of DTP PM Machines

The DTP PM machine can be regarded as two sub three-phase machines with magnetic coupling according to the double three-phase dq model introduced in Section 1.2.2. The concept of FOC in conventional three-phase PM machines can be straightforwardly extended to control the current and torque of each three-phase sets, which is known as double synchronous reference dq frame control [KAR12]. The control block diagram is shown in Fig. 1.10. It is clear that the three-phase currents of each set are transformed to the synchronous reference dq frame as i_{d1} , i_{q1} , and i_{d2} , i_{q2} . Similar to the three-phase FOC, the derived i_{d1} , i_{q2} , and i_{d1} , i_{q2} are also used as the current feedback and controlled by the PI regulators. After the decoupling compensation, the voltage references in dq frame are derived and transformed to the stationary $\alpha\beta$ frame. The voltage references are modulated by two sets of individual SVPWM to generate the drive signals of two three-phase inverters.

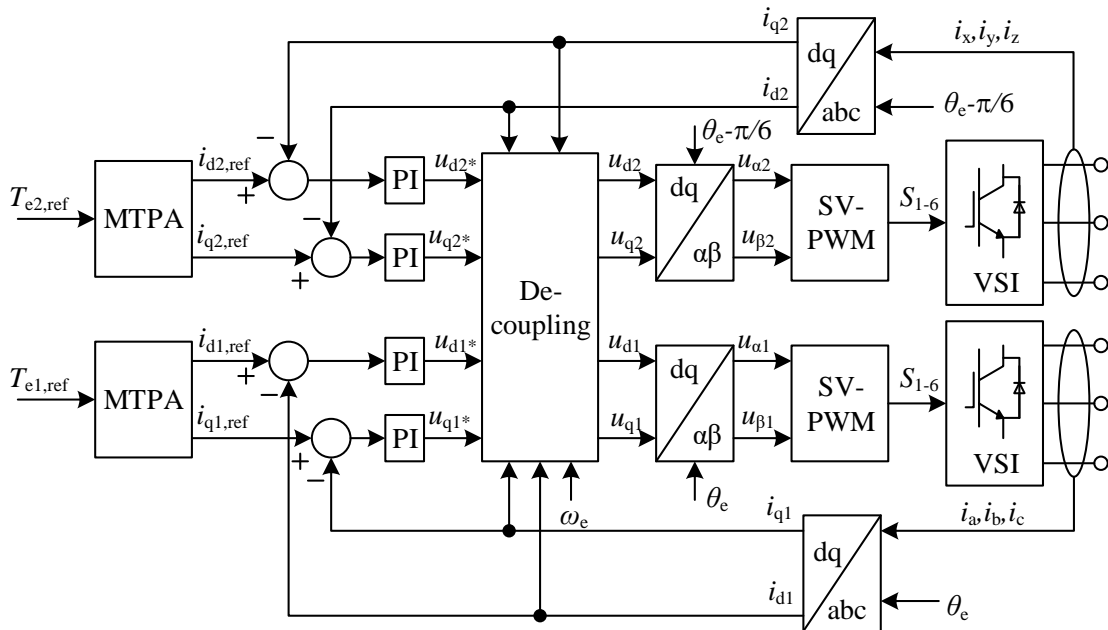


Fig. 1.10. Block diagram of double synchronous reference dq frame control of DTP PM machines using PI controllers [KAR12].

There are still many differences from the conventional three-phase FOC. Because there is a 30 electrical degree phase shifting between two sets of three-phase winding, the coordinate transformation angles of the ABC- dq and dq - $\alpha\beta$ transformations in the control loop of set XYZ should also be shifted by 30 degrees, i.e. $\theta_e - 30^\circ$, with respect to them in the control loop of set ABC. More importantly, due to the magnetic coupling between two three-phase windings,

there are external terms in the decoupling compensation part, which can be designed based on the double three-phase dq model as follows

$$\begin{bmatrix} u_{d1}^{dec} \\ u_{q1}^{dec} \\ u_{d2}^{dec} \\ u_{q2}^{dec} \end{bmatrix} = \begin{bmatrix} \frac{dM_{d1d2}}{dt} - \omega_e L_q i_{q1} - \omega_e M_q i_{q2} \\ \frac{dM_{q1q2}}{dt} + \omega_e L_d i_{d1} + \omega_e M_d i_{d2} + \omega_e \psi_{fd} \\ \frac{dM_{d1d1}}{dt} - \omega_e L_q i_{q2} - \omega_e M_q i_{q1} \\ \frac{dM_{q1q1}}{dt} + \omega_e L_d i_{d2} + \omega_e M_d i_{d1} + \omega_e \psi_{fd} \end{bmatrix} \quad (1-20)$$

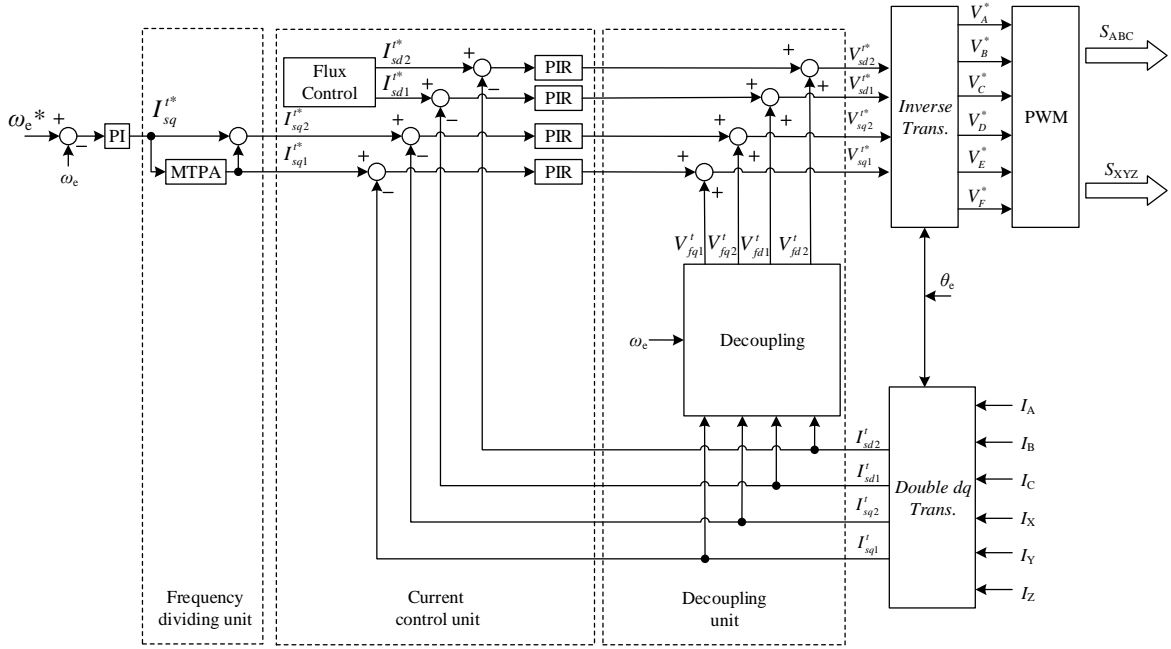


Fig. 1.11. Block diagram of double synchronous reference dq frame control of DTP PM machines using PIR controllers [HU18].

As mentioned in Section 1.2.3, due to small impedance to harmonics, the DTP PM machines suffer more from the current harmonics, mainly the 5th and 7th ones. To reduce these current harmonics, [HU18] modified the current regulators based on the study of [KAR12]. A resonant term is parallel connected to each PI regulator to build the PIR regulator, and the block diagram of the proposed control is shown in Fig. 1.11. The transfer function of the PIR regulator is as follows

$$G_{PIR}(s) = K_p + \frac{K_i}{s} + \frac{K_r s}{s^2 + \omega_0^2} \quad (1-20)$$

where K_p , K_i , and K_r are the proportional coefficient, integral coefficient, and resonant

coefficient, respectively. ω_0 is the resonant frequency and should be set as $6\omega_e$ to suppress 6th current harmonics (the 5th and 7th harmonics in phase current). In synchronous reference dq frame, the PI terms are used to regulate the DC component which represents the fundamental component of phase current. The infinite gain at 0Hz provided by the integral term guarantees that the DC component can accurately track the DC current references i_d^* and i_q^* . Like the integral term, the resonant term can achieve infinite gain at the resonant frequency ω_0 according to the transfer function, which means the 6th current harmonic can accurately track the 6th AC current reference or can be completely suppressed if the 6th AC current reference is zero.

1.3.3 VSD Control of DTP PM Machines

Compared to the double synchronous reference dq frame control, VSD control is based on the VSD model and is more advantageous for DTP PM machines. Since the torque is only related to the variables in $\alpha\beta$ subspace, it is only necessary to control the current in $\alpha\beta$ subspace, and the control system can be simplified as shown in Fig. 1.12 [KIA04]. It is clear that the measured six phase currents are firstly decomposed using the VSD transformation (1-12). Although the currents are decomposed as the currents in $\alpha\beta$ and z_1z_2 subspaces, only the currents in $\alpha\beta$ subspace, i.e. i_α and i_β , are used and transformed to the dq frame as i_d and i_q . Two PI regulators are used to control i_d and i_q , respectively, and the output voltages of PI regulators are inversely transformed to six phase stationary frame. The current references i_d^* and i_q^* are determined by the torque reference. Two sets of SVPWM are used to generate the drive signals of two three-phase inverters based on the voltage references of each set.

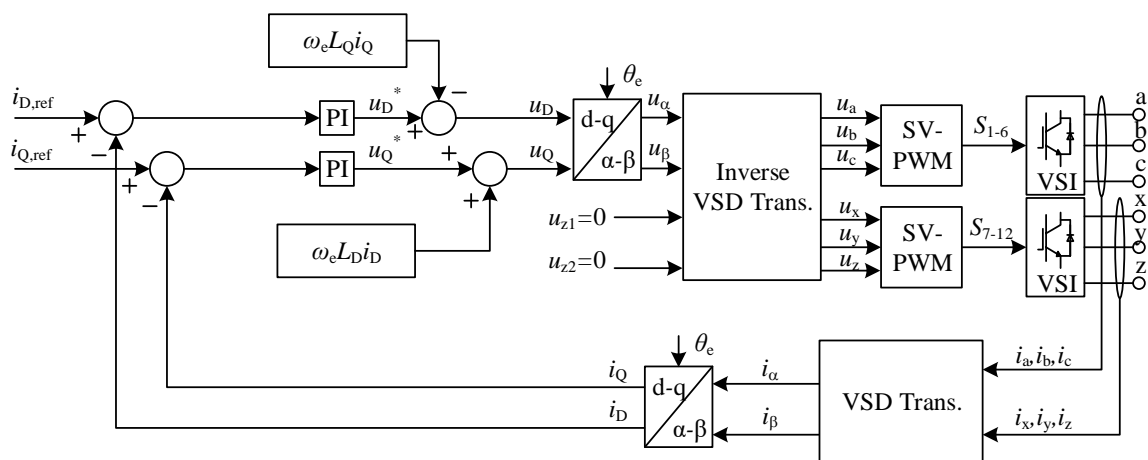


Fig. 1.12. Block diagram of VSD control with two PI regulators for DTP PM machines [KIA04].

Although the VSD control with two PI regulators are simple and easy to implement in the real system, the current regulators do not have control capability to the current harmonics in z_1z_2 subspace because z_1z_2 subspace is isolated from the $\alpha\beta$ subspace. This means the current in z_1z_2 subspace is not controlled and the voltage references in this subspace is zero. The current harmonics, e.g. the 5th and 7th, are mapped in this subspace and is purely limited by the small impedance aforementioned, leading to serious current harmonics. To alleviate this problem, two additional PI regulators are employed in [KAR14] to establish the VSD control with four PI regulators, as shown in Fig. 1.13. It should be noted that [KAR14] defines the two three-phase sets as “a1b1c1” and “a2b2c2”. Frame D_1Q_1 represents the synchronous reference frame in $\alpha\beta$ subspace. Frame D_2Q_2 represents the synchronous reference frame in z_1z_2 subspace. Frames d_1q_1 and d_2q_2 represent the synchronous reference dq frames of two three phase set, respectively. The decomposed current in z_1z_2 subspace, i_{z1} and i_{z2} , are transformed to the synchronous reference dq frame as i_{D2} , i_{Q2} and regulated by the additional two PI regulators. The outputs of the PI regulator are decoupled by the decoupling terms to calculate the voltage references in the dq frame. Then, the voltage references are transformed to stationary frame and modulated by two conventional SVPWM. To suppress the current harmonics, the current references of the two additional PI regulators should be set as 0.

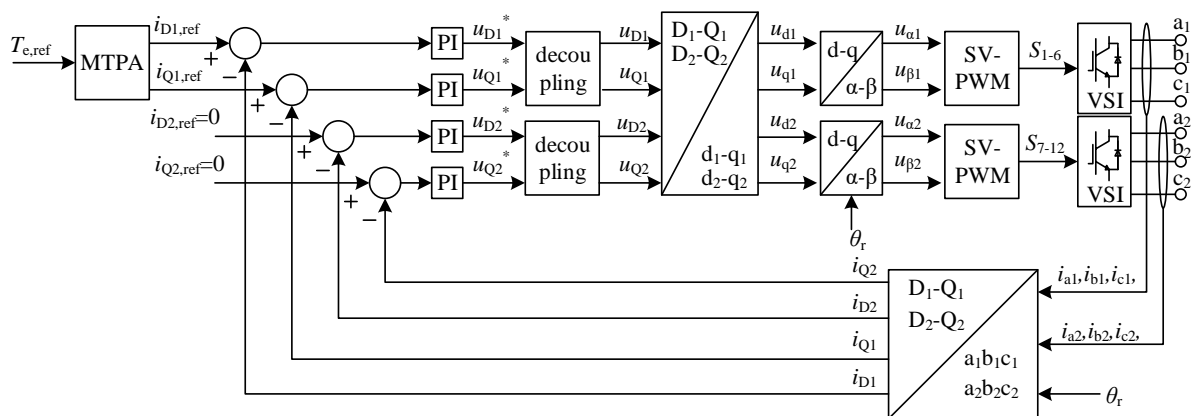


Fig. 1.13. Block diagram of VSD control with four PI regulators for DTP PM machines [KAR14].

The limitation of the PI regulator is the decreasing control capability to the signal as its frequency increases, which results in the weak rejection capability to the harmonic disturbance in z_1z_2 subspace because the harmonic frequency is much higher than the fundamental frequency. If the harmonic disturbance cannot be well rejected, there are still current harmonics existing in the machine system. In other words, although the additional two PI regulators

proposed in [KAR14] can reduce the current harmonics in some degrees, the current harmonics cannot be completely eliminated in z_1z_2 subspace. To enhance the disturbance rejection capability of the current loops in z_1z_2 subspace, [KAR16] proposed a disturbance observer (DOB) and modified the current regulators in z_1z_2 subspace. Fig. 1.14 shows the VSD control with a disturbance observer studied in [KAR16].

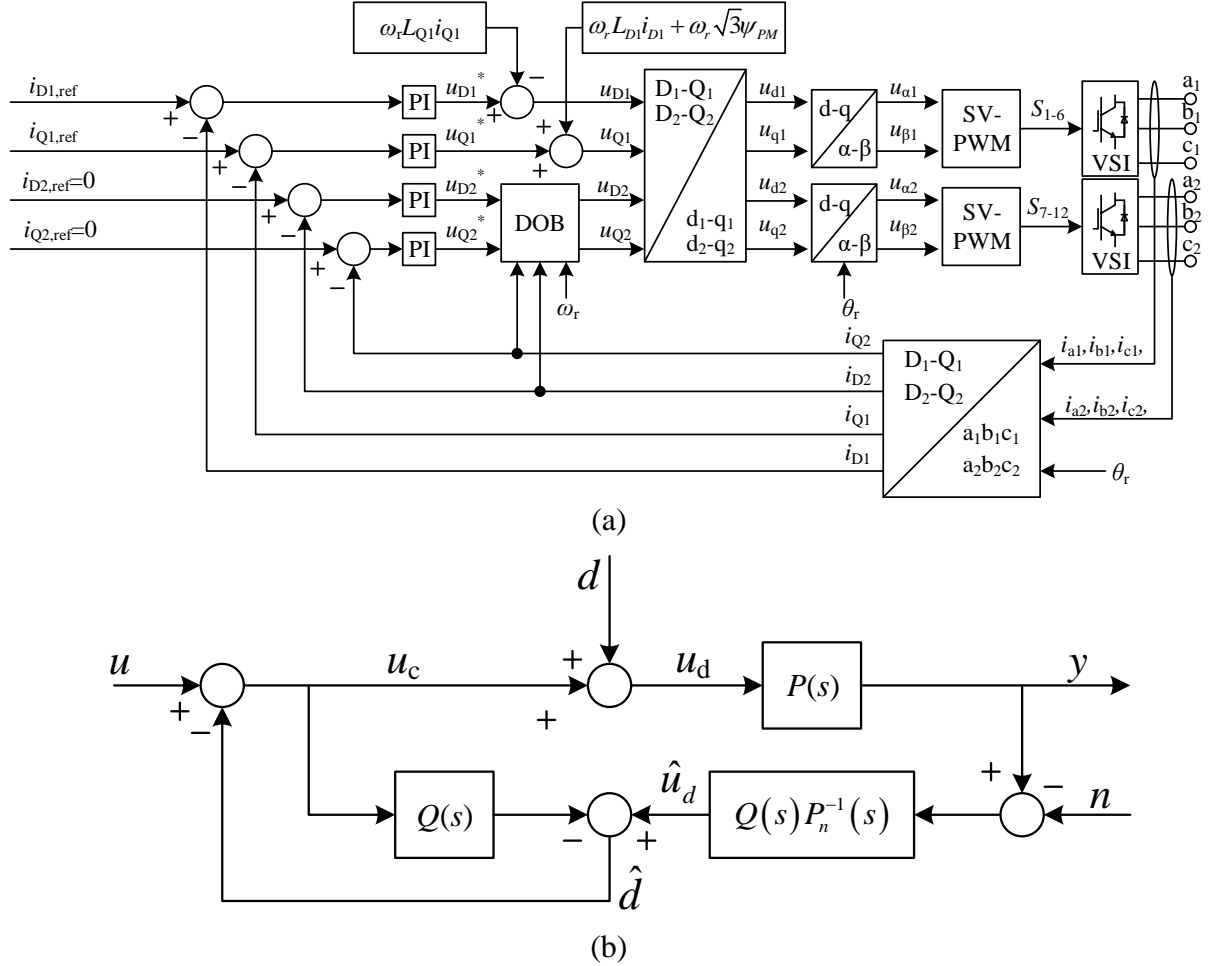


Fig. 1.14. VSD control with a disturbance observer for DTP PM machines [KAR16]. (a) Overall block diagrams. (b) Disturbance observer.

From Fig. 1.14(a), the disturbance observer is series connected to the PI regulators in z_1z_2 subspace, and the outputs of the disturbance observer are the voltage references with compensation to the 6th harmonic disturbance. The details of the disturbance observer are shown in Fig. 1.14(b), where $P(s)$ means the plant and its transfer function in complex vector format is as follows

$$P(s) = \frac{1}{R_s + L_\sigma s + j\omega_e L_\sigma} \quad (1-21)$$

where R_s and L_σ are the stator resistance and leakage inductance, respectively. $Q(s)$ means the bandpass filter that is used to extract the 6th component from the voltage signals, and its transfer function is as follows

$$Q(s) = \frac{K_Q s}{s^2 + K_Q s + (6\omega_e)^2} \quad (1-22)$$

where K_Q is the quality factor of the filter, and $6\omega_e$ is the passband center frequency of this filter. The real disturbance d can be estimated as \hat{d} in the observer and thus \hat{d} is subtracted from the outputs of the PI regulators and compensate the real disturbance d in the system. The results in [KAR16] show that the 6th current harmonic can be completely eliminated by the disturbance observer and the controller shows a good robustness against uncertainties. However, the limitation of this method is that only the current harmonic with single frequency, e.g. the 6th, can be suppressed. When there are multiple current harmonics required to be suppressed, the disturbance observers should also be multiplied, which obviously increases the complexities of the controller and the parameter tuning.

To suppress current harmonics in a wide range of frequency, [XU20] proposed an extended state observer (ESO), as shown in Fig. 1.15. Different from the method proposed in [KAR16], the method in [XU20] does not transform the currents i_{z1} and i_{z2} to synchronous reference dq frame, but directly control them with two PI regulators. Two ESOs are employed to enhance the disturbance rejection capability of the two PI regulators. The details of ESO are shown in Fig. 1.15(b). With the ESO, the disturbance rejection performance can be described using the following transfer function

$$G(s) = \frac{s^3 + \left(\frac{k_p}{L_\sigma} + \beta_{01}\right)s^2 + \frac{k_i}{L_\sigma}s}{(s^2 + \beta_{01}s + \beta_{02})\left(s^2 + \frac{k_p}{L_\sigma}s + \frac{k_i}{L_\sigma}\right)} \quad (1-23)$$

where k_p and k_i are the proportional and integral coefficients of the PI regulators. By tuning the parameters in the ESO, $G(s)$ achieves a large attenuation of magnitude to the signals below 5000Hz, which means the disturbance in this frequency range can be well rejected and the current harmonics are thus suppressed.

asymmetry among six phases. The unbalanced current is mapped in both $\alpha\beta$ and z_1z_2 subspaces, and will be transformed as the 2nd current harmonics in the synchronous reference dq frame. To reduce them, four resonant terms with resonant frequency $2\omega_e$ are parallel connected to the PI regulators in both $\alpha\beta$ and z_1z_2 subspaces. Although the current harmonics and unbalanced current can be suppressed at steady-state, the parameters of the PIR regulators should be carefully tuned to ensure a stable system and achieve a good dynamic performance, which increases the tuning work in the implementation process. In addition, the resonant regulator requires the machine speed to online calculate the resonant frequency. The delay of the speed calculation and speed fluctuation will reduce the control performance of the PIR regulator.

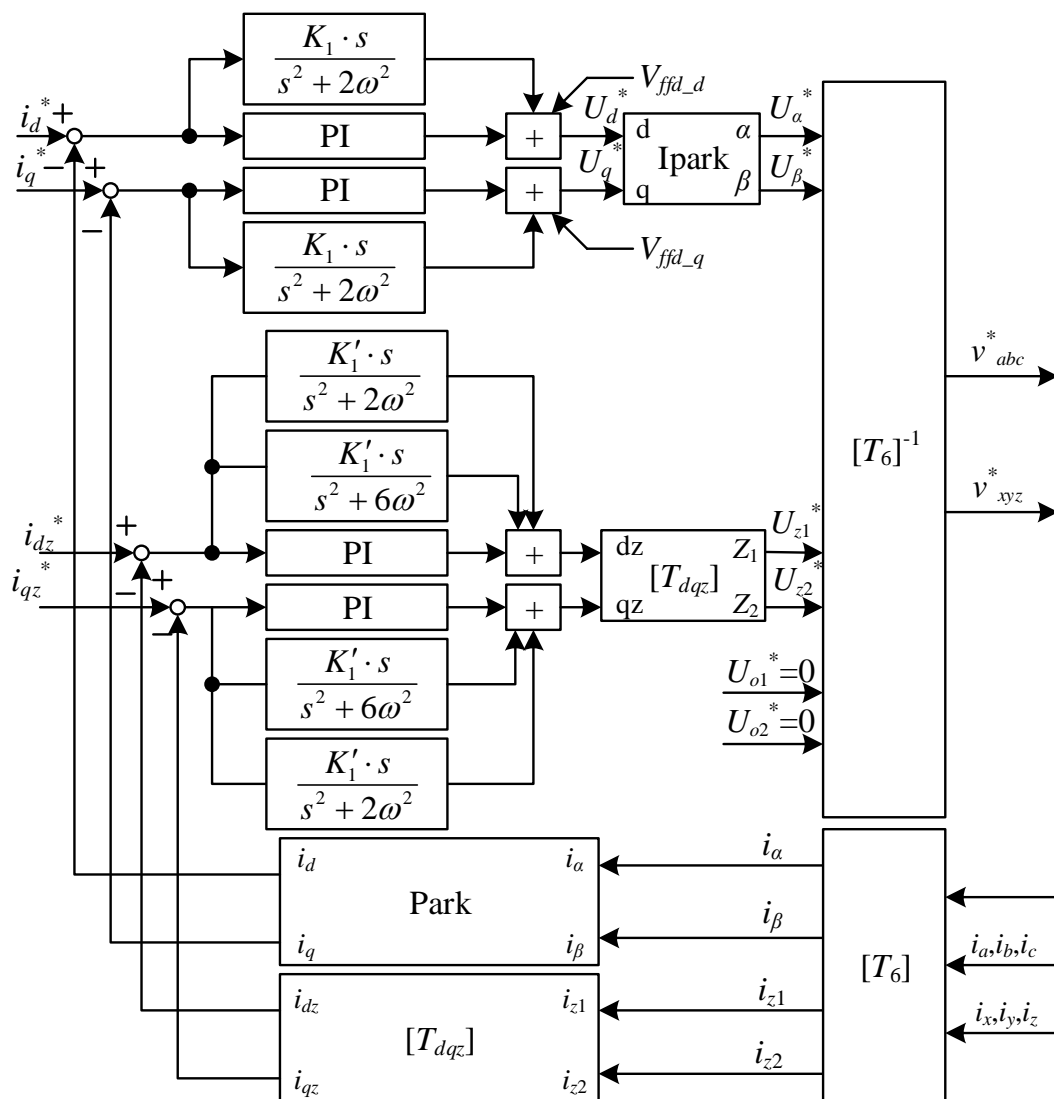


Fig. 1.16. VSD control with PIR regulators for DTP PM machines [HU14].

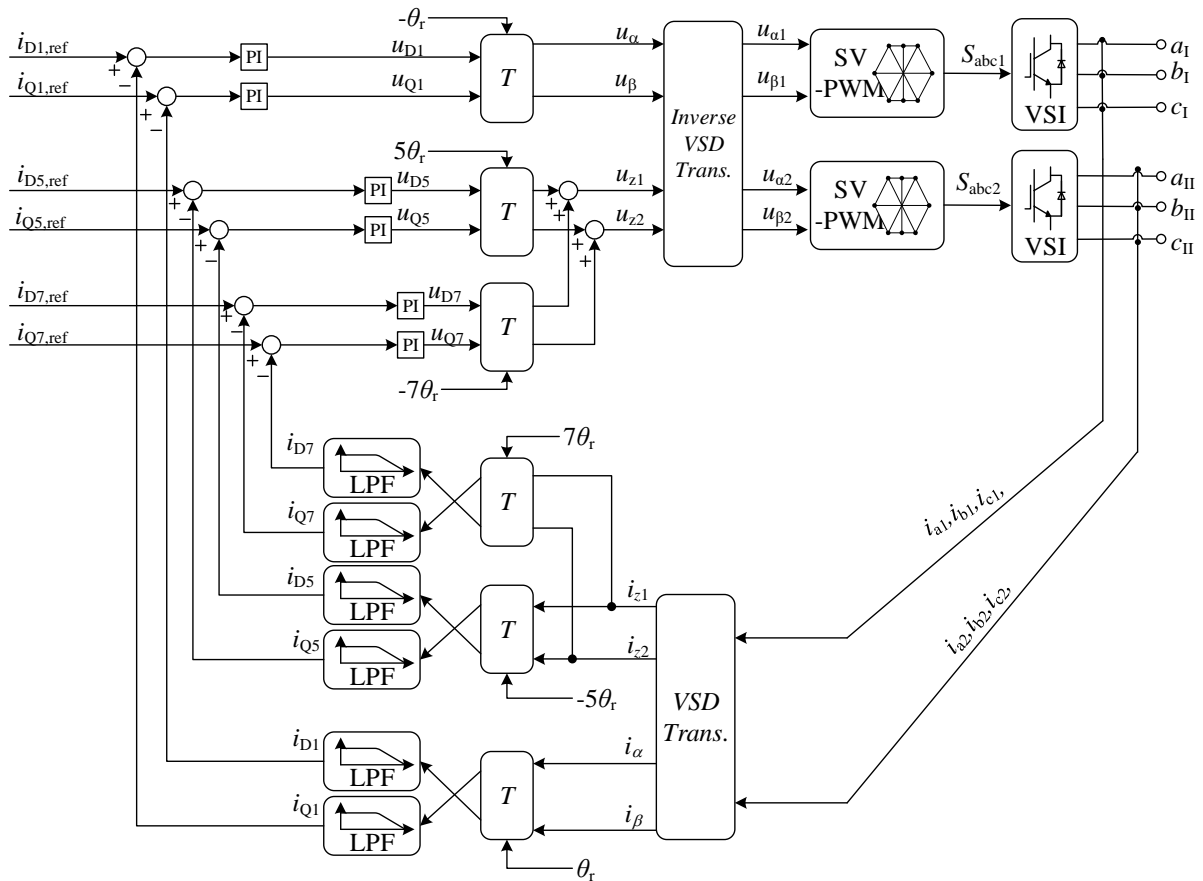


Fig. 1.17. VSD control with MSRF regulators for DTP PM machines [KAR17].

The second kind of approach is known as multiple synchronous reference frame (MSRF) regulators, and the typical literature is [KAR17] which firstly utilize the concept of MSRF in the VSD control. The overall control diagrams are shown in Fig. 1.17. The six phase currents are first decomposed using the VSD transformation. Since the fundamental current is mapped in $\alpha\beta$ subspace, i_α and i_β are transformed to the synchronous reference dq frame, two low pass filters (LPFs) are used to extract the DC components (fundamental current in phase), and two PI regulators are used to control the extracted DC current. The 5th and 7th current harmonics are decomposed in z_1z_2 subspace, and hence i_{z1} and i_{z2} are respectively transformed to the 5th synchronous reference dq_5 frame and the 7th synchronous reference dq_7 frame. Similar to the fundamental current in dq frame, the 5th and 7th current harmonics are also transformed as DC currents in dq_5 frame and dq_7 frame. LPF helps to extract these DC currents so that they can be controlled by the PI regulators. The PI regulator provides infinite gain at 0Hz, resulting in the accurate DC reference tracking and complete DC disturbance rejection. Compared to the PIR regulator, the fundamental and current harmonics are all isolated to each other due to the LPFs, and all the current loops are independent to each other as well. This provides convenience for

implementation because the parameter tuning of each current loop can be individually carried out. Additionally, it is the rotor position angle but not rotor speed that is used in the MSRF transformation, which implies the speed inaccuracy or speed fluctuation will not reduce the control performance. The main problem of the MSRF method is the delay caused by the LPFs. The delay will limit the bandwidth of current control loops and substantially reduce the stability and dynamic performance of the current harmonic regulation.

1.4 Direct Torque Control of DTP PM Machines

Direct torque control (DTC) aims to control directly the stator flux and the torque by selecting the appropriate inverter state. DTC is firstly introduced and employed in three-phase machines in [TAK86] and [DEP88]. Compared to FOC, DTC has the advantages of outstanding transient performance, rapid dynamic torque and speed response, and enhanced robustness against machine parameter variations and sudden load change. DTC was firstly extended from three-phase machine to multiphase machine in [TOL00], where it is employed to drive a five-phase induction machine. In terms of the DTP machines, DTC is firstly investigated in [BOJ05]. The control principle of DTC in a DTP PM machine system can be described by the block diagrams as shown in Fig. 1.18. Torque and flux estimators, torque/flux hysteresis regulators and a switching look-up table are included in this control strategy. Because the torque is only related to the machine variables in $\alpha\beta$ subspace, VSD transformation can be used to calculate the voltage u_α , u_β and current i_α , i_β mapped in $\alpha\beta$ subspace based on the measured machine phase currents and estimated phase voltages. The stator flux linkage can be estimated following the rules

$$\begin{aligned}
 \psi_\alpha &= \int (u_\alpha - R_s i_\alpha) dt \\
 \psi_\beta &= \int (u_\beta - R_s i_\beta) dt \\
 \psi_{mag} &= \sqrt{\psi_\alpha^2 + \psi_\beta^2} \\
 \gamma_s &= \arctan\left(\frac{\psi_\beta}{\psi_\alpha}\right)
 \end{aligned}
 \tag{1-24}$$

where ψ_{mag} and γ_s are the magnitude and phase angle of the stator flux linkage. After the stator flux linkage calculated, the electromagnetic torque can be calculated based on the torque equation

$$T_e = 3p(\psi_\alpha i_\beta - \psi_\beta i_\alpha) \quad (1-25)$$

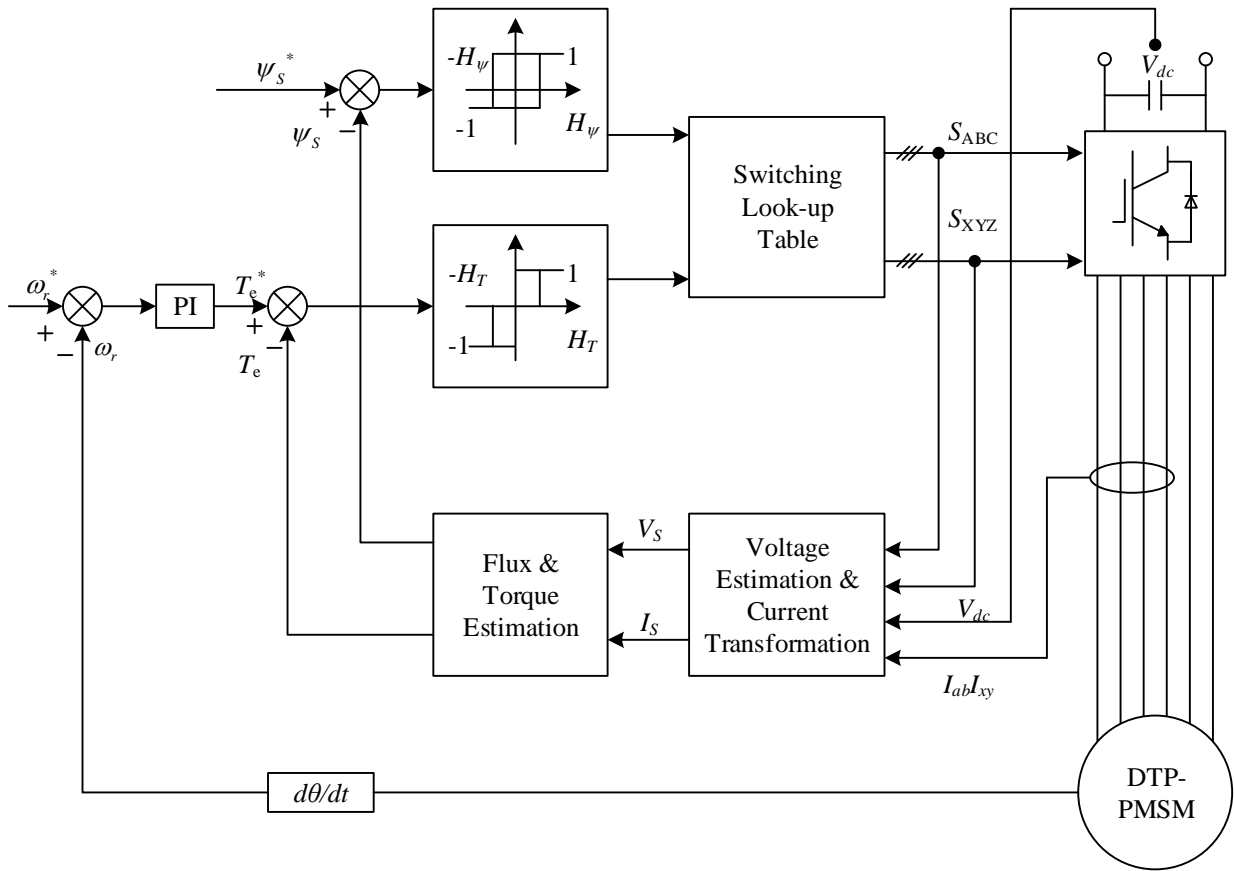


Fig. 1.18. DTC with hysteresis regulators and switching table for DTP PM machines [BOJ05].

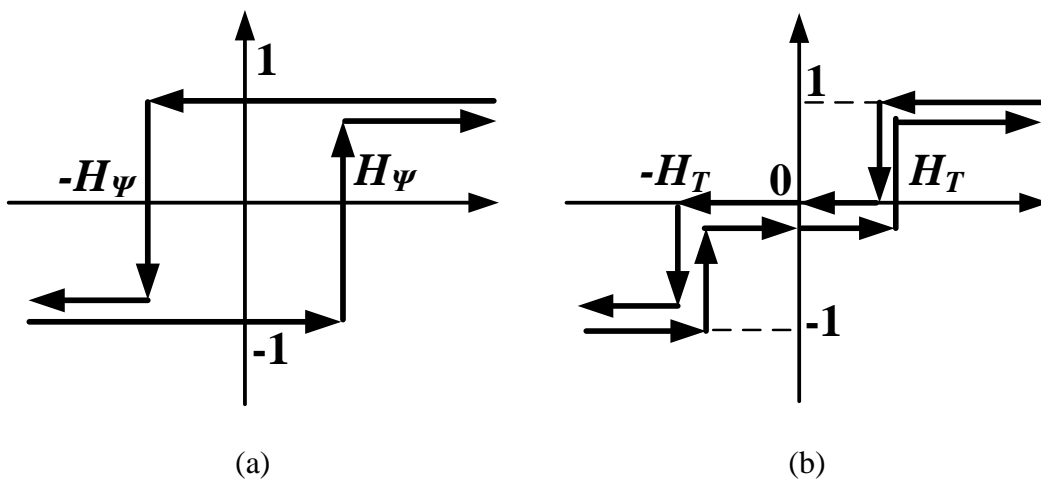


Fig.1.19. Hysteresis regulators in DTC for DTP PMSM. (a) 2-level flux regulator. (b) 3-level torque regulator.

TABLE 1.1.
SWITCHING TABLE OF VECTOR ST-DTC [BOJ05]

ψ_s	T_e	I	II	III	IV	V	VI
	1	V_{27}	V_{26}	V_{18}	V_{22}	V_{54}	V_{52}
1	0	V_0	V_0	V_0	V_0	V_0	V_0
	-1	V_{37}	V_{45}	V_{41}	V_9	V_{11}	V_{27}
	1	V_{26}	V_{18}	V_{22}	V_{54}	V_{52}	V_{36}
-1	0	V_0	V_0	V_0	V_0	V_0	V_0
	-1	V_{36}	V_{37}	V_{45}	V_{41}	V_9	V_{11}
ψ_s	T_e	VII	VIII	IX	X	XI	XII
	1	V_{36}	V_{37}	V_{45}	V_{41}	V_9	V_{11}
1	0	V_0	V_0	V_0	V_{03}	V_0	V_0
	-1	V_{26}	V_{18}	V_{22}	V_{54}	V_{52}	V_{36}
	1	V_{37}	V_{45}	V_{41}	V_9	V_{11}	V_{27}
-1	0	V_0	V_0	V_0	V_{03}	V_0	V_0
	-1	V_{27}	V_{26}	V_{18}	V_{22}	V_{54}	V_{52}

Different from FOC, DTC uses hysteresis regulators but not the PI regulators to control the torque and flux linkage. The structure of the hysteresis regulators is shown in Fig. 1.19. From Fig. 1.18, the difference between the torque/flux linkage reference and feedback is the input of the hysteresis regulator, and the input will be compared with the bandwidth values $\pm H_\psi$ and $\pm H_T$ to generate the states “1”, “-1”, and “0”. State “1” means increase the torque/flux linkage in the next control cycle, state “-1” means decrease the torque/flux linkage in the next control cycle, and state “0” means maintain the torque in the next control cycle. These outputs of the hysteresis regulators are the input of the switching look-up table (LUT). The LUT is shown in TABLE 1.1. The LUT will select the most appropriate switching states or voltage vectors to fulfil the control target in the next control cycle according to the sector that the stator flux linkage locates in. The sectors are defined in Fig. 1.20. Take an example, when the stator flux linkage is located in Sector I, to increase the torque and increase the flux linkage, vector V_{27} is

selected as the optimal voltage vector, which means the switching states of bridges ABCXYZ of the inverter should be “110110”. “1” means the upper switch is turned on and the lower switch is turned off. “0” means the upper switch is turned off and the lower switch is turned on. To increase the torque but decrease the flux linkage, V_{26} should be selected and the switching state should be “010110”.

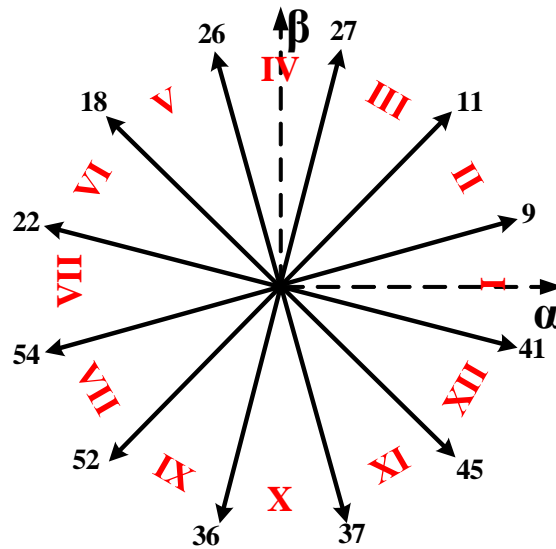


Fig.1.20. Voltage sectors and vectors in [BOJ05].

1.5 Model Predictive Control of DTP PM Machines

Model predictive control (MPC) is based on a model of the real system, also called the “predictive model”, and is used to predict its future evolution. The prediction is carried out for possible switching states to determine which one minimizes a defined cost function. The basic MPC structure is shown in Fig. 1.21, and the MPC follows the steps below:

Step 1: Measuring the current at k moment.

Step 2: Calculating the predictive current at $k+1$ moment by applying all available voltage vectors to the predictive model.

Step 3: Calculating the cost function by means of the predictive current and current reference.

Step 4: Selecting the optimum voltage vector for inverter.

Step 5: $k++$, jump to Step 1.

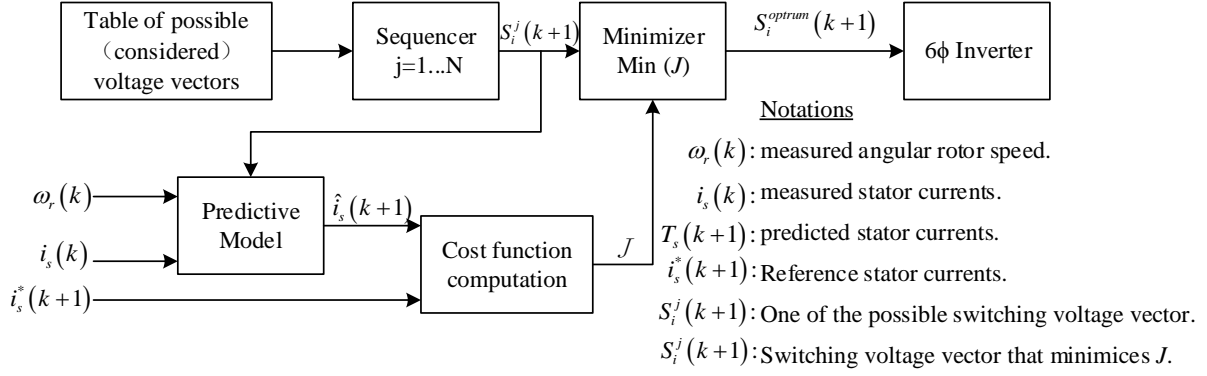


Fig. 1.21. MPC diagram for DTP PMSMs [BAR09a].

The MPC was firstly adapted to DTP drives in [BAR09a], where only the 12 outer vectors of the 64 voltage vectors (VVs) (the largest) are employed to reduce the computation burden. The cost function is expressed as:

$$g = |i_\alpha^* - i_\alpha^{k+1}| + |i_\beta^* - i_\beta^{k+1}| + \lambda(|i_{z1}^* - i_{z1}^{k+1}| + |i_{z2}^* - i_{z2}^{k+1}|) \quad (1-26)$$

where λ is a weighting factor between phase currents in the $\alpha\beta$ and z_1z_2 subspaces; i_α^* , i_β^* , i_{z1}^* , i_{z2}^* are the current references in the $\alpha\beta$ and z_1z_2 subspaces, respectively; and i_α^{k+1} , i_β^{k+1} , i_{z1}^{k+1} , i_{z2}^{k+1} are the predictive currents in the $\alpha\beta$ and z_1z_2 subspaces at instant $k+1$ calculated by the measured currents at instant k .

It is notable that the computation burden increases significantly for multiphase machines, because the VVs increase exponentially with the number of phases. Furthermore, MPC methods with the cost function of minimizing current harmonics and reducing computation cost are investigated in [BAR09b] and [DUR11], respectively. The selected voltage vector combined with a zero vector, namely, one-step modulation predictive current control, or PWM-MPC, where the current harmonics were suppressed further and the steady-state performance improved effectively. However, the active vectors in [BAR09a] [BAR09b] [DUR11] [BAR11] are the same, where only the largest vectors are employed. Although some improved techniques are utilized, the system still suffers from current harmonics caused by uncontrolled harmonics-related components. Hence, a virtual VVs strategy synthesized by the largest and the second-largest actual vectors (synthesized by two groups of VVs) was introduced to MPCC for DTP machines, as described in [GON18]. The virtual vectors ensure null z_1z_2 voltages on average during the sampling period, thereby reducing the current harmonics. Moreover, two groups of virtual vectors (synthesized by three groups of VVs) aiming at harmonic currents reduction are introduced in [LUO19a], and the deadbeat current control method is also introduced to reduce

the computing time with the increase of the number of employed VVs. This technique for two groups of synthesized virtual vectors is further refined in [ACI19][GON19], where a two-step procedure and a dual virtual vector are involved to compensate the harmonics caused by machine asymmetries, dead time effects, and back-EMF harmonics, respectively. The comparison of different control schemes for DTP PM machines is shown in TABLE 1.2.

TABLE 1.2.
COMPARISON OF CONTROL SCHEMES FOR DTP PM MACHINES

	FOC	DTC	MPC
Steady-state performance	High	Low	Normal
Dynamic performance	Slow	Fast	Fast
Switching frequency	Fixed	Variable	Variable
Implementation complexity	Normal	Simple	Complex
Parameter sensitivity	Normal	Normal	High
Sensorless	No	Yes	No
PWM modulator	Yes	No	No
Computation burden	Low	Low	High
Robustness	High	High	Low

1.6 Scope of Research and Contributions

1.6.1 Scope of Research

The aim of this thesis is to investigate the current harmonic control under the framework of VSD control in DTP PM machine systems. The emphasis will firstly be put on the voltage disturbance rejection to reduce the effect of the voltage harmonics and back EMF harmonics, and thus suppress the current harmonics in a wide range of frequency. Then, the current reference tracking capability is investigated and the improved MSRF regulators combined with virtual multi-three-phase systems are proposed to achieve accurate and dynamic current harmonic reference tracking. Furthermore, the scaling error of current measurement will cause current harmonics and its effect is also studied. A high-frequency injection based method is

Chapter 2: DTP PM machines systems usually suffer from small impedance to voltage harmonic disturbance such as inverter voltage errors and back-EMF harmonics. This chapter proposes a virtual impedance technique to increase the machine equivalent impedance and thus enhance the voltage harmonic disturbance rejection capability of the system. This enhancement can contribute to current harmonic suppression in a wide range of frequencies. In addition, the virtual impedance can also reduce the system sensitivity to parameter variation, which helps to suppress the current overshoot, pulsating, and cross-coupling effect caused by parameter mismatch during the dynamic process.

Chapter 3: Although the rejection capability is enhanced compared to the conventional VSD control approach in **Chapter 2**, the attenuation on the voltage harmonic disturbance is still not infinite, which means the current harmonics can merely be reduced but not eliminated or suppressed to zero. More importantly, the proposed virtual impedance can only be utilized to reduce the current harmonics, but in the applications that require current harmonic injection to boost the average torque or minimize the torque ripples, the proposed virtual impedance technique is not applicable anymore. To achieve a better control performance of the current harmonics in DTP PM machines, this chapter proposes an improved multiple synchronous reference frame (MSRF) current harmonic control strategy. A new vector space decomposition transformation combined with auxiliary currents is designed to decouple the current fundamental with current harmonics, and the auxiliary currents can be established by the $\pi/9$ phase shifting of the physical currents in ABC set and the $\pi/18$ phase shifting of the physical currents in XYZ set. By employing the proposed current decomposition, it is easy to detect them using low pass filters in MSRFs. A generic complex vector proportional integral regulator is then employed to control the detected current harmonics to track the current harmonic references. Compared with the virtual impedance technique proposed in **Chapter 2**, the current harmonics can be suppressed to zero or freely controlled to track the required current harmonic reference in this chapter. Compared to the existing MSRF-based methods, the proposed method provides a new current harmonic detection with reduced delay effect, which contributes to enhancing the dynamic performance of current harmonic regulation, and also stabilizing the control system.

Chapter 4: It is proved in **Chapter 3** that the current harmonic decomposition provides convenience for current harmonic regulation due to the reduced delay effect in current harmonic detection. However, it is illustrated that the 5th current harmonic is still coupled with

the 13th current harmonic, while the 7th current harmonic is coupled with the 11th current harmonic. A question that may be easily come up with is that whether it is possible to decompose all the current components into several individual subspaces, and the fundamental and major current harmonics are completely decoupled to each other. Based on the question, this chapter proposes a concept of virtual multi-three-phase systems to achieve complete decomposition of the major current harmonics and independent regulation of the current harmonics in a DTP PM machine system. The control system proposed in **Chapter 3** can be understood as a virtual triple three-phase system. This chapter develops the virtual triple three-phase system to generic virtual multi-three-phase systems, e.g. virtual triple, virtual quadruple, and virtual pentuple three-phase system. The virtual multi-three-phase currents are firstly reconstructed by appropriately shifting the phase of original physical DTP currents, and then, are decomposed with the help of vector space decomposition techniques. As a result, the fundamental and the major current harmonics, i.e. the 5th, 7th, 11th, and 13th, can be completely separated in many isolated subspaces, where the independent current control loops can be easily designed and implemented.

Chapter 5: The previous chapters have investigated the solutions for current harmonic suppression in DTP PMSM systems, while these solutions can only deal with the conventional current harmonics that are caused by the inverter nonlinearity and non-sinusoidal back-EMFs. The scaling errors in the current measurement will also generate current harmonics that the investigated solutions in the previous chapters cannot deal with. Therefore, this chapter proposes an effective method to compensate the current measurement gain and correct the scaling errors, and thus suppress the related current harmonics and torque ripples. A high-frequency carrier voltage is injected to the z_1z_2 subspace of the DTP PMSM, and the resultant high-frequency components in the measured currents are extracted and used to control the current measurement gain and correct the scaling errors.

Chapter 6: This chapter extends the concept of the virtual multi-three-phase system proposed in **Chapters 3** and **4** to the three-phase PMSM systems in order to expand the contribution of this research. For a three-phase PMSM system, the inverter nonlinearity, back-EMF harmonics, and the asymmetry among phases, are firstly considered to derive a comprehensive electrical model of PMSMs in this chapter. Compared to the conventional harmonic analysis in three-phase PMSM systems, the derived model indicates that more new current harmonics can exist in the PMSM system. To regulate the current harmonics with arbitrary orders, a virtual three-phase system is established. By properly shifting the spatial and time phase angles between the

virtual three-phase system and the original physical three-phase system, the selected current harmonics can be decomposed from the phase current. A simple proportional-integral regulator with adjustable phase compensation angle is designed based on the proposed model to regulate the decomposed current harmonics in the corresponding harmonic synchronous reference frame. The implementation details and experimental results are provided to illustrate the feasibility and correctness of the proposed control strategy.

Chapter 7: The general conclusion is drawn in this chapter, and some potential future works are discussed.

1.6.2 Contributions

Main contribution in this thesis include:

- A virtual impedance technique is proposed and employed in the DTP PM machine system for the first time. The voltage disturbance in DTP PM machine system is investigated and the disturbance rejection capability of the system is firstly studied. The analysis shows that the DTP PM machines have weaker disturbance rejection capability due to the small impedance in z_1z_2 subspace compared to conventional three-phase PM machines. The disturbance rejection capability can be greatly enhanced by the proposed virtual impedance and the robustness of the current regulators against parameter variation is also improved.
- A concept of virtual multi-three-phase systems is proposed for the first time. The decomposition capability of VSD transformations is analyzed, and it is found that increasing the number of three-phase sets helps to decompose the current harmonics. By introducing the virtual multi-three-phase systems, the number of the machine phases are virtually increased, and hence, the current harmonics can be more separated or completely separated in many subspaces. Under this circumstance, the MSRF method can be improved by reducing the phase delay of the LPFs in the current harmonic detection or by cancelling the LPFs in the current harmonic detection, which greatly enhances the dynamic performance of current harmonic reference tracking and the stability of the control system.
- The effect of scaling errors of current measurement is analyzed for the first time in DTP PM machines. The analysis shows that the non-identical scaling gains in the current measurements will result in unbalanced current among phases and the 2nd-order torque ripple. The resultant current harmonic cannot be suppressed by the previously

investigated current harmonic control method. A novel high-frequency injection based method is contributed to online tune the scaling gains and suppress the current harmonics due to the scaling errors.

- Still for the first time, a comprehensive model of arbitrary harmonic is established for conventional three-phase PM machines. Various harmonic sources, including odd- and even-order harmonics in back-EMF, inverter nonlinearity, and impedance asymmetry among phases, are investigated in the model. The proposed concept of virtual multi-three-phase systems, which is designed for the DTP PM machine systems, is extended to conventional three-phase PM machines and achieve a better control performance of the current harmonics in a conventional three-phase PM machine system. The extended current harmonic control strategy is novel and shows more rapid current harmonic reference tracking compared to other existing strategies in conventional three-phase systems.

CHAPTER 2

ENHANCEMENT OF VOLTAGE HARMONIC DISTURBANCE REJECTION CAPABILITY IN DUAL THREE-PHASE PMSM SYSTEM BY USING VIRTUAL IMPEDANCE

Dual three-phase (DTP) permanent magnet synchronous machine (PMSM) systems usually suffer from small impedance to voltage harmonic disturbance such as inverter voltage errors and back-EMF harmonics. This chapter proposes a virtual impedance technique to increase the machine equivalent impedance and thus enhance the voltage harmonic disturbance rejection capability of the system. This enhancement can contribute to current harmonic suppression in a wide range of frequencies. In addition, the virtual impedance can also reduce the system sensitivity to parameter variation, which helps to suppress the current overshoot, pulsating, and cross-coupling effect caused by parameter mismatch during the dynamic process. Simulation and experimental results have verified the effectiveness of the proposed control strategy.

This chapter was presented at the IEEE Energy Conversion Congress & Expo (ECCE), Detroit, Michigan, USA, 2020 [YAN20]. The extension of [YAN20] is published in IEEE Transactions on Industry Applications [YAN21a].

[YAN20] L. Yan, Z. Q. Zhu, J. Qi, Y. Ren, C. Gan, S. Brockway, and C. Hilton, "Enhancement of disturbance rejection capability in dual three-phase PMSM system by using virtual impedance," 2020 IEEE Energy Conversion Congress and Exposition (ECCE), 2020, pp. 6104-6110.

[YAN21a] L. Yan, Z. Q. Zhu, J. Qi, Y. Ren, C. Gan, S. Brockway, and C. Hilton, "Enhancement of disturbance rejection capability in dual three-phase PMSM system by using virtual impedance," *IEEE Trans. Ind. Appl.*, vol. 57, no. 5, pp. 4901-4912, Sept. 2021.

2.1 Introduction

Dual three-phase (DTP) permanent magnet synchronous machines (PMSMs) usually have two three-phase winding sets with isolated neutral points and spatially shifted by 30 electrical degrees as shown in Fig. 2.1. Compared to conventional three-phase electrical machines, DTP PMSMs exhibit the advantages of low torque pulsation, low dc-link voltage and low dc-link capacitance requirements, more control degrees of freedom for power and torque distribution, and good fault-tolerant capability [LEV07], as well as the advantages of PM machines, i.e. high torque density, high power density, and high efficiency. Due to such advantages, DTP PMSMs are regarded as good solutions in the applications of high power conversion including electric/hybrid vehicles [PIR19], renewable energy generation [CHE14], aerospace [DE10][BOJ16][THO09], and ship propulsion [QIA16][BOJ03].

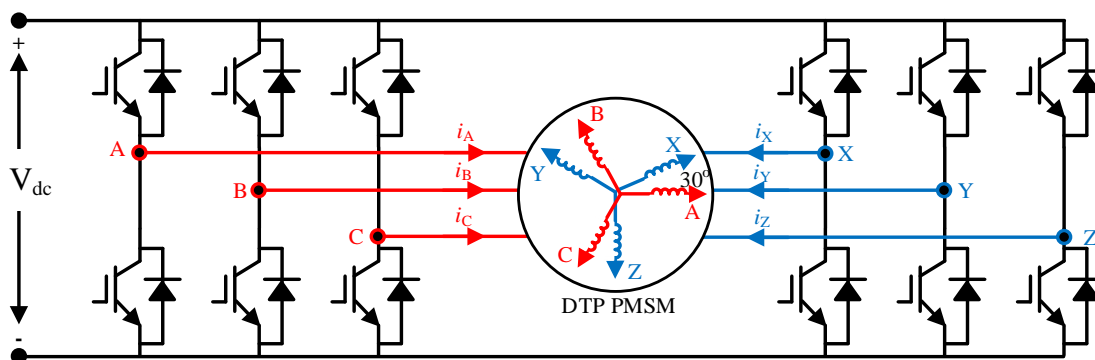


Fig. 2.1. Dual three-phase PMSM with VSI drive.

The winding configuration of DTP PMSM determines the reduction of the torque ripples at the expense of increasing current harmonics. The 30 electrical degrees shifting between two winding sets and the $\pi/6$ time shifting between the corresponding fundamental currents guarantee the cancellation of the spatial harmonics with order of $k = 6m \pm 1$ ($m = 1, 3, 5, \dots$) [ABD15]. Besides, the flux produced by the k^{th} current harmonics in the first winding set will also counteract with the one produced by the second winding set in the air-gap. As a result, both the spatial and time harmonics will not contribute to the $6m^{th}$ torque ripples, which is an inherent advantage of DTP PMSMs. However, although the k^{th} current harmonics will not generate the torque ripples, they can result in the extra loss and reduce the system efficiency. Furthermore, the elimination of synthetic airgap flux produced by the k^{th} current harmonics indicates that the armature airgap inductance is equivalent to zero and the k^{th} current harmonics are only limited by the resistance and leakage inductance, which are usually small

[HU14][REN15]. The small impedance to the k^{th} current harmonics aggregates the phase current distortion and harmonic loss. In addition, the current harmonics with order of $h = 12n \pm 1$ ($n = 1, 2, 3, \dots$) cannot only cause loss but also produce the $12n^{th}$ torque ripples that deteriorates the control performance of the drive system. These current harmonics are usually generated by the voltage harmonic disturbances in the electrical machine system, such as inverter voltage errors and back-EMF harmonics, and thus, the voltage harmonic disturbance rejection capability of system is important and will determine the magnitude of these current harmonics.

The currents are usually transformed into synchronous frames and controlled by the proportional integral (PI) regulators in the vector space decomposition (VSD) control strategy [KAR14][JON09] or double dq -axis frame control strategy [HU17][KAR12]. Although the PI regulator guarantees that the fundamental current can well follow the reference, its weak rejection capability to AC disturbance still results in serious current harmonics. To reject the AC voltage disturbance of a specific frequency, a resonant term in parallel with PI regulator, i.e. proportional integral resonant (PIR) regulator, is considered as the most popular solution to suppress the current harmonics. The resonant term provides the regulator with infinite open-loop gain [ZMO01][ZMO03] at the resonant frequency, which grants the controller the capabilities of both tracking the reference and rejecting the disturbance at the resonant frequency. The resonant frequency is usually pre-configured to the six or twelve times fundamental electrical angular frequency [HU14][CHE14]. The additional resonant terms increase the complexity of the control structure and make the current regulator suffer from complicated parameter tuning and stability issues. Similar to the PIR regulator, the multiply synchronous reference frame (MSRF) PI regulators [KAR17][YAN19] are also proposed to regulate the fundamental current as well as the current harmonics. The currents of different frequencies can be all transformed as dc components in the corresponding synchronous frames and then they can be well controlled by the PI regulators due to PI's ideal control capability to dc components. Nevertheless, the MSRF PI regulators require additional coordinate transformation and regulation of harmonics, which increases the computation burden in implementation. Meanwhile, the dynamic performance of MSRF based method can be reduced by the low pass filters (LPFs) in the current loops.

The parameters of the aforementioned controllers should be carefully tuned to simultaneously achieve good capability of both tracking the reference and rejecting the disturbance, which

leads to complex parameter tuning. To avoid this issue, the controller with two freedom degrees is a preferable solution. [KAR16] proposed a disturbance observer (DOB) combined with the PI regulator to suppress the 5th and 7th current harmonics in dual three-phase PMSMs. The parameters of the PI regulator can be tuned in the traditional way, and the DOB provides infinite damping to the 6th harmonic voltage disturbance but does not change the capability of tracking the current reference. However, the DOB can only reject the disturbance with fixed frequency, and more DOBs should be used to reject the disturbance with multiple harmonic frequencies, which will obviously increase the complexity of the control system. [XU20] replaced the DOB with the extended state observer (ESO). The ESO exhibits a wide bandwidth of disturbance rejection and can suppress the current harmonics of different frequencies. Nevertheless, the ESO is not employed in $\alpha\beta$ subspace and the dynamic current response is also not experimentally evaluated in [XU20].

An alternative method called virtual impedance is proposed in [YAN20] to enhance the voltage harmonic disturbance rejection capability of DTP PMSM system. The early idea of virtual impedance was mentioned in [BLA99], where an active damping term works like a real resistor in the control loop to improve the dynamic performance. Due to the similar function as a real impedance, the virtual impedance can help to suppress the current ripples and robust the current reference tracking [LI18][SON17]. Hence, it has been employed in high performance current regulation of machine drive [YIM09][LIA17][WAN18]. The proposed current regulator in [YAN21a] is a two-freedom-degree controller but does not have complex structure as the observer-based method, which makes it more practical in real systems. This chapter is mainly about the control approach proposed in [YAN21a], and the rest part of this chapter is organized as follows. Section 2.2 introduces the electrical machine model and the basic complex-vector PI regulator in two subspaces of DTP PMSM. In Section 2.3, the proposed virtual impedance method is presented, and the parameter determination as well as the parametric uncertainty are also analyzed. Section 2.4 compares the proposed method with existing methods and highlights the contributions of this chapter. The experimental results are provided in Section 2.5 to validate the advantages of the proposed method, and finally section 2.6 concludes this chapter.

2.2 Control System of DTP PMSM

The VSD technique is advantageous in the modelling and control of multi three-phase machine because it can decompose the variables of machine into several orthogonal subspaces, in which the modelling and control can be individually processed. If no account is taken of the zero

sequence components, the VSD transformation for DTP PMSM is as follows [ZHA95]

$$\begin{bmatrix} \alpha \\ \beta \\ z_1 \\ z_2 \end{bmatrix} = \frac{1}{3} \begin{bmatrix} 1 & -1/2 & -1/2 & \sqrt{3}/2 & -\sqrt{3}/2 & 0 \\ 0 & \sqrt{3}/2 & -\sqrt{3}/2 & 1/2 & 1/2 & -1 \\ 1 & -1/2 & -1/2 & -\sqrt{3}/2 & \sqrt{3}/2 & 0 \\ 0 & \sqrt{3}/2 & -\sqrt{3}/2 & -1/2 & -1/2 & 1 \end{bmatrix} \begin{bmatrix} A \\ B \\ C \\ X \\ Y \\ Z \end{bmatrix} \quad (2-1)$$

where $[A \ B \ C \ X \ Y \ Z]^T$ represents the current, voltage, and back-EMF valuables in six-phase stationary frame. Matrix $[\alpha \ \beta \ z_1 \ z_2]^T$ represents the corresponding decomposed current, voltage, and back-EMF valuables in $\alpha\beta$ and z_1z_2 subspaces.

2.2.1 Electrical Machine Model

By using (2-1), the variables can be decomposed into two orthogonal subspaces, i.e. $\alpha\beta$ and z_1z_2 subspaces, where the machine model can be described by

$$\begin{aligned} u_\alpha &= R_s i_\alpha + \frac{dL_\alpha i_\alpha}{dt} + e_\alpha \\ u_\beta &= R_s i_\beta + \frac{dL_\beta i_\beta}{dt} + e_\beta \\ u_{z1} &= R_s i_{z1} + \frac{dL_\sigma i_{z1}}{dt} + e_{z1} \\ u_{z2} &= R_s i_{z2} + \frac{dL_\sigma i_{z2}}{dt} + e_{z2} \end{aligned} \quad (2-2)$$

where u , i , and e are the voltage, current, and EMF generated by PM flux linkage. L_α and L_β are the stator inductance, and L_σ denotes the stator leakage inductance. The electromagnetic torque can be expressed as

$$T_e = 3P(\psi_\alpha i_\beta - \psi_\beta i_\alpha) \quad (2-3)$$

where ψ_α and ψ_β are the stator flux linkage in $\alpha\beta$ subspace. P denotes the number of pole pairs. The fundamental component and the harmonics with order of $h = 12n \pm 1$ ($n = 1, 2, 3, \dots$), i.e. 11th and 13th harmonics etc., are mapped in $\alpha\beta$ subspace and the k^{th} ones are mapped in z_1z_2 subspace, where $k = 6m \pm 1$ ($m = 1, 3, 5, \dots$), i.e. 5th and 7th harmonics etc. If only considering the 5th, 7th, 11th, and 13th harmonics, the EMFs can be expressed as [JIA15]

$$\begin{aligned}
e_\alpha &= -\omega_e \psi_{f1} \sin(\theta_e) + 11\omega_e \psi_{f11} \sin(11\theta_e) - 13\omega_e \psi_{f13} \sin(13\theta_e) \\
e_\beta &= \omega_e \psi_{f1} \cos(\theta_e) + 11\omega_e \psi_{f11} \cos(11\theta_e) + 13\omega_e \psi_{f13} \cos(13\theta_e) \\
e_{z1} &= 5\omega_e \psi_{f5} \sin(5\theta_e) - 7\omega_e \psi_{f7} \sin(7\theta_e) \\
e_{z2} &= 5\omega_e \psi_{f5} \cos(5\theta_e) + 7\omega_e \psi_{f7} \cos(7\theta_e)
\end{aligned} \tag{2-4}$$

where ω_e is the electrical angular speed, θ_e is the electrical angle of the rotor position, and ψ_{fk} denotes the amplitude of fundamental and harmonic PM flux linkage. In each subspace, the currents, voltages, and EMFs can be transformed into synchronous frames by (2-5).

$$\begin{bmatrix} d \\ q \\ zd \\ zq \end{bmatrix} = \begin{bmatrix} \cos \theta_e & \sin \theta_e & 0 & 0 \\ -\sin \theta_e & \cos \theta_e & 0 & 0 \\ 0 & 0 & \cos \theta_e & \sin \theta_e \\ 0 & 0 & -\sin \theta_e & \cos \theta_e \end{bmatrix} \begin{bmatrix} \alpha \\ \beta \\ z_1 \\ z_2 \end{bmatrix} \tag{2-5}$$

where $[d \ q \ zd \ zq]^T$ represents the decomposed current, voltage, and back-EMF values in synchronous frame.

Then, the voltage equations (2-2) are transformed as (2-6).

$$\begin{aligned}
u_d &= R_s i_d + L_D \frac{di_d}{dt} - \omega_e L_Q i_q + e_d \\
u_q &= R_s i_q + L_Q \frac{di_q}{dt} + \omega_e L_D i_d + e_q \\
u_{zd} &= R_s i_{zd} + L_\sigma \frac{di_{zd}}{dt} - \omega_e L_\sigma i_{zq} + e_{zd} \\
u_{zq} &= R_s i_{zq} + L_\sigma \frac{di_{zq}}{dt} + \omega_e L_\sigma i_{zd} + e_{zq}
\end{aligned} \tag{2-6}$$

where L_D and L_Q are the synchronous inductances. The $\alpha\beta$ and z_1z_2 subspaces are orthogonal and decoupled, and thus theoretically there is no coupling term between dq -axes and $z dq$ -axes. It should be noted that in synchronous frames, the fundamental is transformed as dc component, the 5th and 7th harmonics are converted as the 6th harmonics in $z dq$ -axes, and the 11th and 13th harmonics are the 12th harmonics in dq -axes. Accordingly, the EMFs e_d , e_q , e_{zd} , and e_{zq} can be expressed as

$$\begin{aligned}
e_d &= 12\omega_e\psi_{fd12}\sin(12\theta_e) \\
e_q &= \omega_e\psi_{f1} + 12\omega_e\psi_{fq12}\cos(12\theta_e) \\
e_{zd} &= 6\omega_e\psi_{fd6}\sin(6\theta_e) \\
e_{zq} &= 6\omega_e\psi_{fq6}\cos(6\theta_e)
\end{aligned} \tag{2-7}$$

where ψ_{fd6} , ψ_{fq6} , ψ_{fd12} , and ψ_{fq12} are the amplitudes of the 6th and 12th PM flux linkage harmonics in synchronous frames. The back EMF harmonics in (2-7) can be considered as voltage harmonic disturbance and generate current harmonics in the control system.

2.2.2 Inverter Model

To avoid shoot-through in the dc link of the six-leg inverter shown in Fig. 2.1, a dead time is inserted in the PWM signals to guarantee that both switches of one leg will not be on simultaneously. However, the negative effect of dead time is output voltage distortion that can result in current harmonics, torque ripples, system efficiency reduction, and degradation of control performance. Considering the dead time, the switching time delays, and the voltage drops of switching devices, the output voltage error in phase A can be equivalent to a square wave voltage (2-8) whose polarity is determined by phase A current $i_A(t)$ [PAR12][KIM03].

$$\Delta v_A(t) = V_{dead} \text{sgn}(i_A(t)) \tag{2-8}$$

where

$$V_{dead} = \frac{T_{dead} + T_{on} - T_{off}}{T_s} (V_{dc} - V_{sat} + V_d) + \frac{V_{sat} + V_d}{2} \tag{2-9}$$

T_{dead} is the dead time, T_{on} and T_{off} are the turn-on time and turn-off time, T_s is the switching period. V_{dc} is the dc link voltage, V_{sat} and V_d are the saturation voltage drop of the switching device and the forward voltage drop of the freewheeling diode, respectively. Function sgn is the sign function. According to the FFT principle, the square wave voltage error can be regarded as the sum of sinusoidal components with odd orders. These sinusoidal voltages have the same harmonic orders as the phase back EMFs have. Likewise, the voltage errors can be also regarded as disturbance to deal with.

2.2.3 Basic Current Control Loops in Two Subspaces

The general current regulation method in synchronous frames uses the PI regulator. In order to eliminate the cross-coupling effect and improve the dynamic performance of current loop, the cross-decoupled complex-vector PI regulator is employed in this chapter [BLA99] due to its simple parameter tuning, easy implementation, and rapid dynamic performance, and the regulator structure is as shown in Fig. 2.2. To avoid complicated coefficient tuning, the PI regulators are designed based on the voltage equations (2-6), then the inductance and the resistance are employed as parts of the proportional and integral coefficients. It can be seen in Fig. 2.2, the inverter and the machine are considered together in the blue blocks. The back EMFs and the inverter voltage errors are considered together as the voltage disturbance, i.e. $D_d, D_q, D_{zd},$ and D_{zq} , where D_d, D_q include the dc and $12n^{th}$ AC components, and D_{zd}, D_{zq} include the $6m^{th}$ AC components. To make a brief description, the complex-vector expression method [BLA99] is utilized and the inductance is supposed to satisfy $L_D = L_Q = L_S$. If the inductance and resistance employed in the current regulators are accurate and matched with the machine, the transfer function from the current reference to the current feedback can be derived from Fig. 2.2(a) as follows.

$$H_c(s) = \frac{I_{dq}(s)}{I_{dq}^*(s)} = \frac{K_c \frac{R_s + L_s s + j\omega_e L_s}{s} \frac{1}{R_s + L_s s + j\omega_e L_s}}{1 + K_c \frac{R_s + L_s s + j\omega_e L_s}{s} \frac{1}{R_s + L_s s + j\omega_e L_s}} = \frac{K_c}{s + K_c} \quad (2-10)$$

where current vectors $I_{dq}(s) = I_d(s) + jI_q(s)$, current reference vectors $I_{dq}^*(s) = I_d^*(s) + jI_q^*(s)$. The transfer function of the current loop in z_1z_2 subspace, Fig. 2.2(b), can be conducted similarly and is not written here. As seen in (2-10), the zero-pole cancellation of the open-loop transfer function are achieved and thus the close-loop transfer function is simplified as a first-order LPF, in which K_c represents the cut-off angular frequency and determines the response speed of the current loop. Theoretically, the current step response should be ideal as there will not be any cross-coupling effect, overshoot, or oscillation according to the characteristic of a first-order LPF.

The transfer function from the disturbance to the current feedback in Fig. 2.2(a) can be derived as follows.

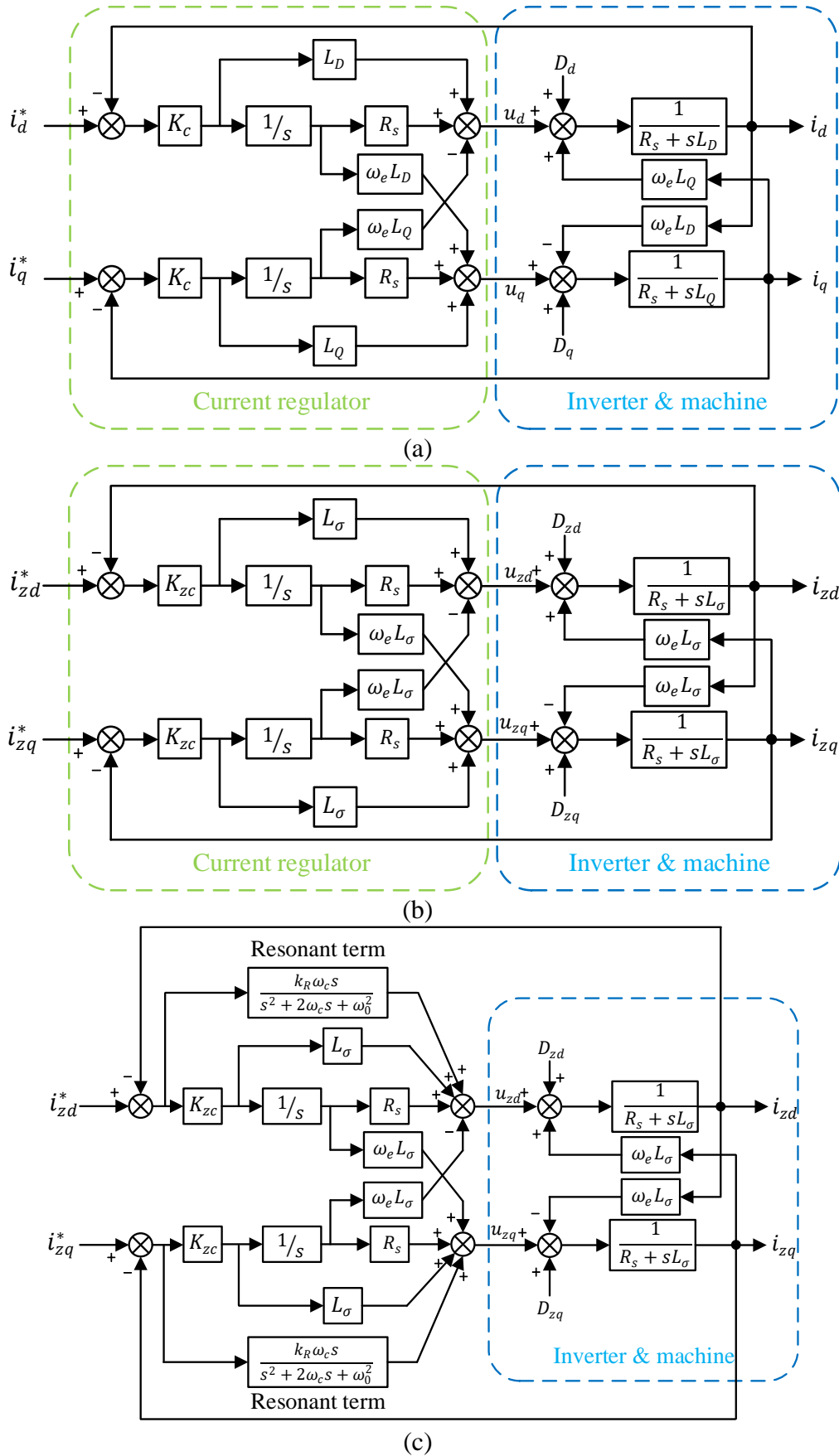


Fig. 2.2. Current control loops in synchronous dq frames. (a) $\alpha\beta$ subspace. (b) z_1z_2 subspace. (c) Proportional-integral-resonant regulator.

$$G_c(s) = \frac{I_{dq}(s)}{D_{dq}(s)} = \frac{s}{(s + K_c)(L_s s + R_s + j\omega_e L_s)} \quad (2-11)$$

where the disturbance vector $D_{dq}(s) = D_d(s) + jD_q(s)$. From (2-11), the gain is not zero to AC components, which means the current harmonics will be generated by the aforementioned AC disturbance.

2.3 Proposed Control Strategy

2.3.1 Current Regulator with Virtual Impedance

The disturbance rejection capability of the current loop in Fig. 2.2(a) depends on K_c and the values of resistance and inductance according to (2-11). Although the current harmonics can be suppressed by increasing K_c , the reference tracking performance will be changed as well. In order to not influence the reference tracking capability of the current loop, K_c is merely adjustable to satisfy the required current response speed. Consequently, the disturbance rejection capability is only determined by the resistance and inductance. One general solution to increase the disturbance rejection capability is using additional symmetrical resistors and inductors between the inverter and the machine, which can increase machine equivalent impedance and suppress the total current harmonics, however, will introduce extra loss and decrease the dc link voltage utilization. In order to maintain the advantages and avoid the shortages of the real impedance, the virtual resistance and inductance terms are proposed to replace the real resistors and inductors, and further improve the control performance of the current regulation.

Fig. 2.3 shows the proposed current regulator with virtual impedance. Like the real impedance, the virtual impedance also acts as a virtual voltage drop, which is online calculated by using the virtual resistance, virtual inductance, and currents. After introducing the virtual impedance, from the perspective of the current regulator, the resistance and inductance of machine is equivalently changed. Since the regulator design is based on the machine model, the virtual inductance and resistance are respectively added to the proportional and integral coefficients to cater that change and maintain the zero-pole cancellation principle.

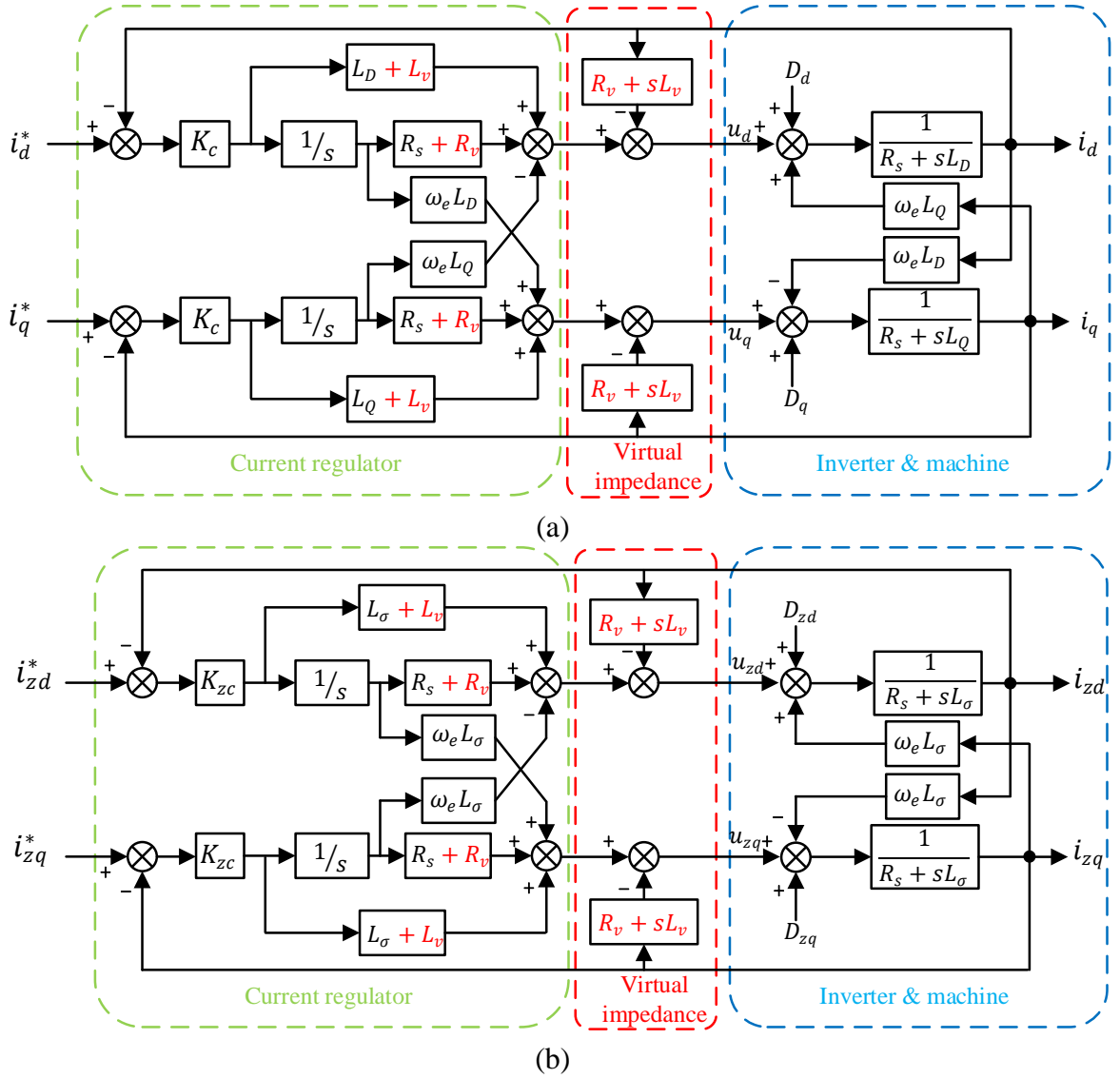


Fig. 2.3. Current control loops with virtual impedance. (a) $\alpha\beta$ subspace. (b) z_1z_2 subspace.

Regarding the proposed current loop in Fig. 2.3(a), the transfer functions from reference to current feedback and disturbance to current feedback can be conducted as

$$H_c^v(s) = \frac{K_c}{s + K_c} \quad (2-12)$$

$$G_c^v(s) = \frac{s}{s + K_c} \frac{1}{(L_s + L_v)s + (R_s + R_v) + j\omega_e L_s} \quad (2-13)$$

where the superscript “ v ” indicates the system with virtual impedance. It should be noted that a LPF is used to filter the current data noise and prevent the instability caused by derivative term in a real system. The effect of this LPF on control performance can be neglected because the frequency of data noise is much higher than the system frequency. Comparing (2-12)(2-13) with (2-10)(2-11), the reference tracking capability is not changed, whereas the disturbance

rejection capability is enhanced by equivalently increasing the inductance and resistance. This means the introduced virtual impedance will not affect the capability of tracking the reference but generate the extra damping to the disturbance. The current regulator is modified to be a two-freedom-degree regulator, i.e. K_c is tuned to satisfy the required dynamic response of current reference tracking, and the virtual resistance and inductance are adjustable to provide additional capability to reject the disturbance.

2.3.2 Determination of Virtual Impedance Values

To maximize the disturbance rejection capability, the values of virtual inductance and resistance can be increased to as high as possible according to (2-13), so that the effect of disturbance can be eliminated. However, due to the digital delay caused by the computation, the virtual impedance cannot be configured to be infinite high, and the range of virtual impedance should be determined. If considering the delay, the open-loop transfer function of Fig. 2.3(a) can be rewritten as

$$H_o^v(s) = \frac{K_c}{s} \frac{(L_s + L_v)s + (R_s + R_v) + j\omega_e L_s}{R_s + L_s s + j\omega_e L_s + (L_v s + R_v)e^{-T_d s}} e^{-T_d s} \quad (2-14)$$

where T_d is the delay time. It can be seen from (2-14) that the structure of zero-pole cancellation is destroyed. To maintain that structure, the current regulator is further improved by processing an active delay to the virtual impedance term in order to compensate the inherent delay effect in the control loop, and hence the transfer is modified to be

$$H_o^v(s) = \frac{K_c}{s} \frac{R_s + L_s s + j\omega_e L_s + (L_v s + R_v)e^{-T_d s}}{R_s + L_s s + j\omega_e L_s + (L_v s + R_v)e^{-T_d s}} e^{-T_d s} \quad (2-15)$$

If the parameters in current regulator are matched with those of the electrical machine, the transfer functions from reference to current feedback and disturbance to current feedback can be conducted as

$$H_c^v(s) = \frac{K_c e^{-T_d s}}{s + K_c e^{-T_d s}} \quad (2-16)$$

$$G_c^v(s) = \frac{s}{s + K_c e^{-T_d s}} \frac{1}{R_s + L_s s + j\omega_e L_s + (L_v s + R_v)e^{-T_d s}} \quad (2-17)$$

To simplify the analysis, the delay effect is linearized by using the first-order Pade approximation.

$$e^{-T_d s} \approx \frac{-\beta s + 1}{\beta s + 1} \quad (2-18)$$

where $\beta = T_d/2$. Substituting (2-18) into (2-17) yields the linearized disturbance transfer function, based on which the Bode diagrams can be conducted, Figs. 2.4 and 2.5.

Figs. 2.4 and 2.5 show the magnitude and phase characteristics of disturbance rejection under different virtual resistances and inductances. Both the positive- and negative-sequence domains are taken into consideration. The simulation parameters are listed in TABLE A.1, see Appendix A. The virtual resistance increases from 0Ω to 10Ω when the virtual inductance is zero. The bandwidth of the current loop is tuned as 200Hz which makes K_c configured as 1256rad/s in Fig. 2.4, and similarly, the virtual inductance increases from 0 to 2mH when the virtual resistance is zero in Fig. 2.5. The current regulator is equivalent to the basic complex-vector PI regulator shown in Fig. 2.2 if the virtual impedance is zero. It is clear that the dc disturbance can be completely rejected due to the integrator in the current regulator. Attenuation of disturbance can be enhanced at low and medium frequency (from -1kHz to 1kHz) but weaken at high frequency region (over 1kHz and below -1kHz) with the virtual resistance increasing. Different from the resistance, the increasing virtual inductance provides stronger attenuation to the disturbance in a wide range of frequency but not obvious attenuation from -0.1kHz to 0.1kHz. This means the virtual resistance and inductance can respectively reject the disturbance at low and high frequency regions, which is consistent with the characteristics of real resistor and inductor. To determine the maximum values of virtual impedance, based on the open-loop transfer function (2-15), the characteristic equation of the current loop can be conducted as follows

$$(s + K_c e^{-T_d s})[L_s s + R_s + j\omega_e L_s + (L_v s + R_v) e^{-T_d s}] = 0 \quad (2-19)$$

Substituting (2-18) into (2-19) yields the stability boundary.

$$K_c < 1/\beta, L_v < L_s, R_v < R_s + (L_v + L_s)/\beta \quad (2-20)$$

The above analysis is based on the current loop in $\alpha\beta$ subspace, Fig. 2.3(a). It is clear that the virtual inductance L_v cannot exceed the synchronous inductance L_s according to (2-20). However, the machine model in $z_1 z_2$ subspace is only relevant to the leakage inductance L_σ . Considering this, the maximum values of the virtual resistance and virtual inductance in $z_1 z_2$ subspace, Fig. 2.3(b), can be similarly derived as

$$K_{zc} < 1/\beta, L_v < L_\sigma, R_v < R_s + (L_v + L_\sigma)/\beta \quad (2-21)$$

From (2-20) and (2-21), the stability boundary in $\alpha\beta$ and z_1z_2 subspaces is not identical due to the different physical inductances, and the virtual impedance should also be tuned individually to optimize the disturbance rejection capability of current loop in each subspace.

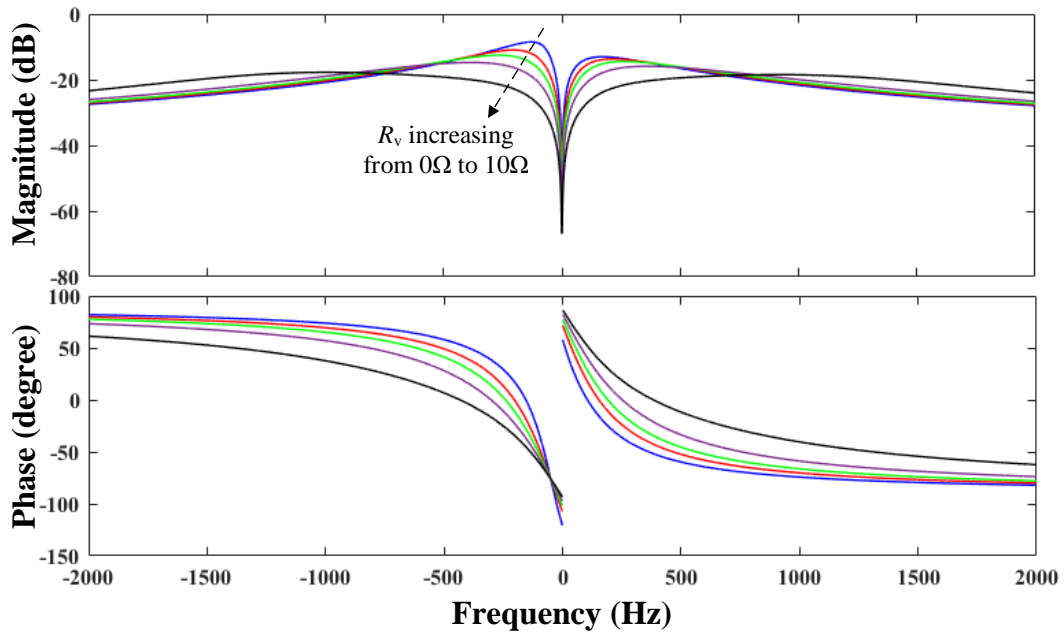


Fig. 2.4. Bode diagram of disturbance rejection with different virtual resistances.

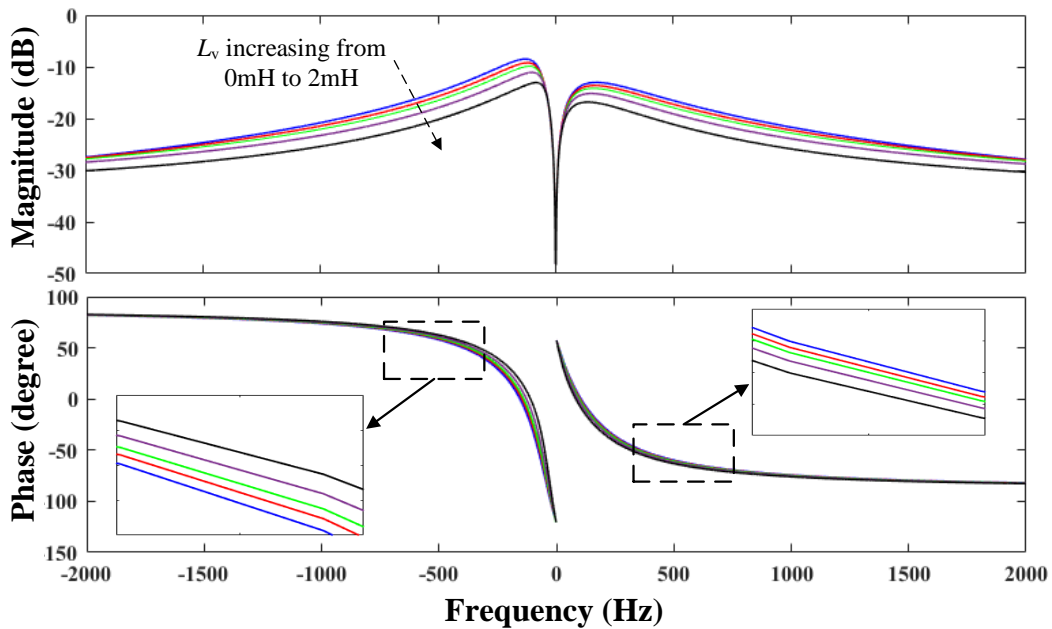


Fig. 2.5. Bode diagram of disturbance rejection with different virtual inductances.

2.3.3 Parametric Uncertainty

The real machine system always includes the parametric uncertainty, such as the resistance variation due to temperature and inductance variation due to saturation. The effect of parametric uncertainty can be evaluated by means of the zero and pole map of open-loop transfer function (2-15). Fig. 2.6 shows the zero and pole maps of (2-15) when the parameters are matched and mismatched. The virtual impedance is configured as 10Ω and 1mH . It can be seen from Fig. 2.6(a), z_3 and p_4 are introduced by the delay term and p_3 represents the integral term. Since the controller design is based on zero-pole cancellation, two pairs of main zeros and poles, i.e. $z_1, p_1, z_2,$ and p_2 , will be cancelled, and hence the open-loop transfer function can be regarded as an integrator with a delay term, which results in the expected current response. However, when the estimated parameters are not matched with those of the machine, as shown in Fig. 2.6(b), the poles p_3, p_4 and the zero z_3 are fixed, but the zeros z_1, z_2 offset the poles p_1, p_2 . The zero-pole cancellation is destroyed and the current regulation will be deteriorated.

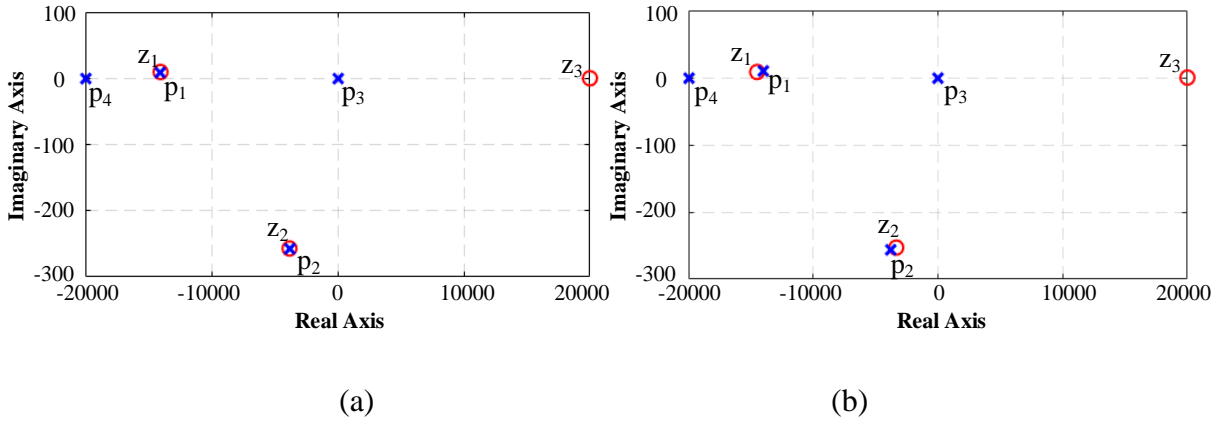


Fig. 2.6. Maps of zeros and poles of open-loop function (14) when R_v is 10Ω and L_v is 1mH . (a) Parameter matched. (b) Parameter mismatched.

To quantify the effect of parametric uncertainty, a factor λ , which indicates the distance between the cancelled zeros and poles, is introduced and can be calculated by

$$\lambda = \frac{|z_1 - p_1|}{|p_1|} + \frac{|z_2 - p_2|}{|p_2|} \quad (2-22)$$

Fig. 2.7 shows the variation of λ without and with the virtual impedance when the parameters are mismatched, i.e. the estimated machine resistance and inductance in regulator change from $0.5R_s$ and $0.5L_s$ to $2R_s$ and $2L_s$, respectively. In Fig. 2.7, factor λ reaches zero when estimated

resistance and inductance are accurate. It is obvious that by using the virtual impedance, the values of λ are much lower when the machine parameters are not accurate. That means even if there is parameter uncertainty in the current loop, the proposed current regulator can still achieve approximate zero-pole cancellation, and thus the control performance will be much better than that of the regulator without the virtual impedance. Actually, if considering the virtual impedance, the inverter, and the machine as an entire control object, the virtual impedance is definitely certain to the PI controller, and the proportion of uncertain machine impedance will decline as the virtual impedance introduced, and hence the influence of the parametric uncertainty is reduced.

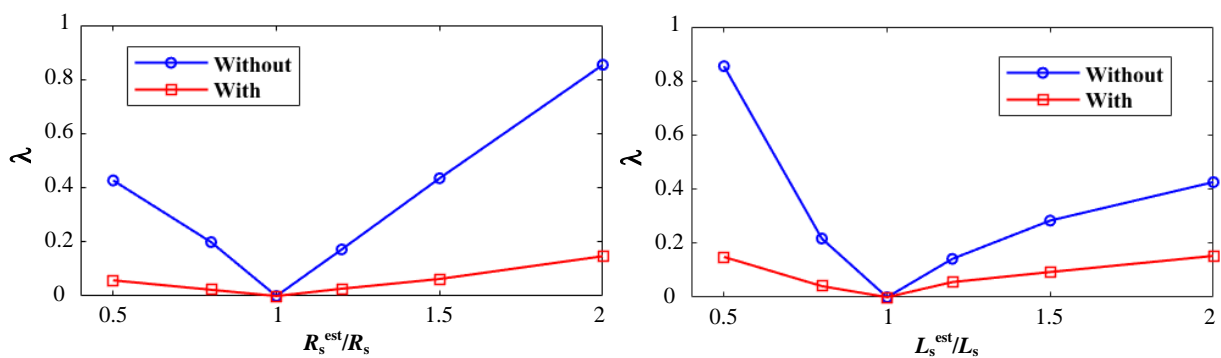


Fig. 2.7. Variation of λ without and with virtual impedance (R_v is 10Ω and L_v is 1mH) when the resistance and inductance in regulator are not matched with machine parameters.

2.4 Comparison with Existing Methods

2.4.1 PIR Regulator

The PIR regulator is considered as the most general approach of rejecting the AC disturbance with certain frequency. The structure of PIR regulator can be understood as parallel connecting a resonant term to the PI regulator as shown in Fig. 2.2(c). The transfer function of the employed resonant term is

$$\frac{k_R \omega_c s}{s^2 + 2\omega_c s + \omega_0^2} \quad (2-23)$$

where ω_0 is the resonant angular frequency and is supposed to be configured as the frequency of voltage disturbance, ω_c is the cut-off angular frequency, and k_R is the resonant coefficient.

It can be seen from Fig. 2.3, the proposed current regulators in $\alpha\beta$ and z_1z_2 subspaces have the same structure, and to simplify the analysis, only the current regulator in $\alpha\beta$ subspace is

analyzed and compared with the corresponding PIR regulator in the simulation, and the current regulator in z_1z_2 subspace can be analyzed similarly. Fig. 2.8 shows the Bode diagrams of the close transfer functions from current reference i_{dq}^* to current feedback i_{dq} and from the disturbance D_{dq} to the current feedback i_{dq} . The simulation parameters of machine and drive are given in TABLE A.1. It is clear from the phase characteristic that the system is stable because the phase delay is smaller than 180 degrees. It should be noted that K_C of the PI regulators in both the PIR regulator and the proposed regulator is equivalent to 1256rad/s. For the virtual impedance, R_v is 10 Ω , L_v is 1mH. For the resonant terms, ω_0 can be configured as 6 and 12 times the fundamental angular frequency, ω_c is 6.28rad/s, and k_R is 10, 100, 1000, respectively.

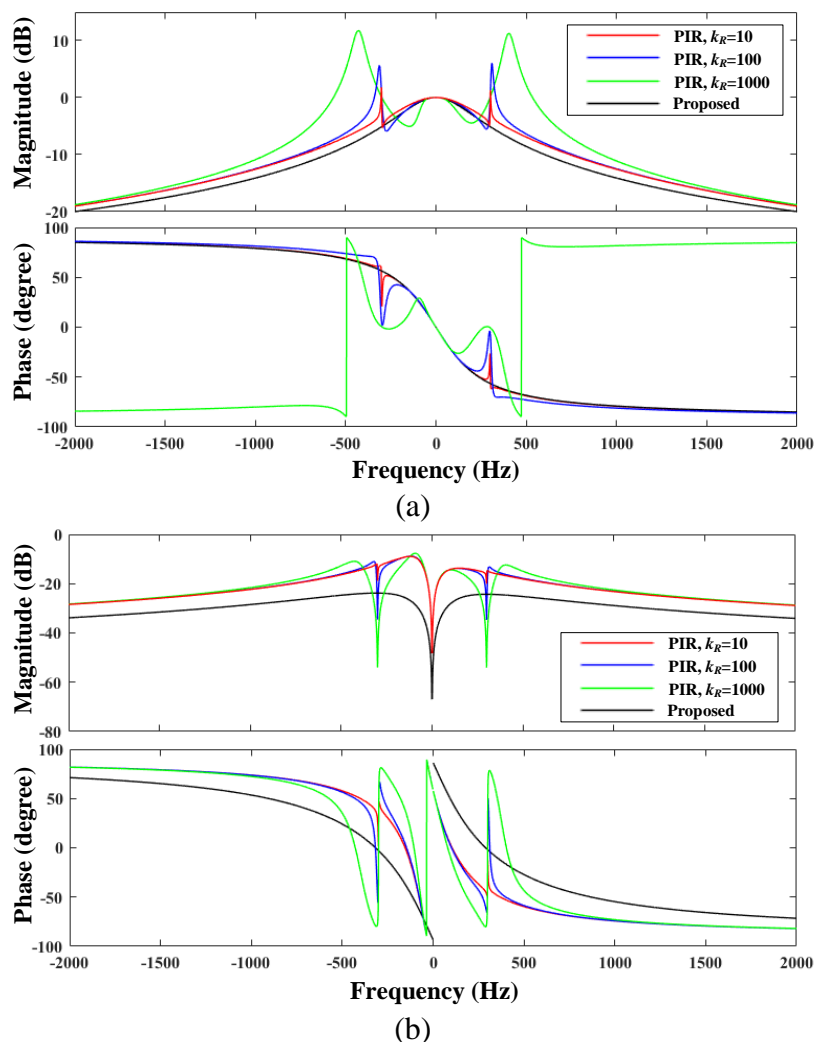


Fig. 2.8. Bode diagrams of close-loop transfer functions. (a) From current reference to current feedback. (b) From disturbance to current feedback. R_v is 10 Ω and L_v is 1mH in the proposed regulator. ω_0 is the frequency of the 12th disturbance harmonic, ω_c is 6.28rad/s, and k_R is 10, 100, and 1000, respectively in the PIR regulator.

To tune the resonant coefficient of PIR regulator, k_R is selected as 10, 100, 1000 to show its influence on the control performance. It is clear that the introduction of the resonant term will change reference tracking capability and disturbance rejection capability, simultaneously. In terms of the reference tracking capability, the resonant term achieves 0dB close-loop gain at the resonant frequency, which makes the PIR regulator capable to track the AC current reference with the resonant frequency. Meanwhile, the close-loop gain greatly increases when the frequency is above the resonant frequency, especially when k_R is 1000. The high close-loop gain near the peak point will cause resonance and instability in the system. In terms of the disturbance rejection capability, the resonant term provides additional attenuation to the disturbance at the resonant frequency. The larger the resonant coefficient is, the larger attenuation to the disturbance is, however, the more instable the system is. Compared with the PIR regulator, the proposed regulator does not change the reference tracking capability of PI regulator, and hence will not suffer from that instability as the PIR regulator does. In addition, the proposed method can achieve -30dB attenuation to the disturbance in a much wider range of frequency, which helps to suppress the current harmonics not only at the resonant frequency, but also at other frequencies from -2kHz to 2kHz.

2.4.2 Active Damping

The virtual resistance is also known as active damping, which is usually utilized to reject the disturbance and robust current regulation [BLA99][YIM09]. If configuring the virtual inductance as zero, the proposed controller is converted to the active-damping-based PI regulator, and in $\alpha\beta$ subspace the transfer functions from reference to feedback current and from disturbance to feedback current are respectively as follows

$$H_c^a(s) = \frac{K_c e^{-T_d s}}{s + K_c e^{-T_d s}} \quad (2-24)$$

$$G_c^a(s) = \frac{s}{s + K_c e^{-T_d s}} \frac{1}{R_s + L_s s + j\omega_e L_s + R_v e^{-T_d s}} \quad (2-25)$$

where the superscript “ a ” means active damping method. Comparing (2-24) (2-25) and (2-16) (2-17), the reference tracking capability is not changed, but the disturbance rejection capability is enhanced in the proposed method due to the virtual inductance term $L_v s e^{-T_d s}$. Moreover, if without the virtual inductance, the stability boundary is changed to

$$K_c < 1/\beta, R_v < R_s + L_s/\beta \quad (2-26)$$

Comparing (2-26) with (2-20), it is clear that the virtual inductance can increase the limitation of virtual resistance, and the larger virtual resistance can provide the proposed method with further improvement of voltage harmonic disturbance rejection capability.

2.4.3 Compensation of Inverter Nonlinearity and Back EMF Harmonics

As studied in Section 2.2, the disturbance includes the voltage errors introduced by inverter nonlinearity and the back EMF harmonics. Feedforward compensation is the most straightforward way to reduce the effect of the disturbance. As studied in [KIM03], the compensation voltage for inverter nonlinearity can be calculated using (2-8) and (2-9). The phase back EMF e_A can be measured and pre-stored in the controller to compensate the effect of back EMF harmonics in phase A. However, the compensation back EMFs are usually measured when the phases are at open-circuit state, and spatial airgap field can be influenced by the armature reaction at load-state, which denotes the back EMF harmonics are variable at different speed and torque conditions. To improve the compensation accuracy, the adaptive feedforward compensation is employed to observe the back EMF as proposed in [WAN20]. The estimated back EMF as well as the dead time compensation voltage can be composed in stationary frames as (2-27) and added to the phase voltage references.

$$\begin{aligned}
 u_{A_c}(t) &= V_{dead}sgn(i_A(t)) + e'_A \\
 u_{B_c}(t) &= V_{dead}sgn(i_B(t)) + e'_B \\
 u_{C_c}(t) &= V_{dead}sgn(i_C(t)) + e'_C \\
 u_{X_c}(t) &= V_{dead}sgn(i_X(t)) + e'_X \\
 u_{Y_c}(t) &= V_{dead}sgn(i_Y(t)) + e'_Y \\
 u_{Z_c}(t) &= V_{dead}sgn(i_Z(t)) + e'_Z
 \end{aligned} \tag{2-27}$$

The superscript “'” in (2-27) represents the estimated value. It is worth noting that the value of V_{dead} depends on dead time, switch characteristic, and dc link voltage. The dc link pulsating and nonidentical switch characteristics can reduce the compensation accuracy. Compared with this method, the proposed method has simpler structure and is easier to implement because it directly increases the rejection capability to both two kinds of disturbance, and neither the observer nor the information of switch characteristic is required. In addition, thanks to the virtual impedance, the proposed current regulator should be more robust and exhibit better dynamic current performance when the machine parameters are mismatched.

2.4.4 Regulator additional PI Gains

It is known that the virtual impedance requires additional PI coefficients in the regulator to achieve zero-pole cancellation, which may lead to the question how the performance is if only increasing the PI gains, i.e. remove the virtual impedance terms from the end of regulators but remain them in the corresponding proportional and integral coefficients. The Bode diagrams of close-loop transfer functions are shown to compare the performance of the proposed regulator and the PI regulator with additional gains in Fig. 2.9, where the PI coefficients are as same as those in Fig. 2.8.

The PI regulator with additional gains exhibits wider bandwidth in Fig. 2.9(a), which indicates fast current response. Nevertheless, the high close-loop gain, especially near 500Hz and -500Hz, will cause pulsating current in dynamics. In Fig. 2.9(b), the PI regulator with additional gains shows less capability to reject the disturbance, and thus will suffer from more current harmonics compared with the proposed method.

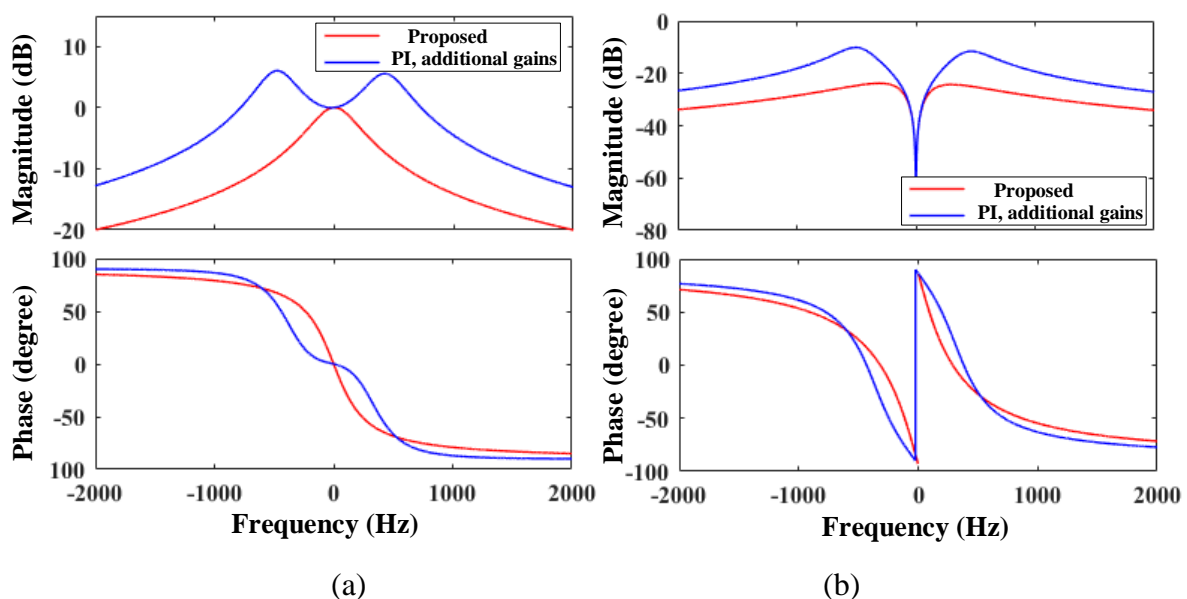


Fig. 2.9. Bode diagrams of close-loop transfer functions. (a) From current reference to current feedback. (b) From disturbance to current feedback.

2.5 Experimental Verification

Experiments are conducted on a DTP PMSM system and the parameters of the prototype machine and drive system are given in TABLE A.1, Appendix A. A PM dc machine is mechanically coupled to the test DTP PMSM and the output of dc machine is connected to an adjustable resistor to be served as the load. Fig. 2.10 shows the block diagram of the overall

control system. The inner loops of the control strategy include two current loops shown in Fig. 2.3. The current references i_{zd}^* and i_{zq}^* are configured to zero to suppress the current harmonics in $z1z2$ subspace, and the current references i_d^* and i_q^* are determined by the outer speed loop. A PI regulator is utilized as the speed regulator and the $i_d = 0$ control strategy is employed. All the experimental results are collected by the dSPACE and analyzed in MATLAB

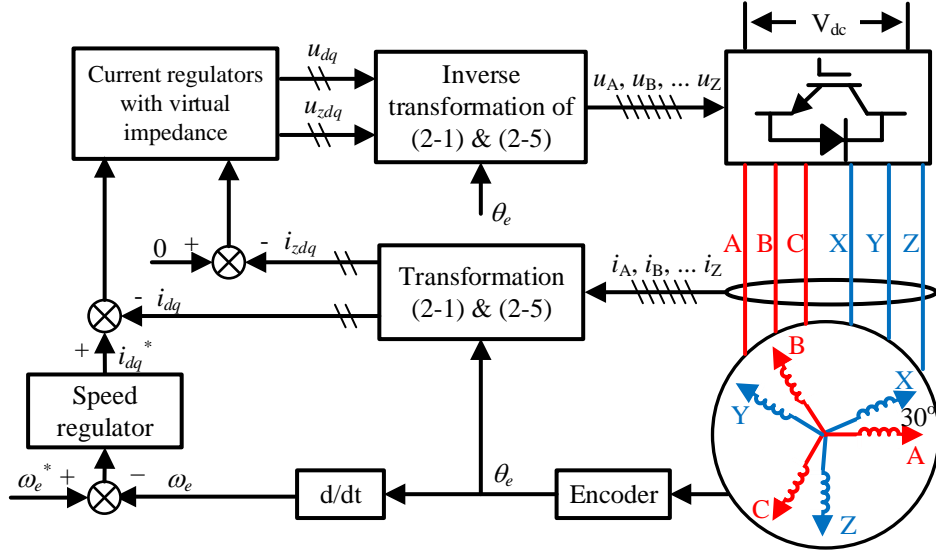


Fig. 2.10. Block diagram of overall control system.

As mentioned in Section 2.3.1, LPFs are required to suppress the current data noise and prevent the amplifying effect of derivative operation in virtual inductance terms. The second order LPF is employed in the experiments, and the transfer function of the LPF is as follows.

$$F(s) = \frac{\omega_n^2}{s^2 + 2\xi\omega_n s + \omega_n^2} \quad (2-28)$$

where ξ is the damping ratio, ω_n is the natural angular frequency of the filter and satisfies $\omega_n = 2\pi f_n$. The maximum speed of machine is 400r/min, the maximum electrical frequency is 33.33Hz, and the frequency of the 12th harmonics in dq -axis frames is 400Hz. To achieve good control performance, the sampling and switching frequencies are designed as 10kHz. The frequency of the current data noise is usually around the sampling frequency, and to reduce the noise but not to significantly attenuate the amplitude of current harmonics, the damp ratio ξ is designed as 0.707, and the natural frequency f_n is 2kHz in the experiments.

To validate the advantages of the proposed method, the comparison with the existing methods is carried out in the experiments. To simplify the description, these methods are referred to

follows.

Method I: Basic PI regulator (as mentioned in Section 2.2.3, Figs. 2.2(a) and 2.2(b))

Method II: PIR regulator (as mentioned in Section 2.4.1, and shown in Fig. 2.2(c))

Method III: PI regulator with active damping (simply configuring virtual inductance to zero, as mentioned in Section 2.4.2)

Method IV: PI regulator with compensation of inverter nonlinearity and back EMF harmonics (as mentioned in Section 2.4.3)

Method V: PI regulator with additional gains (as mentioned in Section 2.4.4)

Proposed: Virtual impedance based PI regulator (as introduced in Section 2.3)

Fig. 2.11 shows the experimental results of Methods I-V as well as the proposed method when the machine is operated at the rated speed and torque, and the fundamental frequency is 20Hz. To make a fair comparison, the PI regulator, Fig. 2.2, is used as the PI regulators in all methods, the machine parameters in TABLE A.1 are served as the PI coefficients, and both K_c , K_{zc} are configured as 1256rad/s. The resonant coefficient k_R in Method II is set as 100. The active damping in Method III is 8Ω. The virtual impedance in the proposed method is selected as 10Ω and 1mH for the current regulator in $\alpha\beta$ subspace, and 10Ω and 0.5mH for the current regulator in z_1z_2 subspace. As analyzed in Section 2.4.2, the maximum value of active damping in Method III is more limited compared with the proposed method, and hence the virtual resistance in proposed method can be higher than the active damping value. In Method V, the virtual resistance and inductance are added to the PI coefficients to provide additional gains, but the virtual voltage drops are not subtracted from the regulator output voltages as the proposed method does.

Method I exhibits serious current harmonics in z_1z_2 subspace according to results in Fig. 2.11(a), and the spectrum shows there are the major 5th and 7th current harmonics as well as the higher odd order harmonics in phase current. These odd order current harmonics are generated by the inverter nonlinearity and back EMF harmonics, as studied in Section 2.2. In addition, the 3rd current harmonic also exists in phase current, and it is caused by the asymmetry among phases [HU14]. Both Methods II and III show obvious suppression on the 3rd, 5th, and 7th current harmonics and reduce the THD (total harmonic distortion) of phase current from 16.95% to 3.21% and 4.44%, respectively. While Method III increases the high order current harmonics as shown in the spectrum of Fig. 2.11(c). Method IV can further suppress the 5th and 7th current harmonics and reduce the THD to 2.28%, Fig. 2.11(d). Method V in Fig. 2.11(e) provides attenuation to most of the odd current harmonics compared with Method I. However, the reduction of the THD is not as significant as other methods due to the residual 5th and 7th current harmonics. The results of the proposed method are shown in Fig. 2.11(f), and it is obvious that

most of current harmonics are greatly suppressed, which leads to the lowest THD 1.77% among these methods.

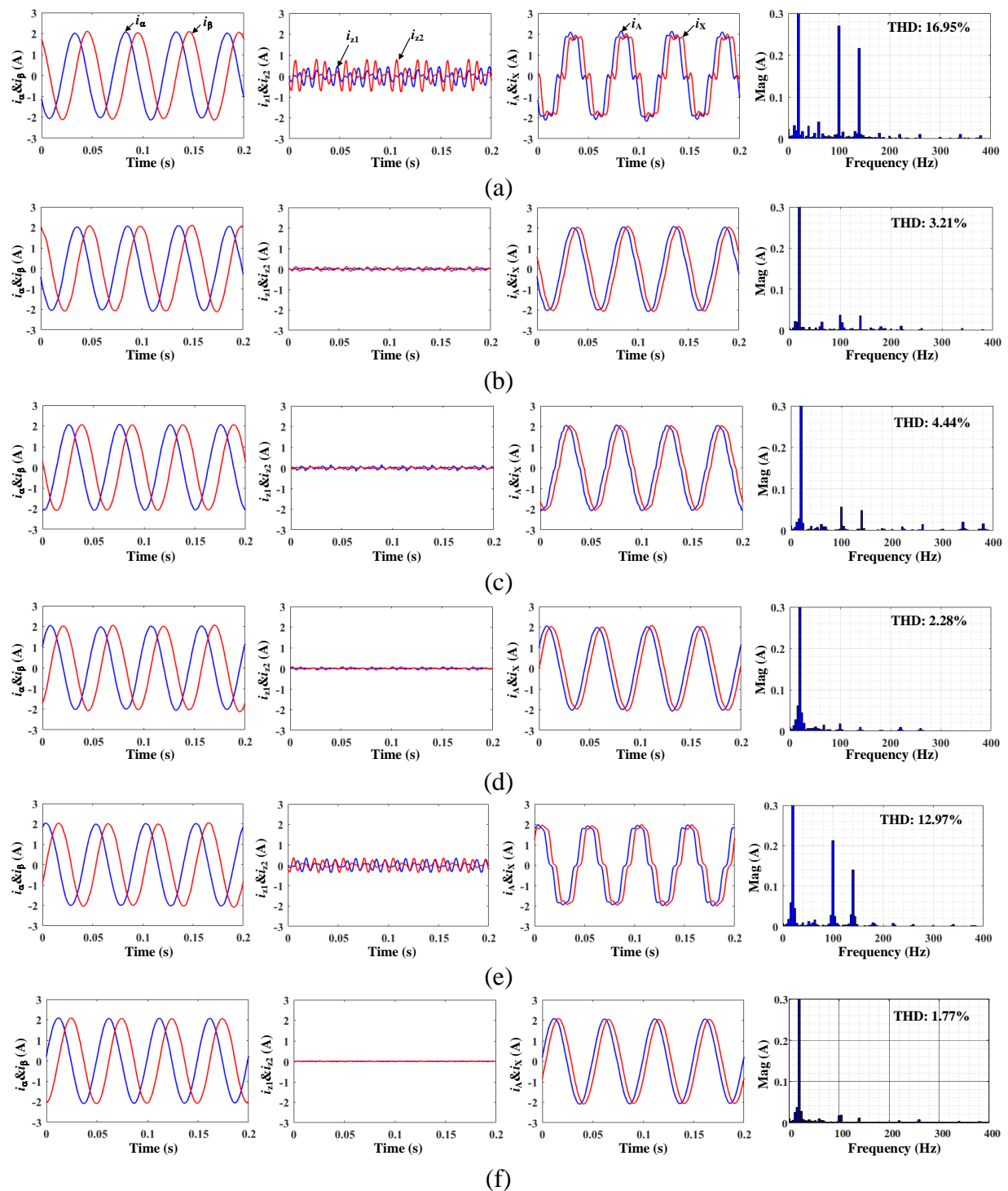


Fig. 2.11. Measured currents and spectra of phase currents under rated speed and torque. (a) Methods I. (b) Method II. (c) Method III. (d) Method IV. (e) Method V. (f) Proposed method.

Fig. 2.12 compares the phase current THDs at rated torque and different speed conditions, where the maximum speed is 400r/min. The basic PI regulator, Method I, shows the highest

THD due to the weak disturbance rejection capability. Using additional PI gains, Method V, helps to suppress the current harmonics and reduce THD, but the reduction is not considerable. Methods II, III, and IV have much better performance on THD reduction compared with Method V, and the proposed method exhibits the lowest THD values at different speed conditions.

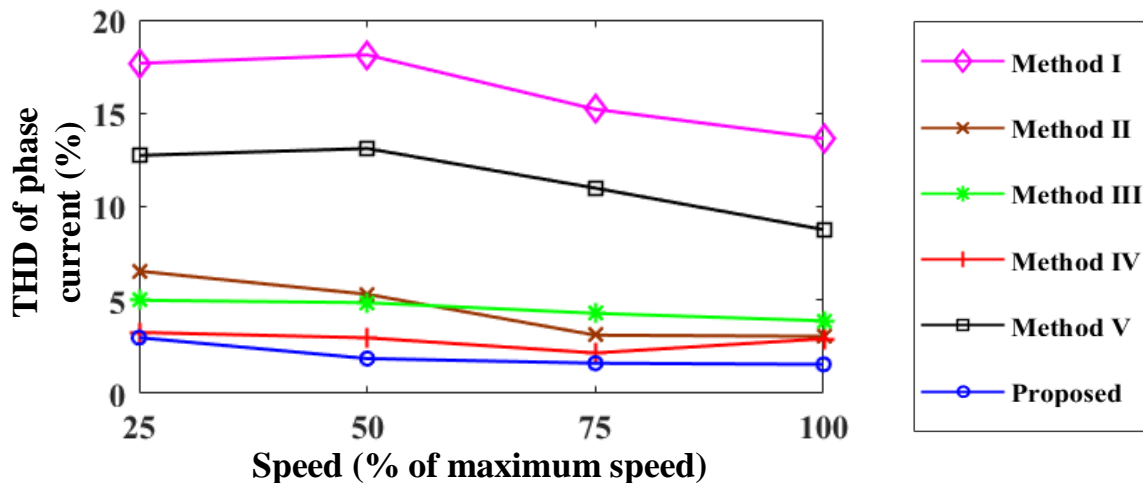


Fig. 2.12. Measured THD of phase current at rated torque and different speed conditions.

The waveforms of electromagnetic torque are provided in Fig. 2.13. According to the torque equation (2-3), the current harmonics in $\alpha\beta$ subspace will contribute to the torque ripples, and thus the methods that can suppress the current harmonics will also reduce the torque ripples. Method IV and the proposed method exhibit lower torque ripple compared with Method I, and the peak-to-peak values of torque ΔT_{e_peak} are reduced from 0.162Nm to 0.0851Nm and 0.0719Nm, respectively.

The dynamic performances of the methods are evaluated by testing the step response of i_{zq} , as shown in Fig. 2.14. To avoid the instability caused by the resonant term in dynamics, the resonant coefficient k_R is set as 50 for the zq -axis term, and k_R remains 100 for the zd -axis term. The coefficients of other methods are as same as those in Fig. 2.11. After the current reference stepped, Method I shows overshoot, cross-coupling effect, and low-frequency pulsating current, which is caused by the mismatched machine parameters. In addition, the serious current harmonics in stationary frames are transformed in zd - and zq -axes as the obvious current ripples. Methods II and IV have faster current response but suffer from more pulsating currents in dynamics due to the high close-loop gains mentioned in Section 2.4. The compensation of the inverter nonlinearity and back-EMF harmonics in Method IV can well

suppress the current ripples, however cannot eliminate the effect due to machine parameter mismatch. Method III and the proposed method exhibit fast and smooth current tracking, and there is no visible overshoot, cross-coupling effect, and pulsating in dynamics. Besides, the use of both virtual resistance and inductance leads to less current ripples in the proposed method, compared with Method III which only utilizes the virtual resistance.

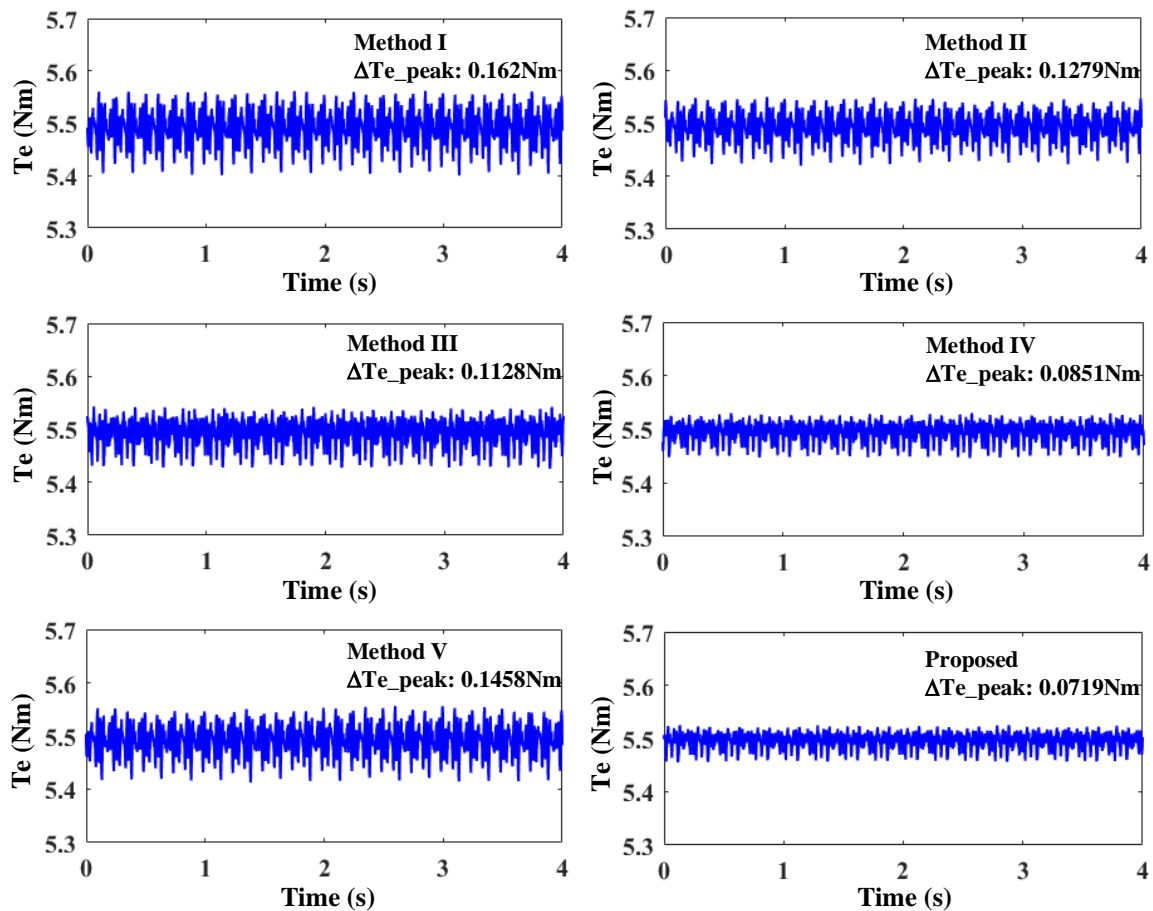


Fig. 2.13. Electromagnetic torque comparison at rated speed and torque. Torque is instantaneously calculated from dSPACE measurement referring to equation (2-3).

It is important to select the appropriate virtual impedance. By way of example, Fig. 2.15 exhibits the situation when the system is out of stability boundary. Before 0.02s, the virtual impedance is configured as 10Ω and 0.5mH , which is inside the stability boundary, and the current ripples in i_{zd} and i_{zq} are controlled. However, at 0.02s, the virtual inductance is artificially changed to 1mH . Since the inductance of the z_1z_2 subspace L_σ is only 0.875mH , and according to the stability boundary (2-21), the virtual inductance in the regulator of the z_1z_2 subspace cannot exceed the leakage inductance L_σ , which means the system is out of stability boundary and thus becomes instable with serious pulsating currents. This clearly shows that

(2-21) can be used as a good guideline for selecting the values of virtual impedance.

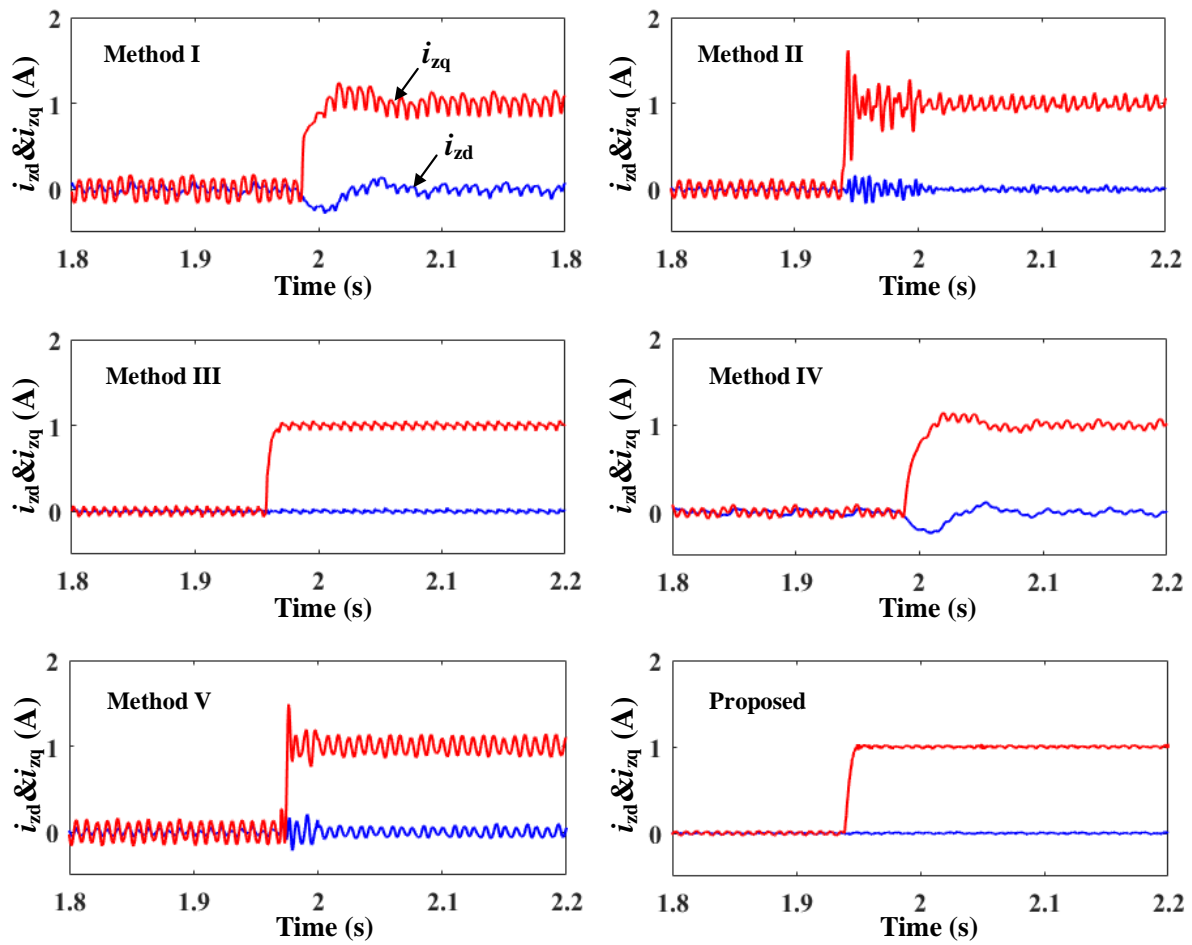


Fig. 2.14. Comparison of dynamic step current response at rated speed. i_{zq}^* stepped from 0A to 1A and i_{zd}^* remained 0A.

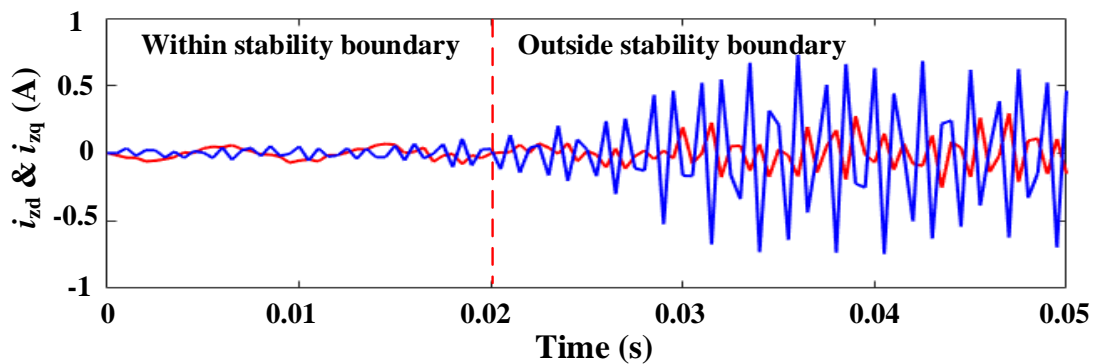


Fig. 2.15. Experimental results of i_{zd} and i_{zq} when system is out of stability boundary. Virtual impedance is changed from 10Ω and 0.5mH to 10Ω and 1mH at the 0.02s.

2.6 Conclusion

This chapter has proposed a method of virtual impedance in the current regulation of the $\alpha\beta$ and z_1z_2 subspaces in a DTP PMSM system. The proposed method can be used to enhance the disturbance rejection capability and suppress the current harmonics with a wide range of frequency. The virtual impedance will also robust the current regulation by eliminating the overshoot, cross-coupling effect, and pulsating currents due to machine parameter mismatch. Comparing with the existing methods, the proposed method has better steady- and dynamic-state performance, which are validated by the experimental results. Additionally, the stability boundary provides a good guideline to determine the values of virtual impedance in a DTP PMSM system.

It is worth noting that compared with conventional three-phase machines, multi three-phase machines, e.g., dual three-phase, triple three-phase, and quadruple three-phase machines, usually exhibit weaker voltage harmonic disturbance rejection capability because of the smaller impedance in harmonic subspaces. That means rejecting the disturbance is a more important topic in the control of multi three-phase machines. Although the proposed current regulators with virtual impedance are analyzed and implemented in a DTP machine system, the regulators have a generic structure and can be extended to other multi three-phase machine systems that may suffer from voltage harmonic disturbance problems.

CHAPTER 3

MULTIPLE SYNCHRONOUS REFERENCE FRAME CURRENT HARMONIC REGULATION OF DUAL THREE-PHASE PMSM WITH ENHANCED DYNAMIC PERFORMANCE AND SYSTEM STABILITY

The previous chapter has proposed a virtual impedance technique to enhance the voltage harmonic rejection capability of the control system. Although the rejection capability is enhanced compared to the conventional VSD-based control approach, the attenuation on the voltage harmonic disturbance is still not infinite, which means the current harmonics can merely be reduced but not eliminated or suppressed to zero. More importantly, the proposed virtual impedance can only be utilized to reduce the current harmonics, but in the applications that require current harmonic injection to boost the average torque or minimize the torque ripples, the proposed virtual impedance technique is not applicable anymore. These are the limitations of the virtual impedance technique proposed in Chapter 2.

To achieve a better control performance of the current harmonics in dual three-phase PMSMs, this chapter proposes an improved multiple synchronous reference frame (MSRF) current harmonic control strategy for dual three-phase permanent magnet synchronous machine drive system. A new vector space decomposition transformation combined with auxiliary currents is designed to decouple the current fundamental with current harmonics, and the auxiliary currents can be established by the $\pi/9$ phase shifting of the physical currents in ABC set and the $\pi/18$ phase shifting of the physical currents in XYZ set. By employing the proposed current decomposition, it is easy to detect them using low pass filters in MSRFs. A generic complex vector proportional integral regulator is then employed to control the detected current harmonics to track the current harmonic references. Compared with the virtual impedance technique, the current harmonics can be suppressed to zero or freely controlled to track the required current harmonic reference in this chapter. Compared to the existing MSRF-based methods, the proposed method provides a new current harmonic detection with reduced delay

effect, which contributes to enhancing the dynamic performance of current harmonic regulation, and also stabilizing the control system. Comprehensive experimental results are given to validate the effectiveness of the proposed control strategy.

This chapter is published in IEEE Transactions on Industrial Electronics [YAN21b].

[YAN21b] L. Yan, Z. Q. Zhu, J. Qi, Y. Ren, C. Gan, S. Brockway, and C. Hilton, “Multiple synchronous reference frame current harmonic regulation of dual three-phase PMSM with enhanced dynamic performance and system stability,” *IEEE Trans. Ind. Electron.*, vol. 69, no. 9, pp. 8825-8838, Oct. 2021.

3.1 Introduction

In the control of dual three-phase PMSM, one general topic that has received intensive discussion is the current harmonic regulation. On the one hand, the current harmonics generate loss and should be suppressed to improve the system efficiency. On the other hand, by configuring the current reference to be pre-designed non-sinusoidal waveform, the current harmonics can also be injected to boost the average torque [WAN15][HU17] or minimize the torque ripples [FEN19][YAN19][FEN19]. Either the suppression or the injection requires a current harmonic regulator with good steady- and dynamic-state performance on tracking the current harmonic reference.

In dual three-phase PMSM system, due to small impedance composed of resistance and leakage inductance, the 5th and 7th components are dominant in the current harmonics [ZHA95]. Besides, the 11th and 13th current harmonics can generate the 12th pulsating torque, which is the major component in the torque ripples of dual three-phase PMSMs. That means not only the 5th and 7th but also the 11th and 13th current harmonics should be controlled in the system. Various solutions have been proposed to achieve the current harmonic regulation. In [KAR16], the 5th and 7th current harmonics are firstly decomposed from phase currents by using vector space decomposition (VSD) technique. Then, they are transformed into the fundamental synchronous reference frame as the 6th current harmonics which are further suppressed by two proportional integral (PI) regulators. The PI regulator has limited rejection capability to AC disturbance, and hence the current harmonics still exist in the system. Many solutions with enhanced disturbance rejection, such as the disturbance observer [KAR16], the extended state

observer [XU20], and the virtual impedance [YAN21], are proposed to improve the capability of PI regulator. These current regulators can suppress the current harmonics, however, exhibit weak capability of tracking the current harmonic references, which makes them not applicable in the current harmonic injection. Two popular kinds of regulators are employed to solve this problem. They are known as the proportional integral resonant (PIR) regulator and multiple synchronous reference frame (MSRF) PI regulators. Regarding the PIR regulator, a lot of papers have discussed about their using in dual three-phase PMSM system [CHE14][HU4][HU20][ZHU20][HU18]. In these papers, the proposed regulators utilize resonant terms to provide additional gain near the harmonic frequencies and thus improve the tracking capability to current harmonic references. However, there are some common problems. PIR regulator aims to control the fundamental and current harmonics simultaneously, which causes the inevitable interference between different frequencies and results in potential resonance in a control system. In addition, the resonant frequency inaccuracy can also deteriorate the control performance of current harmonic reference tracking [YEP11][XIA15]. Different from PIR regulator, the MSRF-based method considers the machine as multiple subsystems with different orders in MSRFs, and controls the fundamental and harmonics separately in several independent current loops [YAN11][CHA00][DHU19][FEN19][LIU19]. Taking that advantage of independent current harmonic regulation, [KAR17] employs MSRF PI regulator to achieve identification of voltage harmonic disturbance and partial suppression of current harmonics, under limited available voltage in dual three-phase PMSM system. Nevertheless, in order to eliminate the interference among different current harmonic loops, low pass filters (LPFs) are required in the current harmonic detection, which leads to significant delay and reduces the dynamic current response as well as the stability of control system. There are other techniques, such as the direct torque controller [REN15][SHA20] and the model predictive controller [LUO18][LIU21], that show good performance on current regulation, while they suffer from high torque ripples and computation burden, respectively.

To make use of the independent current harmonic regulation of MSRF method, an improved MSRF method with enhanced dynamic performance and system stability is proposed in this chapter. The auxiliary currents, established by the $\pi/9$ phase shifting of physical currents in ABC set and the $\pi/18$ phase shifting of physical currents in XYZ set, are combined with a new VSD transformation to decouple the current harmonics with the fundamental. To be precise, the fundamental current can be individually separated into $\alpha\beta$ subspace, the sum of the 5th and 13th current harmonics is mapped into z_1z_2 subspace, and the sum of the 7th and 11th current

harmonics is mapped into z_3z_4 subspace. All the subspaces are decoupled, and in spectrum the current harmonics mapped in the same subspace become further away from each other than the case of conventional VSD. These features make it easier to detect the current harmonics in MSRFs using LPFs. The detected currents are then regulated by complex vector PI regulators, which have a generic structure and are simple to implement and tune for different current harmonics. Compared with the existing MSRF-based methods, the proposed method produces less delay effect in the current harmonic detection, and hence the dynamic performance of current harmonic regulation is improved. Moreover, the stable margin of the current loops can also be enlarged due to the reduced delay effect and the stability of the whole system can be enhanced. This improvement makes the proposed strategy more applicable in the current harmonic suppression and injection of dual three-phase PMSM drive system.

This chapter is organized as follows. Section 3.2 introduces the fundamental and harmonic models of dual three-phase PMSM. The basic MSRF PI regulator is also introduced and the problem is stated in this section. The proposed control strategy is illustrated in Section 3.3, where the dynamic performance and system stability are studied by simulation results. The discussions on implementation and computation burden are presented in this section. The experimental results are provided in Section 3.4, and finally Section 3.5 concludes the chapter.

3.2 MSRF-based Current Harmonic Control in DTP PMSM System

3.2.1 Electrical Machine Model in MSRF

The electrical model of dual three-phase PMSM in ABC-XYZ stationary frame is a sixth-order-matrix model with coupling among phases. To simplify the model and neglect the zero-sequence components, VSD technique is generally employed to decompose the machine variables into two isolated subspaces, i.e. $\alpha\beta$ and z_1z_2 subspaces, where the machine can be considered as two second-order-matrix models. The VSD transformation is as follows

$$\begin{bmatrix} F_{\alpha\beta} \\ F_{z_1z_2} \end{bmatrix} = \frac{1}{2} \begin{bmatrix} T(0) & T(\pi/6) \\ T(0) & -T(\pi/6) \end{bmatrix} \begin{bmatrix} F_{ABC} \\ F_{XYZ} \end{bmatrix} \quad (3-1)$$

where F represents the voltage, current, and flux linkage. Subscripts ‘‘ABC’’ and ‘‘XYZ’’ represent the phase variables, i.e.

$$F_{ABC} = \begin{bmatrix} F_A \\ F_B \\ F_C \end{bmatrix}, F_{XYZ} = \begin{bmatrix} F_X \\ F_Y \\ F_Z \end{bmatrix} \quad (3-2)$$

The definition of phases is shown in Fig. 3.1.

Subscripts “ $\alpha\beta$ ” and “ z_1z_2 ” in (3-1) represent the decomposed variables in $\alpha\beta$ and z_1z_2 subspaces, respectively,

$$F_{\alpha\beta} = \begin{bmatrix} F_{\alpha} \\ F_{\beta} \end{bmatrix}, F_{z_1z_2} = \begin{bmatrix} F_{z_1} \\ F_{z_2} \end{bmatrix} \quad (3-3)$$

The submatrix T represents the 3-phase to 2-phase transformation as follows:

$$T(\theta) = \frac{2}{3} \begin{bmatrix} \cos \theta & \cos(\theta + 2\pi/3) & \cos(\theta - 2\pi/3) \\ \sin \theta & \sin(\theta + 2\pi/3) & \sin(\theta - 2\pi/3) \end{bmatrix} \quad (3-4)$$

The harmonic mapping in $\alpha\beta$ and z_1z_2 subspaces are shown in Fig. 3.2, which denotes the 5th and 7th harmonics are distributed in z_1z_2 subspace, and the fundamental, 11th, and 13th are distributed in $\alpha\beta$ subspace.

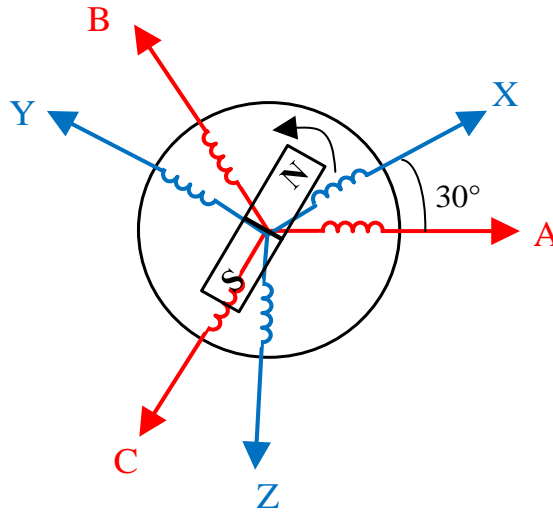


Fig. 3.1. Phase definition of dual three-phase PMSMs.

To derive the individual model of the fundamental, 5th, 7th, 11th, and 13th harmonics, the decomposed variables are further transformed to MSRFs by using the transformation (3-5). The definition of MSRFs is shown in Fig. 3.3. For ease of description, the complex vector expression is used in (3-5), e.g. $F_{\alpha\beta} = F_{\alpha} + jF_{\beta}$, $F_{dq1} = F_{d1} + jF_{q1}$, and the LPF function ensures that the components of other frequencies are removed and only the DC components are remained in MSRFs.

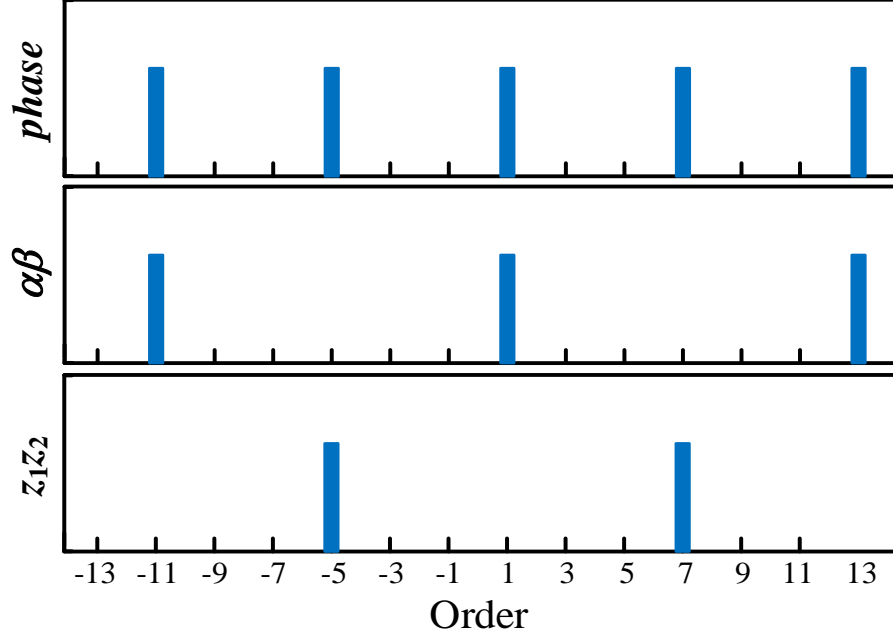


Fig. 3.2. Harmonic mapping in $\alpha\beta$ and z_1z_2 subspaces. The 5th and 7th harmonics are distributed in z_1z_2 subspace, and the fundamental, 11th, and 13th are distributed in $\alpha\beta$ subspace.

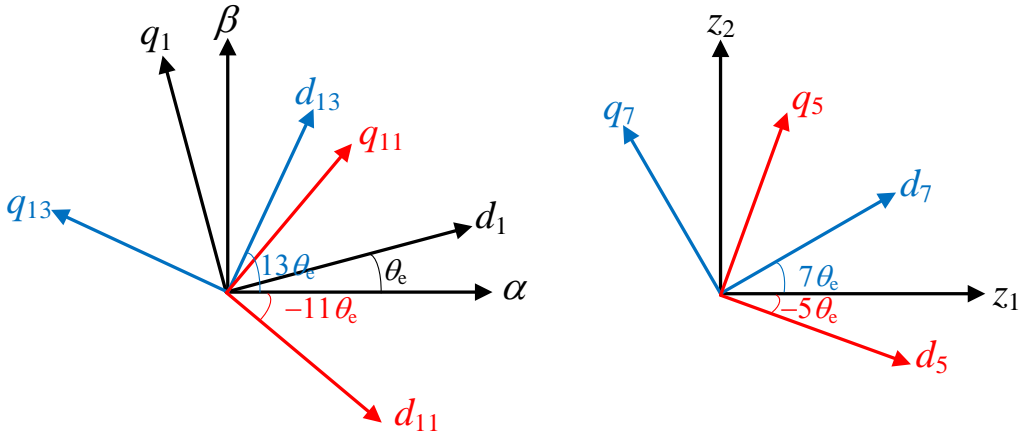


Fig. 3.3. Definition of MSRFs.

$$\begin{bmatrix} F_{dq1} \\ F_{dq5} \\ F_{dq7} \\ F_{dq11} \\ F_{dq13} \end{bmatrix} = LPF \left(\begin{bmatrix} e^{-j\theta_e} & 0 \\ 0 & e^{j5\theta_e} \\ 0 & e^{-j7\theta_e} \\ e^{j11\theta_e} & 0 \\ e^{-j13\theta_e} & 0 \end{bmatrix} \begin{bmatrix} F_{\alpha\beta} \\ F_{z_1z_2} \end{bmatrix} \right) \quad (3-5)$$

The fundamental model in $dq1$ reference frame can be derived as

$$u_{dq1} = R_s i_{dq1} + sL_s i_{dq1} + j\omega_e L_s i_{dq1} + j\omega_e \psi_{fdq1} \quad (3-6)$$

where u_{dq1} , i_{dq1} , ψ_{fdq1} are the complex vectors of fundamental voltage, current, and PM flux linkage. R_s is the stator resistance, L_s is the synchronous inductance, ω_e is the fundamental

electrical angular speed, and s denotes the derivative. The average electromagnetic torque can be expressed as

$$T_e = 3P\psi_{fdq1} \times i_{dq1} \quad (3-7)$$

where P is the number of pole pairs. Similarly, the models of the 5th, 7th, 11th, and 13th harmonics are as follows.

$$\begin{aligned} u_{dq5} &= R_s i_{dq5} + sL_\sigma i_{dq5} - j5\omega_e L_\sigma i_{dq5} - j5\omega_e \psi_{fdq5} \\ u_{dq7} &= R_s i_{dq7} + sL_\sigma i_{dq7} + j7\omega_e L_\sigma i_{dq7} + j7\omega_e \psi_{fdq7} \\ u_{dq11} &= R_s i_{dq11} + sL_s i_{dq11} - j11\omega_e L_s i_{dq11} - j11\omega_e \psi_{fdq11} \\ u_{dq13} &= R_s i_{dq13} + sL_s i_{dq13} + j13\omega_e L_s i_{dq13} + j13\omega_e \psi_{fdq13} \end{aligned} \quad (3-8)$$

where L_σ is the leakage inductance. The other current harmonics whose orders are higher than the 13th are usually negligible but here they are neglected. The machine can be considered as five independent DC subsystems, (3-6) and (3-8).

3.2.2 Basic MSRF Current Regulation

MSRF PI regulator is widely employed in industrial applications that require the current regulation of multiple frequencies. It can be simply extended to the dual three-phase PMSM drive system, Fig. 3.4. This control strategy is composed of two parts, i.e. detection and regulation. In terms of the detection, Fig. 3.4(a), the original phase currents are firstly decomposed as $i_{\alpha\beta}$ and i_{z1z2} by the VSD transformation (3-1). According to the harmonic mapping in Fig. 3.2, $i_{\alpha\beta}$ includes the fundamental, 11th, and 13th current harmonics, and should be transformed into the $dq1$, $dq11$, and $dq13$ frames as the DC values i_{dq1} , i_{dq11} , and i_{dq13} , respectively. However, due to the coupling of the fundamental, 11th, and 13th harmonics in the $\alpha\beta$ subspace, in MSRFs there are residual AC current components that can be eliminated by the LPFs. The 5th and 7th current harmonics are coupled in i_{z1z2} , and their detection is similar. As said, the function of all these LPFs is to attenuate the unexpected AC components, and their bandwidths are supposed to be different due to different amplitudes and frequencies of the current harmonics. Take an example, the amplitude of the fundamental current is usually largest, which determines that the bandwidths of LPF11 and LPF13 must be much smaller than the bandwidth of LPF1 in order to achieve enough attenuation on the fundamental current. Small bandwidth of LPF means significant delay of the current detection, and limit the dynamic response of the current loop.

In terms of current control in Fig. 3.4(b), the detected currents are used as the current feedbacks and the PI regulators are employed to track the DC current references and reject the DC disturbance. The average electromagnetic torque is mainly generated by the fundamental current, and hence the fundamental current reference i_{dq1}^* is determined by the torque requirement of a machine or the output of speed regulator in a speed regulation application. Regarding the current harmonic references, i_{dq5}^* , i_{dq7}^* , i_{dq11}^* , and i_{dq13}^* can be flexibly configured to realize different optimization objectives, e.g. maximum average torque, minimal torque ripple, and minimal loss. The optimization methods have been well discussed in the existing literature and are not studied in this chapter.

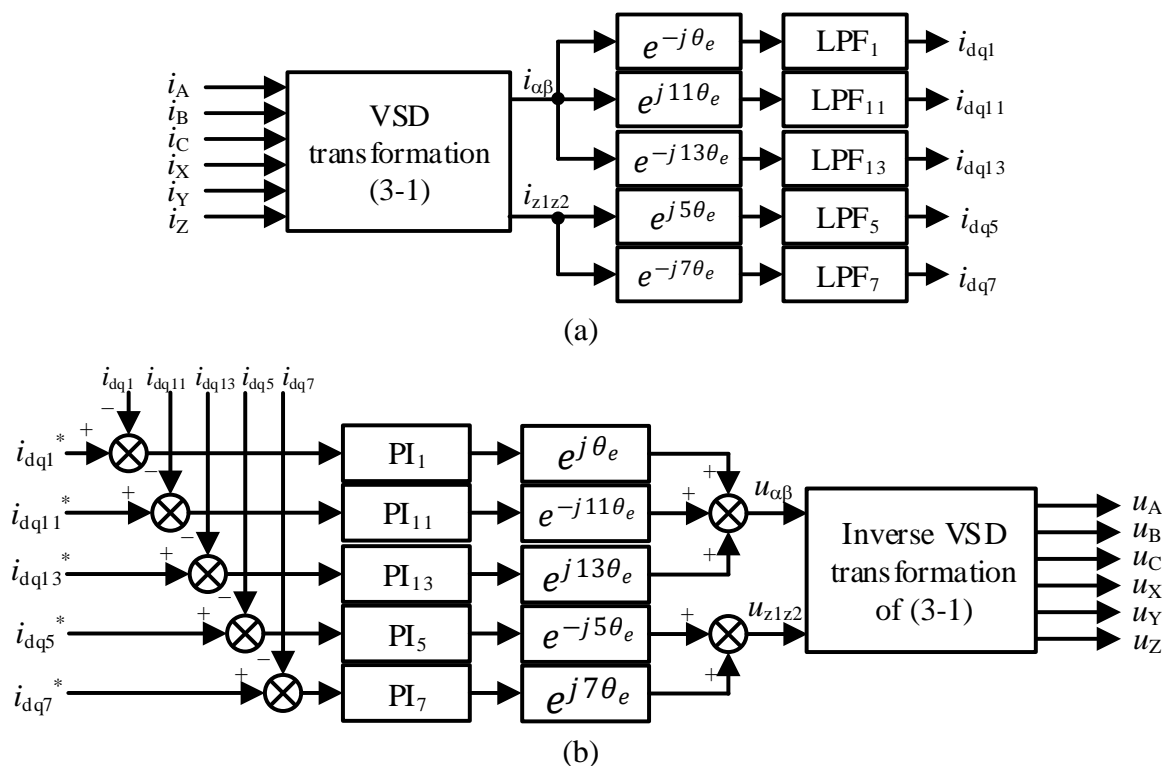


Fig. 3.4. Block diagram of the basic MSRF PI current regulation. (a) Current harmonic detection using VSD transformation (3-1), Park transformation, and LPFs. (b) Current harmonic control using PI regulators.

In Fig. 3.4(a), to realize independent regulation on fundamental and current harmonics, LPFs are required to decouple the fundamental and harmonic current loops from each other. Especially at low speed when these current components are close to each other in spectrum, the current harmonics can be within the bandwidth of fundamental current regulator, and the fundamental current regulator will generate disturbance into the harmonic current loops if there is no LPF in the fundamental current feedback. Likewise, the harmonic current regulator can introduce disturbance into the fundamental current loop if there is no LPF in the harmonic

current feedback. In addition, to achieve partial current harmonic suppression at high speed when the output voltage of inverter is limited, LPFs are also necessary to guarantee the different current components and output voltages of PI regulators are decoupled, and these decoupled currents and voltages can be utilized to identify the harmonic disturbance and optimize the current harmonic references, as studied in [KAR17][FEN21]. The LPFs are necessary in the current detection because they help to decouple the current loops, however, they can also cause significant delay effect of current harmonic detection. The delay effect limits the dynamic performance and stable margin of the current loops, which makes the basic MSRF method usually suffer from poor dynamic response and instability. To simplify the control system, the first-order LPF is selected in this thesis due to its simple structure and easy implementation.

3.3 Proposed Control Strategy

3.3.1 Phase Shifting and Current Decomposition

As aforementioned, the basic approach of current harmonic detection mainly suffers from the delay effect caused by LPFs, and to solve this problem, this section introduces a method of improved current harmonic detection that can reduce the delay effect.

The spatial phase shift angle between two physical three-phase sets of the dual three-phase machine is 30 electrical degrees, as shown in Fig. 3.5(a). Generally, regarding the winding sets with 30 electrical degrees shifting, the optimal time phase shift between the fundamental currents of two sets should be $\pi/6$ to achieve maximum average torque and minimized torque ripple. Assuming the rotor rotating direction is anticlockwise, based on the spatial and time phase shifting, the space vectors of the current fundamental and current harmonics can be derived and shown in Fig. 3.5(b), where I_{1_ABC} indicates the synthesized space vector of the current fundamental from ABC set, I_{5_XYZ} indicates the synthesized space vector of the 5th current harmonics from XYZ set, and so on. It is clear that the vectors of the current fundamental from two sets are consistent with each other, i.e. they have the same magnitude and phase angle, and so as the vectors of the 11th and 13th current harmonics. In terms of the 5th and 7th current harmonics, the current vectors from two sets have the same magnitude but the reversed phase angle. As results, the fundamental, 11th and 13th current harmonics can be decomposed in the $\alpha\beta$ subspace by calculating the sum of the vectors from two sets, i.e. $T(0)i_{ABC} + T(\pi/6)i_{XYZ}$ in (1), The 5th and 7th current harmonics can be decomposed into the z_1z_2 subspace by calculating the difference of the vectors from two sets, i.e. $T(0)i_{ABC} -$

$T(\pi/6)i_{XYZ}$ in (1). This agrees with the harmonic mapping in Fig. 3.2.

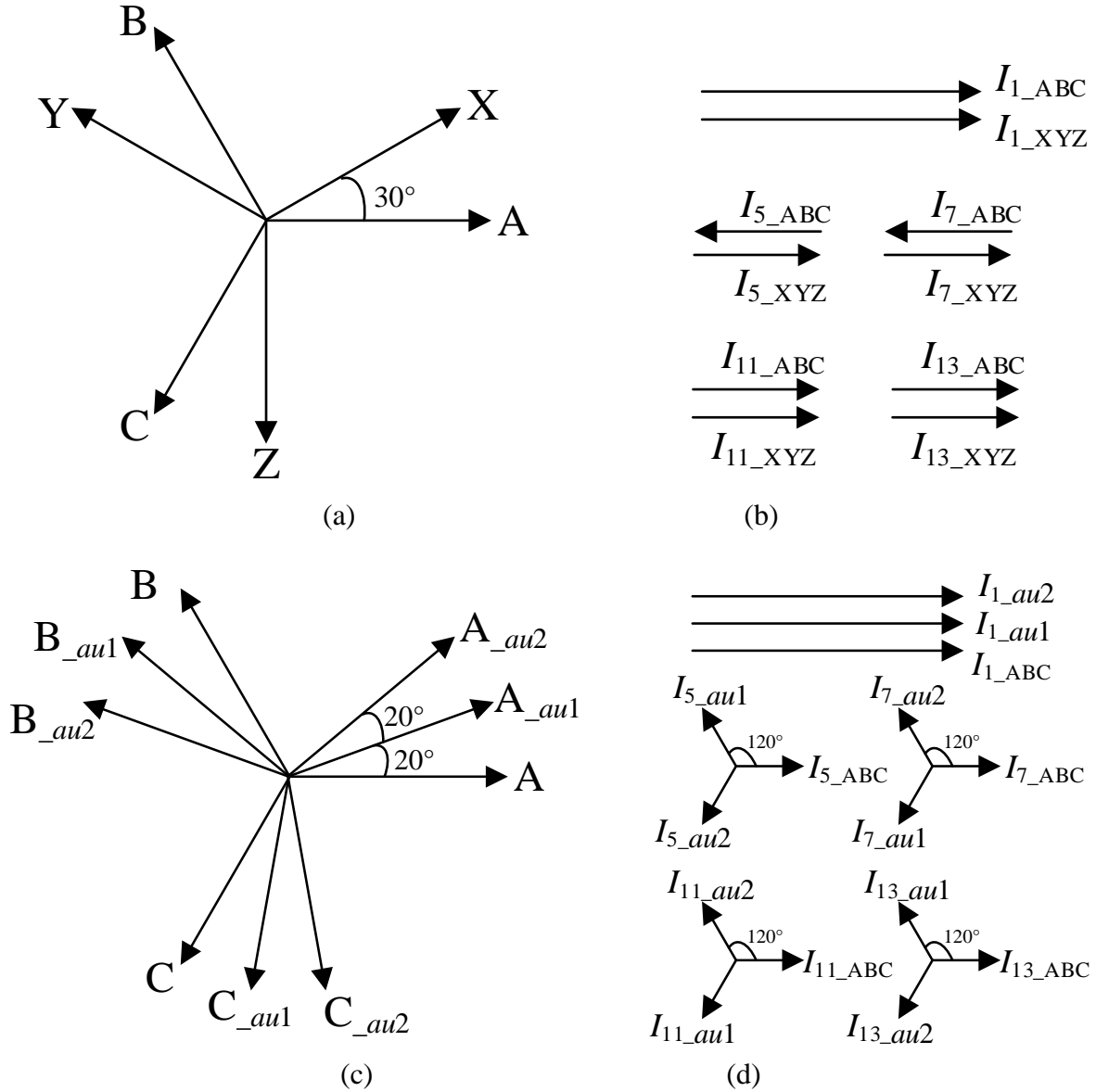


Fig. 3.5. (a) Spatial axes of ABC and XYZ phase currents. (b) Space vectors of the current fundamental and current harmonics. (c) Proposed spatial axes of ABC phase currents and auxiliary currents. (d) Proposed space vectors of the current fundamental and current harmonics.

The limitation of the conventional VSD above is that the fundamental is still coupled with the 11th and 13th current harmonics, and hence the bandwidths of LPF11 and LPF13 in Fig. 3.4(a) should be small enough to attenuate the fundamental components, as introduced in Section 3.2.2. Actually, the physical XYZ phase current i_{XYZ} can be regarded as the auxiliary current, which is the $\pi/6$ time phase shift and the 30 degrees spatial phase shift with reference to ABC phase current i_{ABC} , to help decouple the 5th and 7th current harmonics with the fundamental. Similarly, auxiliary currents with the $\pi/9$ and $2\pi/9$ time phase shifts of i_{ABC} are proposed here

to help decompose all the current harmonics. Fig. 3.5(c) shows the spatial axes of the auxiliary currents, and the subscripts “ $_{au1}$ ” and “ $_{au2}$ ” represents the auxiliary variables. The spatial phase shift angles of the auxiliary axes are respectively 20 and 40 electrical degrees with reference to the axes of ABC set. If the auxiliary currents i_{ABC_au1} and i_{ABC_au2} are also shifted by $\pi/9$ and $2\pi/9$ with reference to i_{ABC} , the space vectors of the fundamental and current harmonics can be derived and presented in Fig. 3.5(d), where I_{1_au1} indicates the synthesized space vector of the current fundamental from i_{ABC_au1} , I_{5_au2} indicates the synthesized space vector of the 5th current harmonic from i_{ABC_au2} , and so on. Similar to the case in Figs. 3.5(a) and 3.5(b), the current components can be decomposed using vector operations.

The three fundamental vectors, i.e. I_{1_ABC} , I_{1_au1} , and I_{1_au2} , are consistent with each other in space, while the three vectors of the current harmonics can be synthesized to zero due to the 120 degrees phase shift from each other. As a result, the fundamental current can be individually decomposed by calculating the sum of the three vectors from i_{ABC} , i_{ABC_au1} and i_{ABC_au2} , i.e.

$$i_{\alpha\beta} = T(0)i_{ABC} + T(\pi/9)i_{ABC_au1} + T(2\pi/9)i_{ABC_au2} \quad (3-9)$$

In terms of the current harmonics, using the vector operation (3-10), the current vectors can be changed to Fig. 3.6.

$$\begin{aligned} i_{z1z2} = T(0)i_{ABC} + T_r(2\pi/3)T(\pi/9)i_{ABC_au1} \\ + T_r(-2\pi/3)T(2\pi/9)i_{ABC_au2} \end{aligned} \quad (3-10)$$

where matrix T_r is

$$T_r(\theta) = \begin{bmatrix} \cos \theta & \sin \theta \\ -\sin \theta & \cos \theta \end{bmatrix} \quad (3-11)$$

It is clear that in Fig. 3.6, the 5th vectors and the 13th vectors are consistent with each other, while the vectors of fundamental, 11th, and 7th are shifted by 120 degrees and can be synthesized to zero. As a result, if calculating the sum of these vectors, only the 5th and 13th current harmonics are mapped in i_{z1z2} .

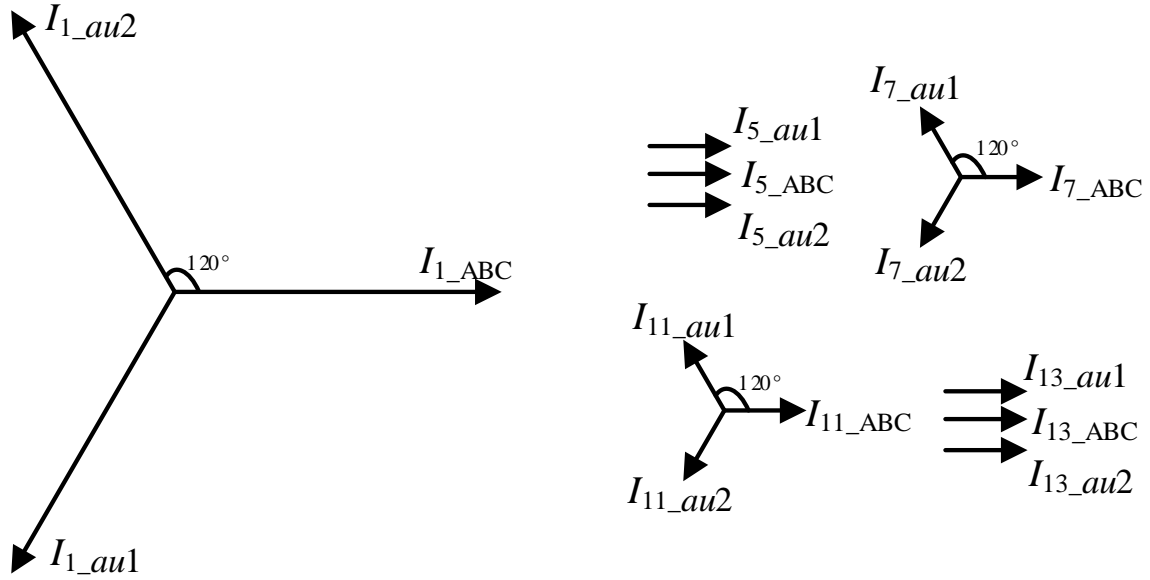


Fig. 3.6. Space vectors of the current fundamental and current harmonics using vector operation (3-10).

Furthermore, using the vector operation (3-12), the current vectors can be changed to Fig. 3.7.

$$i_{z3z4} = T(0)i_{ABC} + T_r(-2\pi/3)T(\pi/9)i_{ABC_au1} + T_r(2\pi/3)T(2\pi/9)i_{ABC_au2} \quad (3-12)$$

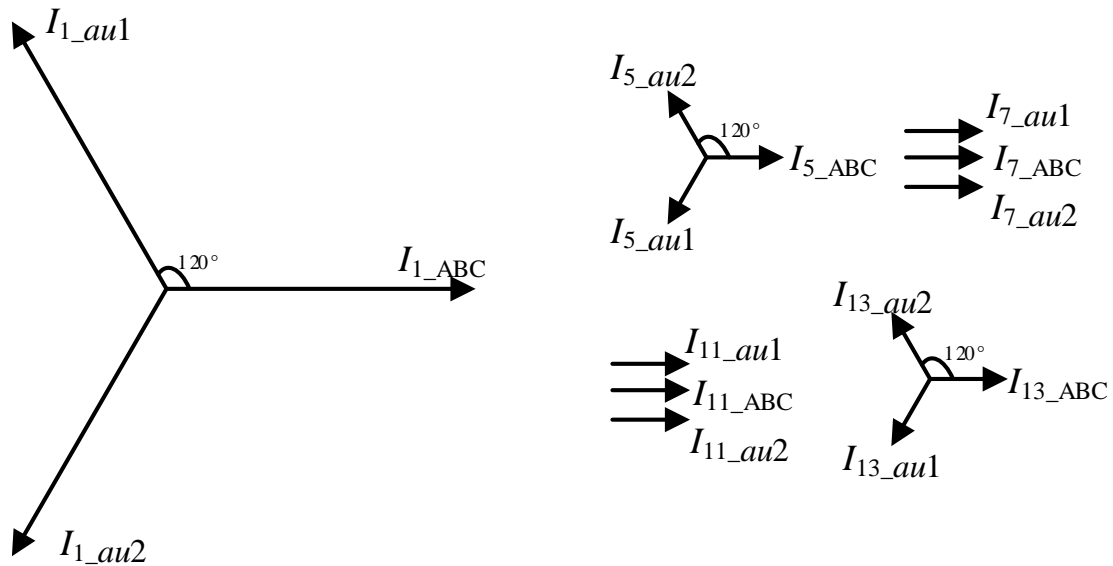


Fig. 3.7. Space vectors of the current fundamental and current harmonics using vector operation (3-12).

Similarly, after using (3-12) to decompose the current in z_3z_4 subspace, the 7th vectors and the 11th vectors are consistent with each other, while the vectors of fundamental, 5th, and 13th are

shifted by 120 degrees and can be synthesized to zero. As a result, only the 7th and 11th current harmonics are mapped in $i_{z_3z_4}$.

From (3-9), (3-10), and (3-12), the current decomposition transformation can be concluded as

$$\begin{bmatrix} i_{\alpha\beta} \\ i_{z_1z_2} \\ i_{z_3z_4} \end{bmatrix} = \frac{1}{3} \begin{bmatrix} T(0) & T(\pi/9) & T(2\pi/9) \\ T(0) & T(-5\pi/9) & T(8\pi/9) \\ T(0) & T(7\pi/9) & T(-4\pi/9) \end{bmatrix} \begin{bmatrix} i_{ABC} \\ i_{ABC_au1} \\ i_{ABC_au2} \end{bmatrix} \quad (3-13)$$

where the coefficient 1/3 means constant amplitude transformation.

By using (3-13), the fundamental and current harmonics can be decomposed into three subspaces, i.e. $\alpha\beta$, z_1z_2 , and z_3z_4 subspaces, and the new harmonic mapping is shown in Fig. 3.8. Different from Fig. 3.2, the fundamental current is decoupled with the other current harmonics and individually mapped in the $\alpha\beta$ subspace. The 5th and 13th current harmonics are mapped in z_1z_2 subspace, while the 7th and 11th current harmonics mapped in the z_3z_4 subspace.

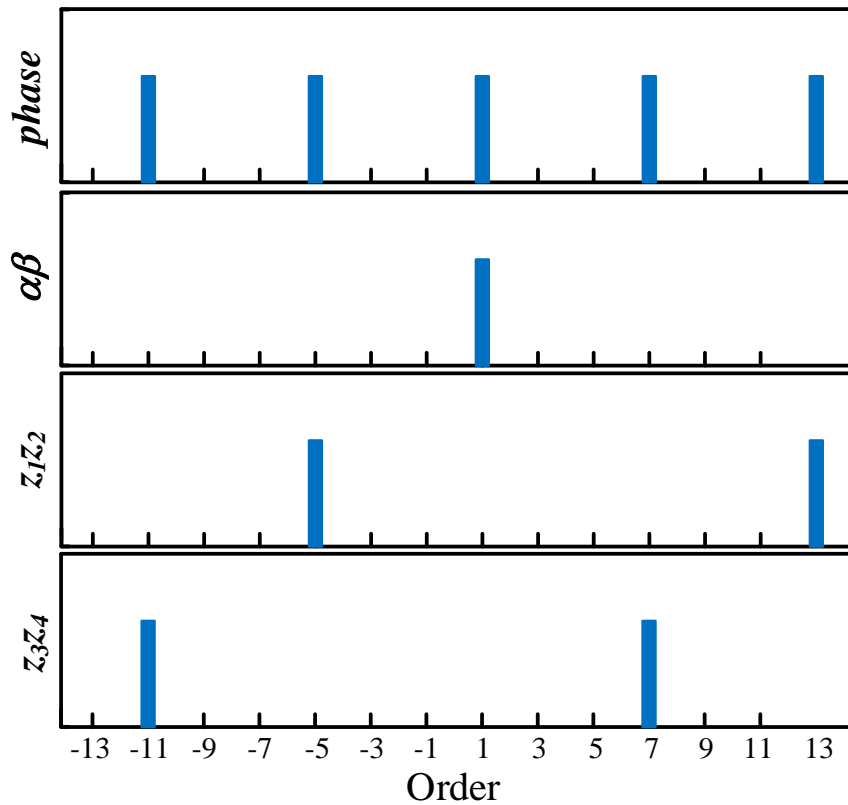


Fig. 3.8. New harmonic mapping in $\alpha\beta$, z_1z_2 , and z_3z_4 subspaces using (11). The fundamental is separated in $\alpha\beta$ subspaces. The 5th and 13th harmonics are distributed in z_1z_2 subspace, and the 7th and 11th are distributed in z_3z_4 subspace.

Based on Fig. 3.8, a new MSRF current detection can be designed as Fig. 3.9. The auxiliary

current i_{ABC_au1} is established by the $\pi/9$ phase shifting of i_{ABC} . i_{ABC_au2} is the $2\pi/9$ phase shift of i_{ABC} and can be established by the $\pi/18$ phase shifting of i_{XYZ} because i_{XYZ} is the $\pi/6$ phase shift of i_{ABC} . It is worth noting that the auxiliary currents are not physical currents like i_{ABC} or i_{XYZ} , and the auxiliary axes in Fig. 3.5(c) are also virtual. Then, i_{ABC} , i_{ABC_au1} , and i_{ABC_au2} are decomposed as $i_{\alpha\beta}$, i_{z1z2} , and i_{z3z4} using (3-13). Since the fundamental is individually mapped into $\alpha\beta$ subspace, it can be directly detected using Park transformation. The sum of the 5th and 13th current harmonics is decomposed as i_{z1z2} , and the sum of the 7th and 11th current harmonics is decomposed as i_{z3z4} . LPFs are required to extract the current harmonics in the corresponding MSRFs. The detected current harmonics are DC components in MSRFs and can be regulated by multiple PI regulators as shown in Fig. 3.4(b).

Compared with the basic MSRF current detection in Fig. 3.4(a), the designed MSRF current detection in Fig. 3.9 provides superiorities for the control system, which are also the major contributions of this chapter. First, the LPF1 is no more required, and the removal of LPF1 eliminates the delay effect in the fundamental current loop and hence helps to improve the dynamic performance of torque and speed regulation. More importantly, Fig 3.8 shows that the current harmonics are decoupled with the fundamental which's amplitude is much larger than the amplitudes of harmonics, and the current harmonics mapped in the same subspace become further away from each other in spectra. As a consequence, it will be easier to extract the current harmonics from phase currents, i.e. the bandwidths of LPFs can be much larger than them in Fig. 3.4(a) and the delay effect is greatly reduced. The reduced delay effect in the current loops will enhance the dynamic control performances of not only the current fundamental but also the current harmonics in MSRFs.

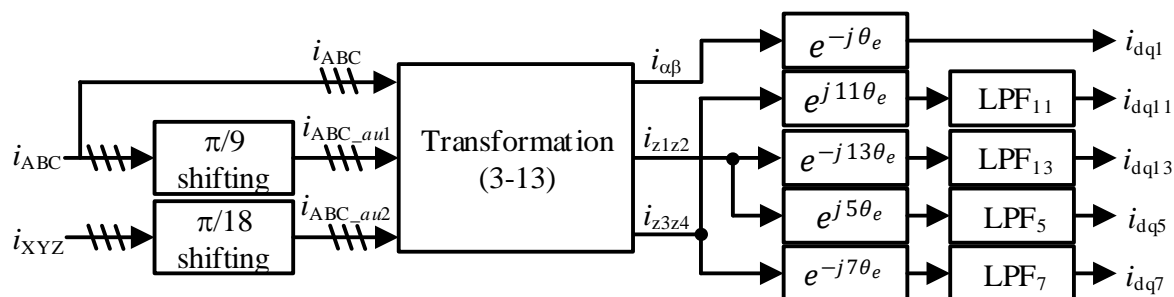


Fig. 3.9. Proposed current harmonic detection. The original phase currents i_{ABC} and the auxiliary currents i_{ABC_au1} , i_{ABC_au2} are decomposed as $i_{\alpha\beta}$, i_{z1z2} , and i_{z3z4} , which are transformed into MSRFs to detect the fundamental as well as the current harmonics, respectively.

3.3.2 Current Regulator Design

Since the current harmonics are all detected as DC components in MSRFs, multiple PI regulators are considered as good solutions to control these current harmonics. The parameters of PI regulators should be well tuned to achieve both fast dynamic response and good stability of current loops. This section introduces a generic regulator for not only the current fundamental but also the current harmonics.

The current loops in MSRFs are independent due to the proposed current decomposition, and they can be described by the block diagram in Fig. 3.10, where $n=1, 5, 7, 11, \text{ and } 13$. $\mathbf{G}_{pn}(s)$, $\mathbf{G}_{dn}(s)$, $\mathbf{G}_{cn}(s)$, and $\mathbf{H}_n(s)$ are the plant, digital delay, current regulator, and LPF, respectively. The expressions of the plant and digital delay are as follows.

$$\begin{aligned}\mathbf{G}_{pn}(s) &= \frac{1}{R_s + L_n s + jh\omega_e L_n} \\ \mathbf{G}_{dn}(s) &= e^{-T_d s} \cdot e^{-jh\omega_e T_d}\end{aligned}\quad (3-14)$$

where $h=1, -5, 7, -11, \text{ and } 13$. L_n is equivalent to L_s when $n=1, 11, \text{ and } 13$, and to L_σ when $n=5$ and 7 . T_d is the delay time. $\mathbf{G}_{pn}(s)$ represents the fundamental or harmonic model of machine, i.e. (3-6) and (3-8). The delay time T_d is caused by the time variation between the sampling moment and voltage update moment in digital control system. Its effect can be regarded as two parts, i.e. the time delay of the output voltage $e^{-T_d s}$ and phase angle variation of MSRFs $e^{-jh\omega_e T_d}$. For easy implementation, the first order LPF is employed in this chapter and its transfer function is as follows.

$$\mathbf{H}_n(s) = \frac{\omega_{cn}}{s + \omega_{cn}} \quad (3-15)$$

where ω_{cn} is the bandwidth. To achieve zero-pole cancellation, the current regulator can be designed as complex vector PI format:

$$\mathbf{G}_{cn}(s) = k_n \frac{R_s + L_n s + jh\omega_e L_n}{s} \quad (3-16)$$

where k_n is the gain coefficient. The transfer function from the reference to the current feedback in Fig. 3.10 can be written as

$$\frac{I_{dq_n}(s)}{I_{dq_n}^*(s)} = \frac{\mathbf{G}_{cn}(s)\mathbf{G}_{dn}(s)\mathbf{G}_{pn}(s)}{1 + \mathbf{G}_{cn}(s)\mathbf{G}_{dn}(s)\mathbf{G}_{pn}(s)\mathbf{H}_n(s)} \quad (3-17)$$

Substituting (3-14), (3-15), and (3-16) into (3-17) yields

$$\frac{I_{dq_n}(s)}{I_{dq_n}^*(s)} = \frac{k_n(s + \omega_{cn})e^{-(s+jh\omega_e)T_d}}{s^2 + \omega_{cn}s + k_n\omega_{cn}e^{-(s+jh\omega_e)T_d}} \quad (3-18)$$

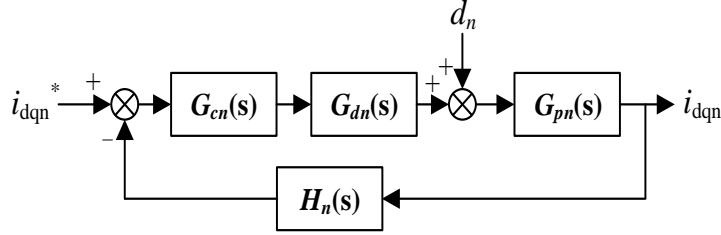


Fig. 3.10. Block diagram of current loops in MSRFs. $\mathbf{G}_{pn}(s)$, $\mathbf{G}_{dn}(s)$, and $\mathbf{G}_{cn}(s)$ represent the plant, digital delay, and current regulator, respectively. $\mathbf{H}_n(s)$ is the LPF. Signal d_n denotes the voltage disturbance introduced by inverter nonlinearity and PM flux linkage harmonics.

The transfer function (3-18) represents the tracking capability to the current reference, and its characteristic is determined by two parameters, namely the gain coefficient k_n and the LPF bandwidth ω_{cn} . Figs. 3.11 and 3.12 show the magnitude characteristic of (3-18) under different k_n and ω_{cn} in positive- and negative-sequence domains. The positive- and negative-sequence domains include the positive- and negative-sequence current components in MSRFs, respectively. The control parameters used in the simulation are as follows: $h=7$; the delay time $T_d=150\mu\text{s}$; the machine electrical angular speed $\omega_e=125\text{rad/s}$. From these pictures, the 0dB gain near 0Hz grants the current loop the capability to track the fundamental and current harmonic reference with no steady-state error, and also completely reject the DC voltage disturbance d_n introduced by inverter nonlinearity and PM flux linkage harmonics. With the increasing of k_n in Fig. 3.11, the bandwidth of the current loop increases, which means the current response becomes more dynamic. However, the magnitude and frequency of the peak point simultaneously increase in both positive- and negative-sequence domains. That will result in pulsating current near the frequency of peak point in dynamic process. In Fig. 3.12, ω_{cn} increases from 3.14rad/s to inf (inf means infinite). It can be understood that the LPF is equivalently removed from the current loop when ω_{cn} is infinite. As ω_{cn} increases, the bandwidth of the current loop is also improved. Besides, the peak point is pushed further away from the system frequency and its magnitude is reduced, which will contribute to the alleviation

of the pulsating current in dynamic current reference tracking.

The complex vector PI regulator (3-16) is generic for not only the fundamental current control but also the harmonic loops by simply changing h and n to the corresponding value, and k_n can be tuned to realize different response speed of current control.

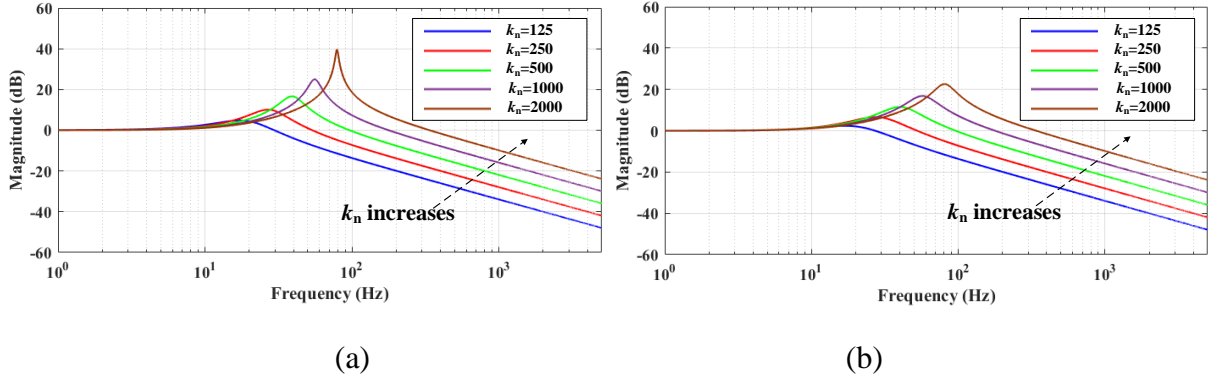


Fig. 3.11. Magnitude characteristic of current regulation when cut-off frequency $\omega_{cn}=125.6\text{rad/s}$ and gain coefficient k_n increases from 125 to 2000. (a) Positive-sequence. (b) Negative-sequence.

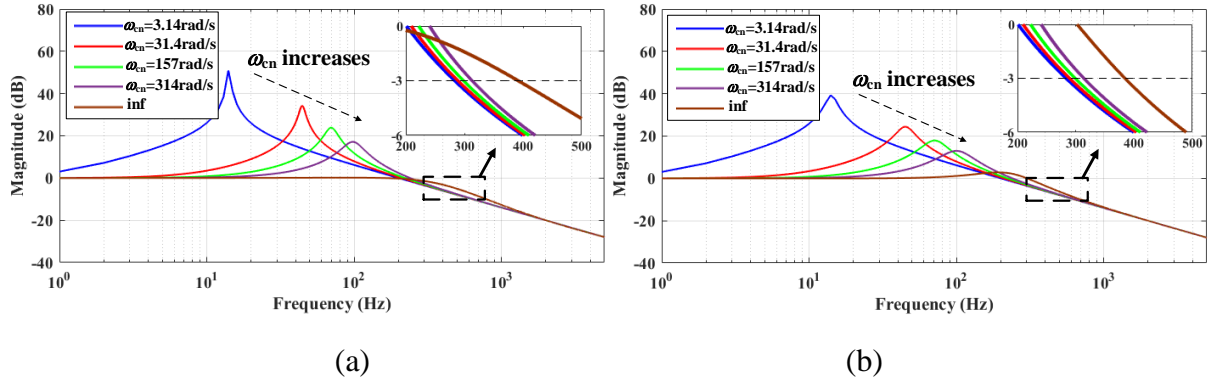


Fig. 3.12. Magnitude characteristic of current regulation when gain coefficient $k_n=2000$ and cut-off frequency ω_{cn} increases from 3.14rad/s to inf . (a) Positive-sequence. (b) Negative-sequence.

3.3.3 Stability Analysis and Phase Compensation

The system stability can be considered as the stability of each independent current loop. In this chapter, the Nyquist diagram is used to analyze the stability of the controller. Fig. 3.13 shows the Nyquist diagram of current loop in Fig. 3.10. The simulation parameters are the same as those used in Fig. 3.12. As the angular frequency ω increases from 0rad/s to inf in positive- and negative-sequence domains, the Nyquist curves start from infinity and end near the original point. It is clear that the system is instable when $\omega_{cn}=3.14\text{rad/s}$ because the crucial point $(-1, j0)$

is enclosed by the arc of the curve. With the increasing of ω_{cn} , the system enters into stable region and curve becomes further away from the crucial point, leading to larger stable margin.

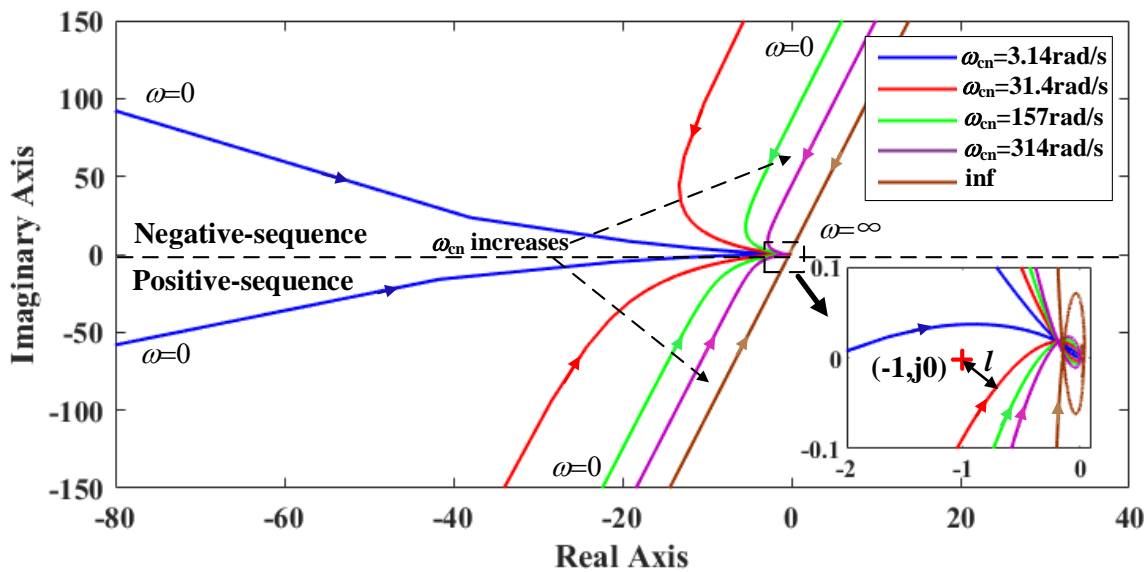


Fig. 3.13. Nyquist diagram of the current loop when gain coefficient $k_n=2000$ and cut-off angular frequency ω_{cn} increases from 3.14rad/s to inf.

The value of the distance l between the arc and the crucial point indicates the stable margin, and Fig. 3.14 shows the values of l under different k_n and ω_{cn} . The horizontal axis represents the cut-off angular frequency ω_{cn} , i.e. f_{cn} in Hz. When k_n increases from 125 to 500, the system is stable in all the range of ω_{cn} , and the stable margin increases with the increasing of ω_{cn} . The system becomes instable in the low frequency region of ω_{cn} when k_n is 1000, and the stable region shrinks when k_n keeps increasing to 2000. It can be concluded from Fig. 3.14, although the current response speed increases with the increasing of gain coefficient k_n , the stable margin of current loop is reduced, and increasing ω_{cn} helps to increase the margin and stabilize the system. It should be noted that compared with the basic MSRF method, the proposed method can well detect the current harmonics with larger ω_{cn} . With reference to the simulation results in Figs. 3.11, 3.12, 3.13, and 3.14, the proposed method should exhibit faster current reference tracking, less pulsating current in dynamics, and larger stable margin.

In $G_{dn}(s)$, the first term $e^{-T_d s}$, time delay of output voltage, is inherent and unavoidable in digital control system. However, the second term $e^{-jh\omega_e T_d}$, whose value is related to the speed and harmonic order, represents phase variation of MSRFs in the delay period and can be compensated by adding the phase variation angle to the inverse transformation angle of voltage, i.e. replacing $e^{jh\theta_e}$ with $e^{jh(\theta_e + \omega_e T_d)}$ in Fig. 3.4(b). The stability of the fundamental and

harmonic current loops under different machine fundamental frequencies is studied in Fig. 3.15. If without compensation, the stable margins of these current loops decrease as the machine speed increases and finally they become out of the stability boundary. Compared with the fundamental current loop, the harmonic current loops have narrower stable region of machine speed and is more likely to suffer from the instability. This is because the higher the harmonic order is, the more phase angle the harmonic reference frame varies during T_d , and the closer to the crucial point the Nyquist curve is. The dotted line in Fig. 3.15 indicates the l values of the fundamental and harmonic current loops after the phase compensation. The effect of $e^{-jh\omega_e T_d}$ is eliminated from the loop after the compensation, so the stability is enhanced at different machine speeds and the fundamental current loop shares the same stable margin with the harmonic ones.

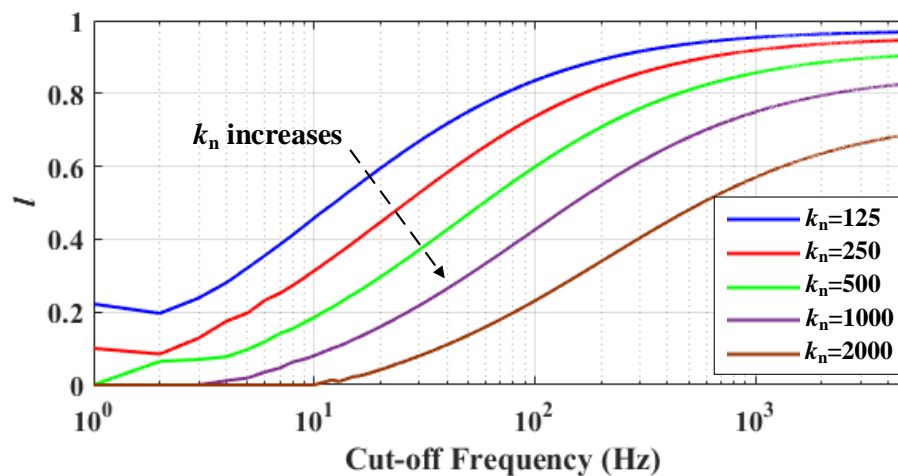


Fig. 3.14. Effect of k_n and ω_{cn} on stability. k_n increases from 125 to 2000.

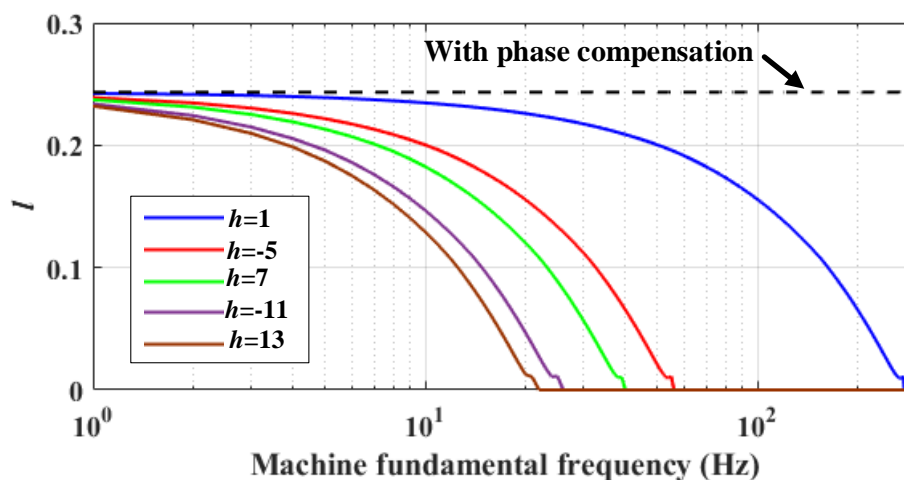


Fig. 3.15. Stability of the fundamental and harmonic current loops against machine fundamental frequency when $\omega_{cn}=125.6\text{rad/s}$ and $k_n=2000$.

3.3.4 Implementation

To achieve the phase shifting of phase currents, the values of phase currents are continuously online recorded in a look-up table (LUT) at different sampling instants with reference to rotor position, as TABLE 3.1. Symbol k is the actual sampling instant, and $k-1$ means the last sampling instant. The LUT should be synchronously updated with the rotor position variation. Since the rotor position angle θ_e is synchronous with the phase angle of the fundamental current, the rotor position angle difference between two sampling instants can be regarded as the phase shift angle between the currents at the two instants. Take an example, if $\theta_e(k) - \theta_e(1) = \pi/9$, phase currents at sampling instant 1, $i_A(1)$ and $i_B(1)$, are the $\pi/9$ phase shift of $i_A(k)$ and $i_B(k)$, respectively, and thus auxiliary currents $i_{A_au1} = i_A(1)$, $i_{B_au1} = i_B(1)$, and $i_{C_au1} = -i_{A_au1} - i_{B_au1}$. The same principle can be applied to auxiliary currents i_{A_au2} , i_{B_au2} , and i_{C_au2} . In a real control system, the sampling instants are discrete, which means the phase shift angle is usually not exactly located at the sampling instant, e.g. located between sampling instants 1 and 2. In this case, the linear interpolation method may be utilized to estimate the auxiliary currents. However, in digital implementation, linear interpolation method requires the use of division operation which causes computation burden and the problem of zero denominator. The dichotomy method is suggested to replace the linear point-slope method for the purpose of reducing computation burden and avoiding zero denominator. It should be noted that at low frequency the LUT becomes long, and hence in this case interval sampling can be used to shorten the LUT.

TABLE 3.1
CURRENTS AND ROTOR ELECTRIC ANGLES AT DIFFERENT SAMPLING INSTANTS

Sampling instants	1	2	3	...	$k-1$	k
θ_e	$\theta_e(1)$	$\theta_e(2)$	$\theta_e(3)$...	$\theta_e(k-1)$	$\theta_e(k)$
i_A	$i_A(1)$	$i_A(2)$	$i_A(3)$...	$i_A(k-1)$	$i_A(k)$
i_B	$i_B(1)$	$i_B(2)$	$i_B(3)$...	$i_B(k-1)$	$i_B(k)$

The established auxiliary currents should be decomposed using Transformation (3-13) according to Fig. 3.9. The transformation matrix in (3-13) is a constant-element matrix, and this transformation will not significantly increase the computation burden. In addition, the generic structure of the designed PI regulators provides convenience for the implementation and parameter tuning of different current loops. Furthermore, these current harmonic regulators are selective and can be flexibly activated or deactivated according to the requirement of a real system.

As studied in [YEP15][YEP13], the main computation burden of the controller usually comes from the calculation of trigonometric functions in rotating transformation and inverse transformation. Since the proposed controller requires multiple rotating transformations and inverse transformations, the computation burden needs to be taken into consideration in implementation. Actually, high computation burden is a common characteristic of the MSRF-based methods. A simple method is employed here to reduce the computation burden. The trigonometric functions in the fundamental current loop, i.e. $\cos \theta_e$ and $\sin \theta_e$, are required in most machine vector control and can be calculated using a Taylor series. The trigonometric functions in the harmonic current loop, e.g. $\cos 5\theta_e$ and $\sin 5\theta_e$, are also calculated using a Taylor series in [YEP15][YEP13]. However, in this chapter, they are suggested to be calculated using Ptolemy's identities, i.e. trigonometric sum and difference formulas. The process is as follows.

$$\begin{aligned}
\cos 2\theta_e &= 2 \cos^2 \theta_e - 1, \quad \sin 2\theta_e = 2 \sin \theta_e \cos \theta_e \\
\cos 4\theta_e &= 2 \cos^2 2\theta_e - 1, \quad \sin 4\theta_e = 2 \sin 2\theta_e \cos 2\theta_e \\
\cos 6\theta_e &= \cos 4\theta_e \cos 2\theta_e - \sin 4\theta_e \sin 2\theta_e, \\
\sin 6\theta_e &= \sin 4\theta_e \cos 2\theta_e + \cos 4\theta_e \sin 2\theta_e
\end{aligned} \tag{3-19}$$

From (3-19), the calculation of $\cos 2\theta_e$ requires one subtraction and two multiplications. A left bit shift operation can be used to replace 2 times $\cos^2 \theta_e$ to save the computation time. Then $\cos 5\theta_e$ and $\sin 5\theta_e$ can be calculated as

$$\begin{aligned}
\cos 5\theta_e &= \cos 6\theta_e \cos \theta_e + \sin 6\theta_e \sin \theta_e, \\
\sin 5\theta_e &= \sin 6\theta_e \cos \theta_e - \cos 6\theta_e \sin \theta_e
\end{aligned} \tag{3-20}$$

The trigonometric functions in the 7th, 11th, and 13th harmonic current loops can be similarly derived as (3-19) and (3-20). TABLE 3.2 shows the required math operation numbers of trigonometric functions using Ptolemy's identities above and using Taylor series, respectively.

TABLE 3.2
OPERATION NUMBERS OF TRIGONOMETRIC FUNCTIONS

Trigonometric functions	Using Ptolemy's identities		Using Taylor series	
	+/-	*	+/-	*
$\cos \theta_e$ & $\sin \theta_e$	7	12	7	12
$\cos 5\theta_e$ & $\sin 5\theta_e$	10	12	7	13
$\cos 7\theta_e$ & $\sin 7\theta_e$	2	0	7	13
$\cos 11\theta_e$ & $\sin 11\theta_e$	5	6	7	13
$\cos 13\theta_e$ & $\sin 13\theta_e$	2	0	7	13
Sum	26	30	35	64

In TABLE 3.2, “+/-” means addition and subtraction, and “*” means multiplication. To simplify the comparison, the bit shift operation is classified into “+/-”. The value of $\cos \theta_e$ is calculated using a Taylor series of sixth order, and $\sin \theta_e$ is transferred to $\cos(\theta_e - \pi/2)$ and then use a Taylor series. The calculation of $\cos \theta_e$ and $\sin \theta_e$ requires 7 additions/subtractions and 12 multiplications. If calculating all the trigonometric functions of harmonics with a Taylor series, the sum of additions/subtractions is 35 and the sum of multiplications is 64. If using Ptolemy’s identities, the numbers of additions/subtractions and multiplications are reduced to 26 and 30, respectively.

Fig. 3.16 compares the numbers of operations that trigonometric functions require using Taylor series with different orders. “**Proposed, +/-**” and “**Proposed, ***” represent the numbers of additions/subtractions and multiplications when calculating only $\cos \theta_e$ and $\sin \theta_e$ with a Taylor series but the other trigonometric functions with Ptolemy’s identities. “**Taylor, +/-**” and “**Taylor, ***” represent the numbers of additions/subtractions and multiplications when calculating all the trigonometric functions with a Taylor series. The higher order of a Taylor series means the higher accuracy of the trigonometric functions. Using the proposed calculation method can reduce the numbers of additions/subtractions and multiplications, and further reduce the computation burden of controller, especially when using a high order Taylor series.

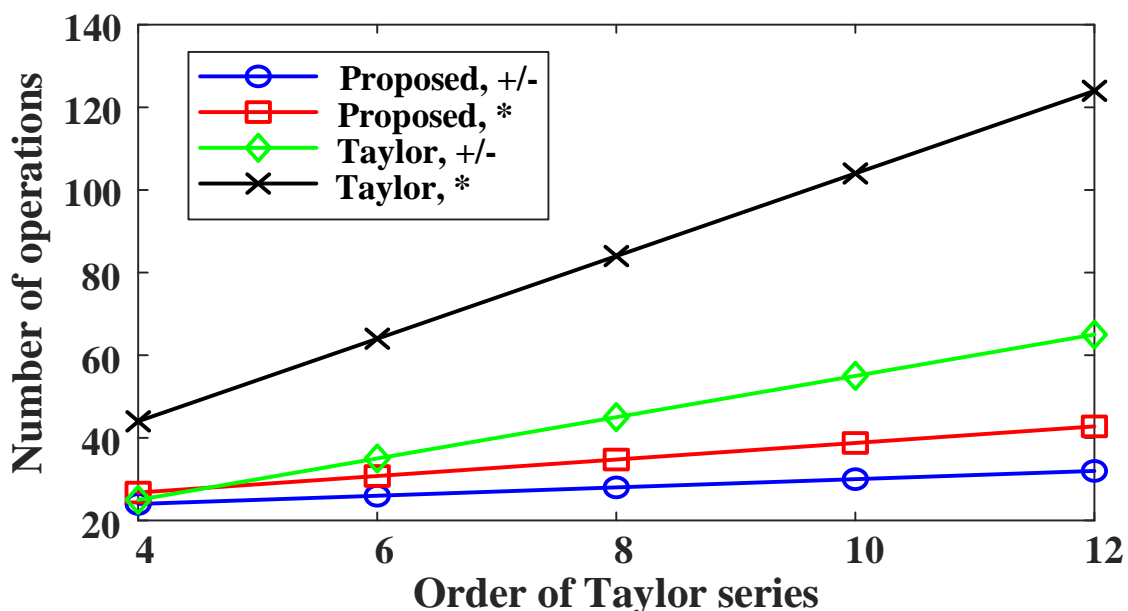


Fig. 3.16. Number of operations that trigonometric functions require, as a function of the order of Taylor series.

3.4 Experimental Verification

Experiments are processed on a laboratory platform which includes dSPACE (DS1005), six-leg VSI (STGIPS20C60 IGBT), DC power supply, dual three-phase PMSM, and load dynamometer, see Appendix A. The machine phase currents are sampled by the analog-to-digital converter and the encoder signals are decoded in DS1005 to derive the rotor position angle. By using the C code generator of MATLAB/SIMULINK software and the real-time interface (RTI) of dSPACE, the proposed control strategy can be implemented and testified. The generated code is loaded and operated in the real-time microprocessor (PowerPC 750) of DS1005. The computation of the proposed method can be finished in half control cycle (50 μ s). The switching signals are then produced and used to drive the IGBTs and control the machine. The experimental results are collected by DS1005 and plotted in MATLAB.

3.4.1 Current Harmonic Detection and Regulation

The proposed current harmonic detection, Fig. 3.9, is experimentally tested and the results are shown in Figs. 3.17 and 3.18. In Fig. 3.17, the measured waveforms of the decomposed current and the spectra are presented, and only the fundamental current loop is activated ($k_1=314.2$) to provide the rated torque at 200r/min. The current harmonic detection is activated but the current harmonic regulators are not activated. The phase current and auxiliary currents are presented in Fig. 3.17(a) (only i_A , i_{A_au1} , and i_{A_au2} are shown here), and it is clear that i_{A_au1} , and i_{A_au2} are the $\pi/9$ and $2\pi/9$ phase shift of i_A . Because the current harmonic regulators are not activated, there are the serious 5th, 7th, 11th, and 13th harmonics in the spectrum of phase current. Using the transformation (3-13), the currents can be decomposed into $\alpha\beta$, z_1z_2 , and z_3z_4 subspaces, as shown in Figs. 3.17(b), 3.17(c), and 3.17(d), respectively. From the spectra, the fundamental current is separated from the 5th, 7th, 11th, and 13th harmonics and individually distributed in $\alpha\beta$ subspace. The 5th and 13th current harmonics are mapped in z_1z_2 subspace together, as well as the 7th and 11th ones mapped in z_3z_4 subspace. The measured result is consistent with the expected harmonic mapping in Fig. 3.8.

Fig. 3.18 shows the measured currents when machine is operated at 200r/min with the rated torque. The current harmonic suppression is activated at 1s. The bandwidths of LPFs are $\omega_{c5}=\omega_{c7}=94.2\text{rad/s}$, $\omega_{c11}=\omega_{c13}=94.2\text{rad/s}$. The coefficients of the designed PI regulators are $k_5 = k_7=62.8$, $k_{11} = k_{13}=31.4$, and $k_1=314.2$. The detected current harmonics are also shown in Fig. 3.18, and can be represented by the DC components: $i_{d5}=0.39\text{A}$, $i_{q5}= -0.2\text{A}$; $i_{d7}= -0.31\text{A}$,

$i_{q7}=0.09\text{A}$; $i_{d11}=0.13\text{A}$, $i_{q11}=0.017\text{A}$; $i_{d13}= -0.09\text{A}$, $i_{q13}=0.01\text{A}$. The amplitudes of current harmonics can be calculated as follows: $I_5=0.438\text{A}$; $I_7=0.323\text{A}$; $I_{11}=0.131\text{A}$; $I_{13}=0.0906\text{A}$. The amplitudes of the current harmonics are consistent with the spectrum in Fig. 3.17(a), which validates the accurate current harmonic detection. After the current harmonic suppression activated at 1s, it is clear that all the current harmonics can well follow the references and were suppressed to 0, which led to the almost sinusoidal waveforms of phase current after 1s.

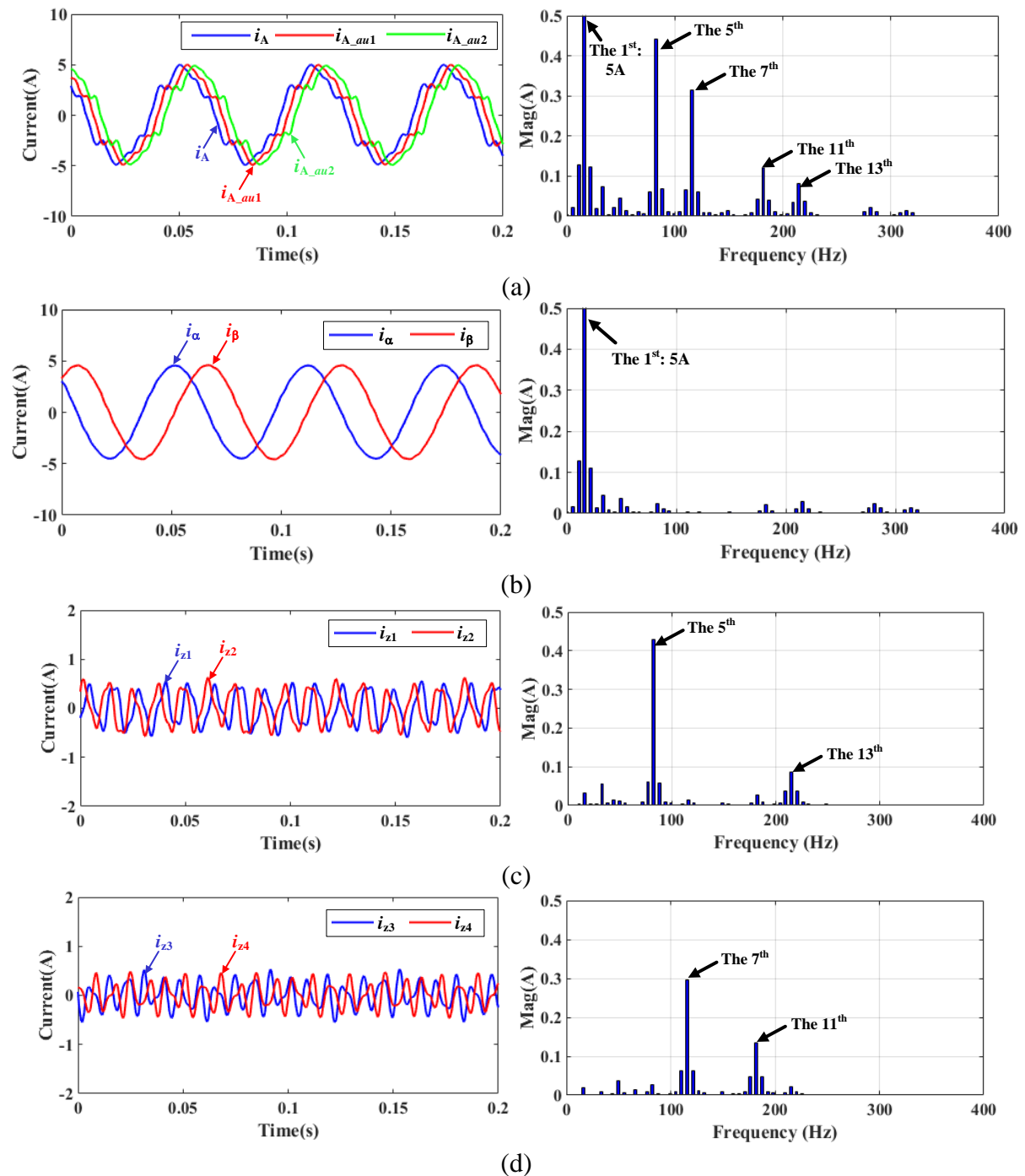


Fig. 3.17. Measured waveforms of decomposed currents and spectra. (a) i_A , i_{A_au1} , and i_{A_au2} . (b) $i_{\alpha\beta}$. (c) i_{z1z2} . (d) i_{z3z4} . Machine is operated with rated torque at 200r/min.

Fig. 3.19 shows the robustness test results when the speed reference was 200r/min and load torque stepped from 50% rated torque to 100% rated torque at 0.2s. Before 0.2s, the phase A current and auxiliary currents are almost sinusoidal due to the good suppression of current harmonics i_{d5} , i_{q5} , i_{d7} , i_{q7} , i_{d11} , i_{q11} , i_{d13} , and i_{q13} . The step load torque will result in the 20r/min speed decrease and the sudden change of phase current amplitude. The auxiliary currents are not accurate during that sudden change because they are derived from the phase shifting of physical phase currents. This inaccuracy causes the disturbance in the detected current harmonics. However, the speed can return to 200r/min and the disturbance in currents disappeared in a short time (around 50ms), the current harmonics can still be suppressed to 0A, and the phase current maintained sinusoidal at steady-state. The experimental results show that the performance of the proposed method is not significantly influenced by sudden torque variation.

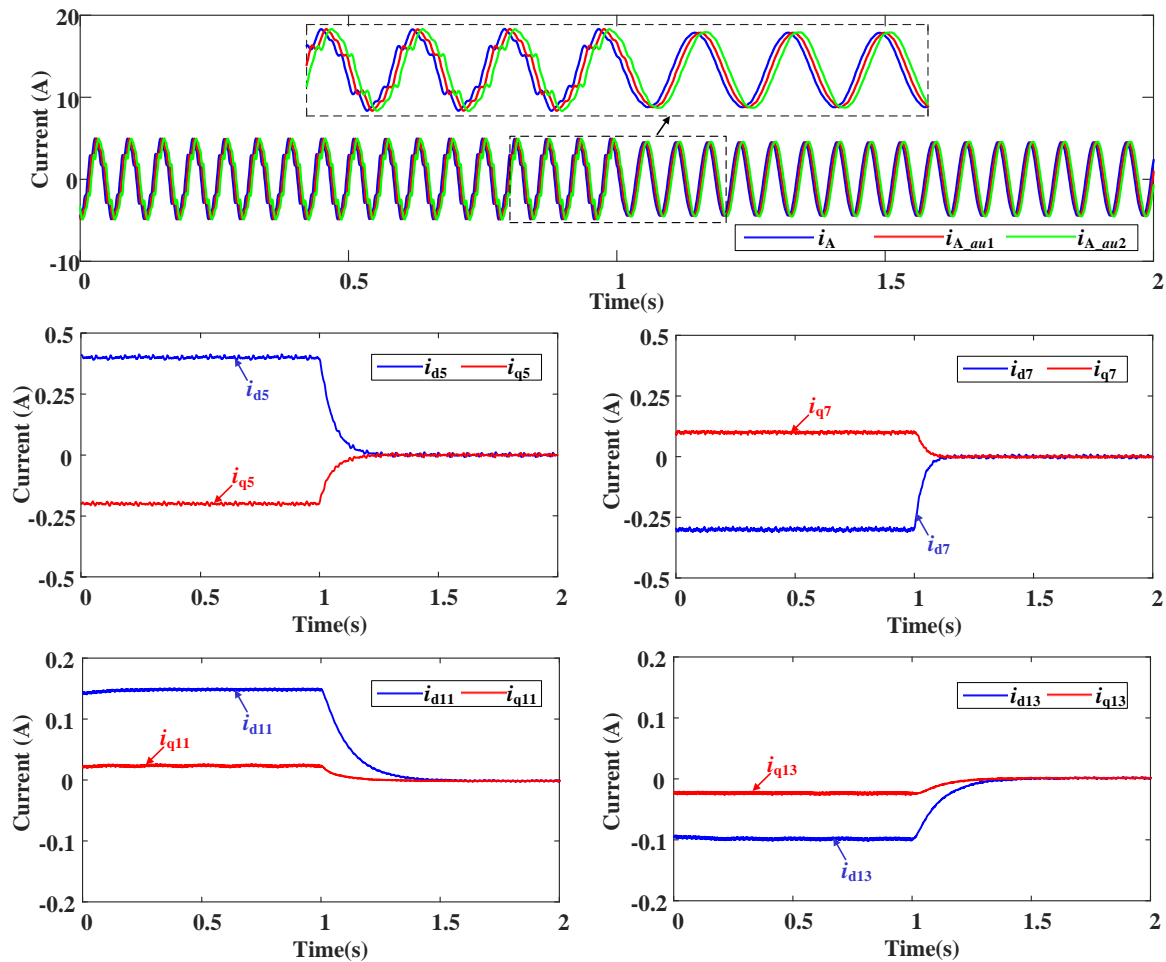


Fig. 3.18. Measured waveforms of phase A current i_A , auxiliary currents i_{A_au1} , i_{A_au2} , and the detected current harmonics i_{d5} , i_{q5} , i_{d7} , i_{q7} , i_{d11} , i_{q11} , i_{d13} , and i_{q13} , when machine was operated at 200r/min with rated torque and the current harmonic suppression was activated at 1s.

The current regulator is generic for not only the fundamental but also the current harmonics, because it is designed based on the machine model and requires the machine parameters to build the coefficients in regulator. To evaluate the effect of parameter variation, the step response of the 5th current harmonic is tested and the results are shown in Fig. 3.20, where reference i_{d5}^* stepped from 0A to 0.4A at 0.5s. $k_5 = 62.8$, and the inductance in the 5th current harmonic regulator is configured as $0.5L_\sigma$, L_σ , and $2L_\sigma$, respectively. From the results, although the parameter mismatch can increase the overshoot in i_{d5} and the pulsating in i_{q5} , the effect is negligible when inductance varies between $0.5L_\sigma$ and $2L_\sigma$.

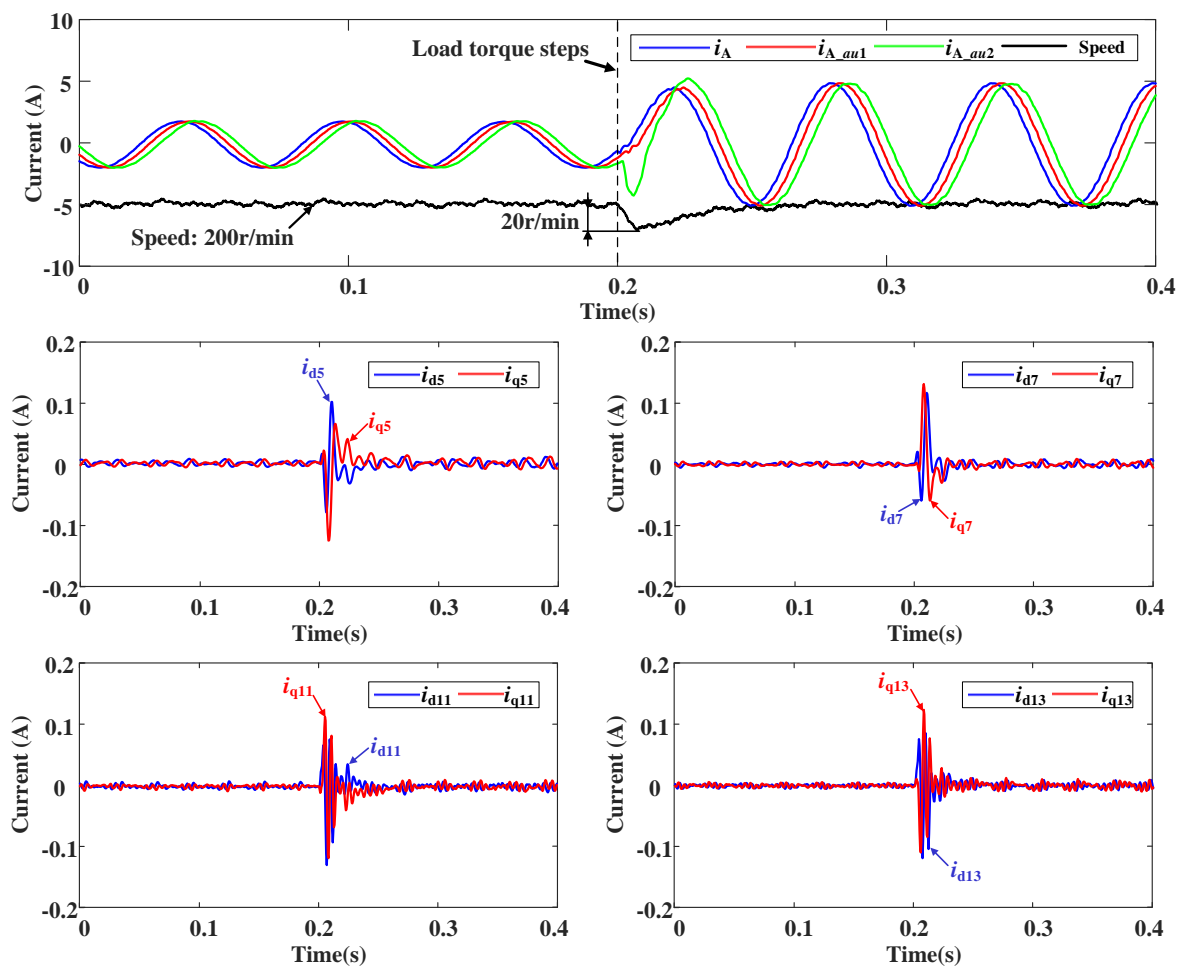


Fig. 3.19. Measured waveforms of speed, phase A current i_A , auxiliary currents i_{A_au1} , i_{A_au2} , and the detected current harmonics i_{d5} , i_{q5} , i_{d7} , i_{q7} , i_{d11} , i_{q11} , i_{d13} , and i_{q13} , when speed reference was 200r/min and the load torque stepped from 50% rated torque to 100% rated torque at 0.2s.

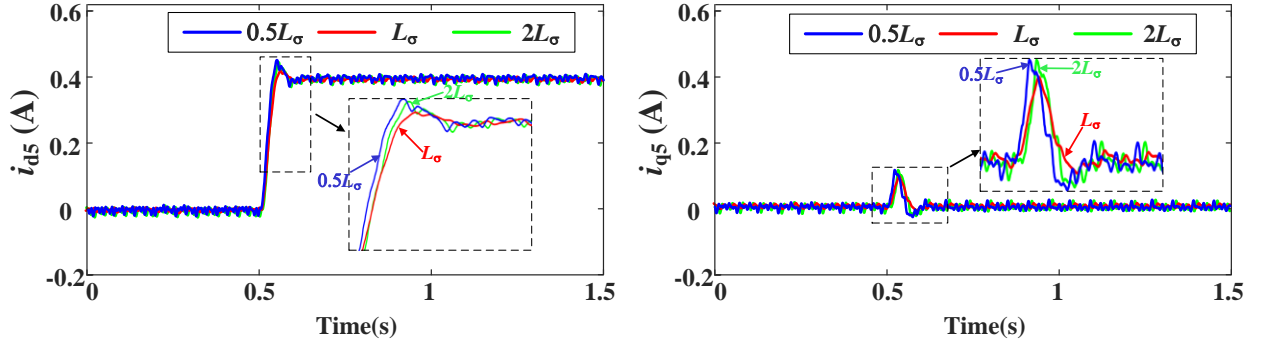


Fig. 3.20. Measured step responses of the 5th current harmonic considering parameter mismatch. The inductance in the 5th current harmonic regulator is configured as $0.5L_\sigma$, L_σ , and $2L_\sigma$, respectively.

3.4.2 Comparison with Other MSRF-based Methods

The experimental results validate that the proposed method can well regulate the current harmonics to track the reference and has good robustness regarding load torque variation and machine parameter variation. To highlight the contribution of this chapter, the proposed method is experimentally compared with other MSRF-based methods. The basic MSRF-based method, employed in [KAR17], is shown in Fig. 3.4 and is referred to method **MSRF 1**. The method proposed in [FEN19] utilizes moving average filter to decompose the current harmonics, and it is referred to method **MSRF 2**. [LIU19] utilizes a PI regulator to achieve close-loop detection of current harmonic, and is referred to **MSRF 3**. The three methods above are considered as the most practical MSRF-based methods and are selected to be compared with the proposed method. It is worth noting that the major difference among these methods is on how to decouple and detect the current harmonics, and the common point is that the decoupled current harmonics can be all regulated by the same PI regulators in MSRFs. Accordingly, these methods are compared following the principles: the coefficients of current harmonic detection, e.g. the bandwidths of LPFs, are tuned to reduce the ripples of the detected currents to below 0.01A; the designed PI regulators are then employed to control the detected currents, and different methods share the same PI coefficients.

Figs. 3.21 and 3.22 show the step response comparison of the 5th and 11th current harmonics, respectively. To quantify the performance measures of the proposed method with regard to the other MSRF-based methods, the current overshoot ΔI , the convergence time t_c , and the steady-state error Δe between feedback and reference in Figs. 3.21 and 3.22 are shown in TABLE 3.3. The THD of the phase current before the harmonic reference step is also given in the table.

In Fig. 3.21, the reference i_{d5}^* stepped from 0A to 0.4A at 0.5s, and the reference i_{q5}^* remained 0A. The gain coefficient k_5 is configured as 31.4, 62.8, 125.6, and 251.3 in all methods. It is clear that the proposed method can smoothly track the reference without obvious overshoot and pulsating when k_5 is 31.4, Fig. 3.21(d). As k_5 increases, the overshoot and pulsating in i_{d5} and i_{q5} of all methods increase, but the proposed method exhibits the smallest overshoot and pulsating, as well as the shortest convergence time. When k_5 increases to 251.3, the systems with **MSRFs 1, 2, and 3** become unstable and there are serious pulsating currents without convergence to current references after i_{d5}^* stepped. The tendency of all these methods is the same, i.e. the higher gain coefficient k_5 results larger overshoot and more pulsating in the dynamic response. However, the difference is that the proposed method always shows the smallest overshoot and the shortest convergence time, and although the proposed method shows obvious overshoot and pulsating when k_5 is 251.3, the system is at least stable compared to the systems with other methods and can converge in 0.65s.

In terms of the 11th current harmonic in Fig. 3.22, the reference i_{d11}^* stepped from 0A to 0.2A at 1s, and the reference i_{q11}^* remained 0A. The gain coefficient k_{11} is configured as 12.5, 31.4, and 94.2, respectively, in all methods. Because the 11th current harmonic is coupled with the fundamental current in **MSRFs 1, 2, and 3**, enough attenuation on the fundamental current is required to reduce the current ripples, which leads to large phase delay of the 11th current harmonic detection. As a result, the step responses of the 11th current harmonic are worse than the step responses of the 5th current harmonic in **MSRFs 1, 2, and 3**, and the system is more likely to turn unstable as k_{11} increases. Since the 11th current harmonic is decoupled with the fundamental current in the proposed method, the phase delay of the detection is not as large as the other methods. Thus, the step response is better, and system is more stable. It can be concluded from Fig. 3.21, Fig. 3.22, and TABLE 3.3 that, compared to other MSRF-based methods, the proposed method has the similar steady-state error and THD, however shows enhanced dynamic performance and stability, i.e. the reduced overshoot and convergence time.

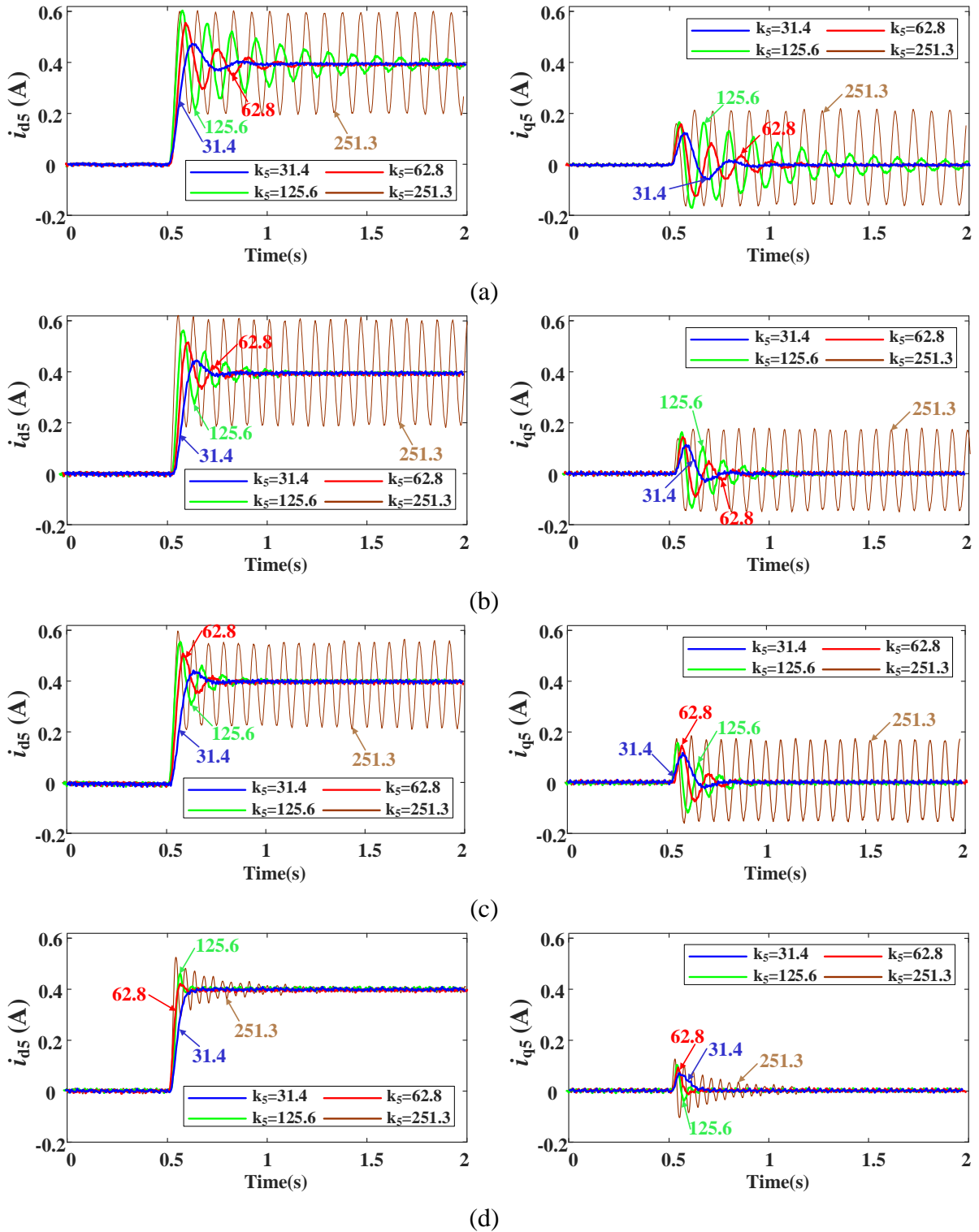


Fig. 3.21. Measured step responses of the 5th current harmonic using MSRF-based methods with different k_5 . Reference i_{d5}^* stepped from 0A to 0.4A at 0.5s, and reference i_{q5}^* remained 0A. Machine is operated at 200r/min with rated torque. (a) **MSRF 1**. (b) **MSRF 2**. (c) **MSRF 3**. (d) **Proposed**.

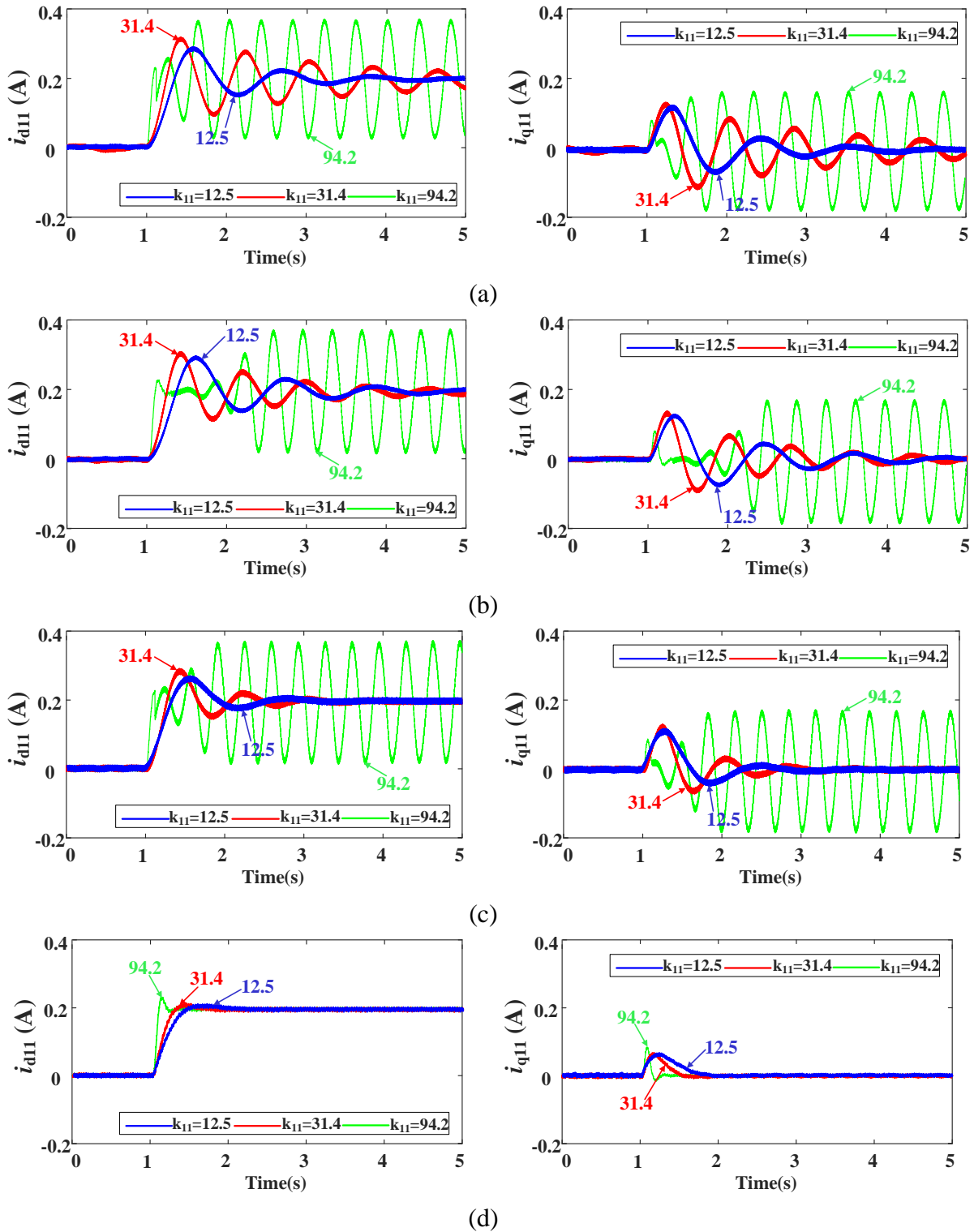


Fig. 3.22. Measured step responses of the 11th current harmonic using MSRF-based methods with different k_{11} . Reference i_{d11}^* stepped from 0A to 0.2A at 1s, and reference i_{q11}^* remained 0A. Machine is operated at 200r/min with rated torque. (a) **MSRF 1**. (b) **MSRF 2**. (c) **MSRF 3**. (d) Proposed.

TABLE 3.3
PERFORMANCE COMPARISON OF DIFFERENT MSRF METHODS

k_5/k_{11}	MSRF 1	MSRF 2	MSRF 3	Proposed
31.4	$\Delta I=61\text{mA}$	$\Delta I=46\text{mA}$	$\Delta I=37\text{mA}$	$\Delta I<10\text{mA}$
	$t_c=0.46\text{s}$	$t_c=0.35\text{s}$	$t_c=0.23\text{s}$	$t_c=0.18\text{s}$
	$\Delta e<10\text{mA}$	$\Delta e<10\text{mA}$	$\Delta e<10\text{mA}$	$\Delta e<10\text{mA}$
62.8	$\Delta I=153\text{mA}$	$\Delta I=107\text{mA}$	$\Delta I=101\text{mA}$	$\Delta I=15\text{mA}$
	$t_c=0.69\text{s}$	$t_c=0.47\text{s}$	$t_c=0.38\text{s}$	$t_c=0.21\text{s}$
	$\Delta e<10\text{mA}$	$\Delta e<10\text{mA}$	$\Delta e<10\text{mA}$	$\Delta e<10\text{mA}$
5 th 125.6	$\Delta I=200\text{mA}$	$\Delta I=160\text{mA}$	$\Delta I=153\text{mA}$	$\Delta I=61\text{mA}$
	$t_c>1.5\text{s}$	$t_c=0.65\text{s}$	$t_c=0.58\text{s}$	$t_c=0.21\text{s}$
	$\Delta e<10\text{mA}$	$\Delta e<10\text{mA}$	$\Delta e<10\text{mA}$	$\Delta e<10\text{mA}$
251.3	$\Delta I=200\text{mA}$	$\Delta I=200\text{mA}$	$\Delta I=200\text{mA}$	$\Delta I=123\text{mA}$
	$t_c=inf$	$t_c=inf$	$t_c=inf$	$t_c=0.65\text{s}$
	$\Delta e:instable$	$\Delta e:instable$	$\Delta e:instable$	$\Delta e<10\text{mA}$
12.5	$\Delta I=98\text{mA}$	$\Delta I=87\text{mA}$	$\Delta I=60\text{mA}$	$\Delta I=11\text{mA}$
	$t_c=3.09\text{s}$	$t_c>4\text{s}$	$t_c=2.09\text{s}$	$t_c=1.1\text{s}$
	$\Delta e<10\text{mA}$	$\Delta e<10\text{mA}$	$\Delta e<10\text{mA}$	$\Delta e<10\text{mA}$
11 th 31.4	$\Delta I=113\text{mA}$	$\Delta I=102\text{mA}$	$\Delta I=84\text{mA}$	$\Delta I=17\text{mA}$
	$t_c>4\text{s}$	$t_c>4\text{s}$	$t_c=2.47\text{s}$	$t_c=0.86\text{s}$
	$\Delta e<10\text{mA}$	$\Delta e<10\text{mA}$	$\Delta e<10\text{mA}$	$\Delta e<10\text{mA}$
94.2	$\Delta I=167\text{mA}$	$\Delta I=167\text{mA}$	$\Delta I=167\text{mA}$	$\Delta I=33\text{mA}$
	$t_c=inf$	$t_c=inf$	$t_c=inf$	$t_c=0.57\text{s}$
	$\Delta e:instable$	$\Delta e:instable$	$\Delta e:instable$	$\Delta e<10\text{mA}$
THDs	2.51%	2.45%	2.24%	2.38%

Inf means no convergence.

The speed step responses are shown in Fig. 3.23. The speed reference stepped from 200r/min to 400r/min at 1s. A PI regulator is utilized as the speed controller, and the integral coefficient is set as 0.4 to guarantee the speed can track the reference without steady-state error. The proportional coefficient k_p is set as 0.03, 0.05, and 0.1, respectively. It should be noted that different methods share the same speed regulator, but the fundamental current is detected and regulated by different MSRF-based methods. The fundamental current reference i_{q1}^* is the output of speed controller, and i_{d1}^* is set as 0A. From Fig. 3.23, all methods have smooth speed response when k_p is 0.03. However, as k_p increases, pulsating arises in speed dynamics, especially in **MSRF 1**. The proposed method can provide a current detection with less delay effect, which will also contribute to a better dynamic performance of speed control, as shown in Fig. 3.23(d).

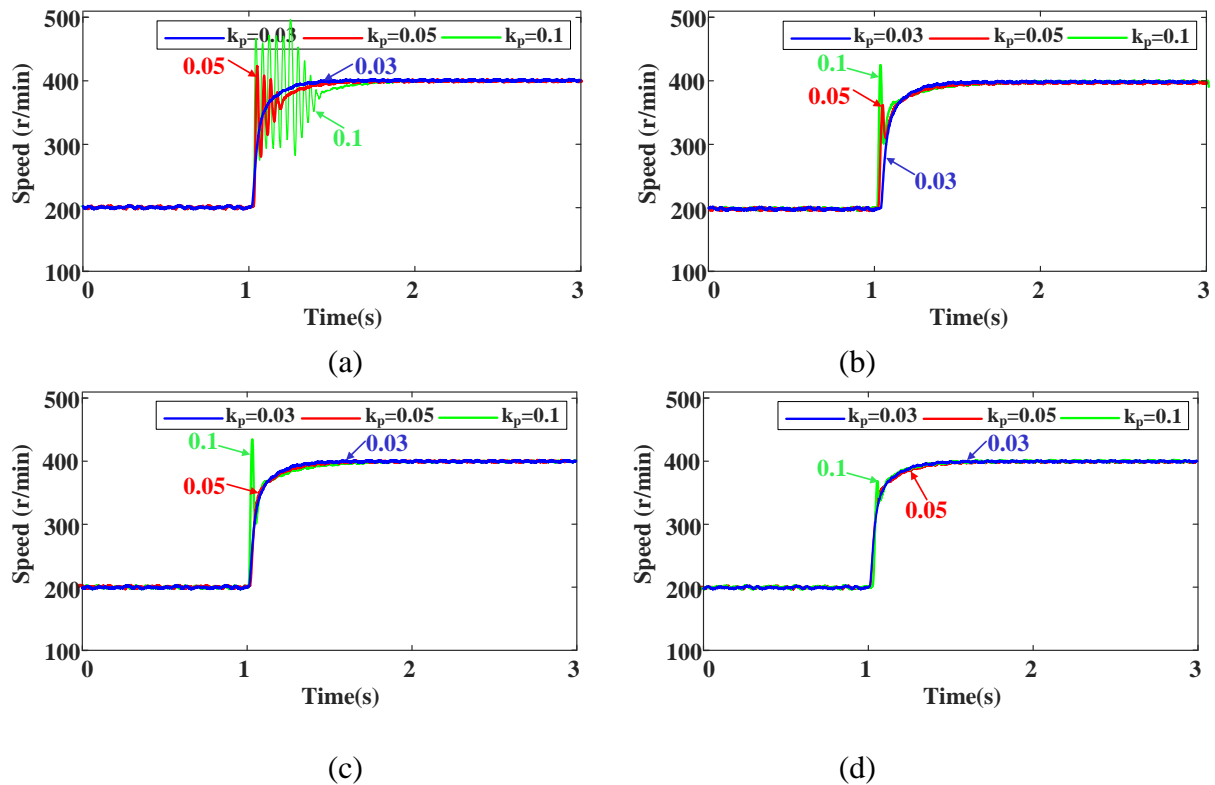


Fig. 3.23. Measured step responses of speed using different MSRF-based methods. Speed reference stepped from 200r/min to 400r/min at 1s. (a) **MSRF 1**. (b) **MSRF 2**. (c) **MSRF 3**. (d) Proposed

3.5 Conclusion

In this chapter, an improved MSRF current harmonic regulation method has been proposed for dual three-phase PMSM. The experimental results confirm that the proposed method can accurately detect the current harmonics, and control the individual current harmonic to track the current harmonic references with good robustness regarding load torque variation and machine parameter variation. Compared with the existing MSRF-based methods, the proposed method can provide a current harmonic detection with reduced delay effect, and hence exhibits a better dynamic performance of current harmonic regulation as well as a better system stability. These enhancements make the proposed method more applicable in both current harmonic suppression and injection of dual three-phase PMSM system.

CHAPTER 4

CONTROL OF CURRENT HARMONICS FOR DUAL THREE-PHASE PMSMS BY VIRTUAL MULTI THREE- PHASE SYSTEMS

The MSRF-based current harmonic control method proposed in the last chapter shows good performance on the suppression and injection of the major current harmonic in DTP PMSM. It is proved that the current harmonic decomposition is convenient for current harmonic regulation due to the reduced delay effect in current harmonic detection. The proposed current harmonic decomposition in the last chapter can separate the major current harmonics, i.e. the 5th, 7th, 11th, and 13th, from the fundamental. However, it is illustrated that the 5th current harmonic is still coupled with the 13th current harmonic, while the 7th current harmonic is coupled with the 11th current harmonic. A question that may be easily come up with is whether it is possible to decompose all the current components into several individual subspaces, and the fundamental and major current harmonics are completely decoupled to each other.

Based on the question, this chapter proposes a concept of virtual multi three-phase systems to achieve complete decomposition of the major current harmonics and independent regulation of the current harmonics in a DTP PMSM system. The control system proposed in the last chapter can be understood as a virtual triple three-phase system. This chapter develops the virtual triple three-phase system to generic virtual multi three-phase systems, e.g. virtual triple, virtual quadruple, and virtual pentuple three-phase system. The virtual multi three-phase currents are firstly reconstructed by appropriately shifting the phase of original physical DTP currents, and then are decomposed with the help of vector space decomposition techniques. As a result, the fundamental and the major current harmonics, i.e. the 5th, 7th, 11th, and 13th, can be completely separated in several isolated subspaces, where the independent current control loops can be easily designed and implemented. The correctness and effectiveness are validated by simulation results and experimental results.

This chapter is published in IEEE Transactions on Industrial Electronics [YAN21c].

- [YAN21c] L. Yan, Z. Q. Zhu, J. Qi, Y. Ren, C. Gan, S. Brockway, and C. Hilton, “Suppression of major current harmonics for dual three-phase PMSMs by virtual multi three-phase systems,” *IEEE Trans. Ind. Electron.*, vol. 69, no. 6, pp. 5478-5490, June 2021

4.1 Introduction

A new concept of a virtual multi three-phase system is proposed in this chapter to achieve independent regulation of the fundamental and major current harmonics with better steady- and dynamic-state performance. Due to the limited decomposition capability of the DTP system, the phase shifting operation on the original physical dual three-phase currents is first utilized to reconstruct the virtual multi three-phase currents. The vector space decomposition (VSD) approaches are then used to decompose the major current harmonics in the virtual multi three-phase systems. As a result, the fundamental and the major current harmonics are individually extracted from the original phase currents and mapped into several isolated subspaces. By using the Park transformations in the corresponding subspaces, these currents can be individually regulated in MSRFs. Compared with the existing approaches, the fundamental and major current harmonics are totally decomposed, and thus the interference among different frequencies, from which the resonance-based regulators mainly suffer, is avoided and the stability of the system is enhanced. Besides, it is the rotor position but not the rotor speed that is utilized in the implementation of the phase shifting operation and coordinate transformation. That avoids the problem of machine frequency inaccuracy in the dynamics. Furthermore, in the existing MSRF methods, as introduced, the bandwidths of LPFs and the PI coefficients should be carefully turned to guarantee the dynamic current response and system stable simultaneously, which leads to complex parameter tuning. Such problems do not appear here because the proposed virtual multi three-phase systems can separate the current harmonics without using LPFs, and the removal of LPFs helps to make the current harmonic regulation more dynamic, stabilize the entire system, and also simplify the parameter tuning.

This chapter is organized as follows. Section 4.2 introduces the decomposition capability of VSD technique. The virtual multi three-phase system combined with MSRF regulator is proposed to suppress the current harmonics in Section 4.3. The simulation and experimental results are provided in Section 4.4 and Section 4.5, respectively. Section 4.6 discusses the applicability and extension of the proposed method. Finally, Section 4.7 concludes the chapter.

4.2 Analysis of Decomposition Capability of VSD Techniques in Multi Three-phase Systems

The ideal result of decomposition is that all the fundamental and major harmonic components in the phase current are respectively mapped into different orthogonal subspaces, so that they can be independently regulated.

Fig. 4.1 shows the harmonic mapping in two subspaces after the decomposition transformation in the DTP system. It can be clearly seen that the sum of 5th and 7th current harmonics is decomposed in the z_1z_2 subspace, while the fundamental, 11th and 13th current harmonics are coupled in $\alpha\beta$ subspace. Obviously, the major current harmonics are not completely separated with each other, and hence the ideal decomposition cannot be realized in the DTP case.

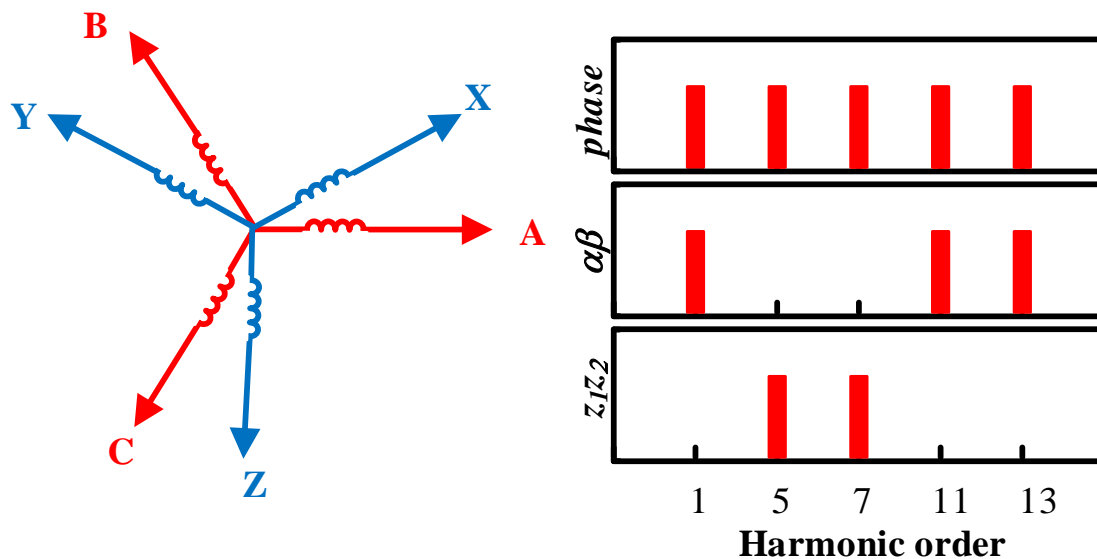


Fig. 4.1. Dual three-phase winding configurations and harmonic mapping of VSD techniques.

In a triple three-phase (TTP) system with 20° electrical degrees shifting between the adjacent sets, Fig. 4.2, the VSD technique merely decomposes the fundamental current into $\alpha\beta$ subspace, the sum of 5th and 13th into z_1z_2 subspace, and the 7th and 11th into z_3z_4 subspace, respectively. Compared with Fig. 4.1, Fig. 4.2 shows the better decomposition capability because the fundamental current is separated and can be individually controlled in the $\alpha\beta$ subspace. However, the 5th and 13th current harmonics are still mixed with each other in z_1z_2 subspace, as well as the 7th and 11th in z_3z_4 subspace.

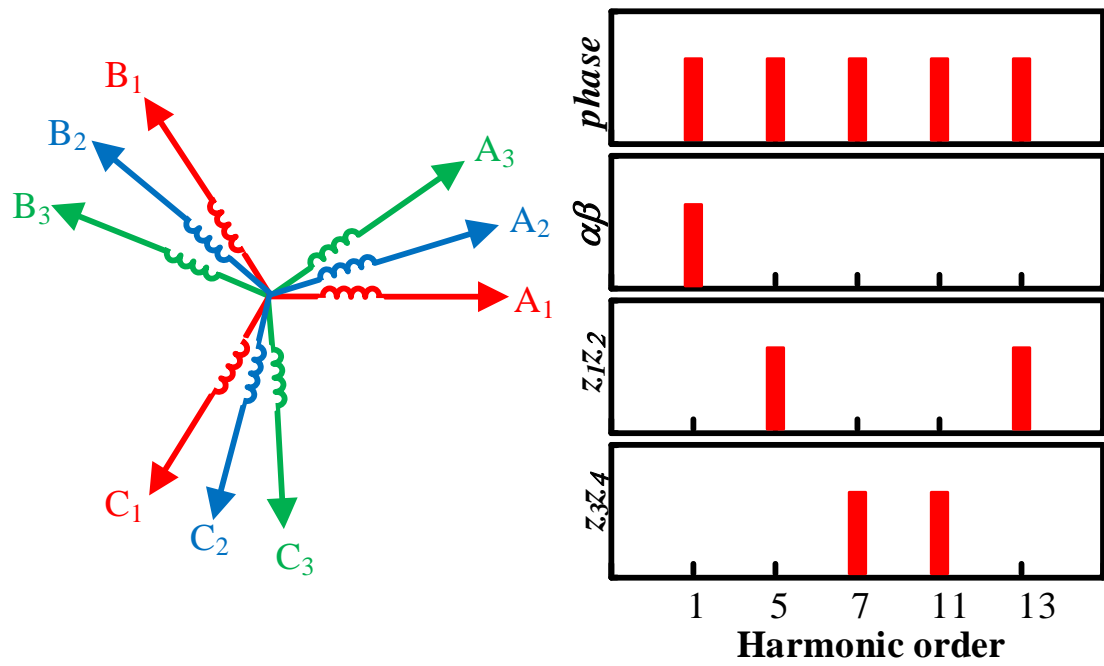


Fig. 4.2. Triple three-phase winding configurations and harmonic mapping of VSD techniques.

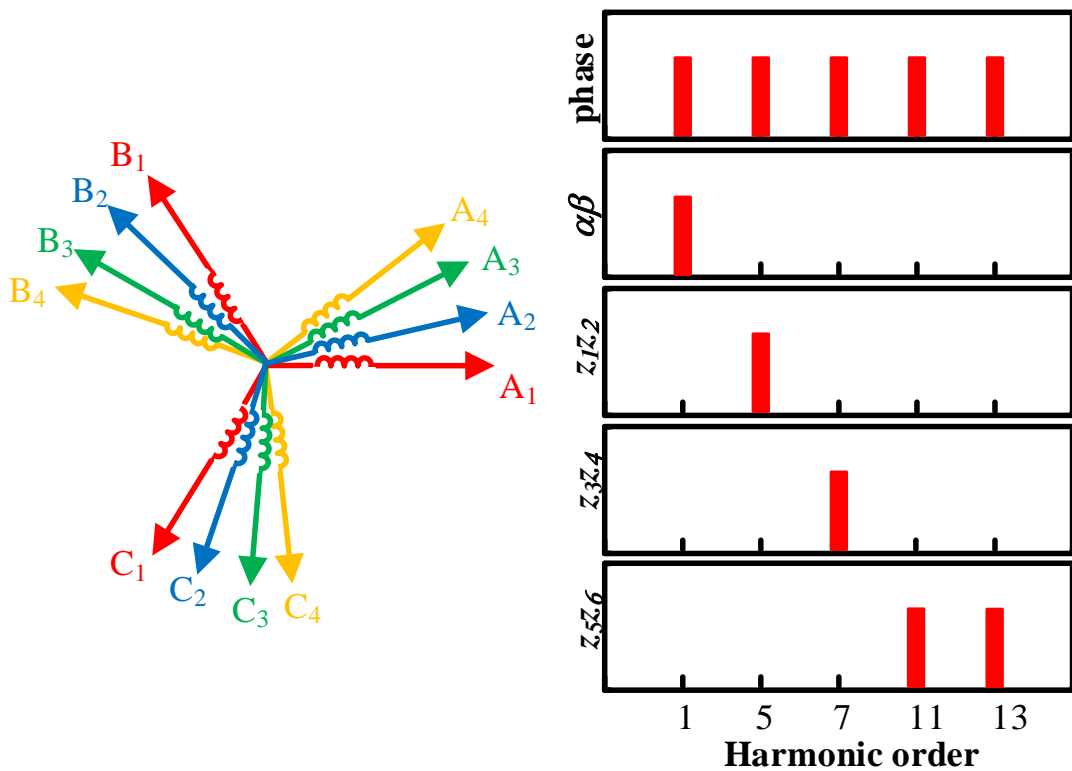


Fig. 4.3. Quadruple three-phase winding configurations and harmonic mapping of VSD techniques.

As the number of three-phase sets increases, the quadruple three-phase (QTP) case, which shifts 15° electrical degrees between the adjacent sets, has improved decomposition capability due to the complete separation of the fundamental, 5th and 7th current harmonics, as shown in Fig. 4.3. As a result, it is possible to individually regulate the fundamental, 5th and 7th current harmonics in three independent current loops without using LPFs, but unfortunately impossible for the 11th and 13th current harmonics.

Finally, the pentuple three-phase (PTP) system with 12° electrical degree shifting has the ideal decomposition capability because the fundamental and major current harmonics (5th, 7th, 11th and 13th) are respectively mapped into five subspaces according to Fig. 4.4, which means their current loops can also be isolated in each subspace.

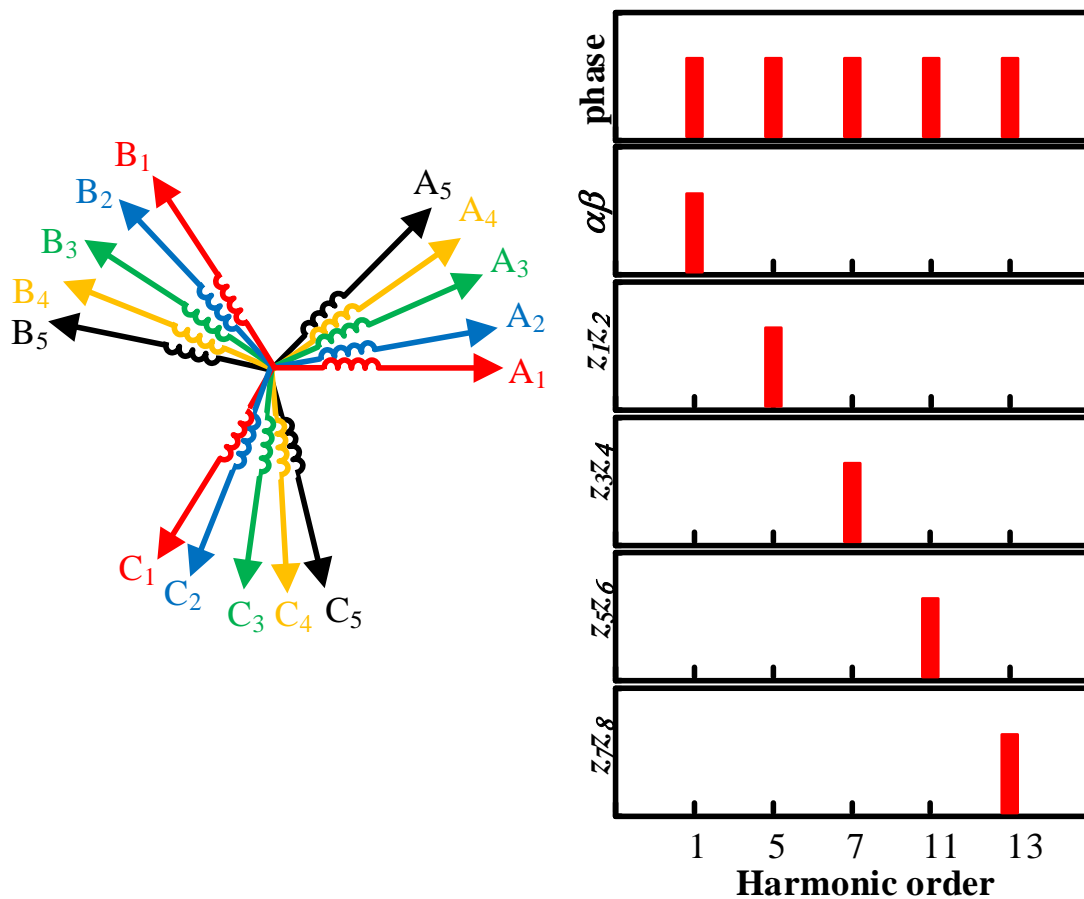


Fig. 4.4. Pentuple three-phase winding configurations and harmonic mapping of VSD techniques.

In summary, the decomposition capability of the VSD techniques increases with the increasing

of set number in a multi three-phase system. The original DTP system cannot achieve the separation of the current harmonics through VSD transformation, the QTP system can only separate the fundamental, the 5th, and the 7th current harmonics, and the best is that the PTP system can completely separate all the major current harmonics, and the independent regulation of them can be achieved as well.

4.3 Virtual Multi Three-phase System

To completely decompose the major current harmonics, the use of LPFs is inevitable under the DTP framework due to its limited decomposition capability. As introduced in Chapter 3, the weakness of using LPFs includes poor dynamic performance, complex parameter tuning, and instability. If not using the LPFs, it is either impractical to increase the number of real three-phase sets to help decomposing the current harmonics. To make full use of the additional decomposition capability provided by multi three-phase system, a generic virtual multi three-phase system is established by reconstructing virtual multi three-phase currents.

According to the phase relationship of currents in multi three-phase sets, the time fundamental phase shifting between the currents of two adjacent sets is $\pi/6$, $\pi/9$, $\pi/12$, and $\pi/15$ in DTP, TTP, QTP, and PTP cases, respectively. Consequently, an appropriate phase shifting of original physical currents in DTP PMSM can be utilized to reconstruct virtual multi three-phase (more than two three-phases) currents, as shown in Fig. 4.5, where $S()$ represents the phase shifting operation, which has been introduced in Chapter 3, Section 3.3. The physical phase currents of the DTP machine, namely i_{ABC} and i_{XYZ} , can be regarded as the virtual currents of the first and third sets in the QTP case, i.e., $i_{A_1B_1C_1}^4$ and $i_{A_3B_3C_3}^4$, where the superscript “4” represents the QTP case and is used to distinguish the currents from those in the other multi three-phase cases. Then, the $\pi/12$ shifting of currents i_{ABC} and i_{XYZ} can be respectively regarded as the virtual phase currents of the second and fourth sets, i.e. $i_{A_2B_2C_2}^4$ and $i_{A_4B_4C_4}^4$. Similarly, the $\pi/9$ shifting of i_{ABC} and the $\pi/18$ shifting of i_{XYZ} can be regarded as virtual phase currents of the second and third sets in TTP case. To reconstruct the virtual PTP system, the $\pi/15$ and $2\pi/15$ shifting of i_{ABC} are the virtual currents of the second and third sets, and then the $\pi/30$ and $\pi/10$ shifting of i_{XYZ} can be regarded as the virtual currents of the fourth and fifth sets.

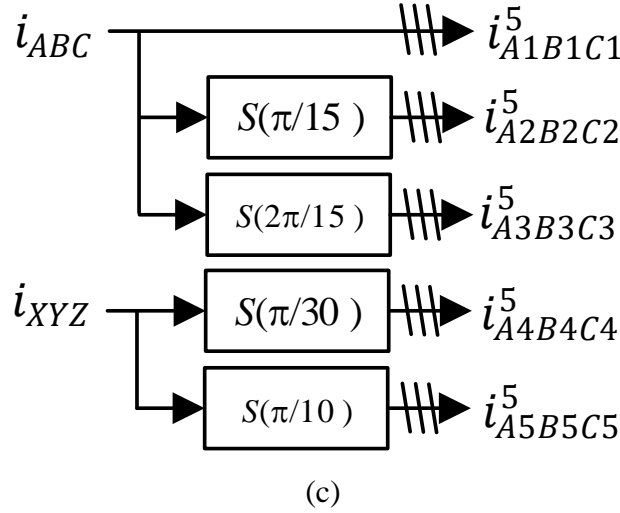
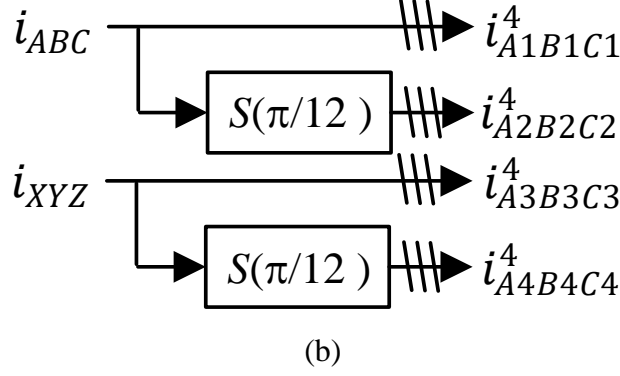
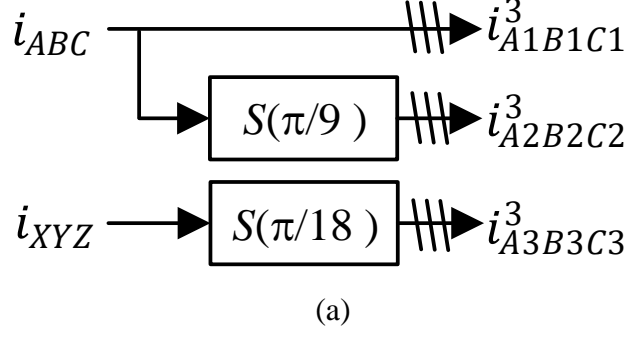


Fig. 4.5. Virtual multi three-phase current reconstruction based on phase shifting operation. (a) Virtual TTP. (b) Virtual QTP. (c) Virtual PTP.

After the virtual multi three-phase currents are reconstructed, the transformation (4-1) can be used to decompose the current components.

$$T_m = \frac{1}{m} \begin{bmatrix} T(0) & T(\gamma_m) & T(2\gamma_m) & \dots & T((m-1)\gamma_m) \\ T(0) & T(-5\gamma_m) & T(-5(2\gamma_m)) & \dots & T(-5(m-1)\gamma_m) \\ T(0) & T(7\gamma_m) & T(7(2\gamma_m)) & \dots & T(7(m-1)\gamma_m) \\ \dots & \dots & \dots & \dots & \dots \\ T(0) & T(n\gamma_m) & T(n(2\gamma_m)) & \dots & T(n(m-1)\gamma_m) \end{bmatrix} \quad (4-1)$$

where m is the number of virtual three-phase sets, $\gamma_m = \pi/(3m)$ is the electrical angle between two adjacent sets, and $n=1, -5, 7, -11, 13, \dots$. The submatrix T is

$$T(\theta) = \frac{2}{3} \begin{bmatrix} \cos \theta & \cos(\theta + 2\pi/3) & \cos(\theta - 2\pi/3) \\ \sin \theta & \sin(\theta + 2\pi/3) & \sin(\theta - 2\pi/3) \end{bmatrix} \quad (4-2)$$

In particular, if only the dominant 5th and 7th current harmonics are required to be controlled, the virtual QTP system is capable enough to decompose them and the virtual QTP phase currents can be used as follows.

$$\begin{bmatrix} i_{\alpha\beta 1} \\ i_{\alpha\beta 5} \\ i_{\alpha\beta 7} \\ i_{\alpha\beta 11} + i_{\alpha\beta 13} \end{bmatrix} = T_4 \begin{bmatrix} i_{A1B1C1}^4 \\ i_{A2B2C2}^4 \\ i_{A3B3C3}^4 \\ i_{A4B4C4}^4 \end{bmatrix} \quad (4-3)$$

where $i_{\alpha\beta h}$ represents the current component with order h in stationary two phase frames. Although the 5th and 7th current harmonics are decomposed and can be independently regulated by using (4-3), the 11th and 13th cannot be decomposed and they are usually required to be suppressed for lower torque ripples in DTP PMSMs. With this, the virtual PTP currents can be employed to decompose all the major current harmonics with the help of the following transformation.

$$\begin{bmatrix} i_{\alpha\beta 1} \\ i_{\alpha\beta 5} \\ i_{\alpha\beta 7} \\ i_{\alpha\beta 11} \\ i_{\alpha\beta 13} \end{bmatrix} = T_5 \begin{bmatrix} i_{A1B1C1}^5 \\ i_{A2B2C2}^5 \\ i_{A3B3C3}^5 \\ i_{A4B4C4}^5 \\ i_{A5B5C5}^5 \end{bmatrix} \quad (4-4)$$

From (4-4), the fundamental and major current harmonics are mapped into five isolated subspaces, and hence it is easy to regulate them in five independent current loops as shown in Fig. 4.6. The decomposed currents are respectively transformed into corresponding MSRFs and the PI regulators are employed to control the fundamental current and suppress the major current harmonics by simply setting the current harmonic references to zero. The output voltages of PI regulators are inversely transformed and composed in the stationary two phase frames, and then the inverse VSD transformation is utilized to yield the phase voltage references of DTP PMSM. The 24-sector six phase continuous SVPWM proposed in [MAR08] is employed in this chapter to modulate the phase voltages.

Due to the fact that the controlled variables in MSRFs, i.e. i_{dq1} , i_{dq5} , i_{dq7} , i_{dq11} , and i_{dq13} , are all DC components, the PI regulators are the ideal choices to regulate the currents because the infinite open-loop gain at 0Hz provided by the integrator ensures the DC current harmonic references are tracked without steady-state errors, and the proportional term can improve the dynamic response. The PI regulators can be grouped as feedback decoupling type [KAR14], feedforward decoupling type [ZHO17], and complex vector decoupling type [HOF16] according to the decoupling methods. The cross-coupling effect between d - and q -axes in MSRFs usually introduces a transient current into the other axis when one axis current changes if it is not compensated in the current regulator. The feedback decoupling PI calculates the cross-coupling voltage using the feedback current, while the feedforward one uses current reference, and the complex vector one uses the output of the integrator. There are also other kinds of advanced PI regulators, such as the fuzzy PI [LI12] and neural PI [XIA10], which exhibit advantageous robustness in the speed and current control.

To achieve a compromise between easy implementation and good performance, the complex vector decoupling PI regulator is employed here due to its simple structure and good dynamic current response, as seen in Fig. 4.6. The machine parameters are utilized as the PI coefficients. The integral coefficient R_h is from the stator resistance and satisfies $R_h=R_s$. The proportional coefficient L_h is from the inductance. $L_h=L_s$ when $h=1, 11$, and 13 , while $L_h=L_\sigma$ when $h=5$ and 7 because the 5th and 7th harmonics are relevant to the leakage inductance. K_{ch} represents the bandwidth of the current loop. It should be noted that in the previous MSRF method which uses LPFs to decompose the current harmonics, due to the different delay effect caused by LPFs in different current loops, the bandwidth K_{ch} is considerably limited and should be tuned individually. Since the LPFs are not required here, the dynamic response and system stability can be enhanced. Moreover, the fundamental and harmonic current loops can share the same bandwidth K_{ch} , which provides convenience for control parameter tuning.

Furthermore, more phase shifting degrees means more required storage, particularly for the introduced virtual PTP system which needs more CPU resource in implementation. Therefore, a simplified implementation method can be employed. The PTP-based decomposition of the major current harmonics (4-4) can be substituted by a simple and lower-order combination of TTP- and QTP-based decomposition. Firstly, the fundamental, 5th, and 7th current harmonics can be extracted by (4-3), and then the 11th and 13th can be calculated by the decomposed results of the virtual TTP system, subtracting the separated 5th and 7th current harmonics as

follows.

$$\begin{bmatrix} 0 \\ i_{\alpha\beta 11} \\ i_{\alpha\beta 13} \end{bmatrix} = T_3 \begin{bmatrix} i_{A1B1C1}^3 \\ i_{A2B2C2}^3 \\ i_{A3B3C3}^3 \end{bmatrix} - \begin{bmatrix} i_{\alpha\beta 1} \\ i_{\alpha\beta 7} \\ i_{\alpha\beta 5} \end{bmatrix} \quad (4-4)$$

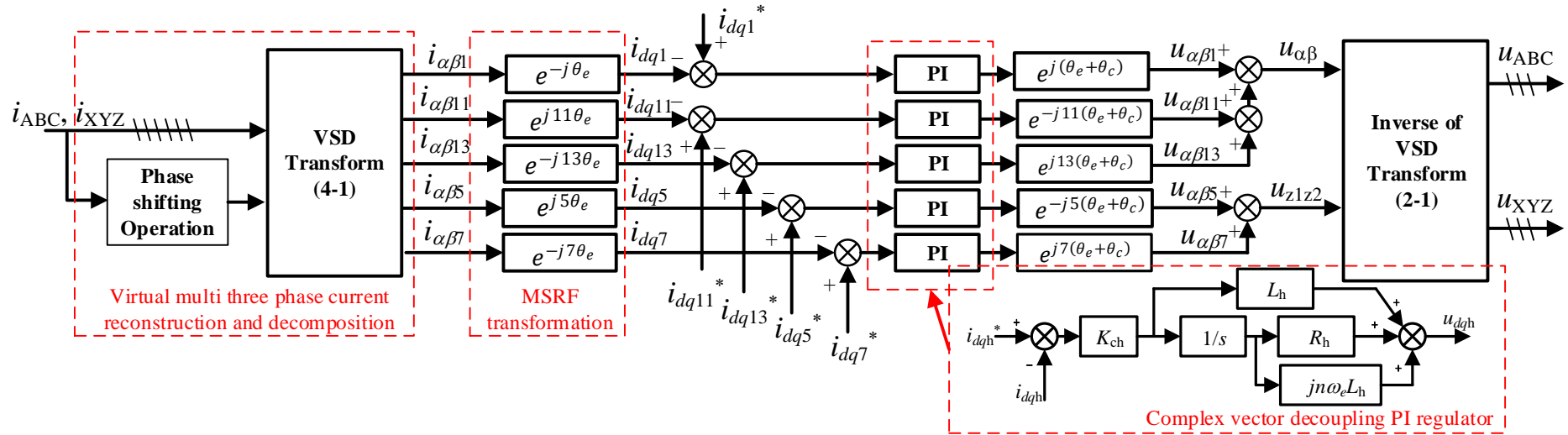


Fig. 4.6. Overall control diagrams of proposed current harmonic regulation.

4.4 Simulation Results

To verify the correctness of the current decomposition using virtual multi three-phase systems, simulation results are given in this section. Fig. 4.7 shows the simulation results of current decomposition using VSD technique in the original DTP system. The fundamental frequency of phase current is 10Hz, and thus the frequencies of the major current harmonics are 50Hz, 70Hz, 110Hz, and 130Hz, respectively. The original physical dual three-phase currents are shown in Fig. 4.7, and using the VSD transformation, the currents can be decomposed into two subspaces, i.e. $\alpha\beta$ and z_1z_2 subspaces. From the spectra of the decomposed currents, it is clear to see that the 1st, 11th, and 13th current harmonics are mapped into $\alpha\beta$ subspace, and the 5th and 7th ones are mapped into z_1z_2 subspace. This result is consistent with the harmonic mapping introduced in Fig. 4.1.

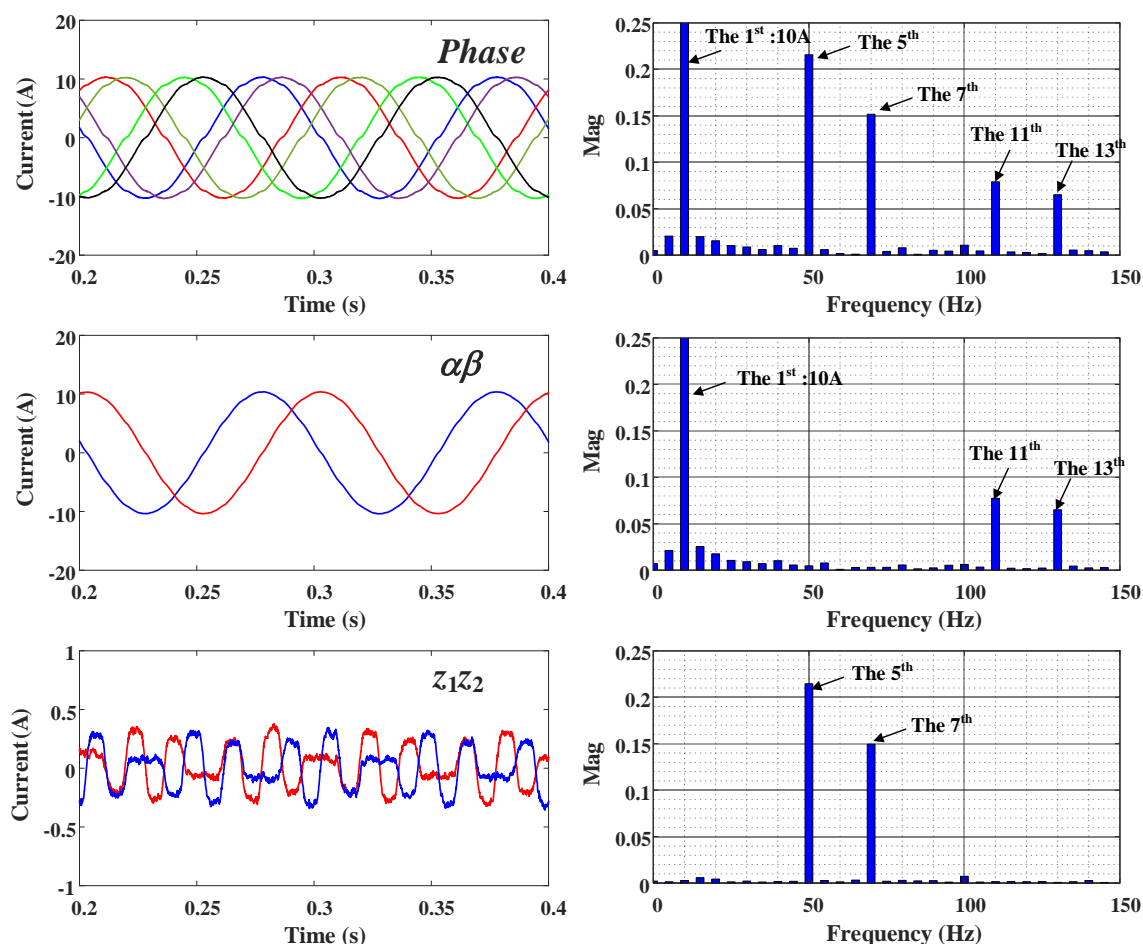


Fig. 4.7. Simulation results of current decomposition using VSD technique in DTP system.

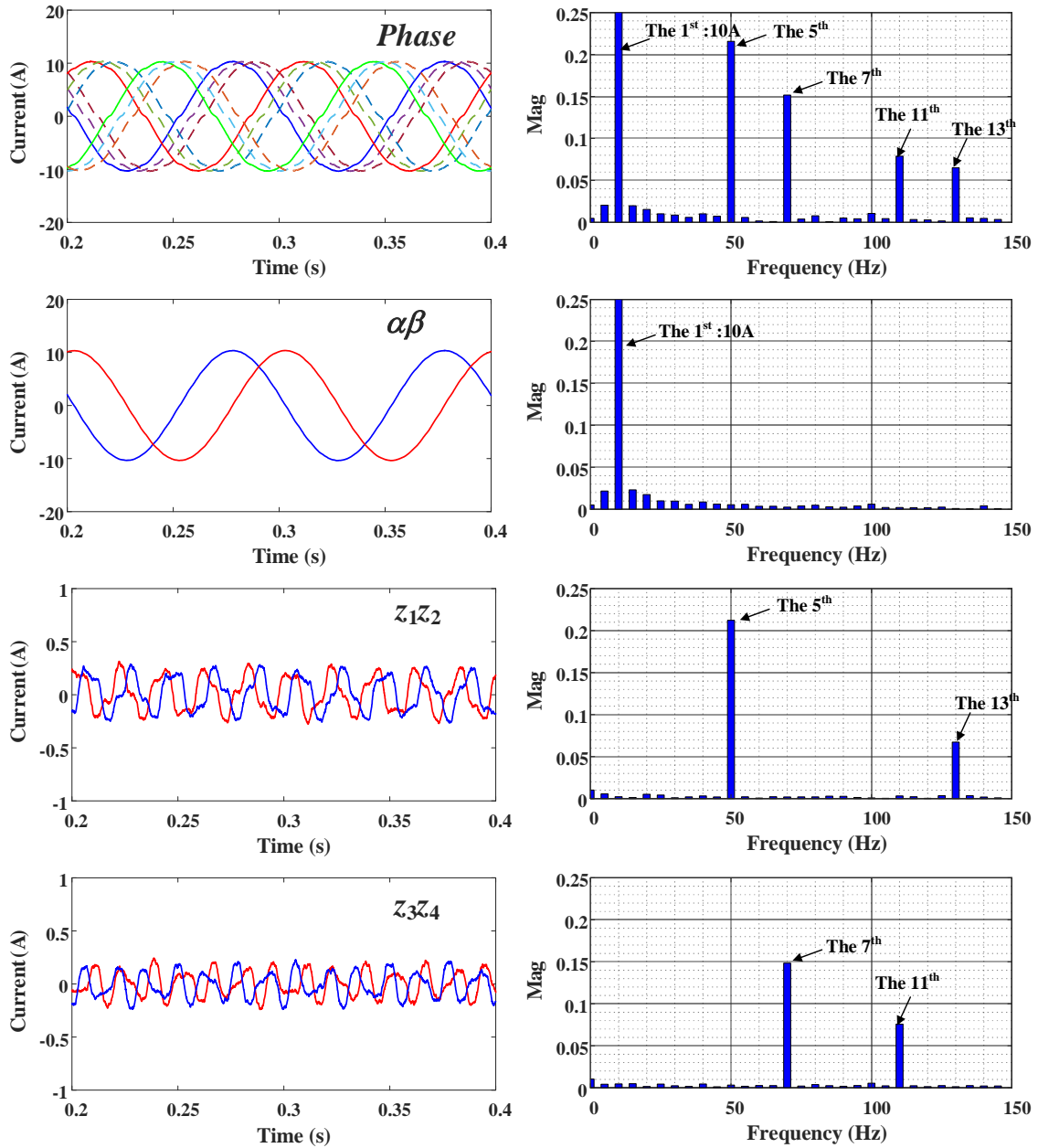


Fig. 4.8. Simulation results of current decomposition using VSD technique in virtual TTP system.

To establish a virtual triple three-phase system, the phase shifting operation in Fig. 4.5(a) is used. In Fig. 4.8, the virtual currents are plotted in dotted line and the phase shifting angle between currents from two adjacent three-phase sets is 20 degrees. Using the VSD transformation (4-1), the physical and virtual currents can be decomposed into $\alpha\beta$, z_1z_2 , and z_3z_4 subspaces. Different from the DTP case, the 1st current is individually decomposed into $\alpha\beta$ subspace, the 5th and 13th current harmonics are decomposed together into z_1z_2 subspace, and the 7th and 11th current harmonics are decomposed together into z_3z_4 subspace, in this

virtual TTP case. These simulation results are consistent with Fig. 4.2.

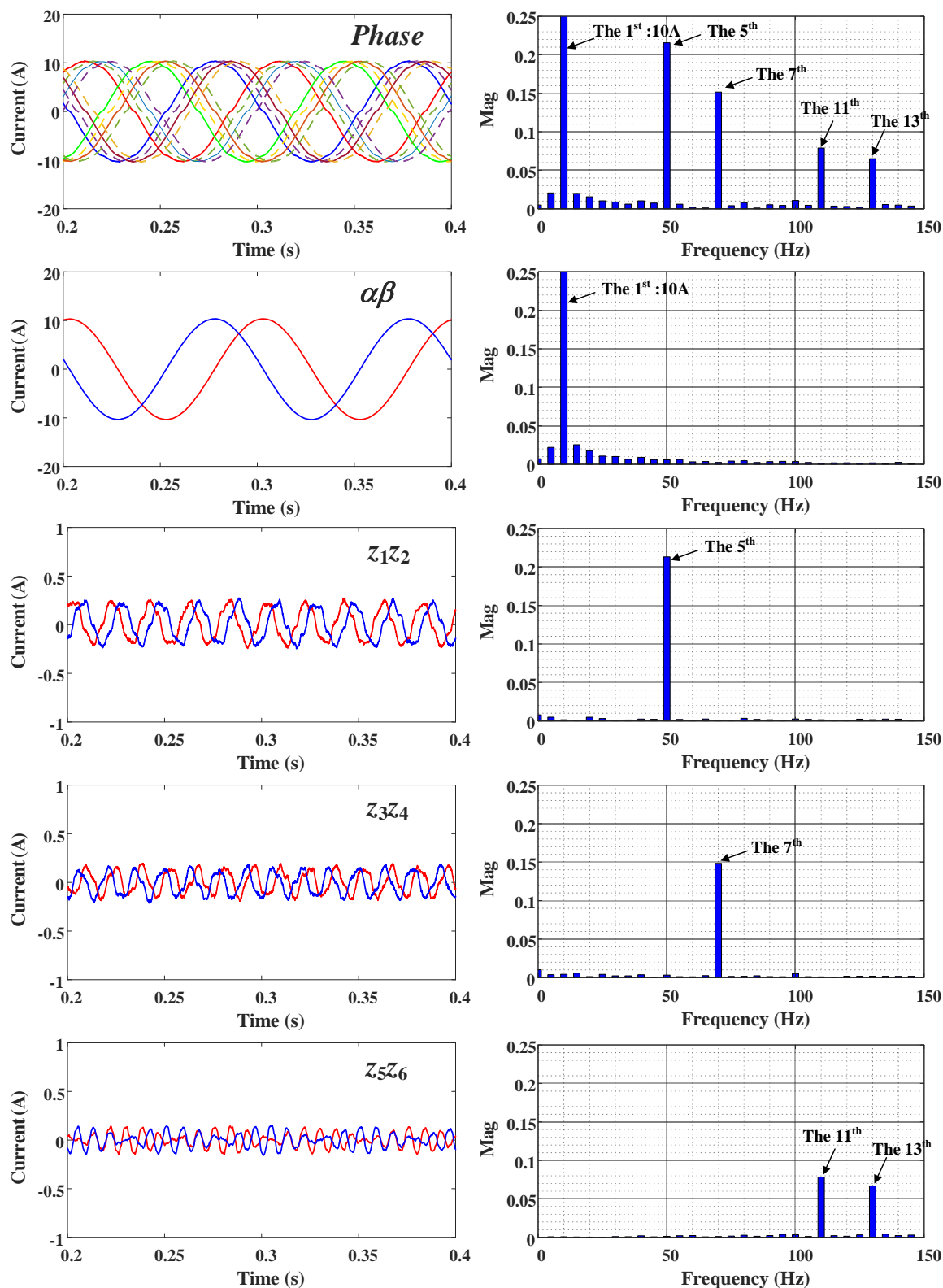


Fig. 4.9. Simulation results of current decomposition using VSD technique in virtual QTP system.

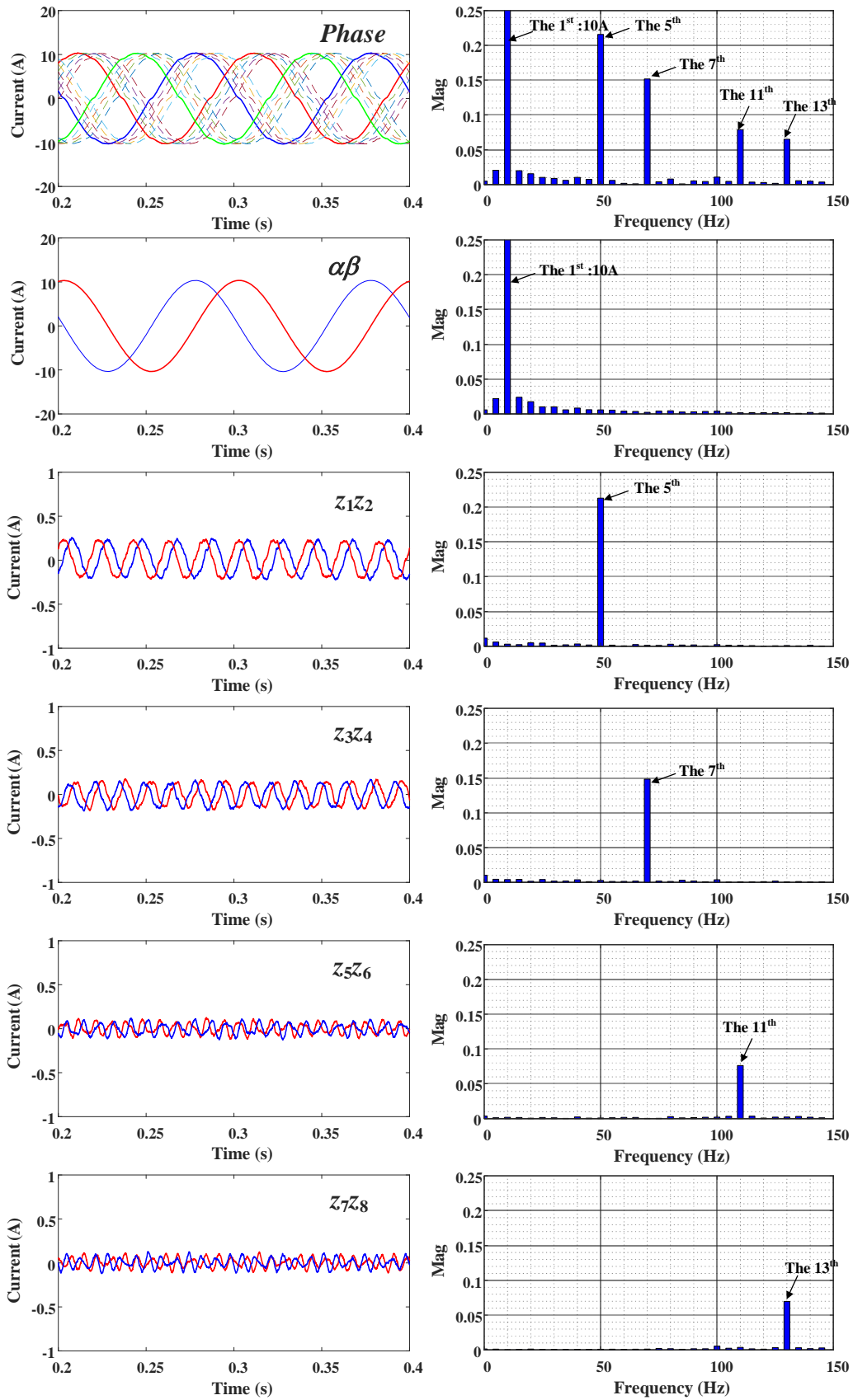


Fig. 4.10. Simulation results of current decomposition using VSD technique in virtual PTP system.

Fig. 4.9 shows the simulation results in virtual QTP system. The virtual currents are shifted by 15 degrees to the original physical currents. After the decomposition, the 1st current is individually mapped into $\alpha\beta$ subspace, and the 5th and 7th are individually mapped into z_1z_2 and z_3z_4 subspaces, respectively. The 11th and 13th current harmonics are decomposed together into z_5z_6 subspace. These results agree with Fig. 4.3.

Fig. 4.10 shows the simulation results in virtual PTP system, and the phase shift angle between the virtual currents of two adjacent virtual three-phase sets is 12 degrees. From the decomposition results, it is clear to see that the 1st current and all the major current harmonics are completely separated into 5 different subspaces, which is consistent with Fig. 4.4. If the major harmonics are completely separated, it is convenient for current harmonic control because the filters can be cancelled from the control loops and the dynamic performance as well as the system stability can be greatly enhanced.

It can be concluded that the simulation results in Figs. 4.7, 4.8, 4.9, and 4.10 are consistent with Figs. 4.1, 4.2, 4.3, and 4.4. This means the established virtual multi three-phase systems have the same current harmonic characteristic as the physical multi three-phase system, and the VSD transformation used in the physical multi three-phase system can be also utilized in the proposed virtual multi three-phase system to decompose the current harmonics, which provides better control performance compared to the conventional VSD technique in physical DTP system.

4.5 Experimental Verification

Fig. 4.11 shows the current decomposition performance when the machine speed is 200r/min. It is clear that the original physical phase currents are distorted and include serious major harmonics, Fig. 4.11(a). The waveforms of the decomposed major current harmonics are shown in Figs. 4.11(b)-(e), whereas they are not completely sinusoidal because there are still a few high order (higher than 13th) current harmonics mixing with the major current harmonics. However, these high order current harmonics can be neglected due to their low amplitudes and insignificant influence on control performance. The spectra show that the major current harmonics are completely separated from each other. The effectiveness of the proposed virtual multi three-phase systems and current harmonic decomposition is verified.

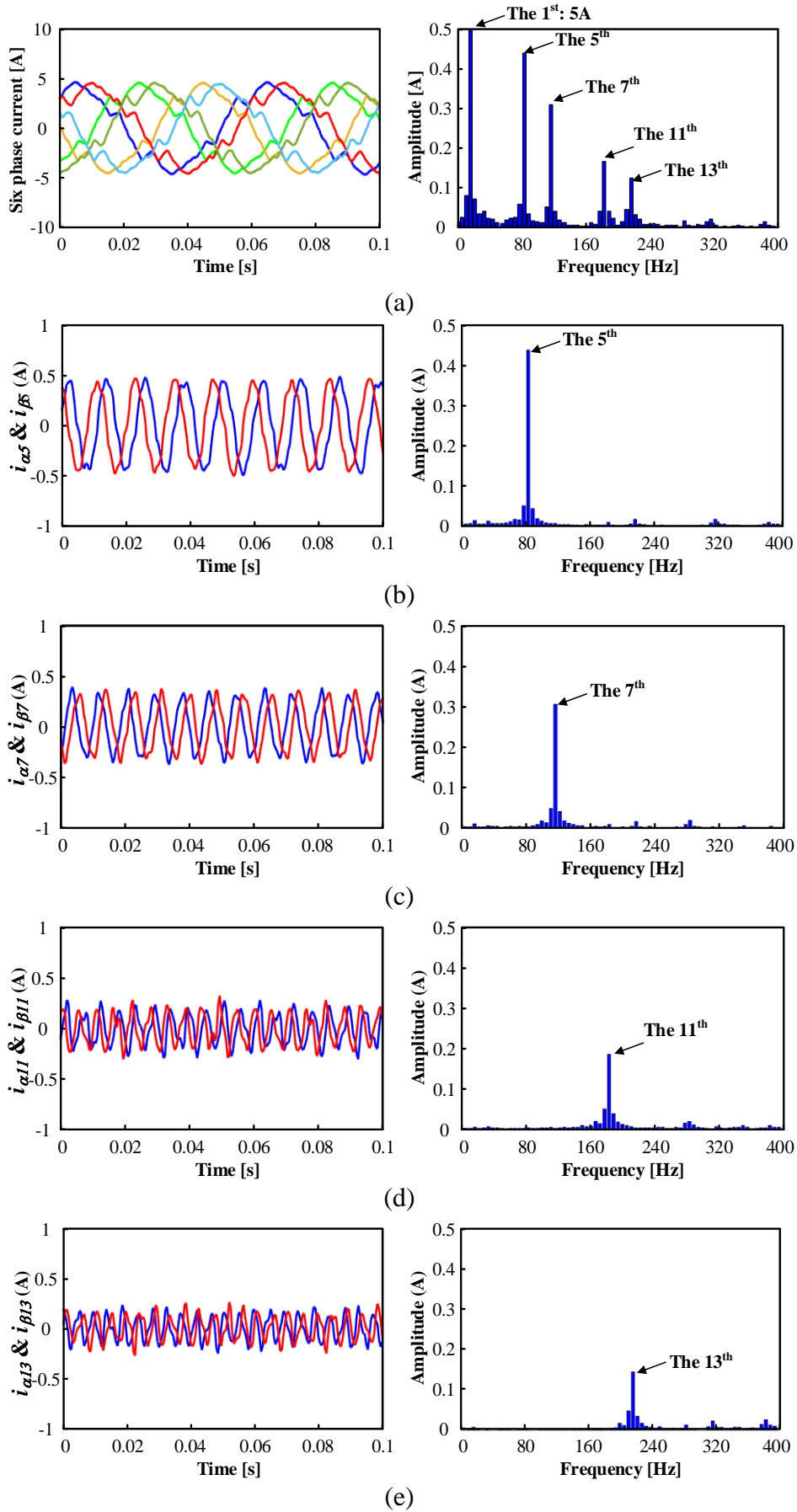


Fig. 4.11. Decomposition results of fundamental and major current harmonics. (a) Original

physical six phase current waveforms and spectra. (b)-(e) The decomposed 5th, 7th, 11th, and 13th current harmonics, and the corresponding spectra.

Fig. 4.12 shows the experimental results of selective current harmonic suppression at 200r/min and rated load torque. The major current harmonic suppressions are successively activated at 0.2s, 0.4s, 0.6s, and 0.8s to illustrate the individual control capability of different current harmonics. It can be clearly seen from the waveform variations of phase A current in different periods, after one suppression works, the selected current harmonic is wiped out in phase current without interference to the other current harmonics. The individual regulations of the major current harmonics are achieved in the proposed method.

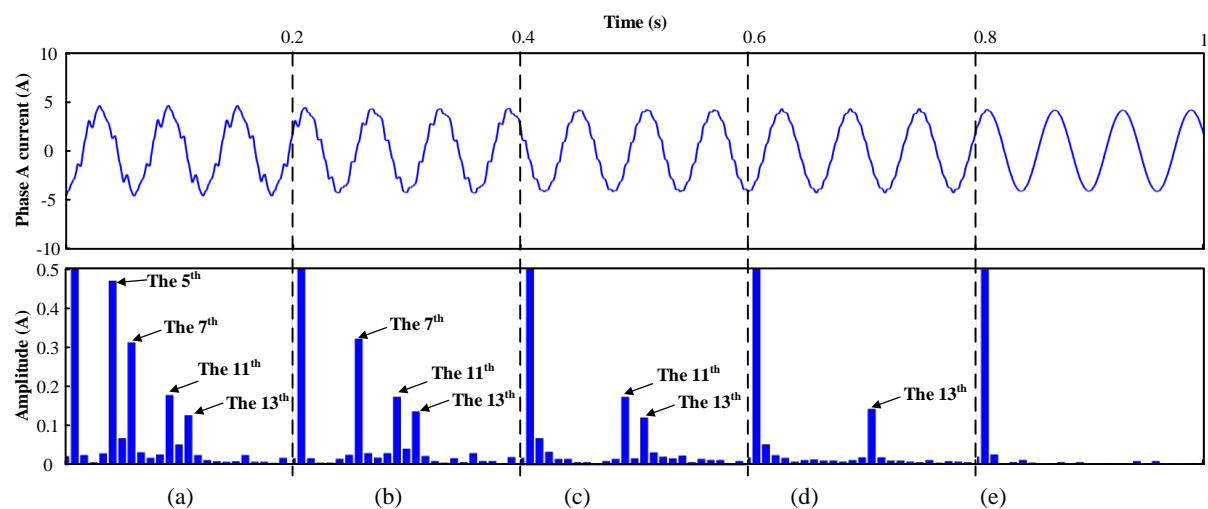


Fig. 4.12. Experimental results of successive individual harmonic suppression. The amplitude of the fundamental current is 5A. (a) Without current harmonic suppression. (b) Only with the 5th harmonic suppression. (c) With both the 5th and 7th harmonic suppression. (d) With the 5th, 7th, and 11th harmonic suppression. (e) With all major harmonic suppression

Fig. 4.13 shows the experimental results at 200r/min when load torque steps from 50% to 100% of the rated torque. Before the torque step, the phase current is sinusoidal because the current harmonics in MSRFs are well suppressed. The torque step will cause sudden variation of phase current amplitude, and further lead to inaccurate phase shifting operation during the dynamics. Disturbances are therefore introduced into the decomposed current harmonics, especially in the 11th and 13th current harmonics as shown in Fig. 4.13. However, the disturbances disappear in a short time, and the current harmonics can be still suppressed after the torque step. The results show that the performance of the proposed method is slightly influenced by the transient load torque variation.

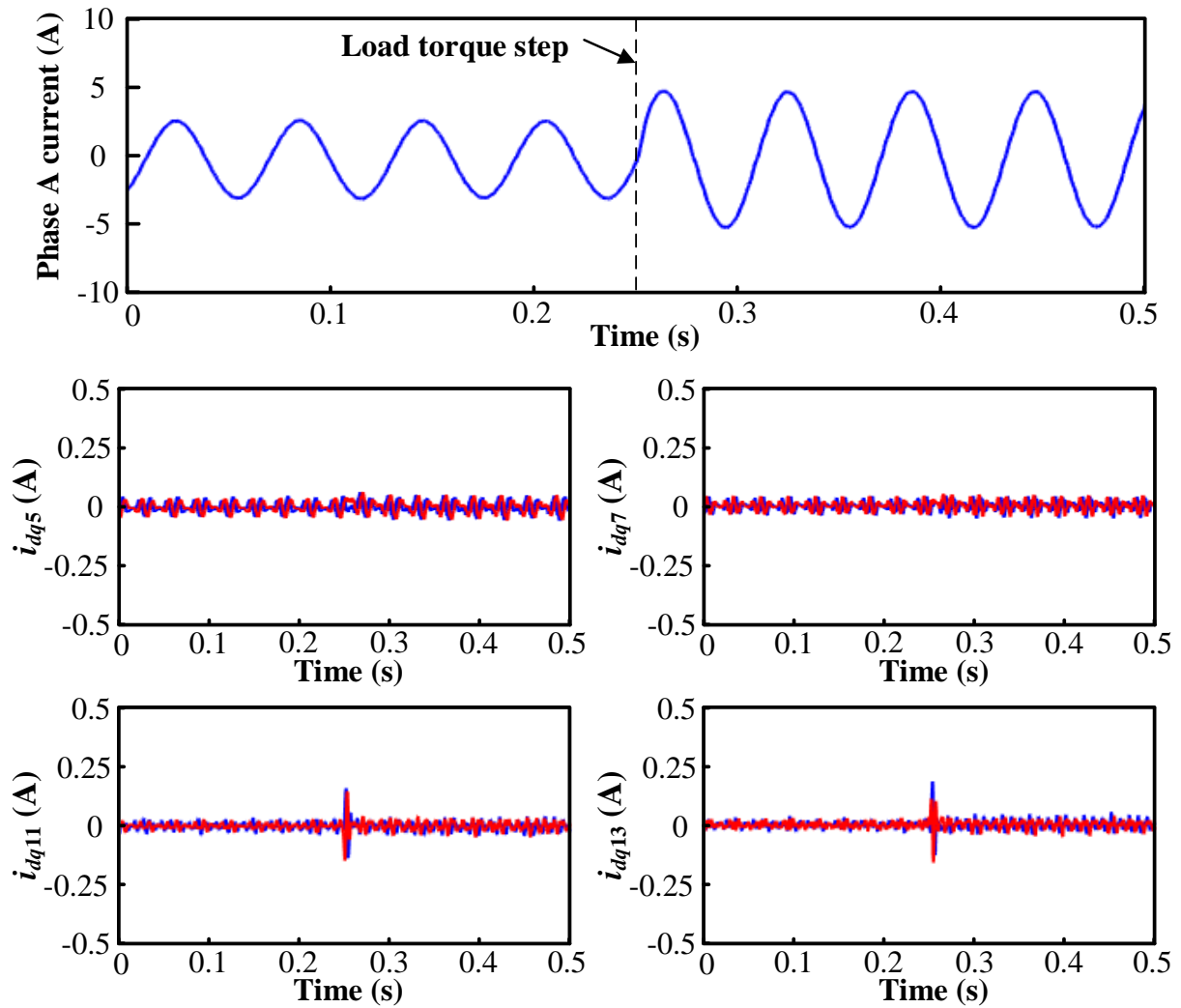


Fig. 4.13. Measured phase A current and the major current harmonics in MSRFs when at 200r/min, load torque steps from 50% to 100% of rated torque at 0.25s.

To evaluate the dynamic performance, the step response of the proposed methods are presented in Fig. 4.14. The current harmonic references i_{q5}^* , i_{q7}^* , i_{q11}^* , and i_{q13}^* step from 0A to 0.5A at 1s. The proposed method shows better dynamic current harmonic response and can better track the references without obvious overshoot and pulsating currents, compared to the method proposed in Chapter 3. To be precise, in the proposed method, the current harmonics can track the references within 40ms after the references stepped according to the detailed dynamic responses in Fig. 4.14(b). The proposed method does not use LPFs as the previous method does, and as aforementioned, the high order (higher than 13) current harmonics make the decomposed current harmonics in Fig. 4.14(a) exhibit more high-frequency ripples, which can be negligible for their low amplitudes and insignificant influence on control performance.

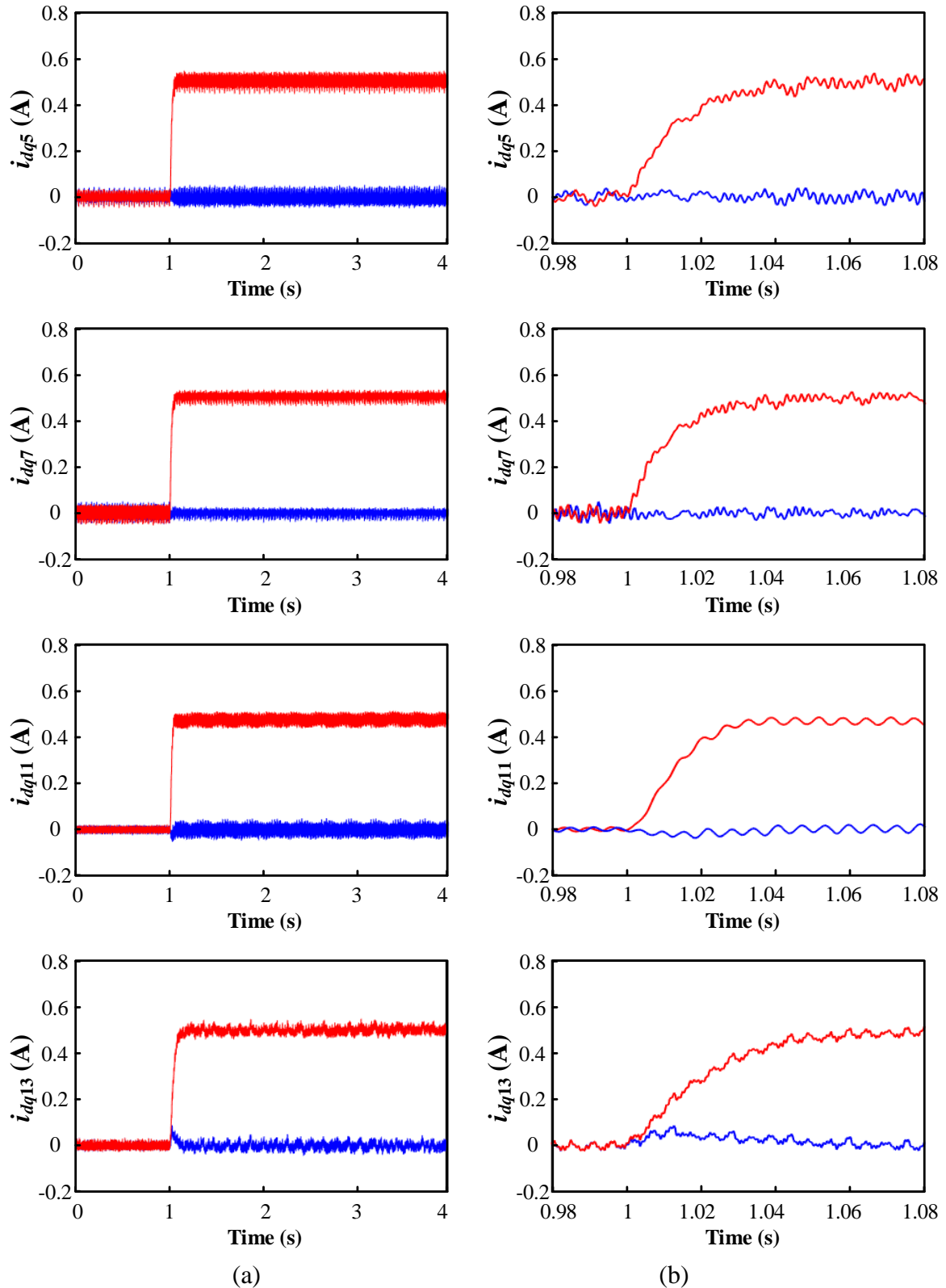


Fig. 4.14. Experimental results of dynamic current harmonic regulation. References of major current harmonics i_{q5}^* , i_{q7}^* , i_{q11}^* , and i_{q13}^* step from 0A to 0.5A, respectively. References i_{d5}^* , i_{d7}^* , i_{d11}^* , and i_{d13}^* remain 0A, and machine speed is 200r/min. (a) Step response. (b) Detailed dynamic responses of the proposed method during 0.98s to 1.08s in (a).

4.6 Discussion

The simulation and experimental results have validated the effectiveness of the proposed current harmonic suppression strategy in a DTP PMSM system. Because there are various operation conditions and control objectives for this kind of machine, the applicability and extension of the proposed method are discussed in this section.

4.6.1 Torque Performance Improvement

For the major current harmonics of DTP PMSM, the 5th and 7th current harmonics can be injected to increase the average torque [HU17]. The suppression of the 11th and 13th current harmonics can generally contribute to the reduction of the 12th torque ripple. However, when there is an inherent 12th torque ripple generated by non-sinusoidal flux field, the 11th and 13th current harmonics still need to be injected to minimize the total torque ripples [YAN19].

Fortunately, the proposed current harmonic regulator can also be employed in the current harmonic injection by simply changing the current harmonic references to the required values. Besides, in the authors' opinion, the enhanced dynamic performance of the proposed strategy is important to the current harmonic injection, because the current harmonic references should be dynamically adjusted to satisfy different operating conditions (torque and speed), and the better reference tracking capability will obviously benefit the dynamic performance of the current harmonic injection.

4.6.2 Flux Weakening Operation

Flux weakening is usually necessary in the applications that require a wide speed range. It is easy for the proposed method to achieve flux weakening control by using the fundamental current loop to track the negative $d1$ -axis current. The current harmonic suppression in the flux weakening region faces the challenge of limited inverter voltage. It is known that the flux weakening is utilized to make sure the voltage reference is inside the linear modulation region. If the used fundamental voltage of a three-phase set reaches the maximum voltage circle, the harmonic voltage references will be outside the voltage hexagon and cannot be realized. There are two solutions to solve this issue. The first, which introduces additional copper loss, is to increase the amplitude of the negative $d1$ -axis current and further reduce the amplitude of fundamental voltage, and then the harmonic voltage references can be relocated inside the hexagon and realized. The second solution, as studied in [KAR17], is still in the category of

optimizing the current harmonic references. Making use of the modulation area between the maximum voltage circle and voltage hexagon, the current harmonics can be partially suppressed, however, not eliminated.

4.6.3 Unbalance Issue

The unbalance currents, due to asymmetry among phases, can be negligible compared with the major current harmonics if the machine is well designed and manufactured, but they should be taken into account when the asymmetry is considerable. The unbalance currents are composed of positive and negative sequence currents [HU14]. Under the framework of the virtual multi three-phase system, the unbalance currents cannot be separated from the phase currents like the major current harmonics, and they will be mapped as AC components in the MSRFs. Although the effect of the DC component regulation, i.e., suppression of the major current harmonics, is not influenced by these AC components, the PI regulator cannot eliminate these AC components due to the limited control capability. That means the unbalance currents still exist in the system, and the control scheme may need modification if containing these unbalanced currents is necessary.

4.6.4 Extension to Other Multi Three-phase Machine

Although the method is proposed and implemented in a physical DTP PMSM, the concept of the virtual multi three-phase system is generic and can be extended to both induction and reluctance machines with DTP winding sets. In addition, regarding physical machines with more than DTP sets, e.g. the TTP and QTP machines, the concept is still applicable. For a physical TTP machine, the harmonic mapping is shown in Fig. 4.2, and the sum of the 5th and 13th current harmonics is decomposed as $i_{z_1z_2}$, and the sum of the 7th and 11th ones is decomposed as $i_{z_3z_4}$. To totally separate the current harmonics in z_1z_2 and z_3z_4 subspaces, a virtual QTP system can be established based on the currents of the physical TTP machine, as shown in Fig. 4.15. Then, the 5th and 7th current harmonics can be decomposed using (4-3), and the 13th and 11th current harmonics can be detected by subtracting the 5th and 7th ones from $i_{z_1z_2}$ and $i_{z_3z_4}$, respectively.

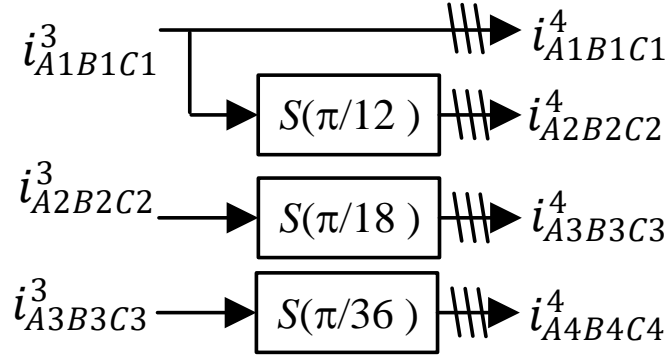


Fig. 4.15. Virtual QTP current reconstruction using physical TTP currents.

4.7 Conclusion

This chapter proposes a concept to convert a physical dual three-phase PMSM system into a virtual multi three-phase system with more three-phase sets, based on which the fundamental and major current harmonics can be decomposed in several isolated subspaces and independently regulated in MSRFs.

The proposed current harmonic suppression has the following advantages:

- 1) Due to the separation of the fundamental and major current harmonics, the currents of different frequencies are independent, the problem of interference between different frequencies is avoided, and consequently the system stability is enhanced.
- 2) The proposed method does not use any LPF as the previous method does, which greatly enhances the dynamic performance and stability of the current loops. In addition, the parameter tuning of the fundamental and current harmonic regulators is simplified.
- 3) All the VSD transformation matrices employed in this chapter are constant-element matrices and can be pre-stored in the controller. Therefore, the computation burden does not significantly increase compared with that of the existing method.

The proposed concept can be extended to suppress any order of current harmonics including the ones higher than the 13th, and the current harmonic can be flexibly selected to be detected and suppressed according to the requirements in real applications. The proposed independent current regulators can also be used in current harmonic injection by simply changing the current harmonic references to achieve the pre-design non-sinusoidal phase currents. Furthermore, the concept of the virtual multi three-phase system together with the MSRFs can be extended to

other multi three-phase machine systems, as well as the current regulation in industrial applications that may suffer from harmonic issues.

CHAPTER 5

CURRENT MEASUREMENT GAIN COMPENSATION USING HIGH-FREQUENCY SIGNAL INJECTION IN DUAL THREE-PHASE PMSM SYSTEMS

The previous chapters have investigated the solutions for current harmonic suppression in DTP PMSM systems. These solutions can only deal with the conventional current harmonics that are caused by the inverter nonlinearity and non-sinusoidal back-EMFs. The scaling errors in the current measurement will also generate current harmonics that the investigated solutions in the previous chapters cannot deal with. Therefore, this chapter proposes an effective method to compensate the current measurement gain and correct the scaling errors, and thus suppress the related current harmonics and torque ripples.

Compared to the existing literature [HAR08][TRI18], the effect of scaling errors in the current measurement is firstly analyzed under the framework of VSD modelling and control. The analysis shows that the scaling errors can generate the 2nd-order current harmonics in synchronous reference frame, which makes the six phase currents unbalanced and generates the 2nd-order torque ripple. To suppress the negative effect, a method based on high-frequency signal injection is investigated to tune the current measurement gain coefficients. A high-frequency carrier voltage is injected to the z_{1z2} subspace of the DTP PMSM, and the resultant high-frequency components in the measured currents are extracted and used to control the current measurement gain and correct the scaling errors. The correctness of the analysis and the effectiveness of the proposed high-frequency signal injection based method are validated by simulation results.

5.1 Introduction

Stator current measurement is required for most high-performance electrical drive since the measured current can be used for torque regulation, fault detection, and protection. The accuracy of the current measurement directly determines the performance of the system. The current measurement errors can be categorized into two groups.

- 1) Scaling error, i.e. the current measurement gain is not equivalent to 1, which causes the amplitudes of the measured current and the real current are not equal. The scaling errors will cause obvious unbalanced phase currents, i.e. the negative-sequence fundamental component, of electrical machines. The negative-sequence fundamental component is converted to the 2nd-order current harmonic in synchronous reference frame. This current harmonic has adverse effect if it is used for torque control or flux linkage estimation, e.g. torque ripple, reduced/increased average torque, increased losses, and estimation errors.
- 2) DC offset, i.e. the mean values of the measured current and the real current are not equal. The DC offset can generate DC components in the phase currents of electrical machines. The DC current can be converted as the 1st current harmonic in synchronous reference frame. Like the scaling errors, the adverse effect can also be the torque ripple, reduced/increased average torque, increased losses, and estimation errors.

The previous chapters aim to solve the general current harmonics in DTP PMSM systems, while this chapter will investigate the solutions for the current harmonics due to current measurement errors, specially focusing on the scaling errors correction.

The current in an electrical machine system is measured by current sensor circuit which usually includes current transformer, amplifying circuit, low pass filtering circuit, analog-to-digital (A/D) converter, and the related calculation in digital signal processors. The gains of these different components can vary with respect to their designed values due to various factors, which result in the scaling error. Manual calibration through hardware or software gain adjustment is the most usual method to correct the scaling error. However, it has obvious issues including: increased time cost, reduced operation time, and the most important is that the correction effect is not continuous because the gains of these circuits are variable with temperature, aging, and noise.

To correct the scaling errors in electrical machine systems, many researchers have investigated

solutions to online correct the current measurement gain. The online correction methods are superior to the manual calibration because the operation of electrical machines does not need to be interrupted and the correction effect is continuous regardless of the variations of temperature, aging, and noise. These online correction methods can be divided into two aspects: those that directly address the current measurement gains and those that compensate the effect of the scaling errors. In terms of the directly correcting the current measurement gains, [LU21] proposed a novel topology of current sensor circuit combined with special design of current measurement moments, and the current measurement gain can be tuned and corrected in one PWM cycle. A measurement-disturbance-observer (MDO) is proposed in [CHO08] to estimate and correct the scaling errors of two phase current measurement, but the accurate machine model and parameters are required in MDO. [HAR08] proposed a novel current measurement gain tuning method using high-frequency signal injection. The injected high-frequency carrier voltage will generate high-frequency current. However, due to the scaling errors, the measured current will include negative-sequence high-frequency current that can be used to tune the current measurement gain. If the negative-sequence high-frequency current is suppressed, the scaling errors are considered as corrected. Since the high frequency current is generated, this method suffers from the issues of increased losses, torque ripples, and acoustic noise. [HAR08] only used the high frequency injection to correct scaling errors in general three phase machines, however not in DTP machines. The second aspect is to compensate the effect of the scaling error, e.g. current harmonic, speed ripple, and torque ripple. [TRI18] proposed a controller which combines the repetitive regulator and proportional resonant regulator to suppress the current harmonic generated by the scaling error, while the controller is too complicated to be practical in a real system, and the test results also show a moderate dynamic response. Since the current harmonic due to the scaling error will cause torque ripple and speed ripple, [XIA15] employs multi resonant regulator to build the speed regulator to suppress the speed ripple and thus compensate the effect of the scaling error. Nevertheless, this method is merely applicable in low speed condition or small inertia motor applications, because the amplitude of the speed ripple decreases as speed increases or rotor inertia increases, and compensation performance of this method will deteriorate if the speed ripple is too small to be detected by the rotor position sensor.

The existing methods above are applied in three-phase systems, and they can be simply extended to each three-phase set of a DTP PMSM. However, the unbalanced current between two three-phase sets cannot be solved by these methods, and more importantly, the freedom

degrees of the DTP system cannot be fully utilized. To the best knowledge of the author, there is no existing literature discussing the compensation method that is specially designed for current measurement gains in DTP PMSM systems. To make full use of the freedom degrees and investigate an advantageous technology for DTP PMSM systems, this chapter proposes a high-frequency signal injection based method to tune the current measurement gains and correct the scaling errors. Section 5.2 firstly analyzes the effect of the scaling errors in the current measurement under the framework of VSD modelling and control. Some simulation results are given in this section to show the effect of the scaling errors in a DTP PMSM system and prove the correctness of the analysis. Section 5.3 introduces the proposed method. A high-frequency carrier voltage is injected in the z_1z_2 subspace of the DTP PMSM. Since the generated high-frequency currents are also in the z_1z_2 subspace, they will not generate high-frequency torque ripples, from which the three-phase PMSM systems suffer a lot when using the high-frequency signal injection. The relationship between the scaling errors and the high-frequency components in the measured currents is derived in this section. Based on the derived relationship, the high-frequency current components are extracted to control the current measurement gains and correct the scaling errors. Compared to the existing methods, the investigated method does not require the parameters of the DTP PMSM or specially design of the current measurement circuit. The tuning of the current measurement gains is based on the control of the high-frequency currents, which means it is independent from the torque and speed regulation, and thus the compensation effect is not affected by the speed and torque conditions. The effectiveness of the proposed method is validated by the simulation results in Section 5.4, and the conclusion of this chapter is given in Section 5.5.

5.2 Effect of Scaling Error

To reduce the cost, not all the phase currents are measured by current sensors and only two current sensors are used for the current measuring in each three-phase set of a DTP PMSM, e.g. currents of phase A, phase B, phase X, and phase Y are measured, and the currents of the phases C and Z are calculated based on Kirchhoff Current Laws. If considering the scaling error, the measured currents of six phases can be expressed as

$$\begin{bmatrix} i_{am} \\ i_{bm} \\ i_{cm} \\ i_{xm} \\ i_{ym} \\ i_{zm} \end{bmatrix} = \begin{bmatrix} i_a \\ i_b \\ -i_a - i_b \\ i_x \\ i_y \\ -i_x - i_y \end{bmatrix} + \begin{bmatrix} K_a i_a \\ K_b i_b \\ -K_a i_a - K_b i_b \\ K_x i_x \\ K_y i_y \\ -K_x i_x - K_y i_y \end{bmatrix} \quad (5-1)$$

where $[i_{am} \ i_{bm} \ i_{cm} \ i_{xm} \ i_{ym} \ i_{zm}]^T$ represent the measured six phase currents, $[i_a \ i_b \ i_c \ i_x \ i_y \ i_z]^T$ represent the real six phase currents, and $[K_a i_a \ K_b i_b \ -K_a i_a - K_b i_b \ K_x i_x \ K_y i_y \ -K_x i_x - K_y i_y]^T$ represent the current measurement errors due to scaling errors. To analyse the effect of the scaling error, the primary real six phase currents can be expressed as follows if there is no scaling error

$$\begin{bmatrix} i_a \\ i_b \\ i_c \\ i_x \\ i_y \\ i_z \end{bmatrix} = \begin{bmatrix} I \cos \theta_1 \\ I \cos \left(\theta_1 - \frac{2\pi}{3} \right) \\ I \cos \left(\theta_1 + \frac{2\pi}{3} \right) \\ I \cos \left(\theta_1 - \frac{\pi}{6} \right) \\ I \cos \left(\theta_1 - \frac{5\pi}{6} \right) \\ I \cos \left(\theta_1 + \frac{\pi}{2} \right) \end{bmatrix} \quad (5-2)$$

where I represents the amplitude of fundamental current. θ_1 represent the phase angle of phase currents, and it satisfies $\theta_1 = \theta_e + \theta_0$. θ_e is the electrical angle of rotor position. θ_0 is the initial phase angle of current. Substituting (5-2) into (5-1) and using the following VSD transformation to convert the measured current into $\alpha\beta$ and z_1z_2 subspaces:

$$\begin{bmatrix} i_{\alpha m} \\ i_{\beta m} \\ i_{z1m} \\ i_{z2m} \end{bmatrix} = \frac{1}{3} \begin{bmatrix} 1 & -\frac{1}{2} & -\frac{1}{2} & \frac{\sqrt{3}}{2} & -\frac{\sqrt{3}}{2} & 0 \\ 0 & \frac{\sqrt{3}}{2} & -\frac{\sqrt{3}}{2} & \frac{1}{2} & \frac{1}{2} & -1 \\ 1 & -\frac{1}{2} & -\frac{1}{2} & -\frac{\sqrt{3}}{2} & \frac{\sqrt{3}}{2} & 0 \\ 0 & \frac{\sqrt{3}}{2} & -\frac{\sqrt{3}}{2} & -\frac{1}{2} & -\frac{1}{2} & 1 \end{bmatrix} \begin{bmatrix} i_{am} \\ i_{bm} \\ i_{cm} \\ i_{xm} \\ i_{ym} \\ i_{zm} \end{bmatrix} \quad (5-3)$$

The currents in $\alpha\beta$ and z_1z_2 subspaces can be regarded as two parts:

$$\begin{bmatrix} i_{\alpha m} \\ i_{\beta m} \\ i_{z1m} \\ i_{z2m} \end{bmatrix} = \begin{bmatrix} i_{\alpha} \\ i_{\beta} \\ i_{z1} \\ i_{z2} \end{bmatrix} + \begin{bmatrix} \Delta i_{\alpha} \\ \Delta i_{\beta} \\ \Delta i_{z1} \\ \Delta i_{z2} \end{bmatrix} \quad (5-4)$$

where $[i_{\alpha m} \ i_{\beta m} \ i_{z1m} \ i_{z2m}]^T$ represent the measured current in $\alpha\beta$ and $z1z2$ subspaces, $[i_{\alpha} \ i_{\beta} \ i_{z1} \ i_{z2}]^T$ represent the real current in $\alpha\beta$ and $z1z2$ subspaces. $[\Delta i_{\alpha} \ \Delta i_{\beta} \ \Delta i_{z1} \ \Delta i_{z2}]^T$ represent current measured errors due to the scaling errors, and it satisfies

$$\begin{bmatrix} \Delta i_{\alpha} \\ \Delta i_{\beta} \\ \Delta i_{z1} \\ \Delta i_{z2} \end{bmatrix} = \frac{I}{12} \begin{bmatrix} (6K_a + 3K_x + 3K_y)\cos\theta_1 + \sqrt{3}(K_x - K_y)\sin\theta_1 \\ (2\sqrt{3}(K_a - K_b) + 3\sqrt{3}(K_x - K_y))\cos\theta_1 + (6K_b + 3K_x + 3K_y)\sin\theta_1 \\ (6K_a - 3K_x - 3K_y)\cos\theta_1 - \sqrt{3}(K_x - K_y)\sin\theta_1 \\ (2\sqrt{3}(K_a - K_b) - 3\sqrt{3}(K_x - K_y))\cos\theta_1 + (6K_b - 3K_x - 3K_y)\sin\theta_1 \end{bmatrix} \quad (5-5)$$

From (5-5), it is clear that the scaling errors in current measurement generate errors with the same frequency as the fundamental current. However, it is obvious that the amplitudes of Δi_{α} and Δi_{β} are not equal, and the amplitudes of Δi_{z1} and Δi_{z2} are not equal either. This means the current measurement errors in both $\alpha\beta$ and $z1z2$ subspaces include the positive-sequence fundamental current and the negative-sequence fundamental current. Since the torque of a DTP PMSM is only related to the current in $\alpha\beta$ subspace, Δi_{α} and Δi_{β} are transformed to the synchronous reference frame as

$$\begin{bmatrix} \Delta i_d \\ \Delta i_q \end{bmatrix} = \frac{I}{18} \begin{bmatrix} 3(K_a - K_b)\cos(2\theta_e + \theta_0) + \sqrt{3}(K_a - K_b + 2(K_x - K_y))\sin(2\theta_e + \theta_0) \\ \sqrt{3}(K_a - K_b + 2(K_x - K_y))\cos(2\theta_e + \theta_0) - 3(K_a - K_b)\sin(2\theta_e + \theta_0) \end{bmatrix} + \frac{I}{18} \begin{bmatrix} 3(K_a + K_b + K_x + K_y)\cos\theta_0 - \sqrt{3}(K_a - K_b + K_x - K_y)\sin\theta_0 \\ 3(K_a + K_b + K_x + K_y)\sin\theta_0 + \sqrt{3}(K_a - K_b + K_x - K_y)\cos\theta_0 \end{bmatrix} \quad (5-6)$$

In synchronous reference frame, the current measurement error includes the DC component and the second-order harmonics. To further simplify the expression of the current measurement error in synchronous reference frame, the complex-vector format is used and (5-6) can be written in the complex-vector format as

$$\Delta i_{dq} = \frac{I}{6}(K_a - K_b)e^{-j(2\theta_e + \theta_0)} + \frac{\sqrt{3}I}{18}(K_a - K_b + 2(K_x - K_y))e^{-j(2\theta_e + \theta_0 - \frac{\pi}{2})} + \frac{I}{6}(K_a + K_b + K_x + K_y)e^{j\theta_0} + \frac{\sqrt{3}I}{18}(K_a - K_b + K_x - K_y)e^{j(\theta_0 + \frac{\pi}{2})} \quad (5-7)$$

where $\Delta i_{dq} = \Delta i_d + j\Delta i_q$. From (5-7), it is easy to know that the second-order harmonic in Δi_{dq}

is negative-sequence and represents the negative-sequence fundamental component in stationary $\alpha\beta$ frame, and the DC component in Δi_{dq} represents the positive-sequence fundamental component in stationary $\alpha\beta$ frame.

To address the effect of these current measurement errors, the simplified current control loop in dq -axes, Fig. 5.1, is used to analyze the control system. The loop is composed of three parts, i.e. the regulator, the delay, and the motor. Signal d represents the disturbance introduced in the control system, such as the voltage disturbance due to inverter nonlinearity and back-EMF due to PM flux linkage. Signal Δi_{dq} represents the current measurement error due to the scaling error. The transfer functions of the regulator, the delay, and the motor are [YAN21b]

$$\begin{aligned} \mathbf{G}_c(s) &= k_c \frac{R_s + L_s s + j\omega_e L_s}{s} e^{j\omega_e T_d} \\ \mathbf{G}_d(s) &= e^{-T_d s} \cdot e^{-j\omega_e T_d} \\ \mathbf{G}_p(s) &= \frac{1}{R_s + L_s s + j\omega_e L_s} \end{aligned} \quad (5-8)$$

The general current harmonics, e.g. the 5th and 7th, are usually generated by the disturbance d , while the current harmonics due to scaling errors are generated by the current measurement error Δi_{dq} . The effect of the current measurement error Δi_{dq} and disturbance d can be described by the transfer function from Δi_{dq} to i_{dq} and from d to i_{dq} , i.e.

$$\begin{aligned} \frac{I_{dq}(s)}{\Delta I_{dq}(s)} &= -\frac{\mathbf{G}_c(s)\mathbf{G}_d(s)\mathbf{G}_p(s)}{1 + \mathbf{G}_c(s)\mathbf{G}_d(s)\mathbf{G}_p(s)} = -\frac{k_c e^{-T_d s}}{s + k_c e^{-T_d s}} \\ \frac{I_{dq}(s)}{D(s)} &= \frac{\mathbf{G}_p(s)}{1 + \mathbf{G}_c(s)\mathbf{G}_d(s)\mathbf{G}_p(s)} = \frac{s}{(s + k_c e^{-T_d s})(R_s + L_s s + j\omega_e L_s)} \end{aligned} \quad (5-9)$$

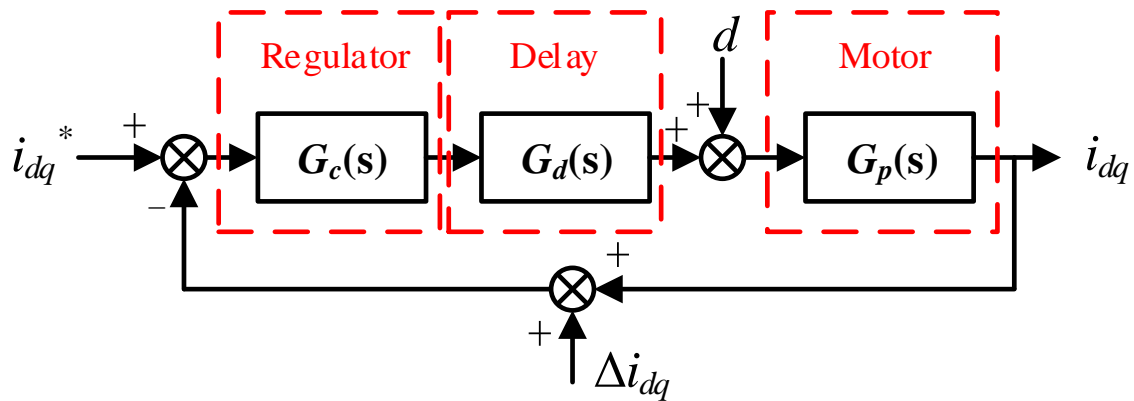
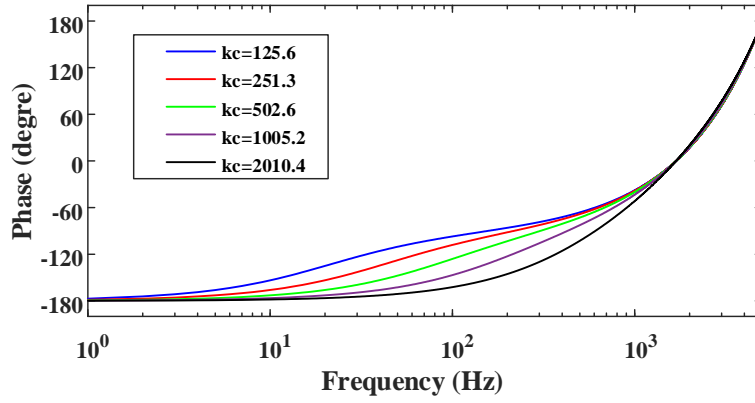
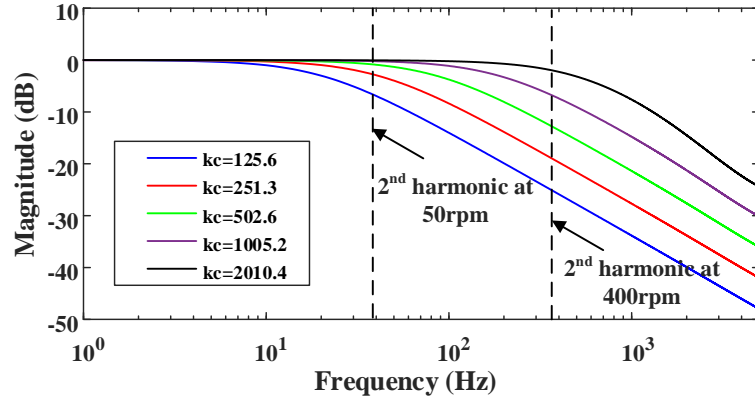
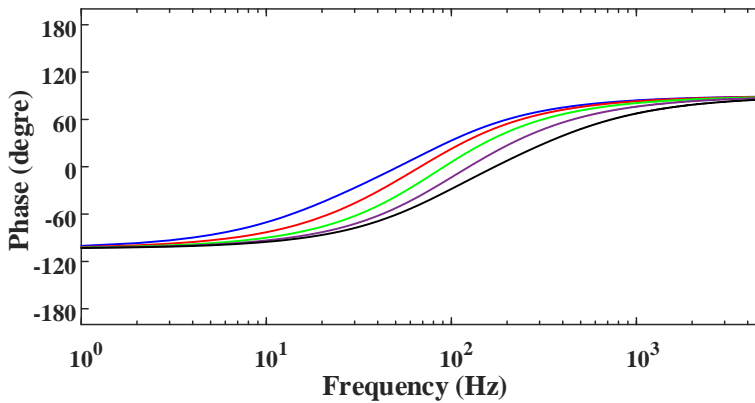
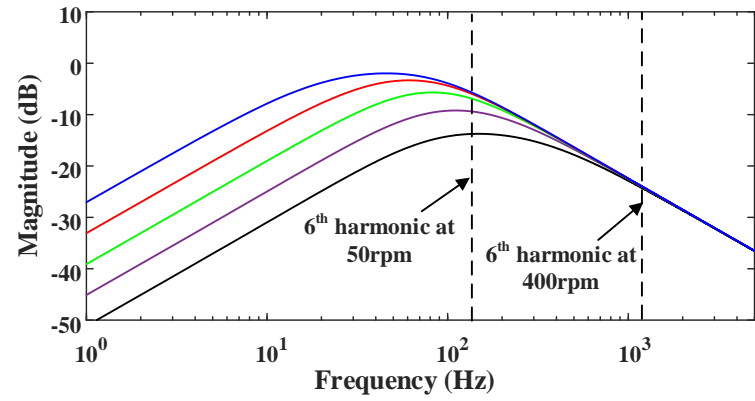


Fig. 5.1. Simplified current control loop in dq -axis. d represents disturbance. Δi_{dq} represents the current measurement errors.

The characteristics of the transfer functions in (5-9) are shown as Bode diagrams in Fig. 5.2. It should be noted that the machine in simulation is a new machine and is not the same as the experimental machine in previous chapters and the parameters of the machine is shown in Table 5.1. From the Bode diagram, it is obvious that the PI current regulator cannot provide infinite attenuation to the 2nd-order harmonic current at around 373Hz, which means the scaling errors will generate the 2nd-order harmonic in the real dq -axis currents, and further cause the 2nd-order torque ripple. By tuning the gain coefficient k_c of the PI regulator, it can be seen that the higher the k_c is, the weaker the attenuation to the 2nd-order harmonic is. This implies that the generated 2nd-order harmonic in the real current will increase as k_c increases. Generally, in terms of the conventional 5th and 7th current harmonics (the 6th harmonic in synchronous reference frame) caused by the disturbance d , as it can be concluded from Fig. 5.2(b), increasing k_c will decrease the magnitude to the 6th harmonic disturbance at low frequency region (0Hz-1000Hz), which means the 6th current harmonic can be suppressed by increasing k_c in this frequency range. However, for the 2nd-order current harmonic caused by the scaling errors, it is not able to do that because the 2nd-order current harmonic will increase as k_c is increased. In addition, the magnitude at low frequency region is higher than the magnitude at high frequency region, which means the 2nd-order harmonic should be more serious in low speed condition than that in high speed condition. Fig. 5.3 shows the current waveforms and torque waveforms at 50r/min, 400Nm using different k_c . It can be concluded from Fig. 5.3, as k_c increases, the 2nd-order harmonics due to scaling errors increases, while the 6th harmonics due to disturbance decreases. This agrees with the analysis regarding the Bode diagram in Fig. 5.2. Based on the theoretical analysis and the simulation results, the harmonic currents due to the scaling errors are different from the harmonic currents due to the disturbance, and it is impossible to use the methods investigated in the previous chapters to suppress this harmonic. This can be understood as the previous methods can only suppress the current harmonics in the measured currents but the current harmonics in the real currents still exist due to the scaling errors.



(a)



(b)

Fig. 5.2 Bode diagram under different k_c . (a) $\frac{I_{dq}(s)}{\Delta I_{dq}(s)}$. (b) $\frac{I_{dq}(s)}{D(s)}$. The simulation parameters are $T_d=150\mu s$, $R_s=0.12\Omega$, $L_s=1.5mH$. The other simulation parameters are shown in Table 5.1.

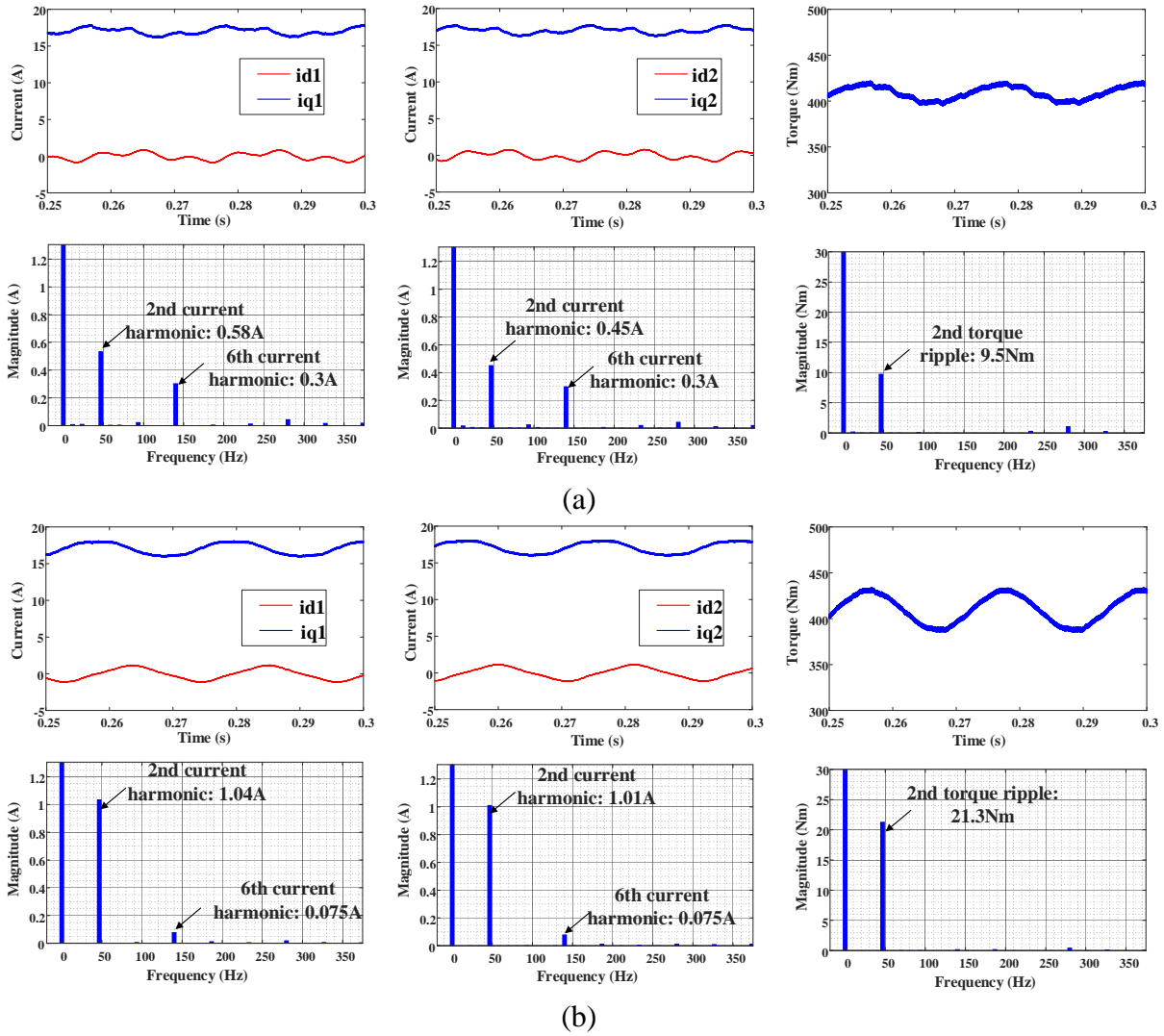


Fig. 5.3 Simulation results of current and torque. The DC current in q-axis is 16.9A and the DC torque component is 410Nm. (a) $k_c=251$. (b) $k_c=2510$. Speed is 50r/min and torque is 400Nm. The proposed current harmonic suppression method in the previous chapters is not activated in this simulation. K_a , K_b , K_x , and K_y are set as 0.2, 0.1, -0.1, and -0.2.

5.3 Scaling Error Correction Using High-Frequency Signal Injection

The high-frequency signal injection is generally used for the estimation of rotor position in sensorless control [LIU14][CON01] or the parameter identification of electrical machines [EBE12], and it is employed in this chapter to correct the current measurement gain coefficients. The adverse effect of the high-frequency signal injection is extra torque ripples and acoustic noise. Therefore, for a DTP PMSM, the high-frequency signals are injected into the z_1z_2 subspace because the electromagnetic torque is not related to the current and flux linkage in z_1z_2 subspace and thus the injected high-frequency signals will cause no torque ripple and the

acoustic noise can be reduced as well. The expression of the injected voltage is

$$u_{c_z} = u_{c_z1} + ju_{c_z2} = U_c e^{j\theta_v} \quad (5-10)$$

where U_c is the amplitude of the injected carrier voltage. θ_v is the phase angle of the injected carrier voltage and it satisfies

$$\theta_v = 2\pi f_c t \quad (5-11)$$

where f_c is the frequency of the injected carrier voltage. The generated carrier current can be expressed as

$$i_{c_z} = i_{c_z1} + ji_{c_z2} = I_c e^{j\theta_c} \quad (5-12)$$

where θ_c is the phase angle of the generated current and I_c is the amplitude of the generated current. The real six phase high-frequency current due to the injected carrier voltage can be expressed as

$$i_{c_abcxyz} = \begin{bmatrix} I_c \cos \theta_c \\ I_c \cos \left(\theta_c - \frac{2\pi}{3} \right) \\ I_c \cos \left(\theta_c + \frac{2\pi}{3} \right) \\ -I_c \cos \left(\theta_c - \frac{\pi}{6} \right) \\ -I_c \cos \left(\theta_c - \frac{5\pi}{6} \right) \\ -I_c \cos \left(\theta_c + \frac{\pi}{2} \right) \end{bmatrix} \quad (5-13)$$

Considering the scaling errors of the current sensors in phases A, B, X, and Y, the measured high-frequency current is

$$i_{c_mabcxyz} = \begin{bmatrix} I_c \cos \theta_c \\ I_c \cos \left(\theta_c - \frac{2\pi}{3} \right) \\ I_c \cos \left(\theta_c + \frac{2\pi}{3} \right) \\ -I_c \cos \left(\theta_c - \frac{\pi}{6} \right) \\ -I_c \cos \left(\theta_c - \frac{5\pi}{6} \right) \\ -I_c \cos \left(\theta_c + \frac{\pi}{2} \right) \end{bmatrix} + \begin{bmatrix} K_a I_c \cos \theta_c \\ K_b I_c \cos \left(\theta_c - \frac{2\pi}{3} \right) \\ -K_a I_c \cos \theta_c - K_b I_c \cos \left(\theta_c - \frac{2\pi}{3} \right) \\ -K_x I_c \cos \left(\theta_c - \frac{\pi}{6} \right) \\ -K_y I_c \cos \left(\theta_c - \frac{5\pi}{6} \right) \\ K_x I_c \cos \left(\theta_c - \frac{\pi}{6} \right) + K_y I_c \cos \left(\theta_c - \frac{5\pi}{6} \right) \end{bmatrix} \quad (5-14)$$

Using VSD transformation (5-3), (5-14) can be transformed as

$$\begin{bmatrix} i_{c_am} \\ i_{c_\beta m} \\ i_{c_z1m} \\ i_{c_z2m} \end{bmatrix} = \frac{1}{3} \begin{bmatrix} 1 & -\frac{1}{2} & -\frac{1}{2} & \frac{\sqrt{3}}{2} & -\frac{\sqrt{3}}{2} & 0 \\ 0 & \frac{\sqrt{3}}{2} & -\frac{\sqrt{3}}{2} & \frac{1}{2} & \frac{1}{2} & -1 \\ 1 & -\frac{1}{2} & -\frac{1}{2} & -\frac{\sqrt{3}}{2} & \frac{\sqrt{3}}{2} & 0 \\ 0 & \frac{\sqrt{3}}{2} & -\frac{\sqrt{3}}{2} & -\frac{1}{2} & -\frac{1}{2} & 1 \end{bmatrix} i_{c_mabcxyz} = \quad (5-15)$$

$$= \frac{I_c}{12} \begin{bmatrix} -3(K_x + K_y - 2K_a)\cos\theta_c - \sqrt{3}(K_x - K_y)\sin\theta_c \\ (2\sqrt{3}(K_a - K_b) - 3\sqrt{3}(K_x - K_y))\cos\theta_c - 3(K_x + K_y - 2K_b)\sin\theta_c \\ 3(K_x + K_y + 2K_a)\cos\theta_c + \sqrt{3}(K_x - K_y)\sin\theta_c \\ (2\sqrt{3}(K_a - K_b) + 3\sqrt{3}(K_x - K_y))\cos\theta_c + 3(K_x + K_y + 2K_b)\sin\theta_c \end{bmatrix}$$

Using the complex-vector format, (5-15) can be rewritten as

$$\begin{aligned} \begin{bmatrix} i_{c_a\beta m} \\ i_{c_zm} \end{bmatrix} &= \\ &= \frac{I_c}{12} \begin{bmatrix} -3(K_x + K_y) + 3(K_a + K_b) + (\sqrt{3}(K_a - K_b) - \sqrt{3}(K_x - K_y)) \\ 3(K_x + K_y) + 3(K_a + K_b) + (\sqrt{3}(K_a - K_b) + \sqrt{3}(K_x - K_y)) \end{bmatrix} e^{j\theta_c} \\ &+ \frac{I_c}{12} \begin{bmatrix} 3(K_a - K_b) + (\sqrt{3}(K_a - K_b) - \sqrt{3}(K_x - K_y)) \\ 3(K_a - K_b) + (\sqrt{3}(K_a - K_b) + \sqrt{3}(K_x - K_y)) \end{bmatrix} e^{-j\theta_c} \\ &+ \frac{I_c}{12} \begin{bmatrix} -\sqrt{3}(K_x - K_y) \\ \sqrt{3}(K_x - K_y) \end{bmatrix} e^{-j(\theta_c - \frac{\pi}{2})} \end{aligned} \quad (5-16)$$

where $i_{c_a\beta m} = i_{c_am} + ji_{c_\beta m}$, $i_{c_zm} = i_{c_z1m} + ji_{c_z2m}$. To simplify the description, define

$$\begin{aligned} \Delta K_1 &= K_a - K_b \\ \Delta K_2 &= K_x - K_y \\ \Sigma K_1 &= K_a + K_b \\ \Sigma K_2 &= K_x + K_y \end{aligned} \quad (5-17)$$

Equation (5-16) can be simplified as

$$\begin{bmatrix} i_{c_a\beta m} \\ i_{c_zm} \end{bmatrix} = \begin{bmatrix} i_{c_a\beta m}^+ \\ i_{c_zm}^+ \end{bmatrix} + \begin{bmatrix} i_{c_a\beta m}^- \\ i_{c_zm}^- \end{bmatrix} \quad (5-18)$$

where the positive-sequences are

$$\begin{bmatrix} i_{c_a\beta m}^+ \\ i_{c_zm}^+ \end{bmatrix} = \frac{I_c}{12} \begin{bmatrix} 3\Sigma K_1 - 3\Sigma K_2 + \sqrt{3}(\Delta K_1 - \Delta K_2) \\ 3\Sigma K_1 + 3\Sigma K_2 + \sqrt{3}(\Delta K_1 + \Delta K_2) \end{bmatrix} e^{j\theta_c} \quad (5-19)$$

and the negative-sequences are

$$\begin{bmatrix} i_{c_ \alpha\beta m}^- \\ i_{c_ zm}^- \end{bmatrix} = \frac{I_c}{12} \begin{bmatrix} 3\Delta K_1 + \sqrt{3}(\Delta K_1 - \Delta K_2) \\ 3\Delta K_1 + \sqrt{3}(\Delta K_1 + \Delta K_2) \end{bmatrix} e^{-j\theta_c} + \frac{I_c}{12} \begin{bmatrix} -\sqrt{3}\Delta K_2 \\ \sqrt{3}\Delta K_2 \end{bmatrix} e^{-j(\theta_c - \frac{\pi}{2})} \quad (5-20)$$

In terms of the measured current errors in dq -axes, if neglecting the dc errors, (5-7) can be rewritten as

$$\Delta i_{dq} = \frac{I}{6} \Delta K_1 e^{-j(2\theta_e + \theta_0)} + \frac{\sqrt{3}I}{18} (\Delta K_1 + 2\Delta K_2) e^{-j(2\theta_e + \theta_0 - \frac{\pi}{2})} \quad (5-21)$$

Based on (5-21), it is clear that Δi_{dq} only depends on ΔK_1 and ΔK_2 . If ΔK_1 and ΔK_2 are tuned to be zero, the scaling errors can be corrected and Δi_{dq} will be eliminated from the control loop. Consequently, the resultant 2nd-order current harmonic and torque ripple can be eliminated. Now the question becomes how to tune ΔK_1 and ΔK_2 to be zero. From (5-20), it is easy to derive that

$$i_{c_ \alpha\beta m}^- + i_{c_ zm}^- = \frac{I_c}{6} (3 + \sqrt{3}) \Delta K_1 e^{-j\theta_c} \quad (5-22)$$

$$i_{c_ \alpha\beta m}^- - i_{c_ zm}^- = -\frac{I_c}{6} \sqrt{3} \Delta K_2 (e^{-j\theta_c} + e^{-j(\theta_c - \frac{\pi}{2})}) = -\frac{I_c}{6} \sqrt{6} \Delta K_2 e^{-j(\theta_c - \frac{\pi}{4})}$$

Then, the expressions of ΔK_1 and ΔK_2 can be derived as

$$\Delta K_1 = \frac{6(i_{c_ \alpha\beta m}^- + i_{c_ zm}^-)}{(3 + \sqrt{3})I_c} e^{j\theta_c} \quad (5-23)$$

$$\Delta K_2 = -\frac{\sqrt{6}(i_{c_ \alpha\beta m}^- - i_{c_ zm}^-)}{I_c} e^{j(\theta_c - \frac{\pi}{4})}$$

From (5-23), ΔK_1 and ΔK_2 are proportional to $(i_{c_ \alpha\beta m}^- + i_{c_ zm}^-) e^{j\theta_c}$ and $(i_{c_ \alpha\beta m}^- - i_{c_ zm}^-) e^{j(\theta_c - \frac{\pi}{4})}$. That means if it is feasible to first extract $(i_{c_ \alpha\beta m}^- + i_{c_ zm}^-)$ and $(i_{c_ \alpha\beta m}^- - i_{c_ zm}^-)$ from phase current, and control $(i_{c_ \alpha\beta m}^- + i_{c_ zm}^-) e^{j\theta_c}$ and $(i_{c_ \alpha\beta m}^- - i_{c_ zm}^-) e^{j(\theta_c - \frac{\pi}{4})}$ to zero by tuning the coefficients of current measurement, ΔK_1 and ΔK_2 will be zero, and then Δi_{dq} will be zero according to (5-21).

Tuning ΔK_1 and ΔK_2 to be zero can eliminate the unbalanced current among the currents inside one three-phase set [HAR08]. However, the unbalanced current between two three-phase sets

$$\begin{bmatrix} u_a \\ u_b \\ u_c \\ u_x \\ u_y \\ u_z \end{bmatrix} = \begin{bmatrix} 1 & 0 & 1 & 0 \\ -\frac{1}{2} & \frac{\sqrt{3}}{2} & -\frac{1}{2} & \frac{\sqrt{3}}{2} \\ -\frac{1}{2} & -\frac{\sqrt{3}}{2} & -\frac{1}{2} & -\frac{\sqrt{3}}{2} \\ \frac{\sqrt{3}}{2} & \frac{1}{2} & -\frac{\sqrt{3}}{2} & -\frac{1}{2} \\ -\frac{\sqrt{3}}{2} & \frac{1}{2} & \frac{\sqrt{3}}{2} & -\frac{1}{2} \\ 0 & -1 & 0 & 1 \end{bmatrix} \begin{bmatrix} u_\alpha \\ u_\beta \\ u_{c_z1} \\ u_{c_z2} \end{bmatrix} \quad (5-25)$$

In Fig. 5.4, the measured currents are required to be processed by the scaling gain tuning (5-26) to derive the tuned currents i_{ma_t} , i_{mb_t} , i_{mx_t} , and i_{my_t} .

$$\begin{aligned} i_{am_t} &= (1 + K_{D3})(1 + K_{D1})i_{am} \\ i_{bm_t} &= (1 + K_{D3})(1 - K_{D1})i_{bm} \\ i_{xm_t} &= (1 - K_{D3})(1 + K_{D2})i_{xm} \\ i_{ym_t} &= (1 - K_{D3})(1 - K_{D2})i_{ym} \end{aligned} \quad (5-26)$$

The tuned current i_{am_t} , i_{mb_t} , i_{mx_t} , and i_{my_t} are decomposed into $\alpha\beta$ and z_1z_2 subspaces by using VSD transformation (5-3). The currents $i_{c_ \alpha\beta m}^-$, $i_{c_ \alpha\beta m}^+$, and $i_{c_ zm}^-$ are required to be extracted for the current measurement gain tuning according to (5-23) and (5-24). The current in $\alpha\beta$ subspace $i_{\alpha\beta m}$ includes $i_{c_ \alpha\beta m}^-$ and $i_{c_ \alpha\beta m}^+$. The measured current in z_1z_2 subspace $i_{z_1z_2 m}$ includes $i_{c_ zm}^-$. Since the fundamental current is also mapped in $i_{\alpha\beta m}$ and coupled with $i_{c_ \alpha\beta m}^-$ and $i_{c_ \alpha\beta m}^+$, using digital filters to attenuate the fundamental and extract $i_{c_ \alpha\beta m}^-$ will result in significant delay and thus affect the control performance. To reduce this delay, the error signal $i_{dq_ \varepsilon}$ between the current reference and measured current feedback is transformed to $\alpha\beta$ -axis as $i_{dq_ \varepsilon} e^{j\theta_e}$, and used to extract $i_{c_ \alpha\beta m}^-$ and $i_{c_ \alpha\beta m}^+$. The signals extraction process shown in Fig. 5.4 is designed based on the following equations

$$\begin{aligned} (i_{c_ \alpha\beta m}^- + i_{c_ zm}^-)e^{j\theta_c} &= LPF \left((i_{z_1z_2 m} - i_{dq_ \varepsilon} e^{j\theta_e}) e^{j\theta_c} \right) \\ -(i_{c_ \alpha\beta m}^- - i_{c_ zm}^-)e^{j(\theta_c - \frac{\pi}{4})} &= LPF \left((i_{z_1z_2 m} + i_{dq_ \varepsilon} e^{j\theta_e}) e^{j(\theta_c - \frac{\pi}{4})} \right) \end{aligned} \quad (5-27)$$

$$i_{c_αβm}^+ e^{-jθ_c} = LPF(-i_{dq_ε} e^{j(θ_e - θ_c)})$$

where LPF means low-pass filter. Because ΔK_1 , ΔK_2 , ΣK_1 , and ΣK_2 are usually constants, $(i_{c_αβm}^- + i_{c_zm}^-) e^{jθ_c}$, $-(i_{c_αβm}^- - i_{c_zm}^-) e^{j(θ_c - \frac{\pi}{4})}$, and $i_{c_αβm}^+ e^{-jθ_c}$ are DC components. The LPFs here are used to attenuate AC components and extract the DC components. After the DC components are extracted, they are used as the feedback of PI controllers. The reference of the PI controller is set as zero to eliminate the DC component and the output of the PI regulators are K_{D1} , K_{D2} , and K_{D3} in the scaling gain tuning part (5-26).

5.4 Simulation Verification

The simulation is carried out in MATLAB/SIMULINK simulation software, and the parameters of the simulation DTP PMSM and the drive are shown in Table 5.1. The amplitude and frequency of the injected carrier voltage are 20V and 800Hz. The first-order LPF is used in the proposed control method, and the cut-off frequency of the LPF is 10Hz. The proportional and integral coefficients of the PI regulators in the scaling errors correction are 0.2 and 10, respectively. Symbol K_a , K_b , K_x , and K_y are set as 0.2, 0.1, -0.1, and -0.2 to simulate the scaling errors in the current measurement. Symbol k_c of the current regulator is set as 2510.

The simulation current and torque waveforms at 50r/min and 600r/min are shown in Figs. 5.5 and 5.6, respectively. To reduce the adverse effect of the injected high-frequency signals, e.g. noise and losses, the proposed method is activated at 0.3s and after the scaling coefficients are corrected, the method is deactivated at 0.6s. Before the method is activated, the six phase currents of the DTP PMSM is not balanced due to the scaling errors, which also generates the 2nd-order torque ripple as seen in Fig. 5.5(b). After the method is activated, the high-frequency carrier voltage is injected and thus the high-frequency ripples are generated in phase currents. However, the unbalanced currents are gradually suppressed by the scaling coefficient tuning and six phase currents become balanced at around 0.5s, which means the scaling errors are corrected. The method is deactivated at 0.6s, when the high-frequency carrier voltage is set to zero, and thus the high-frequency current ripples disappear. After 0.6s, it is clear that six phase currents are balanced compared to the current waveforms before 0.3s. Due to the correction of the scaling errors, the 2nd-order torque ripple is suppressed from 21.3Nm to 1.4Nm. Fig. 5.6 shows the performance of the proposed method at 600r/min. The method is activated at 0.3s and deactivated at 0.6s. It is clear that the unbalanced current is eliminated and the 2nd-order

can also be greatly suppressed from 7.9Nm to 0.5Nm by the proposed method. These simulation results have proved the effectiveness of the proposed method on correcting the scaling errors in a DTP PMSM system.

TABLE 5.1
PARAMETERS OF SIMULATION SYSTEM

Parameters	Values
Number of pole pairs p	28
Stator resistance R_s	0.12Ω
Synchronous inductance L_s	1.5mH
Leakage inductance L_σ	1mH
Rated speed	600r/min
Rated torque	800Nm
DC linkage voltage	400V
Sampling & switching frequencies	16kHz

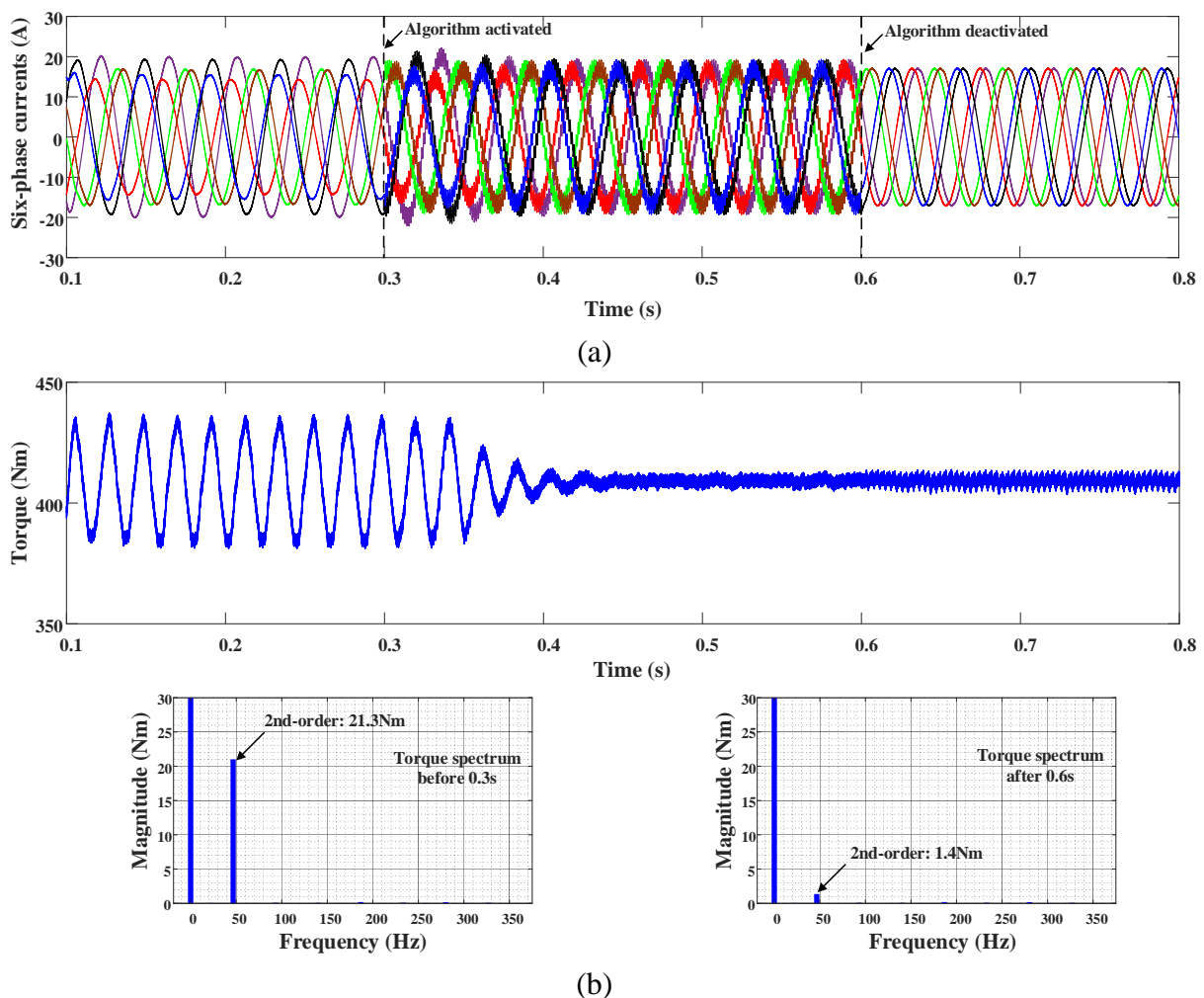


Fig. 5.5. Simulation results of the proposed method when speed is 50r/min, torque is 400Nm. (a) Waveforms of phase currents. (b) Waveform of torque and torque spectra. Algorithm is activated at 0.3s and deactivated at 0.6s. The DC torque components in spectra are 410Nm.

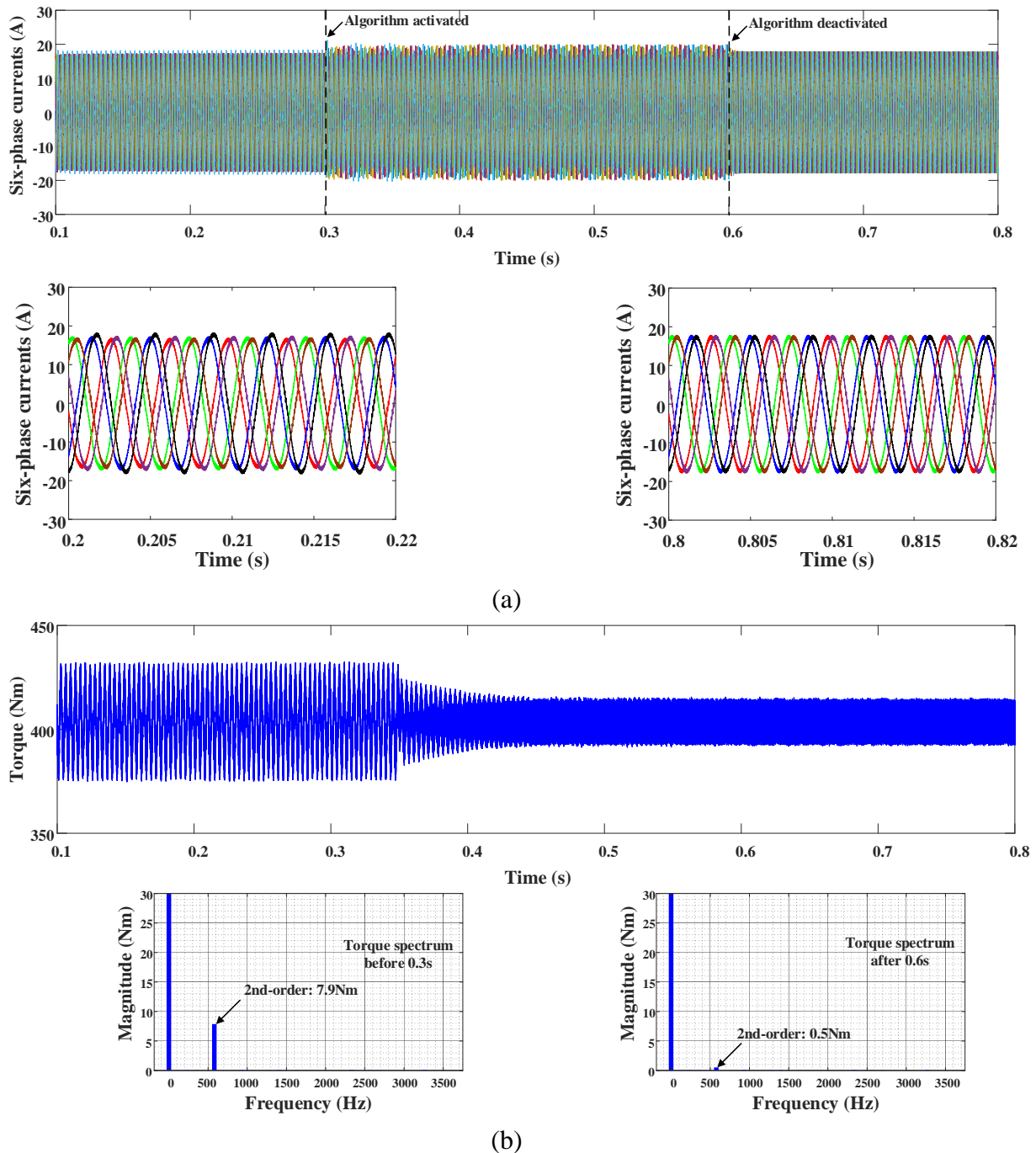


Fig. 5.6. Simulation results of the proposed method when speed is 600r/min, torque is 400Nm. (a) Waveforms of phase currents. (b) Waveform of torque and torque spectra. Algorithm is activated at 0.3s and deactivated at 0.6s. The DC torque components in spectra are 410Nm.

To prove that the good suppression is continuous after the scaling errors corrected and the method deactivated, Figs. 5.7 and 5.8 show the simulation results during the dynamic process of speed change and torque change, respectively. In Fig. 5.7, the proposed method has already corrected the scaling errors and is deactivated from 0.7s. at 0.8s, the machine speed starts to increase from 50r/min and reaches 600r/min at around 1.5s. In Fig. 5.8, similar to Fig. 5.7, the

scaling errors are already corrected, and the speed is 50r/min. The torque reference steps from 400Nm to 1200Nm at 0.8s. It is clear from Figs 5.7 and 5.8 that the phase currents are balanced during the dynamic process of speed and torque change. This means once the scaling errors are corrected, the effect is continuous and is not affected by the speed and torque change unless there are new scaling errors introduced in the current measurement.

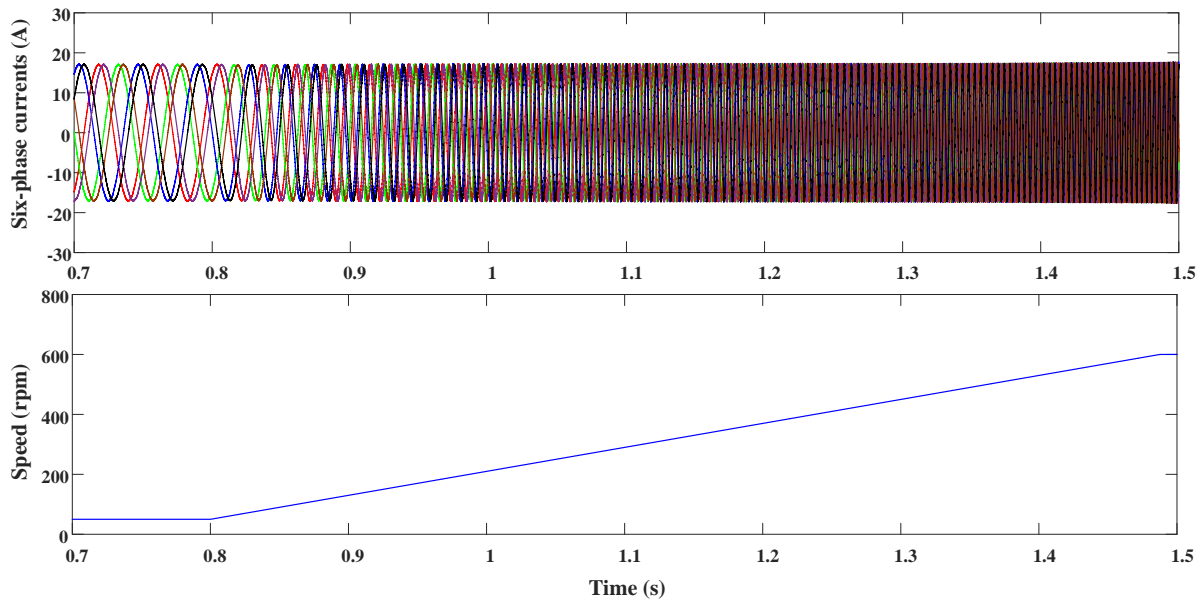


Fig. 5.7 Simulation results of currents and speed after scaling errors corrected and the proposed method is deactivated. Speed increases from 50r/min at 0.8s to 600r/min at around 1.5s. Torque is set as 400Nm.

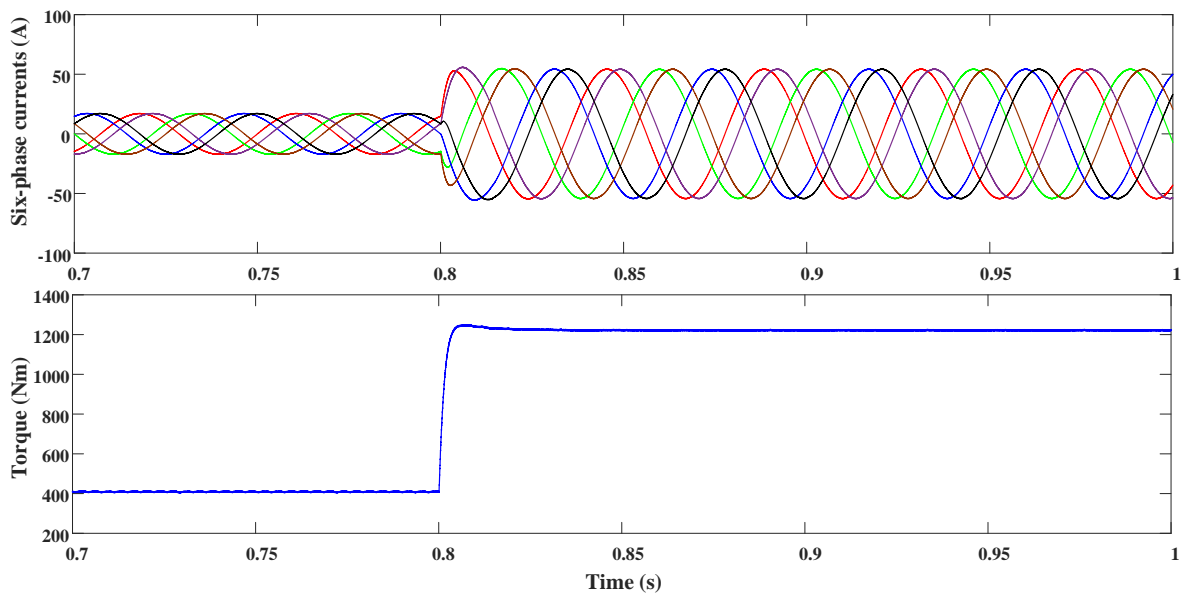


Fig. 5.8 Simulation results of torque step after scaling errors corrected and the proposed method is deactivated. Speed is 50r/min and torque reference steps from 400Nm to 1200Nm at 0.8s.

5.5 Conclusion

This chapter has proposed a high-frequency signal injection method to tune the current measurement gains and correct the scaling errors in DTP PMSM systems. The proposed method only requires high-frequency carrier voltage injection in the z_1z_2 subspace and will not cause serious high-frequency torque ripples, which the three-phase PM machines suffer from a lot if using the high-frequency signal injection. The analysis in this chapter shows that the scaling errors in the current measurement can generate the 2nd-order current harmonic in synchronous reference frame, which further results in the unbalance among six phase currents of the machine as well as the 2nd-order torque ripples. The relationship between the injected high-frequency signals and the scaling errors is derived and analyzed. The relationship indicates that the negative-sequence high-frequency components in the measured currents are related to the difference between the measurement gain coefficients inside each three-phase set, while the positive-sequence high-frequency components are mainly related to the measurement gain coefficient difference between two three-phase sets. Based on this relationship, the high-frequency current control loops are designed to tune the current measurement coefficients, and the scaling errors can be corrected when the related high-frequency current components are suppressed by the control loops. Simulation results show that the proposed method is effective at low speed and rated speed conditions. Furthermore, it is proved that once the current measurement gains are compensated, the method can be deactivated, and the compensation effect is continuous in both dynamic- and steady-states.

CHAPTER 6

ARBITRARY CURRENT HARMONIC DECOMPOSITION AND REGULATION FOR PERMANENT MAGNET SYNCHRONOUS MACHINES

The virtual multi three-phase systems introduced in the previous chapters show good performance for current harmonic regulation. Since three-phase PMSMs are more generally used in industrial applications than dual three-phase PMSMs, this chapter extends the concept of virtual multi three-phase system to the three-phase PMSM systems in order to expand the contribution of this research.

For a three-phase PMSM system, the inverter nonlinearity, back-EMF harmonics, and the asymmetry among phases, are firstly considered to derive a comprehensive electrical model of PMSMs in this chapter. Compared to the conventional harmonic analysis in three-phase PMSM systems, the derived model indicates that more new current harmonics can exist in the PMSM system. To regulate the current harmonics with arbitrary orders, a virtual three-phase system is established. By properly shifting the spatial and time phase angles between the virtual three-phase system and the original physical three-phase system, the selected current harmonics can be decomposed from the phase current. A simple proportional-integral regulator with adjustable phase compensation angle is designed based on the proposed model to regulate the decomposed current harmonics in the corresponding harmonic synchronous reference frame. The implementation details and experimental results are provided to illustrate the feasibility and correctness of the proposed control strategy.

This chapter is published in IEEE Transactions on Industrial Electronics [YAN22]

[YAN22] L. Yan, Z. Q. Zhu, Bo Shao, J. Qi, Y. Ren, C. Gan, S. Brockway, and C. Hilton, "Arbitrary current harmonic decomposition and regulation for permanent magnet synchronous machines," *IEEE Trans. Ind. Electron.*, 2022, doi: 10.1109/TIE.2022.3183351.

6.1 Introduction

Three-phase permanent magnet synchronous machines (PMSMs) are applied to various applications such as electric/hybrid vehicles, more electric airplanes, industrial servo drives, and wind power generation due to the advantages of high torque density, high power density, and high efficiency [ZHU07][NAK05]. In the control of PMSMs, the current harmonic regulation is a hot topic in recent years and is usually employed to optimize the waveform of phase current and achieve a better system performance, such as reduced harmonic loss, reduced torque ripples, and enhanced average torque.

This chapter proposes a novel method for arbitrary current harmonic control in a PMSM system. Firstly, the harmonic analysis is carried out and a comprehensive electrical machine model is derived in Section 6.2. Different from the existing works, not only the general odd-order harmonics but also the even-order harmonics due to the north-south asymmetry in PM air-gap flux density are considered in the PMSM system. Additionally, the effect of the asymmetry among phases will introduce more new harmonics into the phase current. In Section 6.3, a virtual three-phase system is established based on phase shift operation, and by using a simple vector space decomposition, the current harmonics with arbitrary orders can be decomposed with the fundamental component. The decomposed current harmonics are further transformed to the corresponding harmonic SRFs and controlled by PI regulator. Section 6.4 gives experimental results to validate the theoretical analysis and evaluate the performance of the proposed method. Finally, Section 6.5 concludes the chapter.

6.2 Harmonic Analysis of PMSM System

Ignoring hysteresis and eddy current losses, the mathematical model of PMSM in stationary ABC frame can be written as

$$\begin{aligned} \mathbf{U}_{abc} &= \mathbf{R}\mathbf{I}_{abc} + \frac{d\boldsymbol{\Psi}_{abc}}{dt} \\ \boldsymbol{\Psi}_{abc} &= \mathbf{L}_{abc}\mathbf{I}_{abc} + \boldsymbol{\Psi}_{fabc} \\ J \frac{d\omega_m}{dt} &= t_e - t_L - B\omega_m \end{aligned} \quad (6-1)$$

where J is the moment of inertia of the rotor; ω_m is the mechanical angular speed; t_e is the electromagnetic torque; t_L is the load torque; B is the friction coefficient. The phase voltage

\mathbf{U}_{abc} , the phase current \mathbf{I}_{abc} , and the permanent magnet (PM) flux linkage Ψ_{fabc} are

$$\mathbf{U}_{abc} = \begin{bmatrix} u_a \\ u_b \\ u_c \end{bmatrix}, \mathbf{I}_{abc} = \begin{bmatrix} i_a \\ i_b \\ i_c \end{bmatrix}, \text{ and } \Psi_{fabc} = \begin{bmatrix} \psi_{fa} \\ \psi_{fb} \\ \psi_{fc} \end{bmatrix} \quad (6-2)$$

The stator inductance \mathbf{L}_{abc} and resistance \mathbf{R} are

$$\mathbf{L}_{abc} = \begin{bmatrix} L & M & M \\ M & L & M \\ M & M & L \end{bmatrix} \text{ and } \mathbf{R} = \begin{bmatrix} R_s & 0 & 0 \\ 0 & R_s & 0 \\ 0 & 0 & R_s \end{bmatrix} \quad (6-3)$$

The electromagnetic torque can be expressed as the derivative of the magnet co-energy with respect to the rotor position electrical angle θ_e as follows [4]

$$t_e = \frac{1}{2} p \mathbf{I}_{abc}^T \frac{d\mathbf{L}_{abc}}{d\theta_e} \mathbf{I}_{abc} + p \mathbf{I}_{abc}^T \frac{d\Psi_{fabc}}{d\theta_e} + t_{cog} \quad (6-4)$$

where t_{cog} is cogging torque, and p is the number of pole pairs. Under ideal conditions, the phase voltage \mathbf{U}_{abc} and PM flux linkage Ψ_{fabc} should be sinusoidal, and the three-phase inductance and resistance are symmetrical. However, in practice, the terminal voltage of the machine is usually generated by a voltage source inverter (VSI), and includes a series of voltage harmonics due to modulation and the nonlinearity of the VSI. The PM flux linkage may include harmonics due to machine design, manufacture, and armature reaction. Additionally, the asymmetry among three-phases will also contribute to harmonic sources. To detail the properties of harmonics in the PMSM system, different types of factors will be analyzed in the following parts.

6.2.1 General Harmonics with Odd Orders

In a PMSM system, the most general harmonics are the odd-order harmonic and come from both the sides of VSI and machine. In terms of the VSI side, the nonlinearity of inverter introduces disturbance between the reference voltage and the real voltage, and regardless of high-frequency harmonics caused by switching actions, the voltage disturbance in phase A, Δu_A , can be equivalent to a square wave voltage [LEE21] as

$$\Delta u_A(t) = V_{dead} \text{sgn}(i_A(t)) \quad (6-5)$$

where V_{dead} is the amplitude of the square wave which is determined by the dead time, the characteristics of switching devices, and the dc-link voltage. sgn means the polarity function.

Using Fourier series, (6-5) can be rewritten as follows.

$$\Delta u_A(t) = \frac{4\Delta V}{\pi} \sum \frac{1}{2n-1} \sin(2n-1)\omega_e t \quad (6-6)$$

where $n=1, 2, 3, \dots$, and ω_e is the angular frequency of the fundamental current. Following the same principle, the voltage disturbance in other phases can be conducted and shown in (6-7).

$$\Delta \mathbf{U} = \begin{bmatrix} \Delta u_A \\ \Delta u_B \\ \Delta u_C \end{bmatrix} = \frac{4\Delta V}{\pi} \sum \frac{1}{2n-1} \begin{bmatrix} \sin(2n-1)\omega_e t \\ \sin(2n-1)\left(\omega_e t - \frac{2\pi}{3}\right) \\ \sin(2n-1)\left(\omega_e t + \frac{2\pi}{3}\right) \end{bmatrix} \quad (6-7)$$

It is clear that the voltage disturbance includes the fundamental component and the harmonic components with odd orders. The fundamental component can be fully compensated by PI current regulators in the fundamental SRF. The harmonic components with the orders of 3, 9, 15, ..., are zero-sequence components and cannot cause current harmonics due to the isolated neutral point. The rest components, if without effective compensation, will generate current harmonics with the orders of $6n \pm 1$, i.e. 5, 7, 11, 13, ... It is worth noting that the $6n-1$ ones are negative-sequence components and the $6n+1$ ones belong to positive-sequence components.

In terms of the machine side, due to the factors of design, manufacture, and armature reaction, the spatial flux is usually non-sinusoidal and the odd harmonics exist in PM flux linkage as follows:

$$\Psi_{fabc} = \begin{bmatrix} \psi_{fa} \\ \psi_{fb} \\ \psi_{fc} \end{bmatrix} = \sum \psi_{f(2n-1)} \begin{bmatrix} \cos(2n-1)\theta_e \\ \cos(2n-1)\left(\theta_e - \frac{2\pi}{3}\right) \\ \cos(2n-1)\left(\theta_e + \frac{2\pi}{3}\right) \end{bmatrix} \quad (6-8)$$

where $\psi_{f(2n-1)}$ represents the amplitude of fundamental and harmonic components, and θ_e is the electrical angle of rotor position. Since the back-EMF is the derivative of PM flux linkage, there will also be odd-order harmonics in the back-EMF. Similar to the voltage disturbance in (6-7), only the back-EMF components with orders $6n+1$ and $6n-1$, can contribute to current harmonics.

6.2.2 Harmonics with Even Orders

The limitation of manufacture can lead to north-south asymmetry in PM air-gap flux density,

which further results in even-order harmonics, i.e. the 2nd, 4th, 6th, 8th, 10th, ..., in the PM flux linkage and back-EMF. In addition, for many PMSMs with special asymmetric rotor structures [QI21a], the north-south asymmetry effect is inherent. The even-order harmonics in the PM flux linkage can be expressed as

$$\Psi_{fabc}^e = \begin{bmatrix} \psi_{fa}^e \\ \psi_{fb}^e \\ \psi_{fc}^e \end{bmatrix} = \sum \psi_{f2n} \begin{bmatrix} \cos 2n\theta_e \\ \cos 2n\left(\theta_e - \frac{2\pi}{3}\right) \\ \cos 2n\left(\theta_e + \frac{2\pi}{3}\right) \end{bmatrix} \quad (6-9)$$

where the superscript “e” means the even-order harmonics, and ψ_{f2n} is the amplitude of even-order PM flux linkage harmonic. Among these harmonics, the 2nd, 8th, ... are the negative-sequence components, the 4th, 10th, ... are the positive-sequence components, and the 6th, 12th, ... are the zero-sequence components.

Although the even-order PM flux linkage harmonics are not as usual as the odd-order ones, their negative effect on the PMSM system is similar. On the one hand, the even-order current harmonics can be produced and more losses are generated. On the other hand, the even-order harmonics in both current and PM flux linkage will contribute to torque ripples, e.g. the 3rd torque ripple due to the 2nd and 4th harmonics [QI21b]. Furthermore, the even-order harmonics have lower frequencies than the odd-order ones, and thus the generated torque ripples should be more serious if the north-south asymmetry is significant.

6.2.3 Asymmetry among Phases

In ideal conditions, the impedance is symmetrical among the three-phases of machines. However, the real machines usually include asymmetry among phases due to the limitation of manufacture. Taking phase C as the standard phase, the phase resistance and inductance matrices in stationary ABC frame can be rewritten as follows.

$$\mathbf{R} = \begin{bmatrix} R_s & 0 & 0 \\ 0 & R_s & 0 \\ 0 & 0 & R_s \end{bmatrix} + \begin{bmatrix} R_1 & 0 & 0 \\ 0 & R_2 & 0 \\ 0 & 0 & 0 \end{bmatrix} \quad (6-10)$$

and

$$\mathbf{L}_{abc} = \begin{bmatrix} L & M & M \\ M & L & M \\ M & M & L \end{bmatrix} + \begin{bmatrix} L_1 & M_1 & 0 \\ M_1 & L_2 & M_2 \\ 0 & M_2 & 0 \end{bmatrix} \quad (6-11)$$

where R_s , L , and M are the symmetrical stator resistance, self-inductance, and mutual-inductance, respectively. R_1 and R_2 are the asymmetric resistance in phases A and B. L_1 and L_2 are the asymmetric self-inductances. M_1 and M_2 are the asymmetric mutual-inductances.

6.2.4 Arbitrary Harmonic Electrical Model

Considering inverter nonlinearity, non-ideal PM flux linkage, and asymmetry among phases, it is complicated to analyze the current harmonics in the stationary ABC frame. The MSRFs are employed here to derive the electrical model of arbitrary harmonics. Similar to the model in SRF which is synchronous with the rotor, the electrical machine variables can also be transformed to arbitrary harmonic SRF that is synchronous with the selected harmonic vector in the space. The definition of MSRFs is introduced in many studies, such as [YAN19][LIU19], and is not written here. The MSRF transform is

$$\mathbf{C}^h = \frac{2}{3} \begin{bmatrix} \cos h\theta_e & \cos\left(h\theta_e - \frac{2}{3}\pi\right) & \cos\left(h\theta_e + \frac{2}{3}\pi\right) \\ -\sin h\theta_e & -\sin\left(h\theta_e - \frac{2}{3}\pi\right) & -\sin\left(h\theta_e + \frac{2}{3}\pi\right) \end{bmatrix} \quad (6-12)$$

where h is the order of arbitrary harmonic and $h = \pm 1, \pm 2, \pm 3, \pm 4, \dots$. To be precise, $h=1$ means the fundamental, and $h=-1$ means the negative-sequence fundamental, etc. Using (6-12), the electrical machine model in the h^{th} SRF can be derived as

$$\mathbf{U}_{dq}^h = \mathbf{R}_{dq}^h \mathbf{I}_{dq}^h + \frac{d\boldsymbol{\Psi}_{dq}^h}{dt} + h\omega_e \mathbf{Q} \boldsymbol{\Psi}_{dq}^h \quad (6-13)$$

$$\boldsymbol{\Psi}_{dq}^h = \mathbf{L}_{dq}^h \mathbf{I}_{dq}^h + \boldsymbol{\Psi}_{fdq}^h$$

where ω_e is the electrical angular speed of rotor, and the matrices satisfy

$$\mathbf{U}_{dq}^h = \mathbf{C}^h \mathbf{U}_{abc} = \begin{bmatrix} u_d^h \\ u_q^h \end{bmatrix}, \mathbf{I}_{dq}^h = \mathbf{C}^h \mathbf{I}_{abc} = \begin{bmatrix} i_d^h \\ i_q^h \end{bmatrix}, \quad (6-14)$$

$$\boldsymbol{\Psi}_{fdq}^h = \mathbf{C}^h \boldsymbol{\Psi}_{fabc} = \begin{bmatrix} \psi_{fd}^h \\ \psi_{fq}^h \end{bmatrix}, \mathbf{Q} = \begin{bmatrix} 0 & -1 \\ 1 & 0 \end{bmatrix}$$

The resistance and inductance matrices satisfy

$$\mathbf{R}_{dq}^h = \mathbf{C}^h \mathbf{R} (\mathbf{C}^h)^T = \mathbf{R}^{ave} + \mathbf{R}^{asy} \cos 2h\theta_e + \mathbf{R}^{asy} \mathbf{Q} \sin 2h\theta_e$$

$$\begin{aligned} \mathbf{L}_{dq}^h &= \mathbf{C}^h \mathbf{L}_{abc} (\mathbf{C}^h)^T \\ &= \mathbf{L}^{ave} + \mathbf{L}^{sal} \cos 2(h-1)\theta_e + \mathbf{L}^{sal} \mathbf{Q} \sin 2(h-1)\theta_e \\ &\quad + \mathbf{L}^{asy} \cos 2h\theta_e + \mathbf{L}^{asy} \mathbf{Q} \sin 2h\theta_e \end{aligned} \quad (6-15)$$

where the average components are

$$\begin{aligned} \mathbf{R}^{ave} &= \begin{bmatrix} r_1 & 0 \\ 0 & r_1 \end{bmatrix}, r_1 = R_s + \frac{R_1 + R_2}{3} \\ \mathbf{L}^{ave} &= \begin{bmatrix} l_1 & 0 \\ 0 & l_1 \end{bmatrix}, l_1 = \frac{L_d + L_q}{2} + \frac{L_1 - M_1 + L_2 - M_2}{3} \end{aligned} \quad (6-16)$$

The amplitude of the salient-effect pulsating inductance is

$$\mathbf{L}^{sal} = \begin{bmatrix} l_2 & 0 \\ 0 & -l_2 \end{bmatrix}, l_2 = \frac{L_d - L_q}{2} \quad (6-17)$$

The salient-effect pulsating inductance can be understood as that the harmonic SRF is not synchronous with the rotor, and thus the flux path is changing with the rotor rotating. Consequently, the inductance is pulsating with the relative motion between the rotor and the harmonic SRF.

The amplitudes of asymmetric resistance and inductance are

$$\begin{aligned} \mathbf{R}^{asy} &= \begin{bmatrix} r_2 & r_3 \\ r_3 & -r_2 \end{bmatrix}, r_2 = \frac{1}{3} \left(R_1 - \frac{1}{2} R_2 \right), r_3 = -\frac{\sqrt{3}}{6} R_2 \\ \mathbf{L}^{asy} &= \begin{bmatrix} l_3 & l_4 \\ l_4 & -l_3 \end{bmatrix}, l_3 = \frac{1}{3} \left(L_1 - \frac{1}{2} L_2 - M_1 + 2M_2 \right), \\ &\quad l_4 = \frac{\sqrt{3}}{6} (2M_2 - L_2) \end{aligned} \quad (6-18)$$

If only considering the h^{th} harmonic and neglecting the other components, the current, voltage, and PM flux linkage of the h^{th} harmonic are all DC values in (6-13), and (6-13) is a generic electrical model for arbitrary harmonic including the fundamental ($h=1$). The whole PMSM electrical model can be regarded as the set of all individual harmonic electrical models. Symbol Ψ_{fdq}^h represents the h^{th} harmonic in the PM flux linkage. As the rotor rotating, it can generate the h^{th} back-EMF harmonics $h\omega_e \mathbf{Q} \Psi_{fdq}^h$. Symbol \mathbf{U}_{dq}^h represents the h^{th} voltage harmonics,

which include two parts, i.e. the actively injected h^{th} voltage harmonic by the controller and the h^{th} component in the voltage disturbance due to inverter nonlinearity. The difference between the voltage harmonic \mathbf{U}_{dq}^h and the back-EMF harmonic $h\omega_e \mathbf{Q}\Psi_{fdq}^h$ is imposed on the impedance and produces the h^{th} current harmonic. This means the controller can adjust the injected h^{th} voltage harmonic in \mathbf{U}_{dq}^h to achieve the regulation of the h^{th} current harmonic.

According to the expressions of the resistance and inductance, both the rotor salient effect and the asymmetry among phases can cause pulsating impedance. This will lead to the frequency modulation effect. It is difficult to analyze the frequency modulation effect using the model in matrix format. Hence, the model in complex-vector format (6-19) is derived from the model (6-13) and is employed to help analyze the frequency modulation effect.

$$u_{dq}^h = r_1 i_{dq}^h + \left(r_2 e^{-j2h\theta_e} + r_3 e^{j(-2h\theta_e + \frac{\pi}{2})} \right) \overline{i_{dq}^h} + \frac{d\psi_{dq}^h}{dt} + jh\omega_e \psi_{dq}^h \quad (6-19)$$

$$\psi_{dq}^h = l_1 i_{dq}^h + \left(l_2 e^{-j2(h-1)\theta_e} + l_3 e^{-j2h\theta_e} + l_4 e^{j(-2h\theta_e + \frac{\pi}{2})} \right) \overline{i_{dq}^h} + \psi_{fdq}^h$$

where the current complex-vector $i_{dq}^h = i_d^h + j i_q^h$, the voltage complex-vector $u_{dq}^h = u_d^h + j u_q^h$, and the PM flux linkage complex-vector $\psi_{fdq}^h = \psi_{fd}^h + j \psi_{fq}^h$. Complex vector $\overline{i_{dq}^h}$ represents the complex conjugate of i_{dq}^h .

From the complex-vector model (6-19), it is easy to explain the frequency modulation effect. The DC current i_{dq}^h can be considered as the excitation. Since the conjugate of i_{dq}^h is still DC current, $\overline{i_{dq}^h}$ times the pulsating inductances yields the pulsating flux linkage and further induces the pulsating electromotive forces. That means the DC current i_{dq}^h in the h^{th} harmonic SRF can modulate the AC electromotive forces, which further generates the AC current harmonics in other frequencies. The orders of the modulated current harmonics are as the same as the orders of the pulsating inductances, i.e. $-2(h-1)$ and $-2h$. The $-2(h-1)$ one is related to the salient effect and the $-2h$ one is related to the asymmetry among three-phases. For example, regard the -5th current harmonic as the excited current harmonic, because of the salient effect, it can modulate the 12th current harmonic in the -5th harmonic SRF. Meanwhile, it can modulate the 10th current harmonic because of the asymmetry. In the stationary frame, the above modulated 12th and 10th current harmonics are the positive-sequence 7th and positive-sequence 5th current harmonics, respectively.

In conclusion, in terms of salient effect, the excited current harmonic and the modulated current harmonic are symmetrical about the reference of the fundamental SRF in spectrum, e.g. the 7th modulated by the -5th, and the -2nd modulated by the 4th. In terms of the asymmetry among three-phases, the excited current harmonic and the modulated current harmonic are symmetrical about the reference of the stationary frame in spectrum, e.g. the -1st modulated by the 1st, the 5th modulated by the -5th. This also implies that if without effective regulation of the modulated current harmonic, the modulated current harmonic disappears once the excited current harmonic is suppressed, whereas it should exist when the excited current harmonic exists.

The current harmonics can be depicted in spectrum as shown in Fig. 6.1. By considering both even-order and odd-order harmonics, the current harmonics are mapped as shown in Fig. 6.1(a). It is worth noting that these harmonics in Fig. 6.1(a) are originally symmetrical about the reference of the fundamental SRF, and thus, the salient effect will not modulate new current harmonics. Nevertheless, after introducing the asymmetry, more new current harmonics are modulated by the original current harmonics, and the spectrum can be depicted as Fig. 6.1(b).

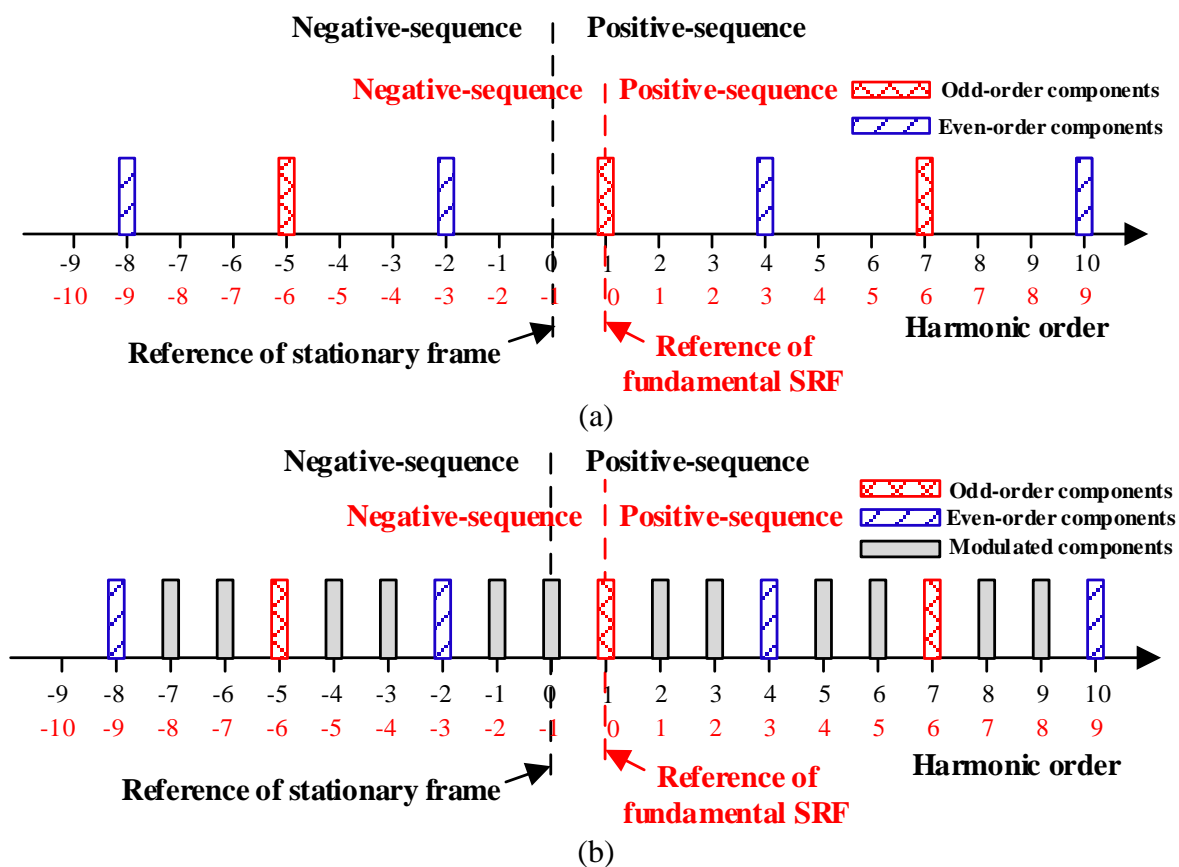


Fig. 6.1. Current harmonics in stationary frame and SRF considering both odd-order and even-order harmonics. (a) Without asymmetry. (b) With asymmetry.

6.3 Proposed Control Strategy

6.3.1 Arbitrary Current Harmonic Decomposition

As aforementioned analysis, considering inverter nonlinearity, non-ideal PM flux linkage, and impedance asymmetry, the orders of current harmonics are not fixed to the general odd orders, e.g. the -5th and 7th in conventional harmonic analysis, and can be arbitrary, as shown in Fig. 6.1(b). To achieve selective closed-loop control of arbitrary current harmonic, the first step is to separate the selected current harmonic from phase current. As introduced in Chapter 1, most existing methods employ digital filter techniques to attenuate the fundamental component as well as the other harmonic components and remain the selected current harmonic. The weakness of these filter-based methods is large delay in current harmonic feedback, which will greatly limit the bandwidth of the current harmonic regulator. Actually, it is only necessary to decouple the fundamental and the selected current harmonic, because compared to the fundamental, the other current harmonics have much smaller amplitudes. If the selected current harmonic is decomposed with the fundamental, filters are not required in the feedback path of the current harmonic regulator.

The three-phase currents can be expressed by the sum of a series of current harmonics as

$$\mathbf{I}_{abc} = \sum \mathbf{I}_{abc}^h = \sum \begin{bmatrix} i_a^h \\ i_b^h \\ i_c^h \end{bmatrix} \quad (6-20)$$

where

$$\begin{aligned} i_a^h &= I_m^h \cos(\theta^h) \\ i_b^h &= I_m^h \cos\left(\theta^h - \frac{2\pi}{3}\right) \\ i_c^h &= I_m^h \cos\left(\theta^h + \frac{2\pi}{3}\right) \\ \theta^h &= h\theta_e + \theta_0^h \end{aligned} \quad (6-21)$$

Current \mathbf{I}_{abc}^h represents the three-phase current harmonic with arbitrary order h . Symbols I_m^h and θ_0^h are the amplitude and initial phase angle of the h^{th} current harmonic, respectively. Current \mathbf{I}_{abc}^h can be transformed into two-phase $\alpha\beta$ stationary frame as follows:

$$\mathbf{I}_{\alpha\beta} = \sum \mathbf{I}_{\alpha\beta}^h = \frac{2}{3} \begin{bmatrix} 1 & -1/2 & -1/2 \\ 0 & \sqrt{3}/2 & -\sqrt{3}/2 \end{bmatrix} \mathbf{I}_{abc} \quad (6-22)$$

where

$$\mathbf{I}_{\alpha\beta}^h = \begin{bmatrix} i_{\alpha}^h \\ i_{\beta}^h \end{bmatrix} = \begin{bmatrix} I_m^h \cos(\theta^h) \\ I_m^h \cos\left(\theta^h - \frac{\pi}{2}\right) \end{bmatrix} \quad (6-23)$$

Using the space vector approach to describe the current components, the axes of three-phase ABC stationary frame and two-phase $\alpha\beta$ stationary frame are shown in Fig. 6.2(a). The axis of phase α is aligned with the axis of phase A. The vector I^h means the space vector of the h^{th} current harmonic, and I^1 represents the fundamental current vector. Current i_{α}^h and i_{β}^h represent the projection of I^h on phase α and phase β , respectively.

To separate the harmonic and the fundamental, a virtual three-phase XYZ winding set is introduced, as shown in Fig. 6.2(b). The virtual three-phase set is spatially shifted by angle λ compared to the physical three-phase ABC winding set. The physical current \mathbf{I}_{abc} is time-shifted by angle γ to build the virtual three-phase current \mathbf{I}_{xyz} of the XYZ set. To be precise, the fundamental component in \mathbf{I}_{abc} is shifted by γ , whereas the h^{th} harmonic component is shifted by $h\gamma$. Then, the virtual current \mathbf{I}_{xyz} can be expressed as follows

$$\mathbf{I}_{xyz} = \sum \begin{bmatrix} i_x^h \\ i_y^h \\ i_z^h \end{bmatrix} = \sum \begin{bmatrix} I_m^h \cos(\theta^h - h\gamma) \\ I_m^h \cos\left(\theta^h - \frac{2\pi}{3} - h\gamma\right) \\ I_m^h \cos\left(\theta^h + \frac{2\pi}{3} - h\gamma\right) \end{bmatrix} \quad (6-24)$$

Transforming the virtual current \mathbf{I}_{xyz} to the $\alpha\beta$ stationary frame yields

$$\mathbf{I}_{\alpha\beta v} = \sum \mathbf{I}_{\alpha\beta v}^h = \sum \begin{bmatrix} i_{\alpha v}^h \\ i_{\beta v}^h \end{bmatrix} = \sum \begin{bmatrix} I_m^h \cos(\theta^h + \lambda - h\gamma) \\ I_m^h \cos\left(\theta^h + \lambda - h\gamma - \frac{\pi}{2}\right) \end{bmatrix} \quad (6-25)$$

where the “v” in the subscript means the virtual variables. Likewise, the virtual current vector can also be depicted as shown in Fig. 6.2(b), where I_v^1 and I_v^h are the virtual fundamental current vector and the virtual h^{th} harmonic current vector, respectively. Comparing (6-23) and (6-25), it is easy to find that the phase angle difference between $\mathbf{I}_{\alpha\beta}^h$ and $\mathbf{I}_{\alpha\beta v}^h$ is $\lambda - h\gamma$, which makes that the space phase angle difference between vectors I^h and I_v^h is also $\lambda - h\gamma$, see Fig. 6.2(b).

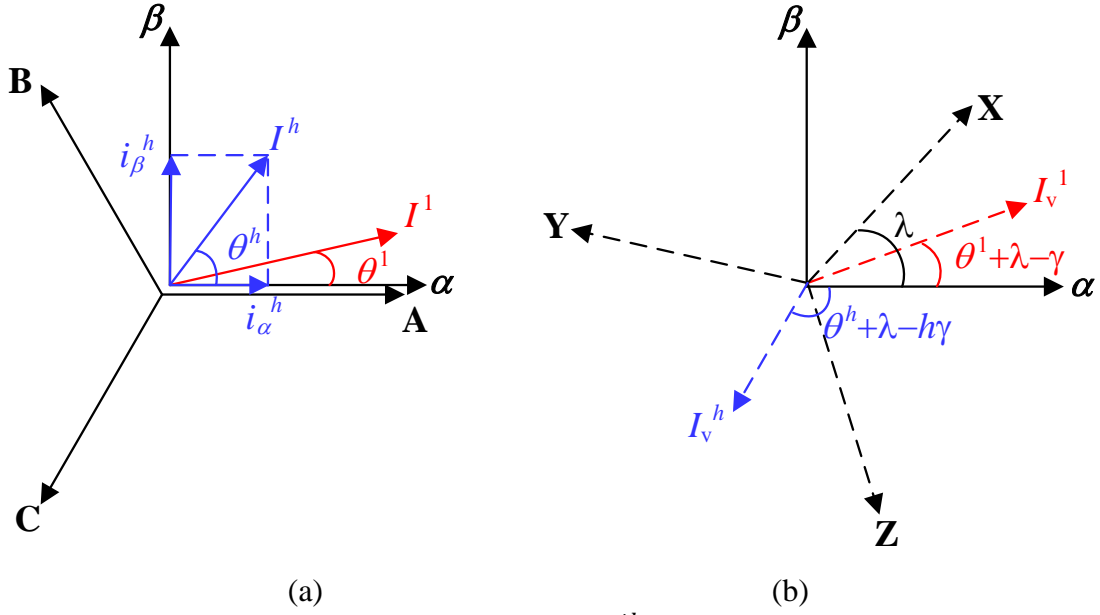


Fig. 6.2. Space vectors of the fundamental and the h^{th} current harmonic. (a) Original physical system. (b) Virtual system.

The vectors of the current fundamental and the h^{th} current harmonic can be decomposed if the angles λ and γ are properly designed. The vector space decomposition follows the principles: the physical fundamental current vector should be in-phase with the virtual fundamental current vector; the physical h^{th} harmonic current vector should be out-of-phase to the virtual h^{th} harmonic current vector. To satisfy such principles, the angles λ and γ are designed as

$$\lambda = \gamma = |\pi/(1 - h)| \quad (6-26)$$

Then, the physical and virtual currents satisfy

$$\mathbf{I}_{\alpha\beta}^1 = \mathbf{I}_{\alpha\beta v}^1, \quad \mathbf{I}_{\alpha\beta}^h = -\mathbf{I}_{\alpha\beta v}^h \quad (6-27)$$

Account is merely taken of the fundamental and the h^{th} harmonic, the currents $\mathbf{I}_{\alpha\beta}$ and $\mathbf{I}_{\alpha\beta v}$ satisfy

$$\begin{aligned} \mathbf{I}_{\alpha\beta} &= \mathbf{I}_{\alpha\beta}^1 + \mathbf{I}_{\alpha\beta}^h \\ \mathbf{I}_{\alpha\beta v} &= \mathbf{I}_{\alpha\beta v}^1 + \mathbf{I}_{\alpha\beta v}^h \end{aligned} \quad (6-28)$$

Substituting (6-27) into (6-28), the fundamental can be decomposed by calculating the sum of $\mathbf{I}_{\alpha\beta}$ and $\mathbf{I}_{\alpha\beta v}$, while the h^{th} current harmonic can be decomposed by calculating the difference between $\mathbf{I}_{\alpha\beta}$ and $\mathbf{I}_{\alpha\beta v}$, i.e.

$$\mathbf{I}_{\alpha\beta}^1 = \frac{\mathbf{I}_{\alpha\beta} + \mathbf{I}_{\alpha\beta v}}{2} \quad (6-29)$$

$$\mathbf{I}_{\alpha\beta}^h = \frac{\mathbf{I}_{\alpha\beta} - \mathbf{I}_{\alpha\beta v}}{2}$$

With the help of virtual three-phase set, the arbitrary current harmonic can be separated from the fundamental, which provides convenience for further current harmonic regulation. Actually, the virtual currents can be regarded as auxiliary currents that are used to eliminate the fundamental component and remain the selected harmonic component.

The simulation waveforms in Fig. 6.3 show the process of the proposed current harmonic decomposition. In the simulation, there are fundamental ($h=1$) and negative-sequence second harmonic ($h=-2$) components coupled in the three-phase currents \mathbf{I}_{abc} . Equation (6-26) shows λ and γ should be designed as $\pi/3$ if $h=-2$, i.e. \mathbf{I}_{abc} should be shifted by $\pi/3$ to derive \mathbf{I}_{xyz} . Then, \mathbf{I}_{abc} and \mathbf{I}_{xyz} are transformed to the $\alpha\beta$ stationary frame as $\mathbf{I}_{\alpha\beta}$ and $\mathbf{I}_{\alpha\beta v}$. Using (6-29), the negative-sequence second current harmonic can be separated from the fundamental, as the i_{α}^{-2} and i_{β}^{-2} . The order of the decomposed current harmonic can be extended from -2 to arbitrary order by changing the time phase shift angle γ between \mathbf{I}_{abc} and \mathbf{I}_{xyz} as well as the spatial phase shift angle λ between the physical and virtual three-phase frames.

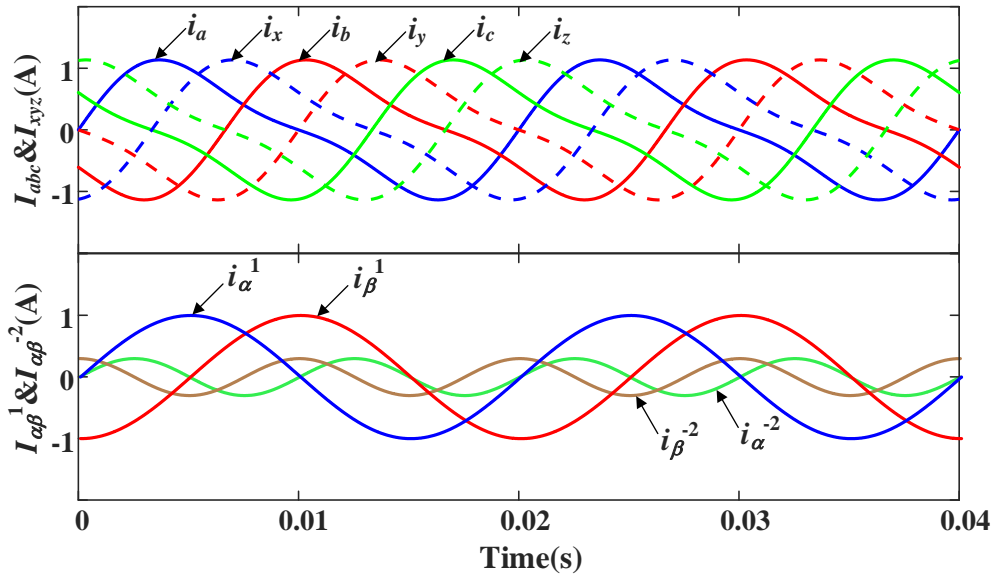


Fig. 6.3. Simulation current waveforms. \mathbf{I}_{abc} is composed of the fundamental ($h=1$) and negative-sequence second harmonic ($h=-2$) components. \mathbf{I}_{xyz} is the $\pi/3$ time phase shifting of \mathbf{I}_{abc} . Using (6-29), the fundamental and harmonic components can be decomposed as i_{α}^1 , i_{β}^1 and i_{α}^{-2} , i_{β}^{-2} , respectively.

6.3.2 Current Harmonic Regulation

Similar to the regulation of the fundamental, the decomposed current harmonics can be transformed into the harmonic SRF and then controlled by the PI regulator. As depicted in Fig. 6.4(a), the proposed control strategy follows the steps:

Step 1: Calculate λ and γ using (6-26) according to the order h of the selected current harmonic.

Step 2: Shift I_{abc} by phase angle γ to build I_{xyz} , and transform I_{abc} and I_{xyz} to $\alpha\beta$ frame as $I_{\alpha\beta}$ and $I_{\alpha\beta v}$.

Step 3: Decompose the h^{th} current harmonic $I_{\alpha\beta}^h$ using (6-29).

Step 4: Transform the decomposed $I_{\alpha\beta}^h$ to the h^{th} harmonic SRF as I_{dq}^h , and regulate I_{dq}^h with the PI regulator.

Step 5: Transform the output of the PI regulator to $\alpha\beta$ frame and added to the output voltage of speed & torque controller.

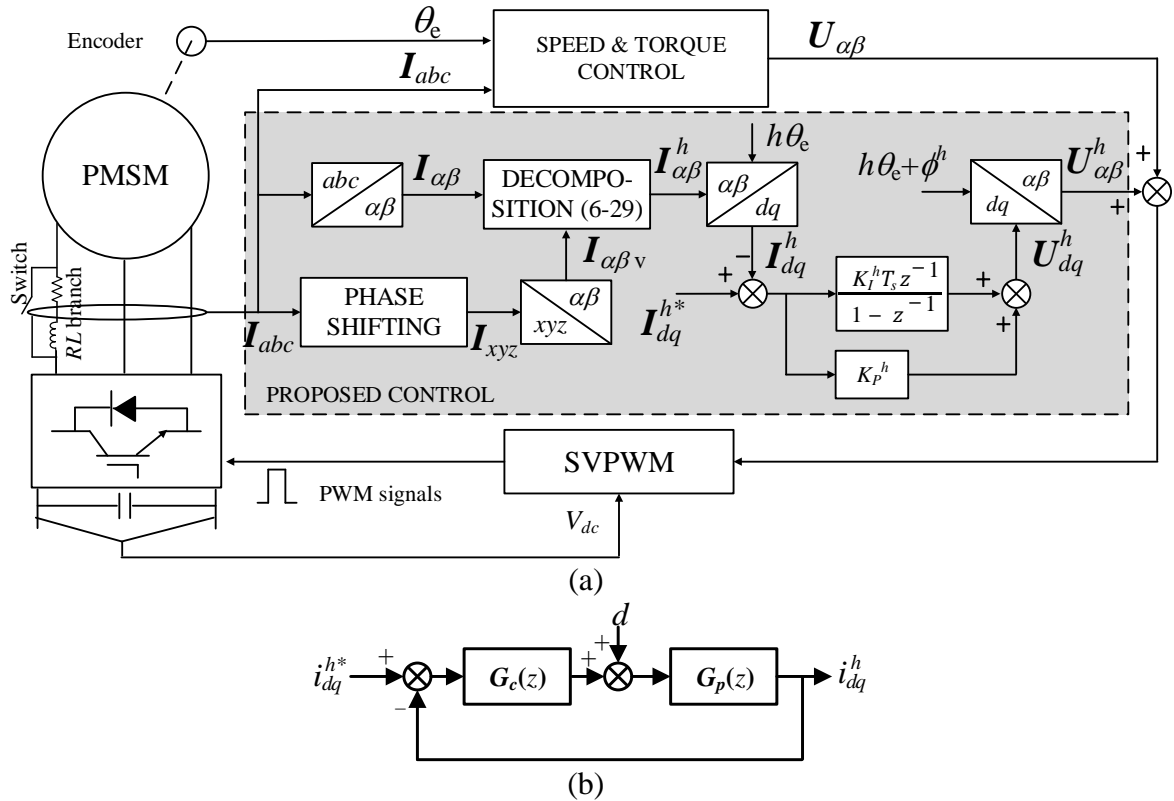


Fig. 6.4. Block diagrams of the proposed control strategy. (a) Overall control block diagrams. (b) Simplified model of current harmonic loop.

Since both the current harmonic and reference are the DC values in the harmonic SRF, the PI regulator is a preferable solution for DC reference tracking and DC disturbance rejection. To simplify the parameter tuning, the stator resistance and inductance are used to build the coefficients K_P^h and K_I^h in the regulators as reported in [YEP11],

$$\begin{aligned} K_I^h &= k_c^h R_s \\ K_P^h &= k_c^h \frac{L_d + L_q}{2} \end{aligned} \tag{6-30}$$

where k_c^h is the gain coefficient of the harmonic current regulator. The integral coefficient K_I^h is related to the resistance. The proportional coefficient K_P^h is related to the inductance. The asymmetric resistance and inductance are usually uncertain and small, and considering that it is the DC component that needs to be regulated, K_I^h and K_P^h can be set as the products of k_c^h and the average values of the certain resistance and inductance, respectively, see (6-30). The current harmonic reference I_{dq}^{h*} can be set as 0 to achieve current harmonic suppression, while it can also be set as the pre-designed values to inject specific current harmonics and achieve different optimization objectives, such as the maximum average torque [WAN15][HU17] and the minimal torque ripples [YAN19][GIR21][CHO21][FEN19][WU21]. Besides, it is assumed that the DC-link voltage is unlimited to provide available voltage for the proposed current harmonic regulation in this chapter. When the motor speed is above the base speed and the inverter voltage is unavailable, as reported in [KAR17], the current harmonic references can be specially designed to make full use of the modulation region between the maximum voltage circle and the voltage hexagon, and the current harmonics can be partially reduced, but not eliminated. This method can also be categorized to the current harmonic injection.

The output of the PI regulator is inversely transformed to the stationary frame, and to enhance the stability, a compensation angle ϕ^h should be employed to adjust the phase of voltage $U_{\alpha\beta}^h$ to compensate the delay effect due to the computation. The value of ϕ^h is determined by the phase variation of the harmonic SRF from the sampling moment to the PWM duty updating moment, and is equivalent to $1.5h\omega_e T_s$ in this chapter.

It is worth noting that for the cases of high-order harmonics or high-speed conditions in which the machine almost becomes a purely inductive load, to increase the stable margin and improve the dynamic performance, a 90 degrees phase lead angle [YEP11] is introduced and it should have the same polarity as the delay compensation angle, as

$$\phi^h = 1.5h\omega_e T_s + \frac{\pi}{2} \text{sgn}(h) \quad (6-31)$$

Fig. 6.4(b) shows the simplified model of the current harmonic loop. Terms $\mathbf{G}_c(z)$ and $\mathbf{G}_p(z)$ represent the transfer functions of the current harmonic regulator and the plant, respectively. From the model (6-19) and considering the zero-order-hold effect of inverter, $\mathbf{G}_p(z)$ can be derived as

$$\mathbf{G}_p(z) = \frac{z^{-2} \left(1 - e^{-\frac{r_1 T_s}{l_1}} \right)}{r_1 e^{jh\omega_e T_s} \left(e^{jh\omega_e T_s} - z^{-1} e^{-\frac{r_1 T_s}{l_1}} \right)} \quad (6-32)$$

where T_s is the sampling period. The pulsating flux linkage and the PM flux linkage can be considered as the disturbance d . Fig. 6.5 shows the open-loop Bode Diagrams of current harmonic loop in Fig. 6.4(b). The employed parameters are as follows: $r_1=1.1\Omega$, $l_1=8.75\text{mH}$, $T_s=0.0001\text{s}$, $K_I^h=288$, $K_P^h=2.12$. The employed machine parameters are the same as the test machines in Section 6.4. Three angular frequencies, 25rad/s, 135rad/s, 3581rad/s, are selected for $h\omega_e$ in the simulation. It can be observed from Fig. 6.5 that there is each 0dB crossing in positive- and negative-sequence frequencies. The smaller difference, between the phase curve and the ± 180 degrees (stability limit) at the frequencies of the two 0dB crossings, represents the phase margin and determines the stability of the current harmonic loop. Both high speed ω_e and high order h can lead to large $h\omega_e$, and from Fig. 6.5, the larger $h\omega_e$ causes smaller bandwidth and the less phase margin. After introducing the phase compensation angle ϕ^h , the phase curve of 3581rad/s is changed to be further away from the -180 degrees, which implies that the stability is enhanced.

For a general PMSM, the -5th and 7th current harmonics are the major components that need to be regulated. According to (6-26), the phase shift angles λ and γ should be $\pi/6$ to decompose the -5th and 7th current harmonics simultaneously, and the harmonic current loop designed in Fig. 6.4 are required for each of them. In a system that requires the regulation of multiple current harmonics, such as the higher odd harmonics, the even harmonics, and the harmonics due to asymmetry among phases, the phase shift angles for each current harmonic can also be calculated using (6-26), and more current harmonic loops should be parallel utilized to control them. The major problems are high computation burden caused by the trigonometric functions and complicated parameter tuning of multiple PI regulators. The computation burden can be reduced by using the sine look-up-table (LUT) method to calculate the values of trigonometric

functions. Since the proposed current harmonic regulator uses the resistance and inductance for PI coefficients, there is only one tuned parameter, k_c^h , for each current harmonic. To further simplify the tuning work, the current harmonics, that share the same phase shift angles λ and γ , share the same k_c^h in this thesis, e.g. k_c^{-5} is equivalent to k_c^7 when tuning. Compared to the existing multiple SRF methods as studied in [CHA00][UZ16][YAN21b][WAN21][WU21][LIU32][FEN33][WU34], the parameter tuning is simplified. Because there are only limited addition and multiplication operations in the proposed current harmonic decomposition, the computation burden does not increase too much.

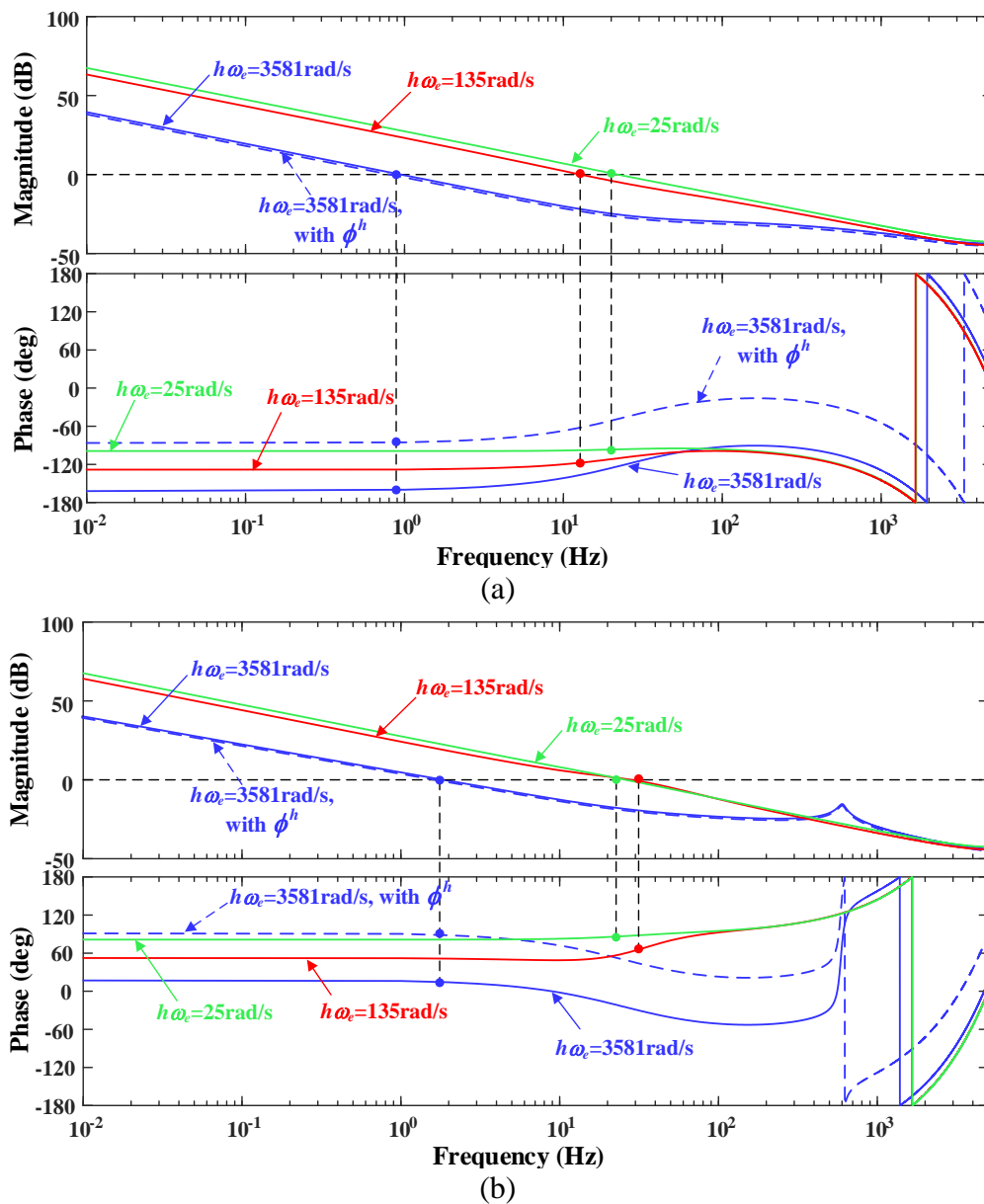


Fig. 6.5. Open-loop Bode Diagrams of the h^{th} current harmonic loop. The employed parameters are: $r_1=1.1\Omega$, $l_1=8.75\text{mH}$, $T_s=0.0001\text{s}$, $K_I^h=288$, $K_p^h=2.12$. (a) Positive-sequence. (b) Negative-sequence.

6.4 Experimental Verification

Experiments are processed on a laboratory platform which includes dSPACE (DS1105), a three-phase VSI, a DC power supply, a PMSM, and a load dyno-machine, Fig. 6.6(a). The parameters of the test machine and drive are given in TABLE 6.1.

TABLE 6.1
PARAMETERS OF TEST MACHINE AND DRIVE

Parameters	Values
Number of pole pairs	4
Stator resistance R_s	0.917Ω
D-axis inductance L_d	6.29mH
Q-axis inductance L_q	7.21mH
Rated speed	400rpm
Rated torque	2.79Nm
DC linkage voltage	48V
Sampling & switching frequency	10kHz

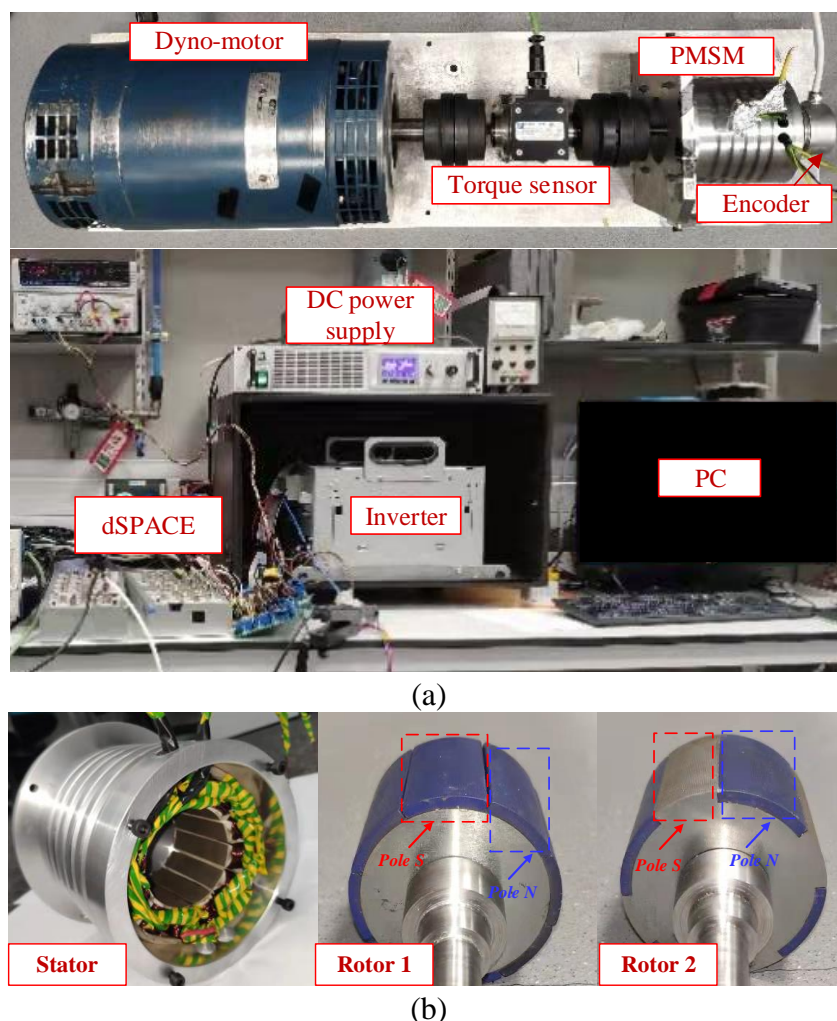


Fig. 6.6. Laboratory test system. (a) Pictures of the platform. (b) Pictures of stator and rotors.

The test results of current harmonic decomposition and suppression are shown in Fig. 6.7. Since the test machine is a general PMSM with a surface-mounted PM rotor (Rotor 1, Fig. 6.6(b)), the even-order harmonics are small and the major current harmonics that need to be regulated are the -5th and 7th ones. In Fig. 6.7(a), it can be seen that the virtual currents i_x , i_y , and i_z are the $\pi/6$ phase shifting of the physical currents i_a , i_b , and i_c , and using the proposed decomposition, the -5th and 7th current harmonics are decomposed from phase current, Fig. 6.7(b). From the spectra in Fig. 6.7(b), the decomposed currents only include the -5th and 7th, and the fundamental current is decomposed and hence negligible. This has proved the effectiveness of the proposed decomposition method in a general PMSM. The suppression is activated at 0.1s, and the gain coefficients k_c^{-5} and k_c^7 are set as 314. The waveforms as well as the spectra in Fig. 6.7(b) show that the -5th and 7th current harmonics are almost eliminated by the designed regulators. As a result, the three-phase currents become more sinusoidal and the THD is reduced from 5.37% to 1.86%.

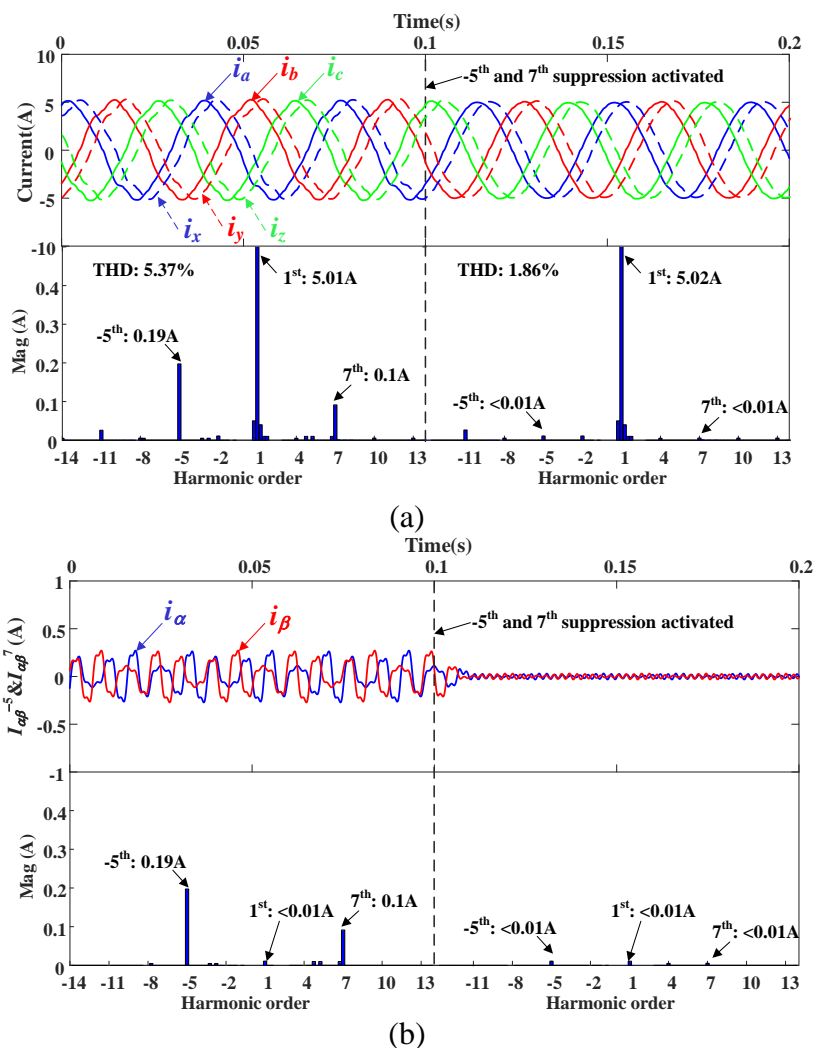


Fig. 6.7. Measured current waveforms and the spectra under rated speed and rated torque of a general PMSM. (a) Phase current. (b) Decomposed -5th and 7th current harmonics.

On the basis of the test in Fig. 6.7, the step response of the -5th current harmonic is carried out, and the test results are compared with three existing methods in Fig. 6.8. The reference i_d^{-5*} stepped from 0A to 0.3A at 0.05s and reference i_q^{-5*} remained 0A. The -5th current harmonic $I_{\alpha\beta}^{-5}$ is decomposed from phase current and can be regulated by the designed PI regulator in the -5th harmonic SRF. That is the proposed method, Fig. 6.8(a). Otherwise, $I_{\alpha\beta}^{-5}$ can also be regulated by the PR regulator in the stationary $\alpha\beta$ frame. That is referred to Method 1 as shown in Fig. 6.8(b), and the high-performance digital PR regulator studied in [YEP11] is employed in Method 1. Method 2 is based on the high-precision current harmonic detection studied in [LIU19]. Method 3 utilizes the PIR regulator proposed in [XIA15] to control the current harmonic. To make a fair comparison, the resonant coefficients and integral coefficients in these methods are set as 288, and all the proportional coefficients are set as 2.12.

From the test results in Fig. 6.8, both the proposed method and Method 2 can rapidly track the current harmonic reference in 0.01s, which is faster than 0.03s in Method 1. Due to the high-precision current harmonic detection, Method 2 shows the smallest current ripples at steady-state but obvious overshoot and pulsating during the dynamics. In Method 3, because the PIR regulator is used to control the fundamental and the harmonic currents simultaneously, the DC current harmonic reference i_d^{-5*} is transformed as the 6th AC reference in the fundamental SRF and added to the dq -axis current references. In Fig. 6.8(d), the DC current harmonic reference i_d^{-5*} steps from 0 to 0.3A which means a 6th sinusoidal current reference with amplitude of 0.3A is added to q -axis current reference so that the PIR regulator will track not only the DC component but also the 6th AC component in the q -axis current reference. From the waveform of q -axis current i_q in Fig. 6.8(d), it takes about 0.05s for the 6th current to track the reference in Method 3, which is slower than the other three methods.

To validate the control performance regarding the even harmonics and the asymmetry-related harmonics, the rotor of the test PMSM in Figs. 6.7 and 6.8 is changed to a rotor with asymmetric north and south poles (Rotor 2, Fig. 6.6(b)), and moreover, an RL branch (3.3Ω and 0.5mH) is series-connected between phase A terminal and the inverter to act as the asymmetry, as shown in Fig. 6.4(a). In Fig. 6.9, the waveforms and spectra of measured current and torque under rated speed and rated torque are obtained in three cases: asymmetry not introduced and current harmonic suppression not activated in Fig. 6.9(a); asymmetry introduced and current harmonic suppression not activated in Fig. 6.9(b); asymmetry introduced and current harmonic suppression activated in Fig. 6.9(c).

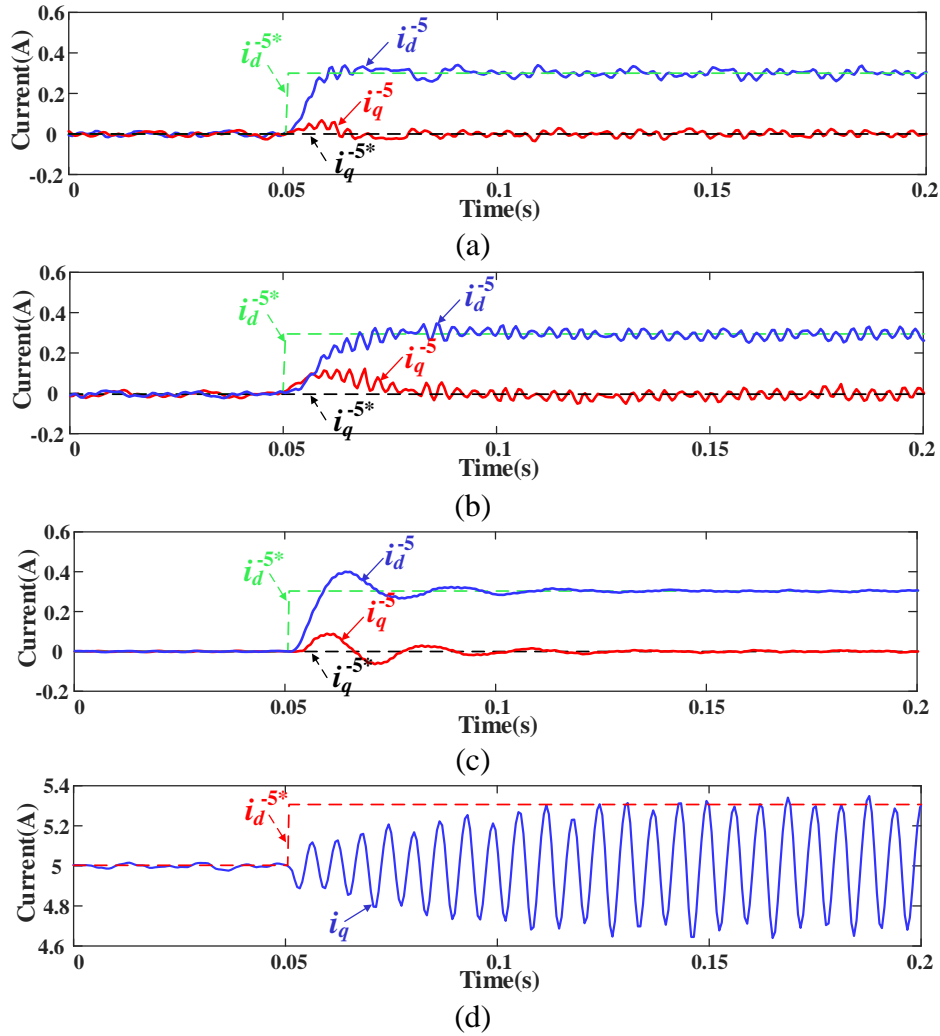
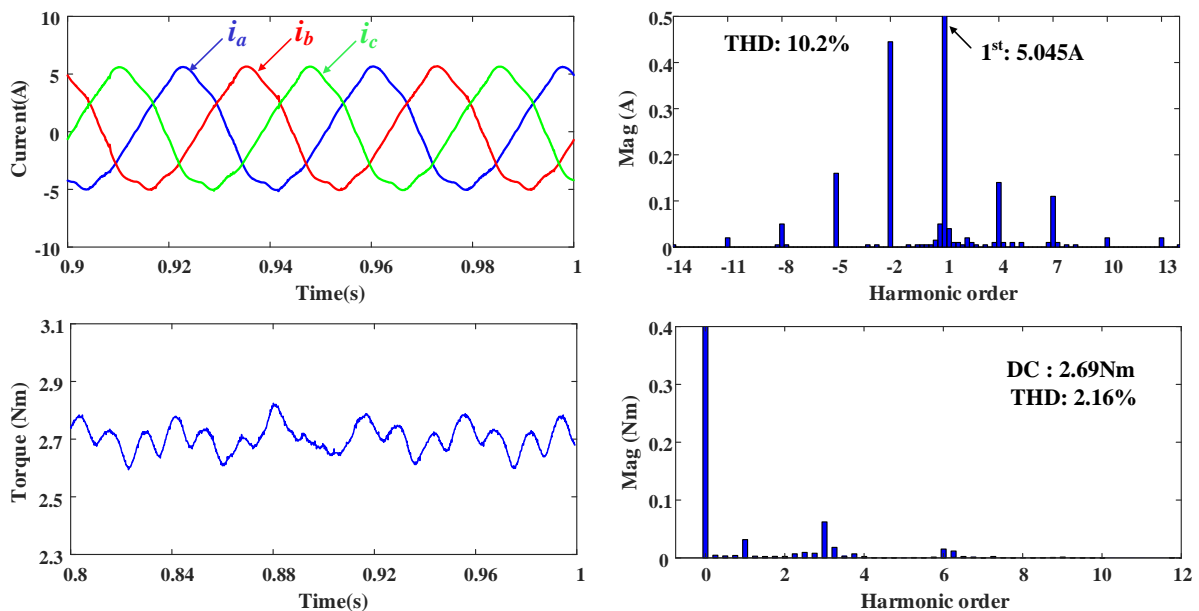


Fig. 6.8. Measured step responses of the -5^{th} current harmonic under rated speed and rated torque of the general PMSM. i_d^{-5*} stepped from 0A to 0.3A at 0.05s and i_q^{-5*} remained 0A. The resonant coefficients and integral coefficients in these methods are set as 288, and all the proportional coefficients are set as 2.12. (a) Proposed. (b) Method 1. (c) Method 2. (d) Method 3.

From the spectrum in Fig. 6.9(a), there are inherent odd- and even-order current harmonics caused by inverter nonlinearity and back-EMF harmonics, which lead to the 1st, 3rd, and 6th torque ripples. After the asymmetry introduced, as shown in Fig. 6.9(b), the three-phase current becomes unbalanced, and there are consequently a lot of new harmonics produced, majorly the harmonics with the orders of -3, -1, 2, 3, and 5. The 2nd torque ripple increases significantly due to the unbalanced currents. The THDs of phase current and torque have increased from 10.2% and 2.16% to 11.7% and 14.16%, respectively. The current spectrum in Fig. 6.9(b) is consistent with the analysis of Fig. 6.1(b) in Section II. Fig. 6.9(c) shows the experimental

results after the proposed current harmonic regulation activated. The current harmonics with the orders -11, -8, -5, -2, -1, 3, 4, 7, 10, and 13 are selected to be suppressed, which means γ and λ should be $\pi/2$ for the decomposition of the -1st and 3rd, $\pi/3$ for the -2nd and 4th, $\pi/6$ for the -5th and 7th, $\pi/9$ for the -8th and 10th, and $\pi/12$ for the -11th and 13th, respectively. The almost sinusoidal currents and the current spectrum in Fig. 6.9(c) indicates that these current harmonics can be effectively suppressed and the hence the current THD is reduced to 2.4%. The torque spectrum shows that the torque ripples are also greatly suppressed and the torque THD is reduced to 1.71% due to the current harmonic suppression. The loss can be roughly evaluated by the difference between the electrical power input from the DC link and the output mechanical power, and these power differences in the three cases of Fig. 6.9 are measured as 45.57W, 48.95W, and 41.09W. It should be noted that the losses on the additional *RL* branch are subtracted from the power differences above. The measured power differences indicate that due to the good suppression of the current harmonics and torque ripples, the proposed method in Fig. 6.9(c) shows the reduced power losses compared to the other two cases in Figs. 6.9(a) and 6.9(b).



(a)

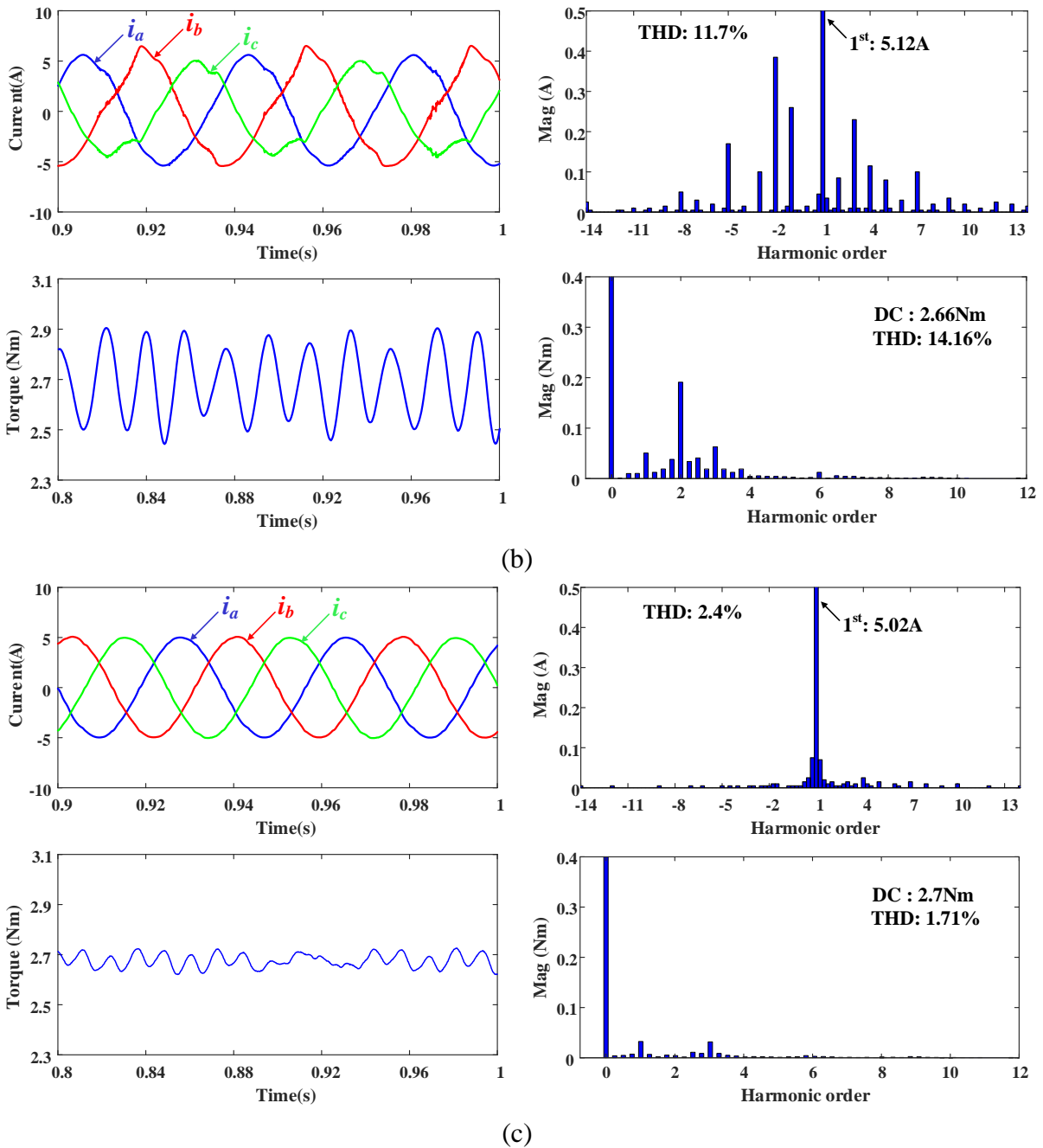


Fig. 6.9. Waveforms and spectra of measured current and torque under rated speed and rated torque of the PMSM with a Rotor 2. (a) Without asymmetry. (b) With asymmetry. (c) With asymmetry and using the proposed harmonic regulation to suppress the current harmonics with orders -11, -8, -5, -2, -1, 3, 4, 7, 10, and 13.

The robustness test is shown in Fig. 6.10, where the test conditions are the same as Fig. 6.9(c) but the load torque stepped from 50% rated torque to 100% rated torque at 1s. It can be seen that the load torque step caused a 42r/min speed drop, and simultaneously the amplitudes of three-phase currents increased from ~2.5A to ~5A. From 1s to 1.5s, the current waveforms are almost sinusoidal, which means the current harmonics are well regulated during the dynamics.

However, the three-phase currents are unbalanced in the dynamics. This is because there are negative-sequence fundamental current increasing as the phase current amplitudes increases. As the amplitudes become stable at around 1.5s, the negative-sequence fundamental can be suppressed by the regulator and thus the three-phase currents are balanced eventually. The robustness test results show that the proposed method is not significantly influenced by the sudden torque variation.

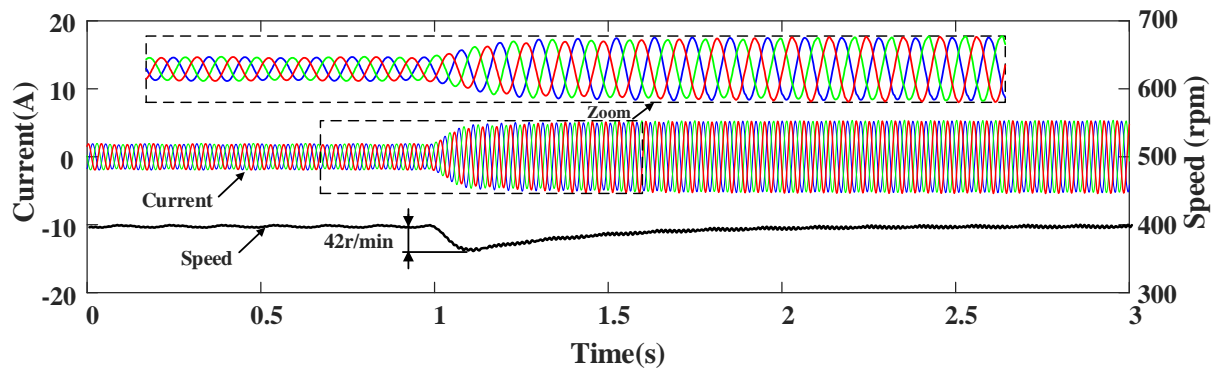


Fig. 6.10. Measured waveforms of current and speed when the speed reference is 400r/min and the load torque stepped from 50% rated torque to 100% rated torque at 1s. The same asymmetry is introduced and the same harmonic regulators are used as they are in Fig. 9(c).

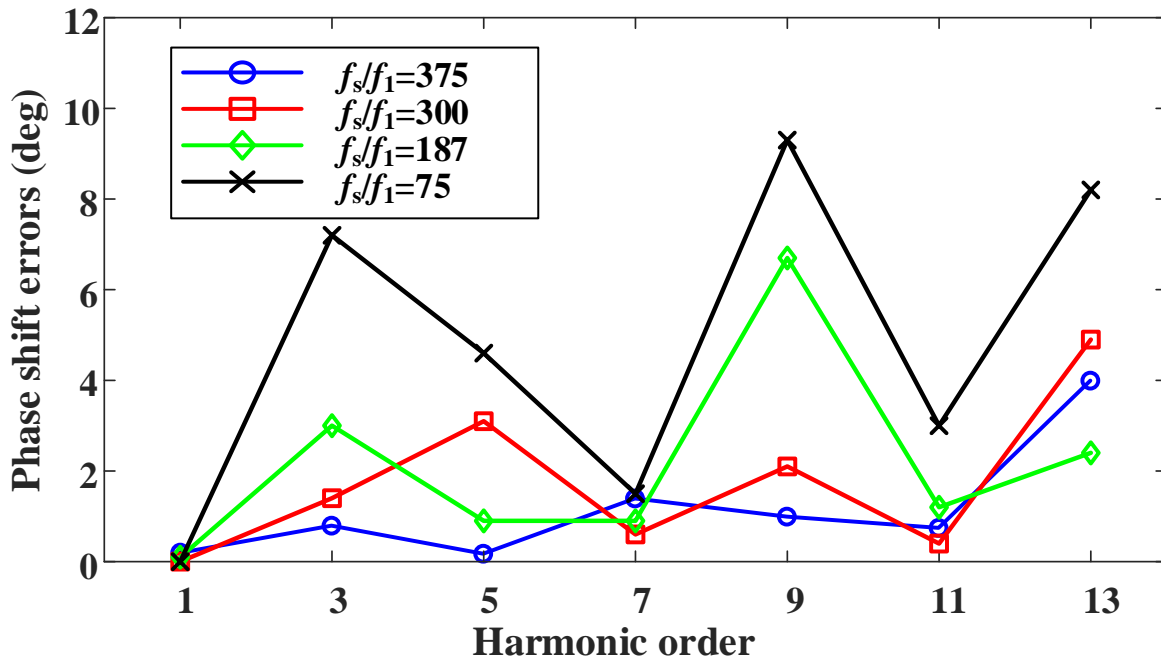


Fig. 6.11. Measured results of phase shift errors under different carrier-to-fundamental ratio. The physical current is shifted by $\pi/6$ to build the virtual current, and the phase shift errors are the phase angle difference between expected virtual current and measured virtual current.

Fig. 6.11 shows the test results of phase shift errors under different carrier-to-fundamental ratios. The physical current is shifted by $\pi/6$ to build the virtual current. Using FFT tool, the phase shift errors can be calculated as the phase angle difference between the expected virtual current and the test virtual current. It can be seen from Fig. 11 that the fundamental phase shift errors are almost zero, which means the fundamental component can be accurately shifted and eliminated in the proposed current harmonic decomposition. However, the harmonic phase shift errors are larger than the fundamental ones, especially under low carrier-to-fundamental ratio. This will lead to the magnitude and phase angle errors between the decomposed current harmonic and the real current harmonic. Since all the tested harmonic phase shift errors are not significant (<10 degrees), their effect on the current harmonic regulation is negligible and the control performance is not obviously affected by these phase shift errors.

6.5 Conclusion

A novel current harmonic control method is proposed in this chapter to achieve arbitrary current harmonic decomposition and regulation. Compared to the conventional harmonic analysis mainly regarding the 5th and 7th, this chapter has developed a comprehensive electrical model to analyze more new current harmonics, e.g. the -2nd, the -1st, the 3rd, and the 4th. A novel virtual three-phase system is proposed to decompose the arbitrary current harmonic from the phase current. Based on the proposed current harmonic decomposition, it is easy to achieve arbitrary current harmonic suppression and injection using the PI regulators in the corresponding harmonic SRFs. Implementation details are introduced to reduce the computation burden and simplify the parameter tuning. Experimental results have validated the correctness of the theoretical analysis. The proposed control method is compared with existing typical methods aimed at rapid current harmonic response, and it is concluded that the proposed method provides better dynamic performance with reduced pulsating, overshoot, and convergence time.

Although the method is analyzed and verified in a PMSM system, the concept of the virtual three-phase system, together with the proposed current harmonic decomposition and regulation, can be extended to any other three-phase electric drives that require arbitrary current harmonic suppression or injection.

CHAPTER 7

GENERAL CONCLUSION

DTP PM machines have small impedance to limit the current harmonics, which makes the current harmonics more serious in DTP PM machines compared to the conventional single three-phase machines. This thesis focuses on the field oriented control (FOC) of DTP PM machines, with particular reference to the control of current harmonics. A brief outline of this thesis is shown in Fig. 7.1. The key techniques contributed by this thesis can be summarized in the following sections.

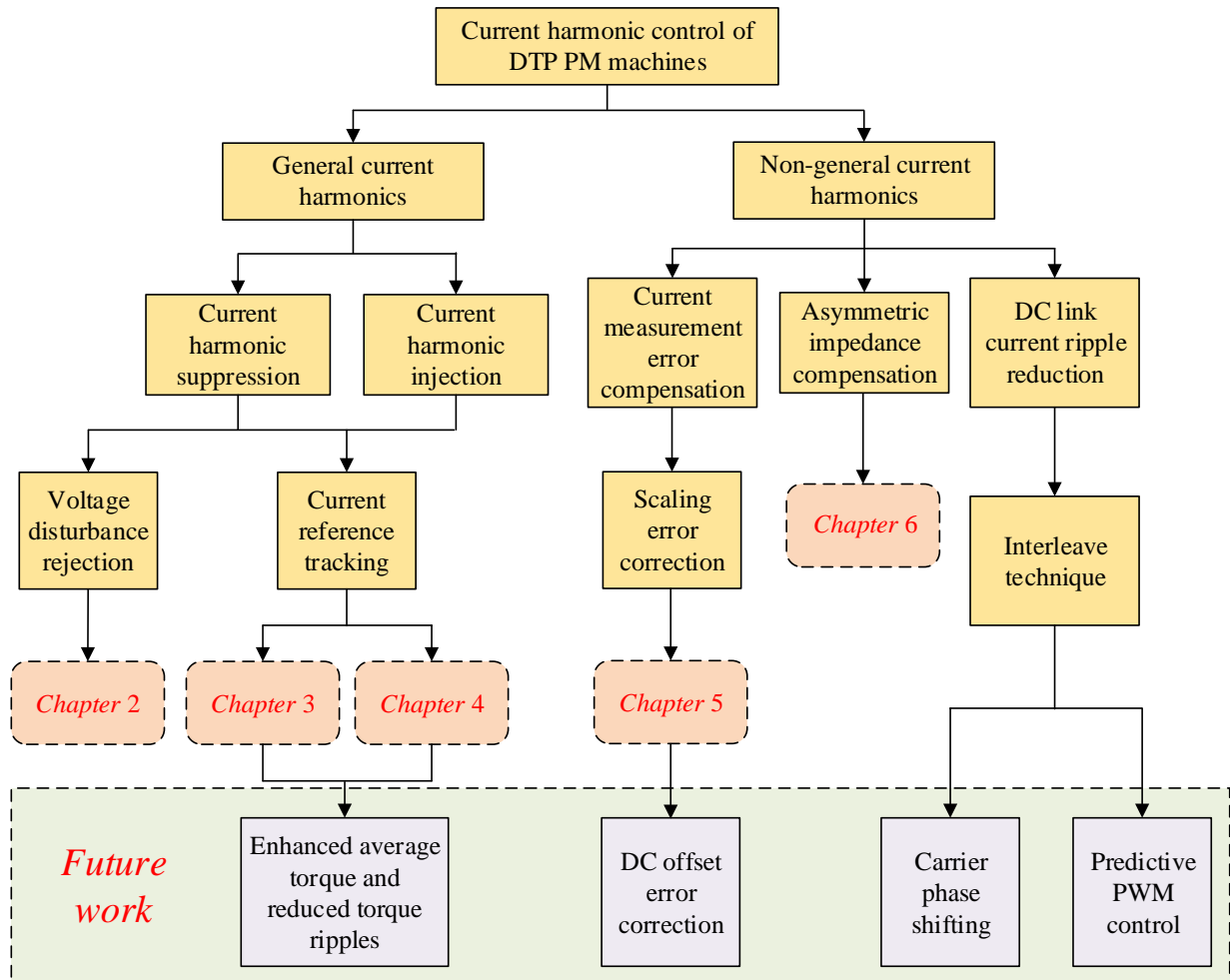


Fig. 7.1. Brief outline of research in this thesis.

7.1 Virtual Impedance Technique

The virtual impedance technique is usually used in the applications of power grid and high-performance machine drives. It is the first time for its application to DTP PM machines which is carried out in Chapter 2 of this thesis.

The investigated virtual impedance technique shows the following advantages:

- ***More Applicable in DTP PM Machines.*** It is found that the virtual impedance technique is more applicable in DTP PM machines than it is in the conventional three-phase machines. This is because DTP PM machines suffer from the aforementioned small impedance against the current harmonics, and the introduced virtual impedance can increase the equivalent impedance of the machine. Consequently, the enhanced impedance will improve the disturbance rejection capability and suppress the current harmonics.
- ***Current Harmonic Suppression in a Wide Range of Frequency.*** The rejection capability to the disturbance is enhanced in a wide range of frequency, which means not only one or two but multiples current harmonics can be suppressed.
- ***Robust Current Control.*** The analysis and test results also show that the virtual impedance will enhance the robustness of the current regulation by eliminating the overshoot, cross-coupling effect, and pulsating currents due to machine parameter mismatch during dynamic process.
- ***Simple Structure and Easy Implementation.*** The current harmonic can be reduced by only simply modifying the structure of current regulators. Neither observer nor dead-time compensation is required.
- ***Applicable to Other Multi Three-phase Machines.*** The regulators with virtual impedance have a generic structure and can be extended to other multi three-phase machine systems, such as induction machines and synchronous reluctance systems etc, and indeed any machine systems which have low impedance, that may suffer from smaller impedance against harmonic disturbance problems.

However, this technique also has disadvantages as follows.

- ***Limited Virtual Impedance Values.*** Based on the theoretical analysis, the ranges of the virtual resistance and inductance values are limited by the machine physical resistance and inductance. The closer to the limitation the virtual impedance values are, the more

instable the system is.

- ***Not Complete Elimination of Current Harmonics.*** Although the current harmonics in a wide range of frequency can be reduced, they cannot be completely eliminated due to the limitation of virtual impedance values.

The comparison of different disturbance rejection methods is shown in TABLE 7.1. The measured current THDs, torque ripples, and current response time at rated speed and torque condition are compared. It is clear that the proposed virtual impedance technique shows the best steady-state performance regarding current THDs and torque ripples, as well as the comparable dynamic response speed to other disturbance rejection methods.

TABLE 7.1
COMPARISON OF DIFFERENT DISTURBANCE REJECTION METHODS

	Current THDs	Torque ripples	Response time
PIR regulator (Method 1)	3.21%	0.1279Nm	~0.1s
Active damping (Method 2)	4.44%	0.1128Nm	~0.01s
Inverter nonlinearity and back EMF compensation (Method 3)	2.28%	0.0851Nm	~0.1s
Additional PI gains (Method 4)	12.97%	0.1458Nm	~0.01s
Virtual impedance (Proposed)	1.77%	0.0719Nm	~0.01s

7.2 Virtual Multi Three-phase Systems

The concept of virtual multi three-phase systems is proposed in this thesis for the first time, i.e. the virtual triple three-phase system in Chapter 3, the virtual quadruple and virtual pentuple three-phase systems in Chapter 4, and the virtual dual three-phase system in Chapter 6. It is concluded that the decomposition capability of harmonics in machine system increases as the phase number increases, as shown in Fig. 7.2 and concluded in TABLE 7.2.

The characteristics of these virtual multi three-phase systems can be summarized as follows.

- **Phase Shifting Operation Required.** The original physical phase currents are time shifted by a designed angle to derive the virtual phase currents. The axes of the virtual phase currents are virtual and should also be spatially shifted by the same angle with reference to the original physical phase axes. The phase shifting operation will need additional memory and computation burden in a digital controller.
- **Generic VSD Transformation Derived.** To decompose the currents in the virtual multi three-phase system, a generic VSD transformation is derived in this thesis as follows

$$\begin{bmatrix} \alpha\beta \\ z_1z_2 \\ z_3z_4 \\ \dots \\ z_{2m-3}z_{2m-2} \end{bmatrix} = \frac{1}{m} \begin{bmatrix} T(0) & T(\gamma_m) & T(2\gamma_m) & \dots & T((m-1)\gamma_m) \\ T(0) & T(-5\gamma_m) & T(-5(2\gamma_m)) & \dots & T(-5(m-1)\gamma_m) \\ T(0) & T(7\gamma_m) & T(7(2\gamma_m)) & \dots & T(7(m-1)\gamma_m) \\ \dots & \dots & \dots & \dots & \dots \\ T(0) & T(n\gamma_m) & T(n(2\gamma_m)) & \dots & T(n(m-1)\gamma_m) \end{bmatrix} \begin{bmatrix} i_{A1B1C1} \\ i_{A2B2C2} \\ i_{A3B3C3} \\ \dots \\ i_{AmBmCm} \end{bmatrix} \quad (7-1)$$

where m is the number of virtual three-phase sets, $\gamma_m = \pi/(3m)$ is the electrical angle between two adjacent sets, and $n=1, -5, 7, -11, 13, \dots$. The submatrix T is

$$T(\theta) = \frac{2}{3} \begin{bmatrix} \cos \theta & \cos(\theta + 2\pi/3) & \cos(\theta - 2\pi/3) \\ \sin \theta & \sin(\theta + 2\pi/3) & \sin(\theta - 2\pi/3) \end{bmatrix} \quad (7-2)$$

- **Decomposition Capability Increases as Phase Number Increases.** It can be clearly seen from Fig. 7.2 and TABLE 7.2, as the number of virtual three-phase sets increases, the number of available subspaces increases as well, and the main current harmonics, i.e. the 5th, 7th, 11th, and 13th, are distributed more separately in these subspaces. For an example, the major current harmonics are completely separated in 4 subspaces if establishing a virtual pentuple three-phase system, see Fig. 7.2(d). However, in a virtual triple three-phase system, Fig. 7.2(b), the 5th is still coupled with the 13th, and so as the 7th and 11th.
- **Independent Current Control Loop in Each Subspace.** Since the subspaces are orthogonal and decoupled, the current regulators can be independent in each subspace. This avoids the interference among different frequencies during the current control process, simplifies the design process and parameter tuning of the current harmonic regulators, and improves the stability of the control system
- **Limitations at low frequency region.** Since the virtual multi three phase system is based on the phase shifting operation, at low frequency region, the LUT in phase shifting operation will be longer and will consume more memories of MCU. Additionally, during the dynamic state of current changing, the phase shifting operation is not

accurate which leads to a short pulsating in current response.

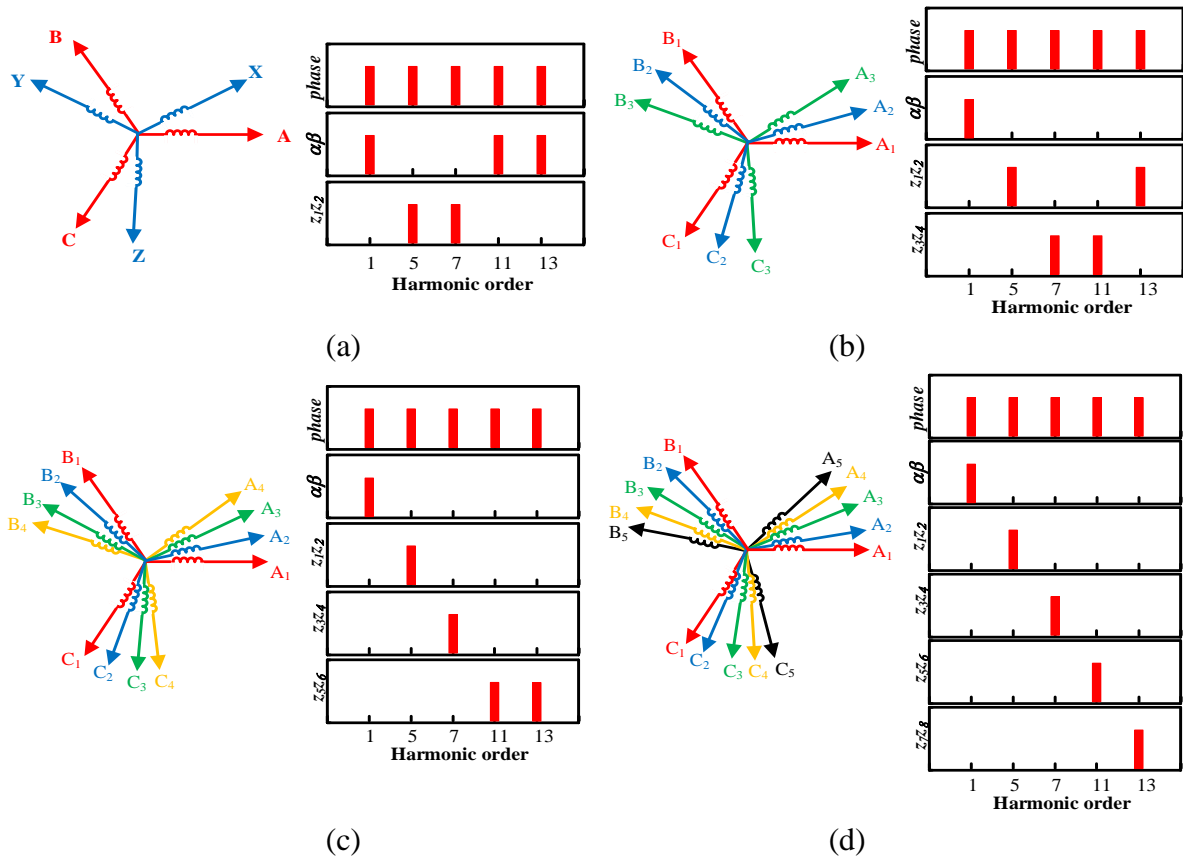


Fig. 7.2. Virtual multi three-phase winding configurations and harmonic mapping of VSD techniques. (a) DTP case. (b) TTP case. (c) QTP case. (d) PTP case.

TABLE 7.2

HARMONIC MAPPING OF DIFFERENT VIRTUAL MULTI THREE-PHASE SYSTEMS				
	Physical DTP	Virtual TTP	Virtual QTP	Virtual PTP
$\alpha\beta$ subspace	1st&11th&13th	1st	1st	1st
z_1z_2 subspace	5th&7th	5th&13th	5th	5th
z_3z_4 subspace		7th&11th	7th	7th
z_5z_6 subspace			11th&13th	11th
z_7z_8 subspace				13th

7.3 Improved MSRF Current Regulators

The multiple synchronous reference frame (MSRF) current regulators are employed and improved in this thesis. Compared to existing MSRF method, the improved MSRF current regulators process the following advantages:

- ***Free Harmonic Reference Tracking.*** The investigated MSRF current regulators can be used to track arbitrary current harmonic reference. This means the current harmonic can be completely eliminated if setting the current harmonic reference to 0, or the current harmonic can be injected if setting the current harmonic reference to other non-zero values.
- ***Generic PI Regulator Design.*** The parameters of the PI regulator are designed based on the machine inductance and resistance, and thus, there is only one parameter, i.e. the gain coefficient k_c , that needs to tune in the control loop for each current harmonic. Additionally, the 5th and 7th current harmonic regulators can share the same gain coefficient, and the 11th and 13th current harmonic regulators can share the same gain coefficient. Compared to the conventional MSRF regulators, the parameter tuning of the investigated MSRF current harmonic regulators is greatly simplified.
- ***Enhanced Dynamic Performance and Stability.*** Thanks to the complete decomposition of the current harmonics under the virtual multi three-phase systems, the LPFs, which are usually used to extract the current harmonics in MSRFs, can be cancelled from the current loops. Due to the fact that the LPFs produce delay in the current harmonic feedback and limit the bandwidth of the PI regulators in MSRFs, the cancellation of the LPFs significantly reduces the delay effect in the current harmonic feedback, leading to a more rapid current harmonic reference tracking and a more stable system.
- ***Digital Delay Compensated.*** The analysis in this thesis shows that the effect of digital delay becomes dominant as rotor speed increases or harmonic order increases. A phase compensation angle is hence employed to adjust the phase angle of the regulator's outputs and compensate the effect of the digital delay, leading to a larger stable margin of the current control loop.

7.4 Scaling Error Correction in Current Measurement

A novel high-frequency signal injection method is proposed in Chapter 5 to suppress the non-general current harmonics caused by the scaling error in the current measurement in DTP PM machine systems. Different from the general current harmonics, e.g. the 5th and 7th, the analysis shows that the scaling error can generate the negative-sequence 1st current harmonic in phase current, which can be also described as the 2nd current harmonics in the synchronous reference dq frame. To reduce these non-general current harmonics, a high frequency carrier voltage is injected into the z_1z_2 subspace. By controlling the scaling gains of the current measurement to eliminate the corresponding high frequency components in the phase currents, the scaling errors can be corrected, and the non-general current harmonics can be eliminated simultaneously. The correction method is proposed for the first time with reference to the previous literature, and it has the following properties:

- ***No Extra Torque Ripples Due to High-frequency Signals.*** In conventional three-phase machines, the high-frequency signal injection usually generate torque ripples and reduce the performance of the system. However, in this thesis, the high-frequency signal is only injected in the z_1z_2 subspace and does not generate any extra torque ripples.
- ***Isolated High-frequency Current Control.*** The control of the high-frequency current is isolated from the original current control loops, and thus it will not affect the control performance of the fundamental current or the current harmonics. It is also flexible to switch the method on/off when the scaling error correction is required/not required.

7.5 Future Work

This thesis has studied the current harmonic control strategies for DTP PM machines. Based on the investigation in this thesis, some future work can be suggested as follows:

- ***Optimization of Current Harmonic Reference.*** Generally, these current harmonic references are set as zero to achieve the current harmonic suppression. They can also be set as pre-designed values or online calculated values to achieve current harmonic injection, so that the average torque can be enhanced and the torque ripples can be reduced. It is concluded in this thesis that the investigated MSRF current harmonic regulators can track the current harmonic references more rapidly and stably compared

to existing regulators. However, how to determine the current harmonic references is not discussed in this thesis. Optimization of the current harmonic reference could be further investigated based on the MSRF current regulators proposed in this thesis.

- ***DC Offset Error Compensation.*** For the non-general current harmonics caused by the current measurement errors, this thesis only investigated the effect of the scaling errors and the method to online correct the scaling gains. The DC offset errors in the current measurement are not investigated here and they will also generate non-general current harmonics in the control system. The DC offset of current measurement can vary with the temperature even if it is compensated during the manual calibration. The online DC offset compensation could be a topic for future work.
- ***DC Link Current Ripple Suppression.*** The DC link current ripple suppression is also an interesting topic because it helps to protect the battery, reduce losses, minimize the DC link capacitor, and save cost. There are two main approaches to reduce the current ripples in DC link. The first one is known as carrier phase shifting, which change the phase angle relationship between the carriers of two inverters so that the high-frequency current components can flow between the two inverters and will not flow into the DC link. The second one is called predictive PWM technique. This technique will pre-calculate (predict) the results of all available switch sequences and select the optimal one that resulting the smallest DC link ripples to be applied in the next control cycle. Due to the time limitation, these two techniques are not investigated in this thesis, and are worth studying for DTP PM machine systems. These are being carried out by another PhD student in the Electrical Machines and Drives Group.

REFERENCES

- [LEV07] E. Levi, R. Bojoi, F. Profumo, H. A. Toliyat, and S. Williamson, "Multiphase induction motor drives - a technology status review," *IET Electr. Power Appl.*, vol. 1, no. 4, pp. 489-516, Jul. 2007.
- [LEV08] E. Levi, "Multiphase electric machines for variable-speed applications," *IEEE Trans. Ind. Electron.*, vol. 55, no. 5, pp. 1893-1909, May 2008.
- [LEV16] E. Levi, "Advances in converter control and innovative exploitation of additional degrees of freedom for multiphase machines," *IEEE Trans. Ind. Electron.*, vol. 63, no. 1, pp. 433-448, Jan. 2016.
- [ZHU07] Z. Q. Zhu and D. Howe, "Electrical machines and drives for electric, hybrid, and fuel cell vehicles," *Proc. IEEE*, vol. 95, no. 4, pp. 746-765, April 2007.
- [BOJ03] R. Bojoi, M. Lazzari, F. Profumo, and A. Tenconi, "Digital field-oriented control for dual three-phase induction motor drives," *IEEE Trans. Ind. Appl.*, vol. 39, no. 3, pp. 752-760, May 2003.
- [BOJ16] R. Bojoi, S. Rubino, A. Tenconi, and S. Vaschetto, "Multiphase electrical machines and drives: A viable solution for energy generation and transportation electrification," *Proc. Int. Conf. Expo. Elect. Power Eng.*, 2016, pp. 632-639.
- [ABD15] A. S. Abdel-Khalik, S. Ahmed, and A. M. Massoud, "Low space harmonics cancelation in double-layer fractional slot winding using dual multiphase winding," *IEEE Trans. Magn.*, vol. 51, no. 5, pp. 1-10, May 2015.
- [HU14] Y. Hu, Z. Q. Zhu, and K. Liu, "Current control for dual three-phase permanent magnet synchronous motors accounting for current unbalance and harmonics," *IEEE J. Emerging Sel. Topics Power Electron.*, vol. 2, no. 2, pp. 272-284, Jun. 2014.
- [REN15a] Y. Ren and Z. Q. Zhu, "Enhancement of steady-state performance in direct-torque-controlled dual three-phase permanent-magnet synchronous

machine drives with modified switching table,” *IEEE Trans. Ind. Electron.*, vol. 62, no. 6, pp. 3338-3350, Jun. 2015.

- [KAR14] J. Karttunen, S. Kallio, P. Peltoniemi, P. Silventoinen, and O. Pyrhönen, “Decoupled vector control scheme for dual three-phase permanent magnet synchronous machines,” *IEEE Trans. Ind. Electron.*, vol. 61, no. 5, pp. 2185-2196, May 2014.
- [JON09] M. Jones, S. N. Vukosavic, D. Dujic, and E. Levi, “A synchronous current control scheme for multiphase induction motor drives,” *IEEE Trans. Energy Convers.*, vol. 24, no. 4, pp. 860-868, Dec. 2009.
- [HU17] Y. Hu, Z. Q. Zhu, and M. Odavic, “Comparison of two-individual current control and vector space decomposition control for dual three-phase PMSM,” *IEEE Trans. Ind. Appl.*, vol. 53, no. 5, pp. 4483-4492, Sept.-Oct. 2017.
- [KAR12] J. Karttunen, S. Kallio, P. Peltoniemi, P. Silventoinen, and O. Pyrhönen, “Dual three-phase permanent magnet synchronous machine supplied by two independent voltage source inverters,” *Inter. Symp. Power Electron., Electr. Drives, Auto. Motion, Sorrento, 2012*, pp. 741-747.
- [Zmo01] D. N. Zmood, D. G. Holmes, and G. H. Bode, “Frequency-domain analysis of three-phase linear current regulators,” *IEEE Trans. Ind. Appl.*, vol. 37, no. 2, pp. 601-610, Mar. 2001.
- [ZMO03] D. N. Zmood and D. G. Holmes, “Stationary frame current regulation of PWM inverters with zero steady-state error,” *IEEE Trans. Power Electron.*, vol. 18, no. 3, pp. 814-822, May 2003.
- [CHE14] H. S. Che, E. Levi, M. Jones, W. Hew, and N. A. Rahim, “Current control methods for an asymmetrical six-phase induction motor drive,” *IEEE Trans. Power Electron.*, vol. 29, no. 1, pp. 407-417, Jan. 2014.
- [CHE16] X. Chen, J. Wang, V. I. Patel, and P. Lazari, “A nine-phase 18-slot 14-pole interior permanent magnet machine with low space harmonics for electric

vehicle applications,” *IEEE Trans. Energy Convers.*, vol. 31, no. 3, pp. 860-871, Sept. 2016.

- [KAR17] J. Karttunen, S. Kallio, J. Honkanen, P. Peltoniemi, and P. Silventoinen, “Partial current harmonic compensation in dual three-phase PMSMs considering the limited available voltage,” *IEEE Trans. Ind. Electron.*, vol. 64, no. 2, pp. 1038-1048, Feb. 2017.
- [YAN19] L. Yan, Y. Liao, H. Lin, and J. Sun, “Torque ripple suppression of permanent magnet synchronous machines by minimal harmonic current injection,” *IET Power Electron.*, vol. 12, no. 6, pp. 1368-1375, May 2019.
- [KAR16] J. Karttunen, S. Kallio, P. Peltoniemi, and P. Silventoinen, “Current harmonic compensation in dual three-phase PMSMs using a disturbance observer,” *IEEE Trans. Ind. Electron.*, vol. 63, no. 1, pp. 583-594, Jan. 2016.
- [XU20] Y. Xu, B. Zheng, G. Wang, H. Yan, and J. Zou, “Current harmonic suppression in dual three-phase permanent magnet synchronous machine with extended state observer,” *IEEE Trans. Power Electron.*, vol. 35, no. 11, pp. 12166-12180, Nov. 2020.
- [BLA99] F. B. del Blanco, M. W. Degner, and R. D. Lorenz, “Dynamic analysis of current regulators for AC motors using complex vectors,” *IEEE Trans. Ind. Appl.*, vol. 35, no. 6, pp. 1424-1432, Nov. 1999.
- [LI18] G. Li, F. Ma, A. Luo, Z. He, W. Wu, X. Wei, Z. Zhu, and J. Guo, “Virtual impedance-based virtual synchronous generator control for grid-connected inverter under the weak grid situations,” *IET Power Electron.*, vol. 11, no. 13, pp. 2125-2132, Oct. 2018.
- [SON17] Y. Song, X. Wang, and F. Blaabjerg, “Doubly fed induction generator system resonance active damping through stator virtual impedance,” *IEEE Trans. Ind. Electron.*, vol. 64, no. 1, pp. 125-137, Jan. 2017.

- [YIM09] J. Yim, S. Sul, B. Bae, N. R. Patel, and S. Hiti, "Modified current control schemes for high-performance permanent-magnet AC drives with low sampling to operating frequency ratio," *IEEE Trans. Ind. Appl.*, vol. 45, no. 2, pp. 763-771, Mar. 2009.
- [LIA17] Y. Liao, F. Li, H. Lin, and J. Zhang, "Discrete current control with improved disturbance rejection for surface-mounted permanent magnet synchronous machine at high speed," *IET Electr. Power Appl.*, vol. 11, no. 7, pp. 1333-1340, Apr. 2017.
- [WAN18] T. Wang, H. Nian, Z. Q. Zhu, L. Ding, and B. Zhou, "Flexible compensation strategy for voltage source converter under unbalanced and harmonic condition based on a hybrid virtual impedance method," *IEEE Trans. Power Electron.*, vol. 33, no. 9, pp. 7656-7673, Sept. 2018.
- [ZHA95] Y. Zhao and T. A. Lipo, "Space vector PWM control of dual three-phase induction machine using vector space decomposition," *IEEE Trans. Ind. Appl.*, vol. 31, no. 5, pp. 1100-1109, Sept. 1995.
- [JIA15] X. Jiang, W. Huang, R. Cao, Z. Hao, and W. Jiang, "Electric drive system of dual-winding fault-tolerant permanent-magnet motor for aerospace applications," *IEEE Trans. Ind. Electron.*, vol. 62, no. 12, pp. 7322-7330, Dec. 2015.
- [PAR12] Y. Park and S. Sul, "A novel method utilizing trapezoidal voltage to compensate for inverter nonlinearity," *IEEE Trans. Power Electron.*, vol. 27, no. 12, pp. 4837-4846, Dec. 2012.
- [KIM03] H. S. Kim, H. T. Moon, and M. J. Youn, "On-line dead-time compensation method using disturbance observer," *IEEE Trans. Power Electron.*, vol. 18, no. 6, pp. 1336-1345, Nov. 2003.
- [WAN20] L. Wang, Z. Q. Zhu, H. Bin, and L. M. Gong, "Current harmonics suppression strategy for PMSM with nonsinusoidal back-EMF based on

- adaptive linear neuron method,” *IEEE Trans. Ind. Electron.*, vol. 67, no. 11, pp. 9164-9173, Nov. 2020.
- [WAN15] K. Wang, Z. Q. Zhu, Y. Ren, and G. Ombach, “Torque improvement of dual three-phase permanent-magnet machine with third-harmonic current injection,” *IEEE Trans. Ind. Electron.*, vol. 62, no. 11, pp. 6833-6844, Nov. 2015.
- [FEN19] G. Feng, C. Lai, M. Kelly, and N. C. Kar, “Dual three-phase PMSM torque modeling and maximum torque per peak current control through optimized harmonic current injection,” *IEEE Trans. Ind. Electron.*, vol. 66, no. 5, pp. 3356-3368, May 2019.
- [HU20] M. Hu, W. Hua, W. Huang, and J. Meng, “Digital current control of an asymmetrical dual three-phase flux-switching permanent magnet machine,” *IEEE Trans. Ind. Electron.*, vol. 67, no. 6, pp. 4281-4291, June 2020.
- [ZHU20] Y. Zhu, W. Gu, K. Lu, Z. Wu, J. Guan, and L. Chen, “Current harmonic elimination method for asymmetric dual three-phase permanent magnet synchronous motor,” *IET Electr. Power Appl.*, vol. 14, no. 10, pp. 1795-1806, Oct. 2020.
- [HU18] S. Hu, Z. Liang, W. Zhang, and X. He, “Research on the integration of hybrid energy storage system and dual three-phase PMSM drive in EV,” *IEEE Trans. Ind. Electron.*, vol. 65, no. 8, pp. 6602-6611, Aug. 2018.
- [YEP11] A. G. Yepes, F. D. Freijedo, Ó. Lopez, and J. Doval-Gandoy, “High-performance digital resonant controllers implemented with two integrators,” *IEEE Trans. Power Electron.*, vol. 26, no. 2, pp. 563-576, Feb. 2011.
- [XIA15] C. Xia, B. Ji, and Y. Yan, “Smooth speed control for low-speed high-torque permanent-magnet synchronous motor using proportional-integral-resonant controller,” *IEEE Trans. Ind. Electron.*, vol. 62, no. 4, pp. 2123-2134, Apr. 2015.
- [CHA00] P. L. Chapman and S. D. Sudhoff, “A multiple reference frame synchronous

- estimator/regulator,” *IEEE Trans. Energy Convers.*, vol. 15, no. 2, pp. 197-202, Jun. 2000.
- [DHU19] H. Dhulipati, S. Mukundan, C. Lai, K. Mukherjee, J. Tjong, and N. C. Kar, “Multiple reference frame-based extended concentrated wound PMSM model considering PM flux linkage and inductance harmonics,” *IEEE Trans. Energy Convers.*, vol. 34, no. 2, pp. 731-740, June 2019.
- [LIU19] G. Liu, B. Chen, K. Wang, and X. Song, “Selective current harmonic suppression for high-speed PMSM based on high-precision harmonic detection method,” *IEEE Trans. Ind. Inform.*, vol. 15, no. 6, pp. 3457-3468, Jun. 2019.
- [FEN21] G. Feng, C. Lai, W. Li, Z. Li, and N. C. Kar, “Dual reference frame based current harmonic minimization for dual three-phase PMSM considering inverter voltage limit,” *IEEE Trans. Power Electron.*, vol. 36, no. 7, pp. 8055-8066, July 2021.
- [REN15b] Y. Ren and Z. Q. Zhu, “Reduction of both harmonic current and torque ripple for dual three-phase permanent-magnet synchronous machine using modified switching-table-based direct torque control,” *IEEE Trans. Ind. Electron.*, vol. 62, no. 11, pp. 6671-6683, Nov. 2015.
- [SHA21] B. Shao, Z. Q. Zhu, J.H. Feng, S. Y. Guo, Y. F. Li, L. Feng, and B. Shuang, “Improved direct torque control method for dual-three-phase permanent-magnet synchronous machines with back-EMF harmonics,” *IEEE Trans. Ind. Electron.*, doi: 10.1109/TIE.2020.3026282.
- [LUO18] Y. Luo and C. Liu, “A simplified model predictive control for a dual three-phase PMSM with reduced harmonic currents,” *IEEE Trans. Ind. Electron.*, vol. 65, no. 11, pp. 9079-9089, Nov. 2018.
- [LIU21] S. Liu and C. Liu, “Virtual-vector-based robust predictive current control for dual three-phase PMSM,” *IEEE Trans. Ind. Electron.*, vol. 68, no. 3, pp. 2048-2058, Mar. 2021.
- [YEP15] A. G. Yepes, J. Malvar, A. Vidal, O. López, and J. Doval-Gandoy, “Current

harmonics compensation based on multiresonant control in synchronous frames for symmetrical n-phase machines,” *IEEE Trans. Ind. Electron.*, vol. 62, no. 5, pp. 2708-2720, May 2015.

- [YEP13] A. G. Yepes, J. Malvar, A. Vidal, O. López, and J. Doval-Gandoy, “Current harmonic compensation in symmetrical multiphase machines by resonant controllers in synchronous reference frames—Part 2: Computational load,” *IECON Annual Conf. of the IEEE Ind. Electron. Society*, 2013, pp. 5161-5166.
- [PIL89] P. Pillay and R. Krishnan, “Modeling, simulation, and analysis of permanent-magnet motor drives. I. The permanent-magnet synchronous motor drive,” *IEEE Trans. Ind. Appl.*, vol. 25, no. 2, pp. 265-273, Mar. 1989.
- [MOH05] K. K. Mohapatra, R. S. Kanchan, M. R. Baiju, P. N. Tekwani, and K. Gopakumar, “Independent field-oriented control of two split-phase induction motors from a single six-phase inverter,” *IEEE Trans. Ind. Electron.*, vol. 52, no. 5, pp. 1372-1382, Oct. 2005.
- [HAD04] D. Hadiouche, H. Razik and A. Rezzoug, “On the modeling and design of dual-stator windings to minimize circulating harmonic currents for VSI fed AC machines,” *IEEE Trans. Ind. Appl.*, vol. 40, no. 2, pp. 506-515, Mar. 2004.
- [KIM07] S. Kim and S. Park, “Compensation of dead-time effects based on adaptive harmonic filtering in the vector-controlled ac motor drives,” *IEEE Trans. Ind. Electron.*, vol. 54, no. 3, pp. 1768-1777, Jun. 2007.
- [LEE21] J. H. Lee and S. K. Sul, “Inverter nonlinearity compensation through dead time effect estimation,” *IEEE Trans. Power Electron.*, 2021. doi: 10.1109/TPEL.2021.3061285.
- [RUA19] Z. Ruan, W. Song, and Y. Yan, “Current harmonic suppression for dual three-phase permanent magnet synchronous motor drives,” *IEEE Access*, vol. 7, pp. 143888-143898, 2019.

- [MAT05] P. Mattavelli, L. Tubiana and M. Zigliotto, "Torque-ripple reduction in PM synchronous motor drives using repetitive current control," *IEEE Trans. Power Electron.*, vol. 20, no. 6, pp. 1423-1431, Nov. 2005.
- [UZ16] E. Uz-Logoglu, O. Salor, and M. Ermis, "Online characterization of interharmonics and harmonics of ac electric arc furnaces by multiple synchronous reference frame analysis," *IEEE Trans. Ind. Appl.*, vol. 52, no. 3, pp. 2673-2683, May 2016.
- [ZAB16] M. Zabaleta, E. Levi, and, M. Jones, "Modelling approaches for triple three-phase permanent magnet machines," in *Prof. Int. Conf. Electr. Mach.*, 2016, pp. 466-472.
- [ZOR17] I. Zoric, M. Jones, and E. Levi, "Vector space decomposition algorithm for asymmetrical multiphase machines," in *Prof Int. Symp. on Power Electron.*, 2017, pp. 1-6.
- [MAR08] K. Marouani, L. Baghli, D. Hadiouche, A. Kheloui, and A. Rezzoug, "A new PWM strategy based on a 24-sector vector space decomposition for a six-phase VSI-fed dual stator induction motor," *IEEE Trans. Ind. Electron.*, vol. 55, no. 5, pp. 1910-1920, May 2008.
- [ZHO17] S. Zhou, J. Liu, L. Zhou, and Y. Zhang, "DQ current control of voltage source converters with a decoupling method based on preprocessed reference current feed-forward," *IEEE Trans. Power Electron.*, vol. 32, no. 11, pp. 8904-8921, Nov. 2017.
- [HOF16] N. Hoffmann, F. W. Fuchs, M. P. Kazmierkowski, and D. Schröder, "Digital current control in a rotating reference frame - Part I: System modeling and the discrete time-domain current controller with improved decoupling capabilities," *IEEE Trans. Power Electron.*, vol. 31, no. 7, pp. 5290-5305, July 2016.
- [LI12] S. Li and H. Gu, "Fuzzy adaptive internal model control schemes for PMSM speed-regulation system," *IEEE Trans. Ind. Inform.*, vol. 8, no. 4, pp. 767-779, Nov. 2012.

- [XIA10] C. Xia, C. Guo, and T. Shi, "A neural-network-identifier and fuzzy-controller-based algorithm for dynamic decoupling control of permanent-magnet spherical motor," *IEEE Trans. Ind. Electron.*, vol. 57, no. 8, pp. 2868-2878, Aug. 2010.
- [KIM10] H. Kim, M. W. Degner, J. M. Guerrero, F. Briz, and R. D. Lorenz, "Discrete-time current regulator design for AC machine drives," *IEEE Trans. Ind. Appl.*, vol. 46, no. 4, pp. 1425-1435, Jul. 2010.
- [RIC16] J. Richter and M. Doppelbauer, "Improving dynamics of repetitive control based current harmonic mitigation in inverter-fed permanent magnet synchronous machines with nonlinear magnetics," *IET Int. Conf. Power Electron., Machines and Drives (PEMD 2016)*, 2016, pp. 1-6.
- [BRI13] F. Briz, P. García, M. W. Degner, D. Díaz-Reigosa, and J. M. Guerrero, "Dynamic behavior of current controllers for selective harmonic compensation in three-phase active power filters," *IEEE Trans. Ind. Appl.*, vol. 49, no. 3, pp. 1411-1420, May 2013.
- [LIU14] J. M. Liu and Z. Q. Zhu, "Novel sensorless control strategy with injection of high-frequency pulsating carrier signal into stationary reference frame," *IEEE Trans. Ind. Appl.*, vol. 50, no. 4, pp. 2574-2583, July-Aug. 2014.
- [CON01] A. Consoli, G. Scarcella, and A. Testa, "Industry application of zero-speed sensorless control techniques for PM synchronous motors," *IEEE Trans. Ind. Appl.*, vol. 37, no. 2, pp. 513-521, March-April 2001.
- [EBE12] S. Ebersberger and B. Piepenbreier, "Identification of differential inductances of permanent magnet synchronous machines using test current signal injection," *IEEE Int. Symp. Power Electron. Gener. Syst., Electr. Drives, Auto. Motion*, 2012, pp. 1342-1347.
- [LU21] J. Lu, Y. Hu, J. Liu, J. Wang, and P. Li, "Fixed-point sampling strategy for estimation on current measurement errors in IPMSM drives," *IEEE Trans. Power Electron.*, vol. 36, no. 5, pp. 5748-5759, May 2021, doi: 10.1109/TPEL.2020.3031352.

- [LEE19] K. Lee and S. Kim, "Dynamic performance improvement of a current offset error compensator in current vector-controlled SPMSM drives," *IEEE Trans. Ind. Electron.*, vol. 66, no. 9, pp. 6727-6736, Sept. 2019, doi: 10.1109/TIE.2018.2877162.
- [CHO08] K. Cho and J. Seok, "Correction on current measurement errors for accurate flux estimation of AC drives at low stator frequency," *IEEE Trans. Ind. Appl.*, vol. 44, no. 2, pp. 594-603, March-april 2008, doi: 10.1109/TIA.2008.916730.
- [HAR08] M. C. Harke, J. M. Guerrero, M. W. Degner, F. Briz, and R. D. Lorenz, "Current measurement gain tuning using high-frequency signal injection," *IEEE Trans. Ind. Appl.*, vol. 44, no. 5, pp. 1578-1586, Sept.-Oct. 2008, doi: 10.1109/TIA.2008.2002170.
- [TRI18] Q. N. Trinh, P. Wang, Y. Tang, L. H. Koh, and F. H. Choo, "Compensation of DC offset and scaling errors in voltage and current measurements of three-phase AC/DC converters," *IEEE Trans. Power Electron.*, vol. 33, no. 6, pp. 5401-5414, June 2018, doi: 10.1109/TPEL.2017.2734809.
- [NAK05] H. Nakai, H. Ohtani, E. Satoh, and Y. Inaguma, "Development and testing of the torque control for the permanent-magnet synchronous motor," *IEEE Trans. Ind. Electron.*, vol. 52, no. 3, pp. 800-806, June 2005.
- [FEN18] G. Feng, C. Lai, and N. C. Kar, "Practical testing solutions to optimal stator harmonic current design for PMSM torque ripple minimization using speed harmonics," *IEEE Trans. Power Electron.*, vol. 33, no. 6, pp. 5181-5191, June 2018.
- [WU21a] L. Wu, Y. Guo, X. Huang, Y. Fang, and J. Liu, "Harmonic torque suppression methods for single-phase open-circuit fault-tolerant operation of PMSM considering third harmonic BEMF," *IEEE Trans. Power Electron.*, vol. 36, no. 1, pp. 1116-1129, Jan. 2021.
- [LEE20] J. H. Lee and S. K. Sul, "Inverter nonlinearity compensation of discontinuous PWM considering voltage drop of power semiconductor and dead time effect," *IEEE Energy Conv. Congr. Expo. (ECCE)*, 2020, pp.

5677-5682.

- [XU19] W. Xu, L. Wang, Y. Liu, and F. Blaabjerg, "Improved rotor flux observer for sensorless control of PMSM with adaptive harmonic elimination and phase compensation," *CES Trans. Electr. Mach. Syst.*, vol. 3, no. 2, pp. 151-159, June 2019.
- [WU19] C. Wu, X. Sun, and J. Wang, "A rotor flux observer of permanent magnet synchronous motors with adaptive flux compensation," *IEEE Trans. Energy Convers.*, vol. 34, no. 4, pp. 2106-2117, Dec. 2019.
- [KIM20a] H. Kim, S. Sul, H. Yoo, and J. Oh, "Distortion-minimizing flux observer for IPMSM based on frequency-adaptive observers," *IEEE Trans. Power Electron.*, vol. 35, no. 2, pp. 2077-2087, Feb. 2020.
- [KIM20b] H. Kim, Y. Han, K. Lee, and S. Bhattacharya, "A sinusoidal current control strategy based on harmonic voltage injection for harmonic loss reduction of PMSMs with non-sinusoidal back-EMF," *IEEE Trans. Ind. Appl.*, vol. 56, no. 6, pp. 7032-7043, Nov. 2020.
- [MUR18] H. Muramatsu and S. Katsura, "An adaptive periodic-disturbance observer for periodic-disturbance suppression," *IEEE Trans. Ind. Informat.*, vol. 14, no. 10, pp. 4446-4456, Oct. 2018.
- [HAN09] J. Han, "From PID to active disturbance rejection control," *IEEE Trans. Ind. Electron.*, vol. 56, no. 3, pp. 900-906, March 2009.
- [GIR21] M. T. Girgin, M. K. Guven, and M. Aydin, "A new harmonic current injection technique to reduce cogging torque in axial flux permanent magnet motors," *IEEE Trans. Magn.*, doi: 10.1109/TMAG.2021.3087460.
- [CHO21] H. J. Cho, Y. C. Kwon, and S. K. Sul, "Torque ripple-minimizing control of IPMSM with optimized current trajectory," *IEEE Trans. Ind. Appl.*, vol. 57, no. 4, pp. 3852-3862, July. 2021.
- [LAS07] C. Lascu, L. Asiminoaei, I. Boldea, and F. Blaabjerg, "High performance current controller for selective harmonic compensation in active power filters," *IEEE Trans. Power Electron.*, vol. 22, no. 5, pp. 1826-1835, Sept.

2007.

- [ROD11] P. Rodríguez, A. Luna, I. Candela, R. Mujal, R. Teodorescu, and F. Blaabjerg, “Multiresonant frequency-locked loop for grid synchronization of power converters under distorted grid conditions,” *IEEE Trans. Ind. Electron.*, vol. 58, no. 1, pp. 127-138, Jan. 2011.
- [WAN21] W. Wang, C. Liu, S. Liu, Z. Song, H. Zhao, and B. Dai, “Current harmonic suppression for permanent-magnet synchronous motor based on chebyshev filter and PI controller,” *IEEE Trans. Magn.*, vol. 57, no. 2, pp. 1-6, Feb. 2021.
- [WU21] Z. Wu, H. Zhang, K. Liu, W. Hua, G. Zhang, B. Wang, S. Ding, and J. Hang, “Dead-time compensation based on a modified multiple complex coefficient filter for permanent magnet synchronous machine drives,” *IEEE Trans. Power Electron.*, vol. 36, no. 11, pp. 12979-12989, Nov. 2021.
- [SIN02] Singh, G.K. “Multi-phase induction machine drive research—A survey.” *Electr. Power Syst. Res.* 2002, 61, 139–147.
- [JON02] Jones, M.; Levi, E. “A literature survey of state-of-the-art in multiphase AC drives.” *In Proceedings of the International Universities Power Engineering Conference (UPEC)*, Stafford, UK, 9–11 September 2002; pp. 505–510.
- [LIU18] Liu, Z.; Li, Y.; Zheng, Z. “A review of drive techniques for multiphase machines.” *CES Trans. Electr. Mach. Syst.* 2018, 2, 243–251.
- [SAL19] Salem, A.; Narimani, M. “A review on multiphase drives for automotive traction applications.” *IEEE Trans. Transport. Electr.* 2019, 5, 1329–1348.
- [ABD16] Abdel-Khalik, A.S.; Ahmed, S.; Massoud, A.M. “A six-phase 24-slot/10-pole permanent-magnet machine with low space harmonics for electric vehicle applications.” *IEEE Trans. Magn.* 2016, 52, 1–10.
- [XU18] Xu, P.L.; Feng, J.; Guo, S.; Feng, S.; Chu, W.Q.; Ren, Y.; Zhu, Z.Q. “Analysis of dual three-phase permanent magnet synchronous machines

- with different angle displacements.” *IEEE Trans. Ind. Electron.* 2018, 65, 1941–1954.
- [SUH19] Suhel, S.M.; Maurya, R. “Realization of 24-sector SVPWM with new switching pattern for six-phase induction motor drive.” *IEEE Trans. Power Electron.* 2019, 34, 5079–5092.
- [YAZ09] Yazdani, D.; Ali Khajehoddin, S.; Bakhshai, A.; Joos, G. “Full utilization of the inverter in split-phase drives by means of a dual three-phase space vector classification algorithm.” *IEEE Trans. Ind. Electron.* 2009, 56, 120–129.
- [MIY16] Miyama, Y.; Hazeyama, M.; Hanioka, S.; Watanabe, N.; Daikoku, A.; Inoue, M. “PWM carrier harmonic iron loss reduction technique of permanent-magnet motors for electric vehicles”. *IEEE Trans. Ind. Appl.* 2016, 52, 2865–2871.
- [HAN19] Han, X.; Jiang, D.; Zou, T.; Qu, R.; Yang, K. “Two-segment three-phase PMSM drive with carrier phase-shift PWM for torque ripple and vibration reduction.” *IEEE. Trans. Power Electron.* 2019, 34, 588–599.
- [ZHA20] Zhang, W.; Xu, Y.; Huang, H.; Zou, J. “Vibration reduction for dual-branch three-phase permanent magnet synchronous motor with carrier phase-shift technique.” *IEEE. Trans. Power Electron.* 2020, 35, 607–618.
- [MEC04] B. C. Mecrow et al., “Design and testing of a four-phase fault-tolerant permanent-magnet machine for an engine fuel pump,” *IEEE Trans. Energy Convers.*, vol. 19, no. 4, pp. 671-678, Dec. 2004,.
- [DOR13] O. Dordevic, M. Jones, and E. Levi, “A comparison of carrier-based and space vector PWM techniques for three-level five-phase voltage source inverters,” *IEEE Trans. Ind. Informat.*, vol. 9, no. 2, pp. 609-619, May 2013.
- [SCU20] F. Scuiller, F. Becker, H. Zahr, and E. Semail, “Design of a bi-harmonic 7-phase PM machine with tooth-concentrated winding,” *IEEE Trans. Energy*

Convers., vol. 35, no. 3, pp. 1567-1576, Sept. 2020.

- [ABD10] A. Abdelkhalik, M. Masoud, and W. Barry, "Eleven-phase induction machine: Steady-state analysis and performance evaluation with harmonic injection," *IET Electr. Power Appl.*, vol. 4, no. 8, pp. 670-685, Jul. 2010.

APPENDIX A

EXPERIMENTAL SYSTEM SETUP

In this appendix, the experimental platform for the DTP-PMSM control is described. The overall setup of experimental system is based on the dSPACE DS1005 system, and is shown in Fig.A.1. The experimental system includes three parts: control system, drive system, and the test rig. The dSPACE DS1005 is used as the controller to measure signals from the machine system and generate the gate drive signals to the six-phase inverter. The test rig includes a test DTP PM machine and a DC machine. The test DTP PM machine is connected to the DC motor with an adjustable power resistor as a load. The pictures of the experimental setup are shown in Fig. A.2. The detailed parameters for test machine and inverter for simulations and experiments are listed as in TABLE A.1. All the experimental results are collected from dSPACE and plotted in MATLAB.

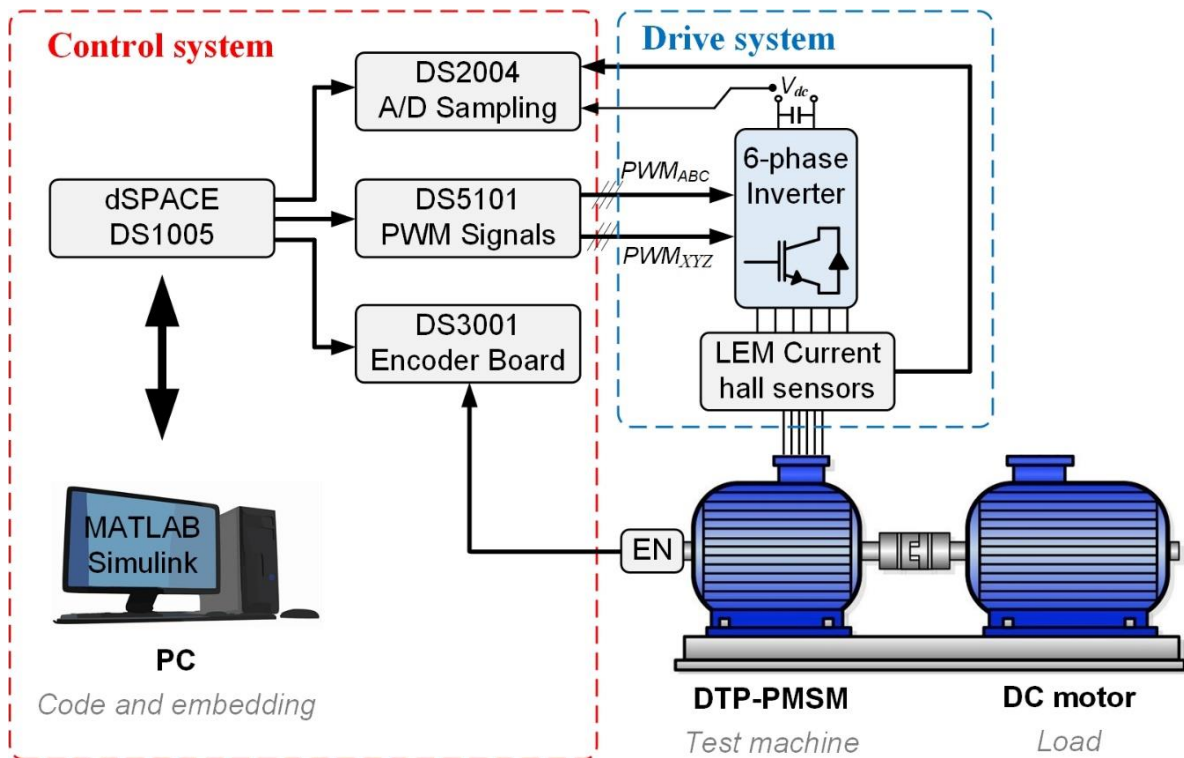
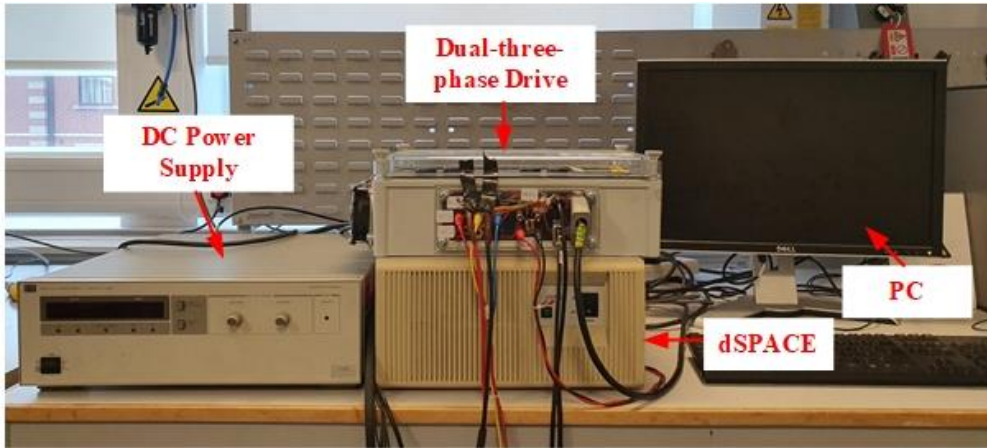
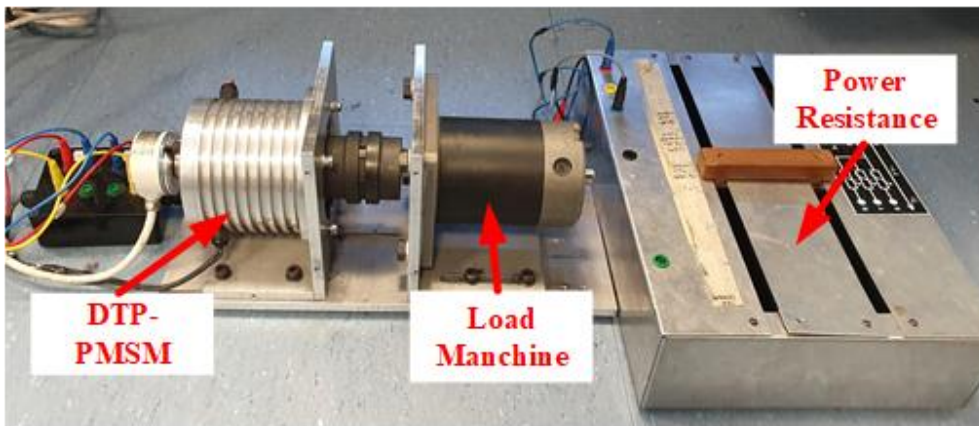


Fig.A.1. Overall setup of experimental system



(a)



(b)

Fig.A.2. Experimental system. (a) Drive control rig. (b) Test rig.

TABLE A.1

PARAMETERS OF TEST PROTOTYPE DTP-PMSM AND DRIVE SYSTEM

Parameters	Value
Number of pole pairs	5
Stator resistance	1.096Ω
α -axis and β -axis inductances	2.142mH
z_1 -axis and z_2 -axis inductances	0.875mH
Rated speed	400rpm
Rated power	240W
Rated torque	5.5Nm
DC-bus voltage	40V
Slot number	12
Pole number	10
Permanent magnet flux	0.734Wb

APPENDIX B

PUBLICATIONS

- [YAN21b] L. Yan, Z. Q. Zhu, J. Qi, Y. Ren, C. Gan, S. Brockway, and C. Hilton, “Multiple synchronous reference frame current harmonic regulation of dual three-phase PMSM with enhanced dynamic performance and system stability,” *IEEE Trans. Ind. Electron.*, vol. 69, no. 9, pp. 8825-8838, Oct. 2021.
- [YAN21c] L. Yan, Z. Q. Zhu, J. Qi, Y. Ren, C. Gan, S. Brockway, and C. Hilton, “Suppression of major current harmonics for dual three-phase PMSMs by virtual multi three-phase systems,” *IEEE Trans. Ind. Electron.*, vol. 69, no. 6, pp. 5478-5490, June 2021
- [YAN22] L. Yan, Z. Q. Zhu, Bo Shao, J. Qi, Y. Ren, C. Gan, S. Brockway, and C. Hilton, “Arbitrary current harmonic decomposition and regulation for permanent magnet synchronous machines,” *IEEE Trans. Ind. Electron.*, 2022, doi: 10.1109/TIE.2022.3183351.
- [YAN21a] L. Yan, Z. Q. Zhu, J. Qi, Y. Ren, C. Gan, S. Brockway, and C. Hilton, “Enhancement of disturbance rejection capability in dual three-phase PMSM system by using virtual impedance,” *IEEE Trans. Ind. Appl.*, vol. 57, no. 5, pp. 4901-4912, Sept. 2021.
- [ZHU21] Z. Zhu, S. Wang, B. Shao, L. Yan, P. Xu, and Y. Ren, “Advances in dual-three-phase permanent magnet synchronous machines and control techniques,” *Energies.*, vol. 14, no. 22, Aug. 2021.
- [WEI22a] F. Wei, Z. Q. Zhu, L. Yan, and J. Qi, “Investigation of stator/rotor pole number combinations and PM numbers in consequent-pole hybrid excited flux reversal machine,” *IEEE Transactions on Energy Conversion*, doi: 10.1109/TEC.2022.3163654.
- [QI22] J. Qi, Z.Q. Zhu, L. Yan, G. W. Jewell, C. Gan, Y. Ren, S. Brockway, and C. Hilton, “Suppression of torque ripple for consequent pole PM machine by asymmetric pole shaping method,” *IEEE Transactions on Industry*

Applications, vol. 58, no. 3, pp. 3545-3557, May-June 2022, doi: 10.1109/TIA.2022.3159629.

- [QI22] J. Qi, Z.Q. Zhu, L. Yan, G. W. Jewell, C. Gan, Y. Ren, S. Brockway, and C. Hilton, "Effect of pole shaping on torque characteristics of consequent pole PM machines," *IEEE Transactions on Industry Applications*, vol. 58, no. 3, pp. 3511-3521, May-June 2022, doi: 10.1109/TIA.2022.3156904.
- [XU22] L. Xu, Z. Q. Zhu, and L. Yan, "Low switching frequency SPWM strategies for open-winding machine with low current harmonics," *IEEE Transactions on Industry Applications*, vol. 58, no. 2, pp. 2042-2054, March-April 2022, doi: 10.1109/TIA.2021.3140191.
- [WEI22b] F. Wei, Z. Q. Zhu, X. Sun, L. Yan, and J. Qi, "Investigation of asymmetric consequent-pole hybrid excited flux reversal machines," *IEEE Transactions on Industry Applications*, vol. 58, no. 3, pp. 3434-3446, May-June 2022, doi: 10.1109/TIA.2022.3151316.
- [WEI22a] F. R. Wei, Z. Q. Zhu, H. Qu, L. Yan, and J. Qi, "New dual-PM spoke-type flux-reversal machines for direct-drive applications," *IEEE Transactions on Industry Applications*, 2022, doi: 10.1109/TIA.2022.3190248.
- [YAN20] L. Yan, Z. Q. Zhu, J. Qi, Y. Ren, C. Gan, S. Brockway, and C. Hilton, "Enhancement of disturbance rejection capability in dual three-phase PMSM system by using virtual impedance," 2020 IEEE Energy Conversion Congress and Exposition (ECCE), 2020, pp. 6104-6110.